TU Delft

Delft University of Technology

Document Version
Final published version

Licence
CC BY

Citation (APA)
Pezone, R. (2025). *Towards wafer-scale multilayer graphene mems condenser microphones*. [Dissertation (TU Delft), Delft University of Technology]. https://doi.org/10.4233/uuid:134c955a-5604-4bfb-bd3f-433be72a04ec

Important note
To cite this publication, please use the final published version (if applicable).
Please check the document version above.

Copyright
In case the licence states "Dutch Copyright Act (Article 25fa)", this publication was made available Green Open Access via the TU Delft Institutional Repository pursuant to Dutch Copyright Act (Article 25fa, the Taverne amendment). This provision does not affect copyright ownership.
Unless copyright is transferred by contract or statute, it remains with the copyright holder.

Sharing and reuse
Other than for strictly personal use, it is not permitted to download, forward or distribute the text or part of it, without the consent of the author(s) and/or copyright holder(s), unless the work is under an open content license such as Creative Commons.

Takedown policy
Please contact us and provide details if you believe this document breaches copyrights.
We will remove access to the work immediately and investigate your claim.

This work is downloaded from Delft University of Technology.

Towards wafer-scale multilayer graphene MEMS condenser microphones

Proefschrift

ter verkrijging van de graad van doctor
aan de Technische Universiteit Delft,
op gezag van de Rector Magnificus Prof.dr.ir. T.H.J.J. van der Hagen,
voorzitter van het College voor Promoties,
in het openbaar te verdedigen op vrijdag 6 juni 2025 om 12:30 uur

door

Roberto Pezone

Elektronisch ingenieur
Università degli Studi di Napoli Federico II, Italië,
geboren te Napels, Italië.

Dit proefschrift is goedgekeurd door de

promotor: em. prof. dr. ir. P.M. Sarro
promotor: prof. dr. P.G. Steeneken
promotor: dr. ir. S. Vollebregt

Samenstelling promotiecommissie:

Rector Magnificus,	voorzitter
Em. prof. dr. ir. P.M. Sarro,	Technische Universiteit Delft, promotor
Prof. dr. P.G Steeneken,	Technische Universiteit Delft, promotor
Dr. ir. S. Vollebregt,	Technische Universiteit Delft, promotor

Onafhankelijke leden:

Prof. dr. P.J. French,	Technische Universiteit Delft
Prof. dr. ir. F.P. Widdershoven,	Technische Universiteit Delft
Prof. dr. F. Niklaus,	KTH Royal Institute of Technology
Dr. H.S. Wasisto,	Infineon Technologies

Keywords: graphene, microphone, MEMS, membrane

Printed by: Proefschrift Maken

Front & Back: Front: SEM image of a multi-layer graphene MEMS condenser microphone. Back: A digital hand-sketch (made by OpenAI) of a MEMS condenser microphone architecture.

Copyright © 2025 by R.Pezone

ISBN 978-94-6510-663-2

An electronic version of this dissertation is available at
http://repository.tudelft.nl/.

A Francesco Maria

Contents

Summary vii

Samenvatting xi

1 Introduction 1
1.1 MEMS microphone demand . . . 3
1.2 MEMS-microphone architectures and key performance parameters . . . 5
1.2.1 MEMS condenser microphone and high sensitivity . . . 8
1.2.2 Down-scaling area and SNR . . . 10
1.3 Graphene . . . 12
1.3.1 Transfer and transfer-free for suspended graphene . . . 13
1.3.2 Graphene-based microphones . . . 16
1.4 Thesis Motivation and outline . . . 17
References . . . 18

2 Materials Selection for Mo-based Graphene in Micromachining 25
2.1 Introduction . . . 26
2.2 Deep reactive ion etching and BOSCH process . . . 26
2.3 Vapor HF . . . 28
2.4 Material compatibility with transfer-free graphene . . . 30
2.4.1 Silicon nitride as buffer layer for graphene synthesis . . . 30
2.4.2 Silicon carbide as buffer layers for graphene synthesis . . . 32
2.4.3 Aluminium oxide as buffer layers for graphene synthesis . . . 34
2.5 Surface micromachining drums using LPCVD SiN_x . . . 38
2.6 Conclusions . . . 41
References . . . 42

3 Miniaturized multi-layer graphene diaphragms 47
3.1 Introduction . . . 48
3.2 Experimental section . . . 48
3.2.1 Bulk micromachining process flow . . . 48
3.2.2 Mechanical compliance measurement . . . 50
3.3 Results and discussion . . . 50
3.3.1 Membrane fabrication results . . . 50
3.3.2 Graphene characterization . . . 53
3.3.3 Resonance frequency and mechanical compliance . . . 54
3.4 Conclusions . . . 58
3.5 Appendix . . . 59
References . . . 67

4 Multi-layer graphene-based MEMS condenser microphones 73
4.1 Introduction 74
4.2 Experimental section 74
4.2.1 Design concept and simulations 74
4.2.2 Bulk micromachining process flow 77
4.3 Results and discussion 80
4.3.1 Sacrificial layer release and device inspection 80
4.3.2 Eigenfrequency analysis 84
4.3.3 Base capacitance and pull-in. 86
4.3.4 Device response under sound actuation 88
4.3.5 Electrical response under sound actuation. 92
4.4 Conclusion 94
4.5 Appendix 95
References 102

5 Air-loading on the performance limits of graphene microphones 107
5.1 Introduction 108
5.2 Experimental Setup 109
5.3 Results and Discussion 112
5.4 Performance Limits and Implications 114
5.5 Conclusion 116
References 117

6 Graphene Microphone Arrays 121
6.1 Introduction 122
6.2 Sensor concept, design, and process-flow. 122
6.2.1 Analytical and lumped circuit simulation 124
6.2.2 Process-flow 130
6.3 Results and discussion 132
6.3.1 Microfabrication outcome 132
6.3.2 Electrical characterization 138
6.3.3 Analysis of Resonance Frequencies 141
6.4 Conclusion 144
References 145

7 Conclusions and recommendations 149
7.1 Conclusions. 150
7.2 Answers to the research questions 153
7.3 Recommendations for future work 153

Acknowledgements 157

List of Publications 163

SUMMARY

This thesis focuses on advancing Micro-Electro-Mechanical Systems (MEMS) microphones by exploring the integration of two-dimensional materials, particularly graphene, as an alternative to traditional silicon diaphragms. MEMS microphones are essential for current sensing solutions because of their small size, low-power consumption, and high-performance, but further miniaturization is increasingly limited by the brittleness and fabrication challenges of very thin silicon diaphragms.
Graphene, with its atomic thickness, exceptional strength, and flexibility, presents a promising solution. Its application in capacitive MEMS microphones could significantly enhance sensitivity, expand dynamic range, and reduce noise by improving the signal-to-noise ratio (SNR). These are critical performance parameters for a high-performance MEMS microphone.
However, integrating graphene into scalable MEMS production presents significant challenges, including fabrication difficulties arising from current transfer methods and uncertainties in device performance.
The introductory **Chapter 1** provides an overview of the MEMS field, with a particular focus on MEMS-microphones. It sets the stage by outlining the motivation behind this research work and formulating the central research questions addressed in this thesis.
Building upon this foundation, **Chapter 2** explores the pursuit of suitable strategies for realizing thin diaphragms based on multi-layer graphene. To this end, different materials grown and deposited on 100 mm silicon wafers, including silicon nitride (SiN_x), silicon dioxide (SiO_2), amorphous silicon carbide (a-SiC), and aluminum oxide (AlO_x) are systematically investigated. These materials are assessed as potential platforms for the subsequent growth of multi-layer graphene films through molybdenum-transfer-free Chemical Vapor Deposition (CVD) processes. The selection and evaluation of these materials represent a critical step toward enabling scalable and reliable integration of graphene into MEMS microphones.
Building on the foundations laid out in **Chapter 2**, **Chapter 3** presents the development of a wafer-scale (100 mm) fabrication process aimed at realizing large-area graphene membranes. In this process, thermal SiO_2 is employed as a sacrificial layer, while SiN_x is used for membrane clamping and etching mask. This approach successfully addressed several transfer-related limitations identified earlier, paving the way for more reliable and scalable integration of graphene diaphragms into MEMS devices.
Small membranes ($2R = 85 - 155\,\mu m$) achieved a 100% yield, whereas larger membranes ($2R = 300 - 350\,\mu m$) exhibited a decline in yield after the sacrificial release, highlighting the need to optimize the process further in order to reliably fabricate larger membrane sizes.
In order to evaluate the potential of these multi-layer graphene membranes as diaphragms for microphone applications, mechanical analyses were conducted, revealing funda-

mental frequencies between 92 kHz and 318 kHz, along with mechanical compliances significantly higher than those of commercial MEMS microphones.
These results provided a strong foundation for further exploration toward achieving electrical read-out, specifically through a capacitive architecture in which the electrical signal is detected by monitoring the graphene membrane's position relative to a counter electrode.
Consequently, **Chapter 4** demonstrates the integration of multi-layer graphene membranes into capacitive MEMS microphone architectures, once again employing the Mo-based transfer-free fabrication method.
The devices exhibited pull-in voltages between $V_{\text{pull-in}} = 2 - 9.5\,\text{V}$, suitable for ASIC-based sensitivity tuning. Mechanical compliances under 1 Pa of acoustic actuation varied across different designs and, despite the high compliance of the membranes, the bandwidth remained limited to below 1.5 kHz due to a device design that was not optimized for such highly compliant diaphragms. The estimated sensitivities reached up to $321\,\text{mVPa}^{-1}$, demonstrating the potential of graphene for achieving higher SNR even within miniaturized device footprints.
In parallel with the work presented in **Chapter 4**, a more in-depth study on the eigenfrequencies of bare membranes fabricated using the transfer-free method to avoid any possible contamination that could affect performance, it is carried out in **Chapter 5**. The influence of environmental pressure ("air-loading") on membrane resonance behavior is systematically investigated, revealing significant frequency shifts between vacuum and atmospheric conditions. This outcome is particularly relevant for microphone applications, as the membrane must maintain a resonance frequency above the audible bandwidth, specifically $f_{01} > 20\,\text{kHz}$.
Analytical modeling and COMSOL simulations show strong agreement with experimental results, highlighting how air-loading effectively increases the membrane's mass, thereby limiting the bandwidth response at atmospheric pressure. These findings provide critical design equations and insights for optimizing membrane radius, tension, and thickness in practical microphone designs.
Building on these results, **Chapter 6** introduces a new device concept aimed at optimizing both performance and fabrication yield, leveraging the understanding developed in the earlier chapters. High mechanical compliance (16.2 nmPa^{-1}) is demonstrated across a wide frequency range (10 Hz–10 kHz) using small-diameter ($R = 35\,\mu\text{m}$) drums, integrated into array-based capacitive read-out architectures. The fabrication yield is significantly improved, despite adopting a slightly modified process flow, underscoring the flexibility of the developed method. Fabrication reproducibility is validated accross same the same wafer evaluating several chips, although challenges remain in achieving uniform pre-tension and controlling membrane topography. Higher pull-in voltages ($V_{\text{bias}} > 20\,\text{V}$) are observed, consistent with expectations due to the smaller drum dimensions.
Overall, this thesis establishes a comprehensive framework including fabrication processes, experimental characterization, and theoretical modeling for graphene-based MEMS microphones.
It demonstrates that graphene diaphragms offer substantial advantages over conventional silicon, particularly in terms of mechanical compliance and sensitivity, while also

identifying key challenges such as air-loading effects and fabrication uniformity that must be addressed for successful commercialization. Furthermore, membrane robustness must be explored to enhance device durability, as current market trends demand highly robust solutions capable of withstanding large pressure differences, typical of portable electronics used in everyday life. Addressing these reliability aspects will be essential for positioning graphene-based MEMS microphones as strong candidates for future market applications. These results finally lay a solid foundation for the development of fully packaged demonstrators compatible with s ASIC systems, paving the way for high-performance devices with strong commercial potential.

SAMENVATTING

Deze thesis richt zich op de vooruitgang van Micro-Electro-Mechanical Systems (MEMS) microfoons door de integratie van tweedimensionale materialen, in het bijzonder grafeen, als alternatief voor traditionele siliciumdiaphragma's te onderzoeken. MEMS-microfoons zijn essentieel voor huidige detectieoplossingen vanwege hun kleine formaat, lage energieverbruik en hoge prestaties, maar verdere miniaturisatie wordt steeds meer beperkt door de brosheid en fabricage-uitdagingen van zeer dunne siliciumdiaphragma's.

Grafeen, met zijn atomaire dikte, uitzonderlijke sterkte en flexibiliteit, biedt een veelbelovende oplossing. De toepassing ervan in capacitieve MEMS-microfoons kan de gevoeligheid aanzienlijk verbeteren, het dynamische bereik vergroten en ruis verminderen door de signaal-ruisverhouding (SNR) te verbeteren. Dit zijn cruciale prestatieparameters voor een hoogwaardige MEMS-microfoon. Het integreren van grafeen in schaalbare MEMS-productie brengt echter aanzienlijke uitdagingen met zich mee, waaronder fabricageproblemen door de huidige transferttechnieken en onzekerheden in de apparaatprestaties.

Het inleidende **Hoofdstuk 1** geeft een overzicht van het MEMS-veld, met een bijzondere focus op MEMS-microfoons. Het vormt de basis door de motivatie achter dit onderzoekswerk en de centrale onderzoeksvragen die in deze thesis worden behandeld, te schetsen.

Voortbouwend op deze basis onderzoekt **Hoofdstuk 2** geschikte strategieën om dunne diaphragma's gebaseerd op meerlagig grafeen te realiseren. Daartoe worden verschillende materialen die zijn gegroeid en afgezet op 100 mm siliciumwafers — waaronder silicium nitride (SiN_x), silicium dioxide (SiO_2), amorf siliciumcarbide (a-SiC) en aluminiumoxide (AlO_x) — systematisch onderzocht. Deze materialen worden geëvalueerd als potentiële platformen voor de daaropvolgende groei van meerlagige grafeenfilms via molybdeen-transfervrije chemische dampdepositie (CVD) processen. De selectie en evaluatie van deze materialen vormen een cruciale stap om schaalbare en betrouwbare integratie van grafeen in MEMS-microfoons mogelijk te maken.

Voortbouwend op de basis die is gelegd in **Hoofdstuk 2**, presenteert **Hoofdstuk 3** de ontwikkeling van een wafer-scale (100 mm) fabricageproces gericht op het realiseren van grote grafeenmembraanoppervlakken. In dit proces wordt thermisch SiO_2 gebruikt als offerlaag, terwijl SiN_x wordt toegepast voor het vastklemmen van de membranen en als etsingsmasker. Deze aanpak heeft met succes verschillende beperkingen met betrekking tot transferproblemen, die eerder werden geïdentificeerd, opgelost, en effent de weg voor een betrouwbaardere en schaalbare integratie van grafeendiaphragma's in MEMS-apparaten.

Kleine membranen ($2R = 85 - 155\,\mu m$) behaalden een 100% opbrengst, terwijl grotere membranen ($2R = 300 - 350\,\mu m$) een afname in opbrengst vertoonden na het vrijmaken van de offerlaag, wat de noodzaak benadrukt om het proces verder te optimaliseren om

betrouwbaar grotere membranen te kunnen fabriceren.
Om de potentie van deze meerlagige grafeenmembraan als diaphragma's voor microfoonapplicaties te evalueren, werden mechanische analyses uitgevoerd. Hierbij werden fundamentele frequenties tussen 92 kHz en 318 kHz vastgesteld, evenals mechanische compliances die aanzienlijk hoger zijn dan die van commerciële MEMS-microfoons.
Deze resultaten boden een sterke basis voor verdere verkenning richting elektrische uitlezing, specifiek via een capacitieve architectuur waarbij het elektrische signaal wordt gedetecteerd door de positie van het grafeenmembraan ten opzichte van een tegenelektrode te monitoren.
Bijgevolg demonstreert **Hoofdstuk 4** de integratie van meerlagige grafeenmembraan in capacitieve MEMS-microfoonarchitecturen, opnieuw gebruikmakend van de molybdeengebaseerde transfervrije fabricagemethode.
De apparaten vertoonden pull-in spanningen tussen $V_{\text{pull-in}} = 2 - 9.5\,\text{V}$, geschikt voor ASIC-gebaseerde gevoeligheidsafstemming. Mechanische verplaatsingen onder 1 Pa van akoestische activering varieerden tussen verschillende ontwerpen en, ondanks de hoge compliance van de membranen, bleef de bandbreedte beperkt tot onder de 1.5 kHz door een ontwerp dat niet was geoptimaliseerd voor zulke hoog-compliantie diaphragma's. De geschatte gevoeligheden bereikten tot $321\,\text{mVPa}^{-1}$, wat de potentie van grafeen aantoont om een hogere SNR te bereiken, zelfs binnen miniaturiseerde apparaatfootprints.
Parallel aan het werk gepresenteerd in **Hoofdstuk 4**, wordt in **Hoofdstuk 5** een diepgaandere studie uitgevoerd naar de eigenfrequenties van kale membranen, vervaardigd via de transfervrije methode om mogelijke verontreinigingen die de prestaties kunnen beïnvloeden te vermijden. De invloed van de omgevingsdruk (äir-loading") op het resonantiegedrag van de membranen wordt systematisch onderzocht, waarbij aanzienlijke frequentieverschuivingen tussen vacuüm- en atmosferische omstandigheden aan het licht komen. Deze uitkomst is bijzonder relevant voor microfoonapplicaties, aangezien het membraan een resonantiefrequentie boven de hoorbare bandbreedte moet behouden, namelijk $f_{01} > 20\,\text{kHz}$.
Analytische modellering en COMSOL-simulaties tonen een sterke overeenkomst met experimentele resultaten en benadrukken hoe air-loading effectief de massa van het membraan verhoogt, waardoor de bandbreedterespons bij atmosferische druk wordt beperkt. Deze bevindingen leveren cruciale ontwerpvergelijkingen en inzichten op voor het optimaliseren van membraanradius, spanning en dikte voor praktische microfoontoepassingen.
Voortbouwend op deze resultaten introduceert **Hoofdstuk 6** een nieuw apparaatconcept gericht op het optimaliseren van zowel de prestaties als de fabricageopbrengst, voortbouwend op het begrip dat in de eerdere hoofdstukken is ontwikkeld. Hoge mechanische compliance ($16.2\ \text{nmPa}^{-1}$) wordt aangetoond over een breed frequentiebereik (10 Hz–10 kHz) met behulp van kleine trommels ($R = 35\,\mu\text{m}$), geïntegreerd in op arrays gebaseerde capacitieve uitleesarchitecturen. De fabricageopbrengst wordt aanzienlijk verbeterd, ondanks een licht gewijzigde processtroom, wat de flexibiliteit van de ontwikkelde methode onderstreept. Fabricagereproduceerbaarheid wordt gevalideerd over dezelfde wafer door evaluatie van meerdere chips, hoewel uitdagingen blijven bestaan in het bereiken van uniforme voorspanning en controle over de membraantopografie. Hogere pull-in spanningen ($V_{\text{bias}} > 20\,\text{V}$) worden waargenomen, in overeenstemming met

de verwachtingen door de kleinere trommeldimensies.
Al met al stelt deze thesis een uitgebreid raamwerk op, inclusief fabricageprocessen, experimentele karakterisering en theoretische modellering voor grafeengebaseerde MEMS-microfoons.
Het wordt aangetoond dat grafeendiaphragma's aanzienlijke voordelen bieden ten opzichte van conventioneel silicium, met name op het gebied van mechanische compliance en gevoeligheid, terwijl ook belangrijke uitdagingen worden geïdentificeerd zoals air-loading effecten en fabricage-uniformiteit die moeten worden aangepakt voor succesvolle commercialisatie. Bovendien moet de robuustheid van de membranen verder worden onderzocht om de duurzaamheid van het apparaat te vergroten, aangezien de huidige markttrends sterkere oplossingen vereisen die bestand zijn tegen grote drukverschillen, typisch voor draagbare elektronica die dagelijks wordt gebruikt. Het aanpakken van deze betrouwbaarheidseisen zal essentieel zijn om grafeengebaseerde MEMS-microfoons als sterke kandidaten voor toekomstige markttoepassingen te positioneren.
Deze resultaten leggen uiteindelijk een solide basis voor de ontwikkeling van volledig verpakte demonstrators die compatibel zijn met geavanceerde ASIC-systemen, waarmee de weg wordt vrijgemaakt voor hoogwaardige apparaten met een sterk commercieel potentieel.

1

INTRODUCTION

The growing significance of Micro-Electro-Mechanical Systems (MEMS) in both contemporary settings and future applications underscores the need for innovative approaches. These innovations should aim to enhance device performance, reduce size, and introduce new functionalities to the existing state-of-the-art. This thesis focuses on MEMS microphones, essential components in a wide range of consumer electronics. MEMS microphones are among the most important MEMS devices used daily by everyone, offering superior sound quality, lower power consumption, and greater durability. They are crucial for interfacing with other people and machines, where high quality is paramount for improved communication and functionality. Investigations into new concepts and materials, notably 2D materials, stem from their unique properties, which are expected to offer improvements over traditional silicon-based materials in the current state-of-the-art. Despite the initial achievements obtained with 2D materials such as graphene in MEMS devices, numerous constraints limit their future applications. A critical bottleneck lies in the physical integration of graphene into MEMS, where a fully automated fabrication system has yet to be established. Ultimately, it remains uncertain whether graphene can consistently enhance the current state-of-the-art MEMS microphones while reducing the device-sensitive area footprint.

Micro-electro-mechanical systems (MEMS) are a significant innovation in modern device engineering, integrating mechanical and electrical components at microscopic scales from a few micrometers to several millimeters.

MEMS technology has revolutionized production efficiency and cost-effectiveness by using mass-production techniques similar to those for integrated circuits (ICs) [1–4].

The genesis of MEMS can be traced back to the late 1960s, originating from early research at Westinghouse Laboratories. This work laid the foundation for integrating mechanical elements with electronic circuits on a single silicon chip, transforming both concept and function in microsystems. These works delivered a final optimized device in 1965 by Nathanson et al., where cantilever-based resonant gate transistors were fabricated (Figure 1.1) [5]. Subsequent advancements, like Bean's anisotropic etching of silicon in 1978, were also essential to leading new concept designs (Figure 1.1) [6].

By the 1980s, advancements in MEMS actuators, based on various driving principles and integrating different fabrication processes into mainstream manufacturing (Figure 1.1), marked a significant technological leap.

The 1990s saw the maturing of MEMS technologies with the commercialization of complex devices like accelerometers, gyroscopes, and microphones (Figure 1.1) underscoring the shift from simple electromechanical components to sophisticated electromechanical systems suitable for various applications.

MEMS devices exploit unique material properties and mechanical characteristics that emerge prominently at microscale dimensions. For instance, the high surface-area-to-volume ratio characteristic of microscale devices amplifies influential forces per unit area, enhancing force production and wear resistance. These properties are crucial for applications where traditional macro-scale devices cannot compete in size, efficiency, and cost.

Today, MEMS are ubiquitous, embedded in consumer electronics, automotive systems, medical devices, and more [7, 8]. In smartphones, MEMS sensors enhance user interaction; automotive applications contribute to greener, smarter, and safer vehicle technologies by improving emission controls and enhancing safety features.

The integration of MEMS into daily life is profound and pervasive, driven by their small size, high performance, and cost-effectiveness. This integration is expected to deepen as advancements in MEMS technology continue, driven by improvements in materials, fabrication processes, and new integrations with other technologies where a lower footprint is continuously demanded.

In the persistent pursuit of miniaturization within MEMS, a significant challenge emerges from the limitations of conventional materials, predominantly silicon, which has been the backbone of device fabrication. As devices shrink further, silicon's physical and functional limits constrain further advancements. To overcome these barriers, new materials, concepts, and breakthrough technologies are needed to target the next generation of microsystems.

The most promising candidates for this challenge as new materials are 2D materials, which offer exceptional properties ideal for nanoelectromechanical systems (NEMS) [9–15]. These materials, such as graphene and transition metal dichalcogenides, are characterized by their ultra-thin thickness (one atom or few nm) and high aspect ratios, enabling superior electrical, thermal, and mechanical properties compared to traditional

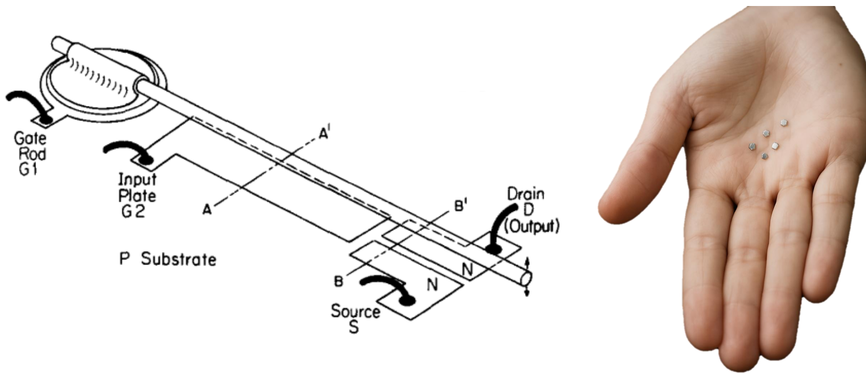

Figure 1.1: **Evolution of MEMS Devices.** This figure illustrates the progression of MEMS from their inception in the 1960s (reprinted from [5], with the permission of AIP Publishing) to today's highly miniaturized architectures. From left to right, the figure includes examples of the first fabricated MEMS [5] and images of various packaged MEMS.

bulk materials. The intrinsic strength, flexibility, and high conductivity make them suitable for applications where traditional materials might stumble under extreme miniaturization.

1.1. MEMS MICROPHONE DEMAND

MEMS microphones are established acoustic sensors with manufacturing volumes of billions of pieces per year in the consumer market [16, 17]. They have largely replaced the traditional electret condenser microphone (ECM) due to higher stability against environmental conditions such as temperature, humidity, and vibration, and better electro-acoustical performance, and more cost-effective production at smaller sizes.

In 2007, the year of the first iPhone's introduction, more than 90% of the microphones were ECMs, but only ten years later, more than 60% were based on MEMS technology for the overall microphone market. For mid-to-high-end smartphones, the penetration rate of MEMS microphones is even more than 90%. This technology change has enabled new use cases in different applications, leading to a considerable demand for silicon MEMS microphones [17].

These devices are used in many different markets and applications. Commercially, the consumer market with smartphones, smartwatches, PC/laptops, tablets, smart TVs, headsets, and voice personal assist devices is dominating by far. It is followed by hearing aid microphones and microphones for automotive applications.

According to Qualcomm's 2023 State of Sound Report, the daily use of headphones is increasing as more people work in noisy environments like cafés and require noise reduction for concentration or virtual meetings [18].

In consumer electronics and automotive sectors, voice recognition and generation are becoming vital features, yet challenges such as accent recognition, linguistic nuances, and background noise persist. Advanced Artificial Intelligence (AI) technologies are set to revolutionize these human-machine interactions by improving voice assistants and creating lifelike synthetic voices, enhancing accessibility for the visually impaired, and enriching user experience across digital platforms and customer support.
Moreover, Natural Language Processing (NLP) is essential for this, aiming to interpret spoken language accurately despite variances in expression or pronunciation and to detect emotions through speech dynamics. Practical NLP depends on high-quality audio input, whereas MEMS microphones excel due to their superior performance and low power consumption in a compact design. Thus, high-performance and miniaturized microphones are crucial in capturing speech with the highest quality, even in challenging environments, making them integral to developing AI-driven audio applications.
In conclusion, underscoring their increasing significance, the market for MEMS microphones is projected to grow from $2.26 billion in 2024 to $3.07 billion by 2029 [16]. This forecast is part of a broader market prediction for all types of MEMS, which is expected to rise from $14 billion in 2022 to $20 billion by 2028, according to Yole Development (Figure 1.2) [16, 19].

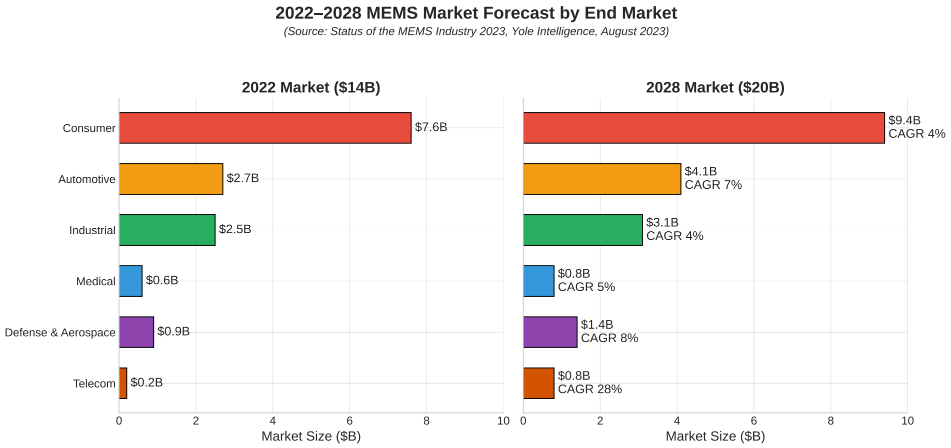

Figure 1.2: **Projected Growth in the MEMS Market by Sector (2022-2028)** This chart displays the forecasted market size for MEMS devices from 2022 to 2028 across various sectors. In 2022, the consumer sector dominated with $7.6B in revenue, followed by automotive and medical sectors. By 2028, the market is expected to grow to $20B, with the consumer sector still leading at $9.4B. Notably, the telecom sector is projected to experience the highest compound annual growth rate (CAGR) of 28%, although from a smaller base. Overall, the MEMS market is anticipated to grow at a CAGR of 5% from 2022 to 2028, driven by technological advances and expanding applications in these key industries. (Source: Status of the MEMS Industry 2023, Yole Intelligence, August 2023 [19].

1.2. MEMS-MICROPHONE ARCHITECTURES AND KEY PERFORMANCE PARAMETERS

The eardrum predominantly regulates human hearing, and the tympanic membrane vibrates in response to sound waves. These vibrations are converted into electrical signals transmitted to the brain, allowing us to perceive sound.

Conventional microphone technology emulates this natural mechanism through a sensitive vibrating membrane that captures sound. This concept is refined and miniaturized in the case of MEMS microphones, utilizing silicon to construct membranes typically around 1 mm in diameter and several hundreds of nm thick [17, 20, 21].

In order to increase the performance of silicon-based MEMS microphones, focusing solely on the physical MEMS structure, it is essential to create large and highly flexible membranes. These membranes, when subjected to the same sound pressure, can achieve significant displacement, translating into a higher electrical signal output, as detailed in subsection 1.2.1. For silicon membranes, decreasing the thickness is advisable to achieve larger displacement for same footprint. However, silicon's brittle nature poses significant challenges. Silicon is prone to cracking and fracture, especially when processed into ultra-thin films. This brittleness results in a high risk of mechanical failure, which severely limits the reliability and durability of the device. Moreover, fabricating uniform silicon diaphragms thinner than 10 nm across a wafer scale is complex and challenging. Critical factors such as maintaining consistent thickness, controlling stress, and preventing defects that can lead to mechanical failure or affect performance and resonance frequency are essential. These factors require highly precise and controlled fabrication processes, which must be meticulously managed to prevent the introduction of stress concentrators that could result in fractures.

Within these limitations, two-dimensional materials like graphene are gaining significant attention due to their remarkable physical properties, which hold great promise for overcoming these challenges. This approach enables the development of highly flexible and ultra-thin diaphragms, allowing researchers to study their performance in alignment with their theoretical properties.

To convert the mechanical signal from the movable membrane, induced by sound pressure, into an electrical signal, various architectural designs are employed.

Below, these various designs are explored in detail:

- **Condenser Microphones:** Standard in the industry, these microphones utilize a capacitive sensing principle with a movable membrane (first electrode) over an air gap and a rigid backplate (second electrode). This configuration is created using standard silicon materials and MEMS manufacturing processes. The bias voltage required to charge the capacitor is provided by an ASIC (application-specific integrated circuit), with the entire assembly mounted on a PCB (Figure 1.3).

- **Piezoelectric Microphones:** These microphones require only a flexible membrane without a backplate, simplifying manufacturing and reducing costs. They operate without an air gap, making them robust against particles that could cause reduced sensitivity or increased noise. The piezoelectric effect in materials such as aluminum nitride (AlN), zinc oxide (ZnO), or lead zirconate titanate (PZT) converts

mechanical stress into an electrical charge, which is then utilized as the electrical signal (Figure 1.3).

- **Optical Microphones:** These devices detect sound-induced deflections of a membrane by modulating light intensity. They typically include components like a light source (laser diode), an optical reflective membrane, a diffraction grating, and an optical sensor (photodiode array), creating a complex, power-intensive assembly(Figure 1.3).
- **Piezo-resistive Microphones:** They operate based on changes in resistance within the diaphragm's material under mechanical stress [22–25]. This deformation alters the distribution of charge carriers in the material, thereby changing its electrical resistance. This change is directly proportional to the applied stress, allowing the device to convert sound-induced mechanical movements into a variable electrical signal.

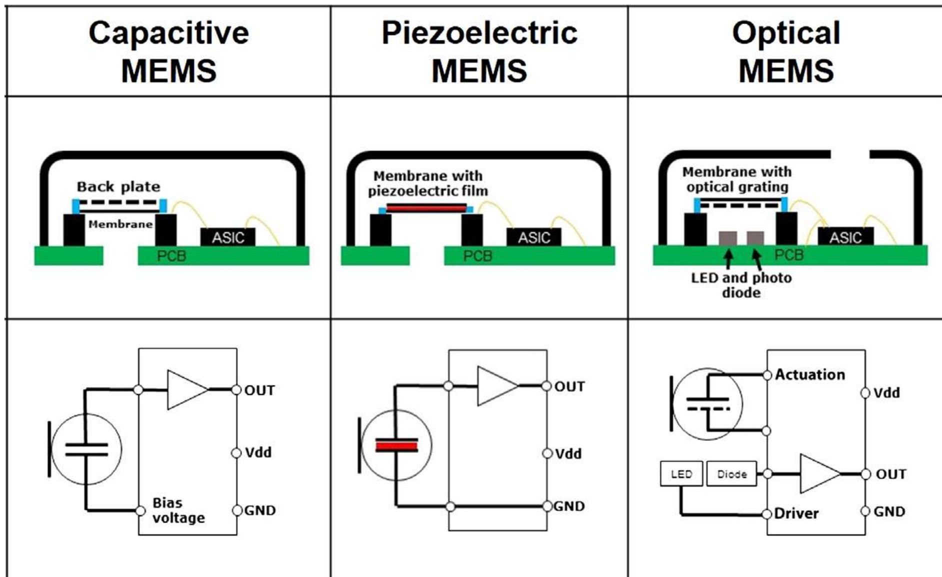

Figure 1.3: **Schematic Illustrations of the main MEMS Microphone Architectures**. This diagram depicts three distinct architectures for MEMS microphones: capacitive, piezoelectric, and optical MEMS. Each schematic provides an overview of the device layout within its packaging alongside an electrical circuit schematic highlighting the readout concept. Reprinted from [17] (Copyright 2020), with permission from Elsevier.

MEMS microphones are divided into analog and digital types, differing significantly in signal processing and susceptibility to disturbances. Analog MEMS microphones produce continuous signals within a defined range, making them more susceptible to electromagnetic interference, which can introduce noise and distort the signal. Achieving high-performance electrical implementation with analog microphones requires more time, effort, and precision.
In contrast, digital MEMS microphones convert the analog signal into a digital format,

typically using Pulse Density Modulation (PDM). Digital signals, represented as binary values (e.g., 0 V and 1.8 V), are more robust against disturbances. The binary nature of digital signals requires significant interference to cause bit errors, enhancing immunity to electromagnetic and radio frequency interference.
Digital MEMS microphones offer several advantages: superior disturbance immunity, shorter development times due to reduced design effort, and longer permissible trace lengths without signal degradation. These features make digital microphones easier to integrate into complex systems like laptops and smartphones. Additionally, digital interfaces simplify design by mitigating issues related to ground voltage fluctuations and signal coupling.
However, digital MEMS microphones also have drawbacks. The analog-to-digital conversion process within the microphone can consume more power and introduce noise, potentially resulting in a lower performance compared to analog microphones. Moreover, digital microphones are often more expensive due to the need for integrated analog-to-digital converters.
MEMS microphones are generally evaluated and classified based on various performance metrics or key parameters. These parameters are essential across various microphone technologies to assess their functionality and ensure they meet specific application requirements. Notably, this thesis does not focus on certain properties, such as current consumption in different operational modes, interface specifications, signal latency, and part-to-part matching. These aspects are excluded because they do not directly relate to the fundamental design principles of MEMS microphones.
The key parameters of microphones [17, 26] that are directly tied to the device's design and materials include:

- **Sensitivity:** The output per pressure signal is typically measured in dBV/Pa. For analog microphones, this is the voltage response to pressure.

- **Signal-to-Noise Ratio (SNR):** Describes the microphone's self-noise relative to a standard 1 Pa sine wave , crucial for effectively capturing quieter sounds.
  High SNR values are essential for applications involving distant sound sources or noisy environments. The unit measure is defined in dB(A).

- **Total Harmonic Distortion (THD):** Measures the harmonic distortion introduced by the microphone at high sound pressure levels (measured in %).
  Low THD is vital for maintaining sound fidelity, particularly in loud environments.

- **Acoustic Overload Point (AOP):** The maximum sound pressure level the microphone can handle without significant distortion is typically expressed in dBSPL (for THD = 10%). High AOP is critical in environments with loud background noises.
  Based on the key performance parameters of MEMS microphones, Table 1.1 is presented to delineate the current state-of-the-art MEMS microphones available in the market. This table exclusively considers analog MEMS microphones, as digital microphones incorporate a digital processing block whose performance metrics are not directly influenced by the MEMS design itself, thus rendering direct comparisons between analog and digital MEMS microphones impractical.

1

Manufacturer	Model	Dimensions W(mm) X L(mm) X H(mm)	Type	Sensitivity (dBV) at 1 kHz @ 94 dBSPL	SNR (dBA)	AOP (dBSPL)
STMicroelectronics	IMP23ABSU	2.65 X 3.5 X 1.08	Single	-38	64	130
STMicroelectronics	IMP23ABS1	2.65 X 3.5 X 1.08	Single	-38	64	130
Infineon Technologies AG	IM68A130A	2.50 X 3.33 X 0.98	Single	-38	68	130
Infineon Technologies AG	IM73A135	4.00 X 3.00 X 1.20	Differential dual	-38	73	135
TDK	ICS40730	4.72 X 3.76 X 3.50	Differential dual	-32	74	123
TDK	ICS40730	3.50 X 2.65 X 0.98	Single	-38	66	123
Knowles	SPK0410ALR5H1	4.00 X 3.00 X 1.20	Single	-38	71.8	130
Knowles	SPV610ALR5H1	2.75 X 1.85 X 0.90	Single	-42	64.5	134
Vesper	VM1010	3.76 X 2.95 X 1.30	Single	-38	60	125
Vesper	VM2002	3.76 X 2.95 X 1.30	Single	-63	50	152

Table 1.1: **State-of-the-Art MEMS Analog Microphones in the Market**. This table lists MEMS microphones currently exhibiting the highest sensitivity and SNR available. All reported devices use capacitive read-out, except for those from Vesper Technology, which utilize piezoelectric read-out. It includes the overall dimensions of the complete device packages without any details of the individual MEMS chips or membrane sizes. The specific chip sizes and further membrane specifications are not disclosed due to proprietary constraints and industry confidentiality agreements. Finally, single-ended interfaces are simple and inexpensive, requiring only two wires: one for signal and one for ground. They are suitable for environments with minimal electromagnetic interference but offer little protection against disturbances like radiated signals, cross-talk, and ground voltage fluctuations, which can complicate design and increase the risk of project delays. Differential interfaces, while more complex and costly, are ideal for high-quality signal capture in challenging environments. They use two complementary signal lines, with the effective output being the voltage difference between them. This configuration cancels out common-mode noise, providing better disturbance protection and more reliable signal integrity.

1.2.1. MEMS CONDENSER MICROPHONE AND HIGH SENSITIVITY

The central focus of this thesis is to explore the potential for reducing the size of MEMS microphones, or maintaining their current size while achieving higher performance, by replacing the silicon diaphragm with two-dimensional materials such as graphene. This approach aims to overcome the physical limitations of silicon described in Section 1.2. Among various MEMS microphone architectures, the capacitive type is preferred for this study due to its compatibility with the investigated material, which lacks significant piezoresistive and piezoelectric properties. The choice of this particular microphone architecture is more detailed explained accordingly with the capacitive trandusction functionality and in the next subchapter, demonstrating how the proposed research harmonizes with the inherent qualities of the condenser microphone architecture.

A capacitive MEMS microphone performance is mainly based on the pressure-sensitive membrane relationship, which deflects an average distance $x(P)$ [m], positioned against a fixed backplate at a separation g_0 [m] [17, 20, 21].

Typically, the microphone operates under a constant charge condition, denoted as $Q_0 = C_0 \cdot V_{\text{bias}}$, where V_{bias} [V] is the steady bias voltage supplied by the ASIC across the capacitor C_0.

$$V(P) = \frac{Q_0}{C(P)} = \frac{Q_0 \cdot (g_0 + x(P))}{C_0 \cdot g_0} = \frac{V_0 \cdot (g_0 + x(P))}{g_0} \tag{1.1}$$

Derived from Equation 1.1, an expression for microphone sensitivity S [V/Pa] is outlined as:

$$S = \frac{dV(P)}{dP} = \frac{V_{\text{bias}}}{g_0} S_{\text{m0}} \tag{1.2}$$

where $S_{\text{m0}} = \frac{dx(P)}{dP}$ [m/Pa] represents the membrane's mechanical compliance, calculated based on the mean deflection of the membrane under pressure. To express the sensitivity (S) of Equation 1.2 in decibels relative to 1 V (dBV) as in the Table 1.1, $S_{\text{dBV}} = 20\log_{10}\left(\frac{S}{1\,\text{V/Pa}}\right)$ is used.
According to Equation 1.2, achieving optimal microphone sensitivity requires a high bias voltage at a reduced air gap, coupled with significant membrane compliance.
However, these three design parameters are interdependent, complicating their optimization. An example of critical design constraint in capacitive MEMS microphones is the pull-in voltage $V_{\text{pull-in}}$ (Equation 1.3), which limits the V_{bias} and the consequence of the device performance.

$$V_{\text{pull-in}} = \sqrt{\frac{8kg_0^3}{27\epsilon_0\epsilon_{\text{air}}A}} \tag{1.3}$$

In this equation, ϵ_0 is the vacuum permittivity, ϵ_{air} is the dielectric (air) permittivity, k is the membrane spring constant, and A is its area. At this voltage level, referred to as the pull-in voltage, the membrane adheres to the backplate, rendering it unable to oscillate in response to incoming sound waves. The MEMS condenser microphone's membrane is pulled downward due to the electrostatic force generated by the electric field created by the bias voltage necessary to activate the device. Therefore, any adjustments to the sensitivity through higher bias voltages must be carefully balanced against the threshold set by the pull-in voltage to avoid compromising the microphone's operational integrity.
Another approach to enhancing the sensitivity S involves optimizing the membrane's performance through modifications in its geometry, tension, and clamping mechanisms [17]. Specifically, for fully clamped membranes, the compliance is influenced significantly by physical dimensions like membrane thickness (t), radius (R), and mechanical stress (σ) ($S_{\text{m0,circular}} = \frac{R^2}{8t\sigma}$). Larger membranes with lower stress (σ) typically exhibit greater compliance. However, to maintain performance within compact designs, adjustments must be made to the membrane's thickness and pre-tension.
Alternative methods, such as adjusting the gap depth, can also enhance sensitivity. More details on these approaches and their limitations are discussed in subsequent chapters.
Figure 1.4 presents schematic illustrations of different clamping geometries and summarizes various MEMS microphones from multiple manufacturers, highlighting their distinct clamping strategies.

- **Stress-controlled membranes** diameter and thickness are typically constrained by reliability requirements. Designing large and thin membranes poses significant challenges in ensuring robustness under high pressure. The primary factors influencing membrane stress include the deposition temperature of the membrane layer, the doping level, and the annealing steps (Figure 1.4a).

- **Free-floating membranes**, which are minimally constrained, allowing considerable stress relaxation and enhancing sensitivity (Figure 1.4b).

- **Corrugated membranes** that reduce high tensile stresses via etched trenches. These modifications can significantly decrease intrinsic tensile stresses, with compliance (C_m) being enhanced by minimizing the amplitude and increasing the frequency of the corrugations (Figure 1.4c).
- **Spring-supported membranes** incorporate beams or meander structures to distribute stress evenly, enhancing the microphone's robustness against mechanical shocks (Figure 1.4d).

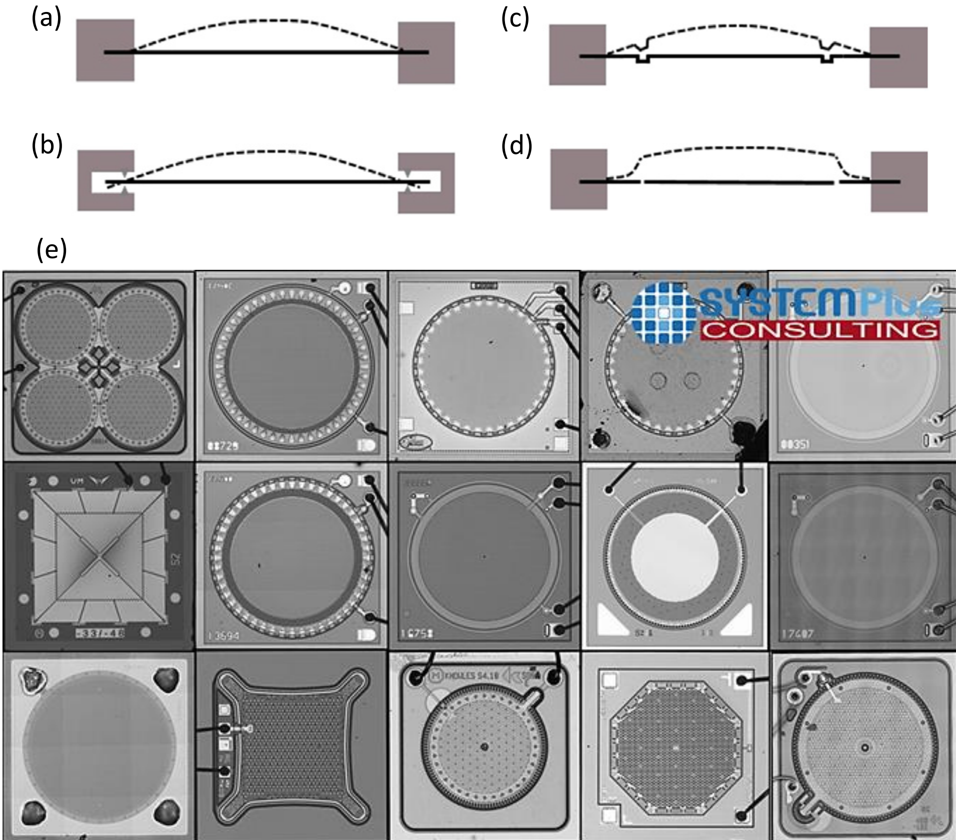

Figure 1.4: **Diaphragm clamping geometries in MEMS microphones**. Schematics (a-d) illustrate various diaphragm clamping configurations used to tune the membrane response to sound actuation. The image is reprinted from [17] (Copyright (2020), with permission from Elsevier. (e) it displays a collection of devices from various companies, showcasing different clamping geometries. Image is reprinted with permission from SystemPlus Consulting.

1.2.2. DOWN-SCALING AREA AND SNR

Reducing the device size generally leads to a decrease in sensitivity (S) due to lower R (radius), as ($S_{\text{m0,circular}} = \frac{R^2}{8t\sigma}$ for stress-controlled membranes) it correspondingly reduces

the SNR, as outlined in Equation 1.4 [27]. Despite a low stress and low mass membrane, given that the SNR's dependency on A is quadratic compared to its relation with other terms, it becomes essential to identify which parameter predominantly influences the SNR. Thus, scaling MEMS microphones presents significant challenges, mainly because reductions in size can adversely affect microphone sensitivity. For such type of device, the SNR can be quantitatively assessed through the following equation:

$$SNR = \frac{Q(p_s A)^2}{4k_B \sigma \omega_0 m} \tag{1.4}$$

This formula illustrates that improvements in SNR can be achieved by increasing the membrane area (A), enhancing the quality factor Q, reducing the resonance frequency ω_0, and decreasing the mass (m) and the σ. Targeting a lower footprint, 2D materials such as graphene, characterized by minimal tension, stress, and thickness, can still lead to high SNR. Moreover, p_s and k_B represent the spectral density of the signal pressure (sound) and the Boltzmann constant, respectively.
To visualize the effect of downscaling on the SNR, Figure 1.5 illustrates a variety of MEMS microphones, with sizes ranging from $0.8 \times 0.8\,\text{mm}^2$ to $1.9 \times 1.9\,\text{mm}^2$. The reported SNR values are based on empirical measurements; however, these values are influenced by factors beyond just membrane size, such as differences in package size and ASIC versions across the samples.

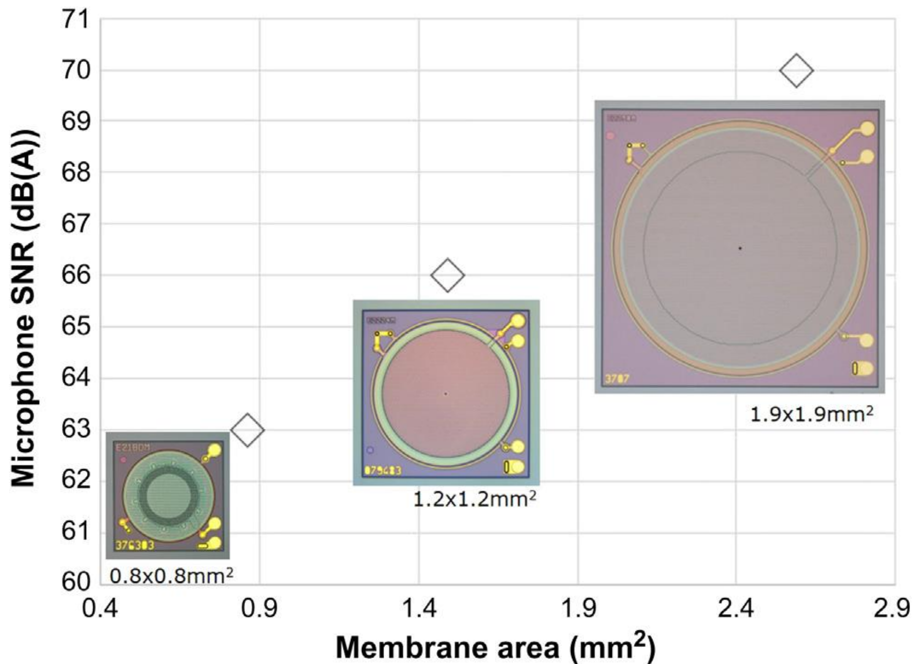

Figure 1.5: **SNR vs membrane size**. A comparison between the MEMS SNR and the membrane size. The image is reprinted from [17] (Copyright 2020), with permission from Elsevier.

1

1.3. GRAPHENE

Graphene, a revolutionary two-dimensional (2D) material, consists of a single layer of sp^2 hybridized carbon atoms arranged in a dense honeycomb lattice where each atom is bonded to the neighbors at a distance of approximately 1.42 Å(Figure 1.6a-e).
Known as the precursor to other carbon allotropes, graphene can transform into various forms: it can be wrapped into zero-dimensional fullerenes, rolled into one-dimensional carbon nanotubes, and stacked to form three-dimensional graphite.
The isolation of graphene was first achieved through a groundbreaking experiment by K.S. Novoselov and A.K. Geim in 2004, which led them to win the 2010 Nobel Prize in Physics. Their research not only introduced the "Scotch tape method" for isolating few-layer graphene (FLG) but highlighted graphene's unique electronic properties (Figure 1.6a-e) that were fully characterized in subsequent studies. This simple yet effective method marked a significant advancement in understanding graphene's potential, particularly its exceptional electronic, mechanical, thermal, and optical properties (Figure 1.6e) [28–31].
Its isolation marked a new era in materials science, particularly in surpassing the limitations of traditional materials such as silicon. Thus, graphene's electron mobility is nearly 100 times greater than silicon's, facilitating the development of faster, more efficient electronic devices, and its mechanical properties are unparalleled, with an ultrahigh Young's modulus of approximately 1 TPa and the ability to endure strains up to 25% without fracturing. Additionally, its flexibility and transparency overcome many limitations of traditional materials, making graphene essential for next-generation applications.

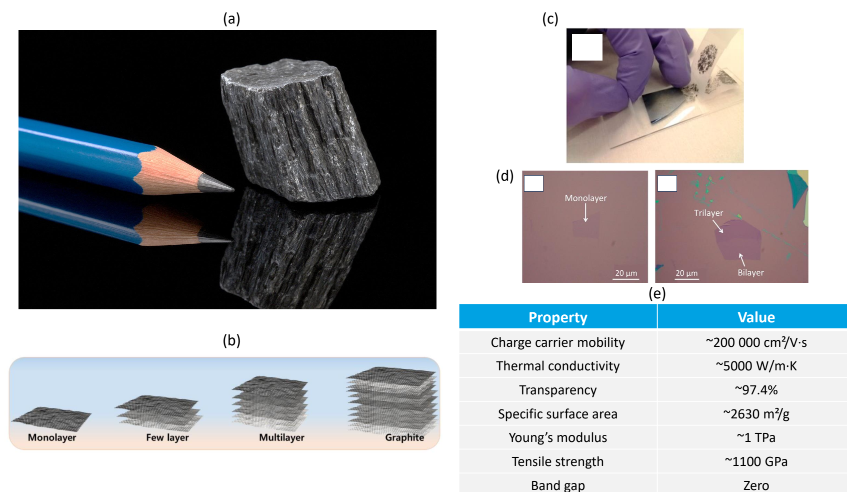

Property	Value
Charge carrier mobility	~200 000 cm^2/V·s
Thermal conductivity	~5000 W/m·K
Transparency	~97.4%
Specific surface area	~2630 m^2/g
Young's modulus	~1 TPa
Tensile strength	~1100 GPa
Band gap	Zero

Figure 1.6: **From Graphite to Graphene**. (a) a graphite block, shown with a common application as the tip of a pencil. (b) Various materials derived from graphite, along with their schematics [32]. This image is reprinted with permission from [32], copyright (2022) MDPI.(c) The process of isolating graphene from graphite using the tape-stamping method [33]. (d) Images of graphene flakes as viewed under an optical microscope on silicon chip substrates [33]. Images c and d are reprinted with permission from [33], copyright (2015) American Chemical Society. (e) Key physical properties of pristine graphene that make graphene ideal for numerous applications.

In recent years, various methods have been developed to isolate and fabricate atomically thin 2D materials like graphene [34–36]. Each of these techniques is specifically tailored to produce materials of particular sizes, thicknesses, and qualities, which in turn affect their intrinsic electrical and mechanical properties. As a result, graphene has emerged as a vital material for next-generation applications, and the choice of synthesis method becomes critical to achieving desired properties.

One widely used technique for producing graphene is mechanical exfoliation, which is a simple yet effective way to obtain high-quality two-dimensional sheets. This method involves peeling off thin crystalline flakes from bulk-layered materials using adhesive tape. Although mechanical exfoliation is limited by factors such as flake thickness and deposition control, it offers the advantage of producing atomically thin flakes that can be identified and differentiated through optical microscopy techniques. This method's simplicity makes it a valuable tool, though its limitations mean it may not be suitable for all applications.

A second approach is liquid-phase exfoliation, which involves immersing bulk-layered materials in a liquid medium and using techniques such as sonication or chemical agents to exfoliate the material into thinner layers. This method is highly valued for its ability to produce large quantities of graphene at relatively low cost. However, it often yields smaller flakes that may not be suitable for certain applications. Despite this drawback, liquid-phase exfoliation is considered a practical and efficient way to synthesize graphene, particularly when high yield and low cost are critical factors.

A third method, chemical vapor deposition (CVD), along with epitaxial growth, represents a more advanced, bottom-up approach. In these processes, 2D materials are synthesized directly onto substrates, such as metals like copper and nickel, or silicon carbide. These techniques allow for the growth of high-quality, nearly pristine graphene directly on desired substrates. This makes them particularly well-suited for applications in electronics and other fields that require graphene with highly controlled properties and minimal defects.

Finally, when selecting a method for synthesizing graphene, it is essential to carefully evaluate and choose the technique based on the intended application. The synthesis method has a significant impact on the material's final properties, and the trade-offs between different techniques must be weighed. Each approach offers specific advantages and limitations, and the decision ultimately depends on the application's requirements, whether it be high-quality materials for electronics or cost-effective production for large-scale uses.

1.3.1. TRANSFER AND TRANSFER-FREE FOR SUSPENDED GRAPHENE

Transferring graphene or other two-dimensional materials from the source substrate, usually metal, for CVD growth materials to a final functional substrate is crucial for their integration into real applications, particularly in MEMS.

Numerous methods have been developed to transfer graphene, primarily polymer-assisted techniques [37–42]. One common approach involves using polymethyl methacrylate (PMMA) as a carrier, where the final transfer can be achieved through either wet or dry methods (Figure 1.7a).

For the wet transfer method, PMMA is coated onto the graphene-layered metal sub-

strate, which can be either flexible or rigid. The metal is then removed using wet etchants, leaving the polymer graphene heterostructure floating in the solution. After proper acid neutralization, the PMMA/graphene heterostructure is transferred to the desired substrate, and finally, the PMMA is removed using suitable solvents such as acetone (Figure 1.7a).

Alternatively, dry transfer methods include covering the graphene/metal stack with PMMA and a thermal release tape. After etching the catalyst metal, washing, and drying, the thermal tape/graphene/PMMA heterostructure is transferred to the target substrate. The thermal tape is released at high temperatures, securing the graphene/PMMA onto the final substrate.

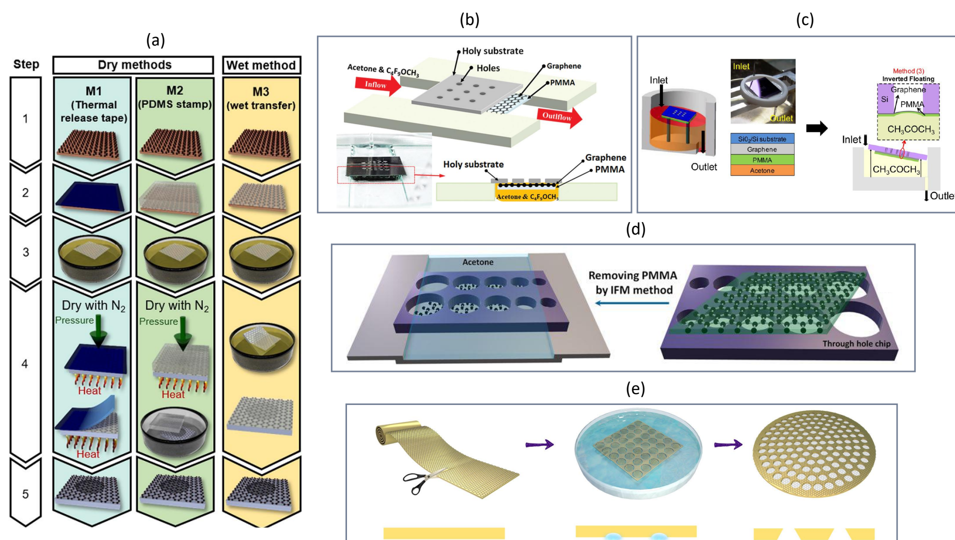

Figure 1.7: **Methods for Fabricating Graphene Membranes.** (a) illustrates three approaches: a dry-transfer method employing thermal release tape and PMMA, a semi-dry method incorporating PDMS with PMMA, and a wet-transfer method utilizing solely PMMA. This image is reprinted from [37], Copyright (2016), with permission from Elsevier. Panels (b-d) depict wet transfer methods featuring IFM techniques [30, 40, 43]. (b) Image is used with permission from [40] (Copyright 2009), permission conveyed through Copyright Clearance Center, Inc. (c) Reprinted with permission from [30] (Copyright 2014 American Chemical Society). (d) Image is reproduced from [43] under the terms of the CC BY 4.0 license. (e) shows an example of a transfer-free method used to create free-standing graphene suitable for TEM grids [44]. Image is reproduced from [44] under the terms of the CC BY 4.0 license.

Another semi-dry approach involves covering the photoresist/PMMA/graphene stack with a polydimethylsiloxane (PDMS). After the metal etching by wet chemistry, the stack is pressed onto the target substrate, and the photoresist is dissolved, leaving the PMMA/-graphene on the substrate.

However, the removal of PMMA presents significant challenges. Although solvents like acetone can dissolve PMMA, residues often remain, potentially causing doping and mass increase of the graphene, which affects its carrier mobility and mechanical properties. These residues can degrade its properties so significantly that its exceptional advantages are no longer evident. Also, the described methods show lower yields with the increase

of the target topography of the substrates.
Based on these methods, new approaches have been developed to fabricate free-standing graphene membranes to improve yield.
These include innovative techniques for removing the polymer support to minimize membrane damage, particularly from capillary forces during drying. For instance, several Inverted Floating Method (IFM) approaches were introduced, improving the final yield of the fabricated free-standing graphene (Figure 1.7b-d) [30, 40, 43]. This integration results in the inclusion of graphene in MEMS, where movable membranes are generally needed.
Transfer-free methods have also been developed for fabricating suspended graphene suitable for TEM grids (Figure 1.7e). In these instances, the copper foil on which graphene is grown via CVD is locally etched following lithography, releasing the suspended graphene. In these cases, the drying is generally done using critical point drying (CPD) methods.
These methods have shown promise in producing high-quality large membranes with diameters less than 1.5 mm. However, they generally do not scale well for mass production. Furthermore, these methods are incompatible with further patterning processes to finalize MEMS devices on a wafer scale. This compatibility issue presents a significant challenge in integrating these methods into broader manufacturing practices for electrically read-out sensors.
Table 1.2 is included to primarily outline the most significant methods employed in the production of free-standing graphene, highlighting yields and sizes.

Authors	Transfer	Membrane 2R [μm]	Yield
Zheng et al.	No	15 - 60	18x18 TEM grids (64 cm^2) 95-40% for 2R=15-40 μm(single-layer) 97-88% for 2R=20-50 μm (bi-layer) 100-95% for 2R=30-60 μm (few-layers)
Wagner et. al	Yes	2 - 10	2x si-substrates 13 mm x 13 mm (partial covered by graphene) 120x closed cavities (t=1.4 μm), 0% (single-layer) with thermal tape 5% (bi-layer) with thermal tape 2.7% (single-layer) with PDMS, 0% (single-layer) with PDMS 0% (single-layer) with wet-step, 16% (bi-layer) with wet-step
Lee et al	Yes (IFM)	5 - 500	61/75(81%) for 2R=5 μm all single-layer 58/75(77%) for 2R=10 μm, 56/75(75%) for 2R=20 μm 54/75(72%) for 2R=30 μm, 17/24(71%) for 2R=60 μm 20/31(65%) for 2R=100 μm, 14/28(50%) for 2R=110 μm 2/12(17 %) for 2R=500 μm
Aleman et al.	NO	30 - 60	TEM grid (~1000-3000 μm^2) all single-layer 75% for 2R=30-60 μm TEM grid (~300 μm^2) 100 % for 2R=20 μm
Akbari et al.	Yes (IFM)	500 - 750	40-4% for 2R=10-75 μm (single-layer with 20 μm grain-size) 70-1% for 2R=10-500 μm (single-layer with 50 μm grain-size) 90-2% for 2R=10-750 μm (bi-layer)
Chen et al.	Yes	100 - 1500	86% for 2R=100 μm all five-layers 82% for 2R=200 μm, 72% for 2R=400 μm, 55% for 2R=600 μm 43% for 2R=800 μm, 43% for 2R=1000 μm, 22% for 2R=1200 μm 17% for 2R=1500 μm

Table 1.2: **Summary of Transfer and Transfer-Free Techniques for Producing Free-Standing Graphene**. This table includes detailed information on targeted membrane sizes, thickness, and yield rates [30, 37, 43–46].

1.3.2. GRAPHENE-BASED MICROPHONES

Graphene has been used in capacitive read-out configurations in microphones owing to its high flexibility and minimal thickness, making it an excellent choice for a movable diaphragm according to Equation 1.2. This implementation should enhance the detection of very quiet sound pressures due to the minimum stress, mass, and thickness, expanding the dynamic range and reducing the equivalent input noise (EIN), leading to high SNR.

Despite its single atomic thickness, theoretically, pristine graphene exhibits substantial tensile strength up to 1100 GPa, enabling it to withstand significant displacements without damage to the membrane. This characteristic makes graphene highly appealing as a diaphragm, as it can endure high sound pressures and shocks without breaking. Although the sound pressure typically encountered is much lower than the maximum elongation graphene can theoretically withstand, this suggests that graphene diaphragms can support very large displacements, potentially leading to a significantly high sensitivity, SNR and AOP.

However, in a capacitive read-out, with very high membrane displacement, read-out would not be linear, offering an issue for read-out. However, this case might need a new technique to linearize the response from a sensor, physical design, or circuit.

Figure 1.8, where the main graphene-microphone works are summarized, revealing the absence of viable methods for wafer-scale integration. These methods largely depend on transfer techniques and often involve adding a polymer layer to the graphene to improve fabrication feasibility.

Although, using polymer supports, it is crucial to define which factor, increased stiffness or increased mass, has a more significant impact on the resonance frequency as in Equation 1.5.

$$f_0 = \frac{2.405}{2\pi R}\sqrt{\frac{n_0}{\rho t}} \tag{1.5}$$

Here, ρ stands for the mass density of the membrane, and n_0 is its pre-tension related to its stress and t is the thickness.

Nonetheless, from a sensitivity perspective, adding a polymer layer plays a critical role in influencing the overall performance of the microphone.

Present methodologies (Figure 1.8) for integrating graphene in microphones lack automation and predominantly rely on manual assembly processes unsuited for scaling up production. These manually assembled devices often feature diaphragms with diameters exceeding 2 mm, which are considerably larger than those in state-of-the-art microphones, thereby limiting opportunities for miniaturization. To overcome these limitations, developing innovative approaches is critical for graphene future MEMS integration. Such approaches would enable significant reductions in footprint, evaluating if graphene can still provide advantages due to its properties.

More particularly, Wittman et al.[47] conducted a study on a graphene microphone with a 40 μm diaphragm composed of a single graphene layer. This study demonstrated low sensitivity, likely due to the device's small geometry and the diaphragm's restricted displacement. Notably, the sensitivity was assessed through indirect methods, which did not directly measure the membrane's movement or utilize electrical read-out, introducing possible uncertainties in the findings. Consequently, the feasibility of employing

graphene in microphone devices smaller than 1 mm that meet or outperform the technological state-of-the-art remains an open challenge, as does the viability of manufacturing devices at such a micro-scale.

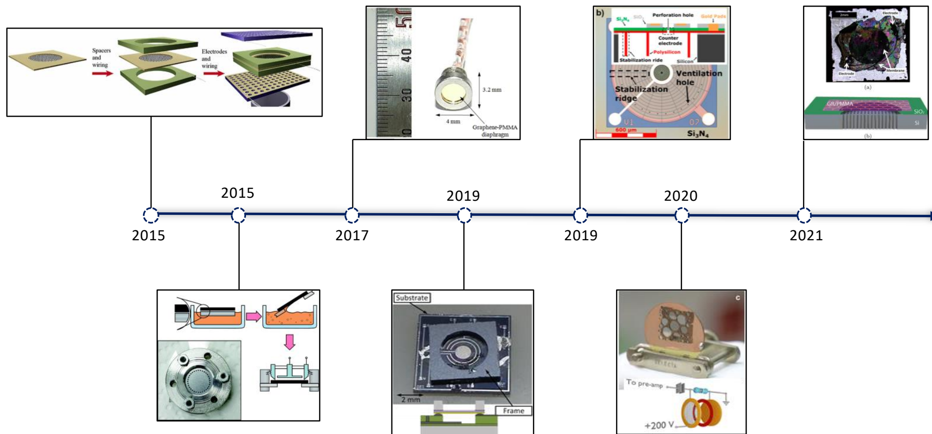

Figure 1.8: **Graphene in Microphones.** Evolution from 2015 to present [47–53]. Further details about the device performances and metrics are summarized in Chapter 3. From left the the right the figure reprint permissions are described. Image 1 is reprinted from [48]. Image 2 (used with permission of [49] under copyright 2014 and permission conveyed through Copyright Clearance Center, Inc. Image 3 (reprinted with permission from [50], copyright (2017) American Chemical Society. Image 4 (reprinted with permission from [51], © (2019) IEEE. Image 5 is reproduced from [47] under the terms of the CC BY 4.0 license. Image 6 is reprinted from [52] Copyright (2020), with permission from Elsevier. Image 7 is reproduced from [53] under the terms of the CC BY 4.0 license.

1.4. THESIS MOTIVATION AND OUTLINE

This thesis explores the potential of using graphene in MEMS condenser microphones, a crucial step toward advancing MEMS-sensitive area miniaturization. The research aims to address several existing limitations in the integration of graphene with MEMS technology. The following key questions guide this investigation:

1. **Process Integration:** Is it feasible to develop a microfabrication method compatible with standard MEMS production lines to realize graphene-based MEMS condenser microphones?

2. **Suitability and Performance:** Can graphene be an effective diaphragm material for miniaturized microphones, and does its use lead to enhanced device performance (as Sensitivity and SNR) despite the reduced sizes?

3. **Maximum Performance:** What is the highest level of performance (sensitivity vs audible bandwidth) achievable with graphene microphones based on experimental evidence?

4. **Packaged demonstrator:** Based on the findings of this study, what would be an

optimal design that integrates with current state-of-the-art packaging and ASIC read-out systems? This would allow for creating a complete demonstrator for benchmarking against state-of-the-art products in the market. The final question aims to assess the device's market potential through a comprehensive evaluation of its performance.

This thesis is structured into five experimental chapters, framed by an introductory and a concluding chapter, each written to answer the described research questions. **Chapter 2** delves into the characterization of graphene, exploring its fundamental properties when combined with various materials and under differing conditions. This initial study is crucial, as it lays the groundwork for selecting the appropriate process-flow required for high-throughput fabrication of graphene-based MEMS condenser microphones. Moving forward, **Chapter 3** proposes a specific process flow for fabricating free-standing multi-layer graphene membranes without the need for transfer methods. It includes preliminary acoustic tests to quantify the membranes' responses to sound actuation, setting the stage for potential further development. **Chapter 4** advances the research by integrating a back-plate essential for capacitive read-out, expanding the investigation to include additional properties influenced by the back-plate that complement the basic membrane response to sound. **Chapter 5** focuses on a more theoretical approach, examining how graphene's behavior transitions between vacuum and atmospheric conditions. This study aims to pinpoint graphene's limits and maximum performances (sensitivity vs bandwidth) in microphone applications, adding a fundamental layer to the research. Finally, **Chapter 6** culminates with the proposal of an optimized design to integrate the device within contemporary microphone packages. This allows for a full evaluation of the microphone's performance with graphene, intending to provide a comprehensive assessment of the technology's market viability. Through addressing these questions, the thesis aims to overcome current barriers and delineate both the practical and theoretical capabilities of graphene in MEMS microphone technology.

REFERENCES

[1] *Advanced MEMS/NEMS Fabrication and Sensors* (Springer International Publishing, 2022).

[2] S. Franssila, *Introduction to Microfabrication* (Wiley, 2010).

[3] S. K. Koul and S. Dey, *Micromachined Circuits and Devices: Microwave to Submillimeter Applications* (Springer Singapore, 2022).

[4] J. D. Plummer and P. B. Griffin, *Integrated Circuit Fabrication: Science and Technology* (Cambridge University Press, 2023).

[5] H. C. Nathanson and R. A. Wickstrom, *A resonant-gate silicon surface transistor with high-q band-pass properties,* Applied Physics Letters **7**, 84–86 (1965).

[6] K. Bean, *Anisotropic etching of silicon,* IEEE Transactions on Electron Devices **25**, 1185–1193 (1978).

[7] S. Finkbeiner, *Mems for automotive and consumer electronics*, in *2013 Proceedings of the ESSCIRC (ESSCIRC)* (IEEE, 2013).

[8] *MEMS and Microfluidics in Healthcare: Devices and Applications Perspectives* (Springer Nature Singapore, 2023).

[9] M. C. Lemme, S. Wagner, K. Lee, X. Fan, G. J. Verbiest, S. Wittmann, S. Lukas, R. J. Dolleman, F. Niklaus, H. S. J. van der Zant, G. S. Duesberg, and P. G. Steeneken, *Nanoelectromechanical sensors based on suspended 2d materials*, Research **2020** (2020), 10.34133/2020/8748602.

[10] Z. Torkashvand, F. Shayeganfar, and A. Ramazani, *Nanomaterials based micro/-nanoelectromechanical system (mems and nems) devices*, Micromachines **15**, 175 (2024).

[11] J. H. Cho, D. Cayll, D. Behera, and M. Cullinan, *Towards repeatable, scalable graphene integrated micro-nano electromechanical systems (mems/nems)*, Micromachines **13**, 27 (2021).

[12] A. F. Carvalho, B. Kulyk, A. J. S. Fernandes, E. Fortunato, and F. M. Costa, *A review on the applications of graphene in mechanical transduction*, Advanced Materials **34** (2021), 10.1002/adma.202101326.

[13] S. L, A. Deekshitha, S. Shreya, S. Verma, S. C, and M. C, *Advances in graphene based mems and nems devices: Materials, fabrication, and applications*, ECS Transactions **107**, 10997–11005 (2022).

[14] Y. Xiao, F. Luo, Y. Zhang, F. Hu, M. Zhu, and S. Qin, *A review on graphene-based nano-electromechanical resonators: Fabrication, performance, and applications*, Micromachines **13**, 215 (2022).

[15] B. Xu, P. Zhang, J. Zhu, Z. Liu, A. Eichler, X.-Q. Zheng, J. Lee, A. Dash, S. More, S. Wu, Y. Wang, H. Jia, A. Naik, A. Bachtold, R. Yang, P. X.-L. Feng, and Z. Wang, *Nanomechanical resonators: Toward atomic scale*, ACS Nano **16**, 15545–15585 (2022).

[16] *Yole Group - Follow the latest trend news in the Semiconductor Industry — yolegroup.com*, https://www.yolegroup.com/product/report/consumer-mems-microphone-comparison-2022/ (), [Accessed 26-05-2024].

[17] M. Fueldner, *Microphones*, in *Handbook of Silicon Based MEMS Materials and Technologies* (Elsevier, 2020) p. 937–948.

[18] EE Times, *Advancements in generative ai audio: The crucial role of high-snr mems microphones*, https://www.eetimes.eu/advancements-in-generative-ai-audio-the-crucial-role-of-\protect\penalty\z@high-snr-mems-microphones/ (2024), [Accessed 26-May-2024].

[19] *MEMS market to grow to US$20 billion by 2028 — yolegroup.com,* https://www.yolegroup.com/press-release/mems-market-to-grow-to-us20-billion-by-2028/ (), [Accessed 26-05-2024].

[20] S. A. Zawawi, A. A. Hamzah, B. Y. Majlis, and F. Mohd-Yasin, *A review of mems capacitive microphones,* Micromachines **11**, 484 (2020).

[21] M. A. Shah, I. A. Shah, D.-G. Lee, and S. Hur, *Design approaches of mems microphones for enhanced performance,* Journal of Sensors **2019**, 1–26 (2019).

[22] F. P. Burns, *Piezoresistive semiconductor microphone,* The Journal of the Acoustical Society of America **29**, 248–253 (1957).

[23] A. Kumar, A. Varghese, D. Kalra, A. Raunak, Jaiverdhan, M. Prasad, V. Janyani, and R. Yadav, *Mems-based piezoresistive and capacitive microphones: A review on materials and methods,* Materials Science in Semiconductor Processing **169**, 107879 (2024).

[24] R. Schellin and G. Hess, *A silicon subminiature microphone based on piezoresistive polysilicon strain gauges,* Sensors and Actuators A: Physical **32**, 555–559 (1992).

[25] Z. Zhou, M. Wong, L. Rufer, E. Salze, P. Yuldashev, and S. Ollivier, *Wide-band piezoresistive microphone for aero-acoustic applications,* in *2012 IEEE Sensors*, Vol. 120 (IEEE, 2012) p. 1–4.

[26] G. Baglioni, R. Pezone, S. Vollebregt, K. C. Zobenica, M. Spasenović, D. Todorović, H. Liu, G. J. Verbiest, H. S. J. van der Zant, and P. G. Steeneken, *Ultra-sensitive graphene membranes for microphone applications,* Nanoscale **15**, 6343 (2023).

[27] T. Gabrielson, *Mechanical-thermal noise in micromachined acoustic and vibration sensors,* IEEE Transactions on Electron Devices **40**, 903–909 (1993).

[28] K. S. Novoselov, A. K. Geim, S. V. Morozov, D. Jiang, Y. Zhang, S. V. Dubonos, I. V. Grigorieva, and A. A. Firsov, *Electric field effect in atomically thin carbon films,* Science **306**, 666–669 (2004).

[29] A. King, G. Johnson, D. Engelberg, W. Ludwig, and J. Marrow, *Observations of intergranular stress corrosion cracking in a grain-mapped polycrystal,* Science **321**, 382–385 (2008).

[30] C.-K. Lee, Y. Hwangbo, S.-M. Kim, S.-K. Lee, S.-M. Lee, S.-S. Kim, K.-S. Kim, H.-J. Lee, B.-I. Choi, C.-K. Song, J.-H. Ahn, and J.-H. Kim, *Monatomic chemical-vapor-deposited graphene membranes bridge a half-millimeter-scale gap,* ACS Nano **8**, 2336–2344 (2014).

[31] V. Kumar, *Linear and nonlinear optical properties of graphene: A review,* Journal of Electronic Materials (2021), 10.1007/s11664-021-08904-w.

[32] N. Parvin, V. Kumar, S. W. Joo, S.-S. Park, and T. K. Mandal, *Recent advances in the characterized identification of mono-to-multi-layer graphene and its biomedical applications: A review,* Electronics **11**, 3345 (2022).

[33] Y. Huang, E. Sutter, N. N. Shi, J. Zheng, T. Yang, D. Englund, H.-J. Gao, and P. Sutter, *Reliable exfoliation of large-area high-quality flakes of graphene and other two-dimensional materials,* ACS Nano **9**, 10612–10620 (2015).

[34] V. B. Mbayachi, E. Ndayiragije, T. Sammani, S. Taj, E. R. Mbuta, and A. u. khan, *Graphene synthesis, characterization and its applications: A review,* Results in Chemistry **3**, 100163 (2021).

[35] J. R. Prekodravac, D. P. Kepić, J. C. Colmenares, D. A. Giannakoudakis, and S. P. Jovanović, *A comprehensive review on selected graphene synthesis methods: from electrochemical exfoliation through rapid thermal annealing towards biomass pyrolysis,* Journal of Materials Chemistry C **9**, 6722–6748 (2021).

[36] A. R. Urade, I. Lahiri, and K. S. Suresh, *Graphene properties, synthesis and applications: A review,* JOM **75**, 614–630 (2022).

[37] S. Wagner, C. Weisenstein, A. Smith, M. Östling, S. Kataria, and M. Lemme, *Graphene transfer methods for the fabrication of membrane-based NEMS devices,* Microelectronic Engineering **159**, 108 (2016).

[38] S. Ullah, X. Yang, H. Q. Ta, M. Hasan, A. Bachmatiuk, K. Tokarska, B. Trzebicka, L. Fu, and M. H. Rummeli, *Graphene transfer methods: A review,* Nano Research **14**, 3756–3772 (2021).

[39] X. Langston and K. E. Whitener, *Graphene transfer: A physical perspective,* Nanomaterials **11**, 2837 (2021).

[40] Y.-M. Chen, S.-M. He, C.-H. Huang, C.-C. Huang, W.-P. Shih, C.-L. Chu, J. Kong, J. Li, and C.-Y. Su, *Ultra-large suspended graphene as a highly elastic membrane for capacitive pressure sensors,* Nanoscale **8**, 3555–3564 (2016).

[41] I. Cheliotis and I. Zergioti, *A review on transfer methods of two-dimensional materials,* 2D Materials **11**, 022004 (2024).

[42] M. Chen, R. C. Haddon, R. Yan, and E. Bekyarova, *Advances in transferring chemical vapour deposition graphene: a review,* Materials Horizons **4**, 1054–1063 (2017).

[43] S. Afyouni Akbari, V. Ghafarinia, T. Larsen, M. M. Parmar, and L. G. Villanueva, *Large suspended monolayer and bilayer graphene membranes with diameter up to 750µm,* Scientific Reports **10** (2020), 10.1038/s41598-020-63562-y.

[44] L. Zheng, Y. Chen, N. Li, J. Zhang, N. Liu, J. Liu, W. Dang, B. Deng, Y. Li, X. Gao, C. Tan, Z. Yang, S. Xu, M. Wang, H. Yang, L. Sun, Y. Cui, X. Wei, P. Gao, H.-W. Wang, and H. Peng, *Robust ultraclean atomically thin membranes for atomic-resolution electron microscopy,* Nature Communications **11** (2020), 10.1038/s41467-020-14359-0.

[45] B. Alemán, W. Regan, S. Aloni, V. Altoe, N. Alem, C. Girit, B. Geng, L. Maserati, M. Crommie, F. Wang, and A. Zettl, *Transfer-free batch fabrication of large-area suspended graphene membranes,* ACS Nano **4**, 4762–4768 (2010).

1

[46] Y.-M. Chen, S.-M. He, C.-H. Huang, C.-C. Huang, W.-P. Shih, C.-L. Chu, J. Kong, J. Li, and C.-Y. Su, *Ultra-large suspended graphene as a highly elastic membrane for capacitive pressure sensors,* Nanoscale **8**, 3555 (2016).

[47] S. Wittmann, C. Glacer, S. Wagner, S. Pindl, and M. C. Lemme, *Graphene membranes for hall sensors and microphones integrated with CMOS-compatible processes,* ACS Applied Nano Materials **2**, 5079 (2019).

[48] Q. Zhou, J. Zheng, S. Onishi, M. F. Crommie, and A. K. Zettl, *Graphene electrostatic microphone and ultrasonic radio,* Proceedings of the National Academy of Sciences **112**, 8942–8946 (2015).

[49] D. Todorović, A. Matković, M. Milićević, D. Jovanović, R. Gajić, I. Salom, and M. Spasenović, *Multilayer graphene condenser microphone,* 2D Materials **2**, 045013 (2015).

[50] S. Woo, J.-H. Han, J. H. Lee, S. Cho, K.-W. Seong, M. Choi, and J.-H. Cho, *Realization of a high sensitivity microphone for a hearing aid using a graphene–pmma laminated diaphragm,* ACS Applied Materials amp; Interfaces **9**, 1237–1246 (2017).

[51] G. S. Wood, A. Torin, A. K. Al-mashaal, L. S. Smith, E. Mastropaolo, M. J. Newton, and R. Cheung, *Design and characterization of a micro-fabricated graphene-based mems microphone,* IEEE Sensors Journal **19**, 7234 (2019).

[52] A. F. Carvalho, A. J. Fernandes, M. B. Hassine, P. Ferreira, E. Fortunato, and F. M. Costa, *Millimeter-sized few-layer suspended graphene membranes,* Applied Materials Today **21**, 100879 (2020).

[53] J. Xu, G. S. Wood, E. Mastropaolo, M. J. Newton, and R. Cheung, *Realization of a graphene/pmma acoustic capacitive sensor released by silicon dioxide sacrificial layer,* ACS Applied Materials amp; Interfaces **13**, 38792–38798 (2021).

2

Materials Selection for Mo-based Graphene in Micromachining

This chapter examines the strategic use of materials for fabricating graphene membranes using bulk-micromachining and Vapor HF without transferring techniques. Our investigation centers around a suite of materials readily available in our lab, identified for their potential for this application due to their intrinsic physical properties. Through a detailed analysis, we aim to discern the impact of each material on the synthesis and resultant quality of graphene fabricated with Mo-based transfer-free method. By the conclusion of this chapter, readers will be equipped with essential knowledge to comprehend the rationale supporting the advanced process flowcharts presented subsequently.

2.1. INTRODUCTION

THE process of synthesizing graphene through chemical vapor deposition (CVD) is well-established and capable of producing graphene on silicon wafers larger than 6" and other substrate materials[1, 2]. The properties of the resulting graphene, which vary based on substrate choice and CVD parameters, must be tailored to its specific application[3].

This thesis explores the possibility of using a transfer-free, wafer-scale method for fabricating free-standing multi-layer graphene suitable for a MEMS-microphone architecture and other possible applications. Monolayer graphene is not preferred for such applications due to its lack of mechanical support and high damage risk [4]. Notably, the demand for pristine, single-layer graphene is neglected in this scenario since the critical property of high electrical mobility is not essential for such an application. We use a transfer-free method for synthesizing and patterning multi-layer graphene directly on a Mo metal catalyst, evaluating its suitability for this specific application. In addition, Mo rises as a catalyst substrate, enabling the transfer-free growth of multi-layer graphene and aligning well with CMOS-metal processes, which could extend benefits to various electronic applications[5].

Before delineating a potential process flow for the fabrication of multi-layer graphene membranes, this chapter thoroughly examines materials, including SiN_x, AlO_x, and a-SiC that would be used as clamping support and etch mask layer. This detailed assessment is crucial for identifying the most effective techniques for constructing micromachined graphene membranes.

Before proceeding to the evaluation and discussion of experimental outcomes, it is essential to introduce two key micromachining techniques fundamental for clarifying the flowcharts of the next chapters designed to manufacture graphene membranes.

2.2. DEEP REACTIVE ION ETCHING AND BOSCH PROCESS

Reactive ion etching (RIE), known as plasma or dry etching, and its advanced form, Deep RIE (DRIE), are techniques that merge physical and chemical effects to etch material from a wafer's surface [6]. These processes enhance desorption through ion bombardment, create ion-induced damage, enable spontaneous chemical etching, generate radicals, and can also deposit films, all contributing to the etching result. RIE achieves etch rates significantly higher than purely physical methods and, unlike wet etching, offers the ability to etch directionally anisotropic etching without depending on the material's crystal planes.

DRIE generally allows for etching deep, patterned structures compared to RIE methods. As for RIE, it employs an inductively coupled plasma (ICP) source to create a plasma with a density up to two orders of magnitude higher than that generated by capacitive coupling plasma (CCP) sources, significantly increasing the etch rate. The Bosch process, also known as deep reactive ion etching (DRIE), is an essential technique in advanced MEMS applications and through-silicon via (TSV) fabrication. This method is distinguished by its ability to achieve high aspect ratio microstructures with remarkable anisotropy, etch rate, and etch mask selectivity, which surpass conventional plasma etching processes limited to shallower depths [6]. This process unfolds in a three-step

cycle as in Figure 2.1.

1. **Film Deposition**: a passivation film is deposited using C_4F_8 gas, which forms a protective membrane on the sidewalls and bottom surface of the trench (Figure 2.1a).

2. **Bottom Film Etching**: the etching agents (ions and radicals) are directed vertically due to the influence of the bias voltage (electric field) applied across the plasma. This bias enhances the vertical momentum of the ions, enabling them to specifically target the bottom surfaces of the trenches(Figure 2.1b).

3. **Silicon Etching**: the radicals from SF_6 react specifically with the silicon where it is exposed, forming volatile byproducts like SiF_4 that are evacuated from the chamber. The passivation film prevents these reactions from occurring on the sidewalls(Figure 2.1c).

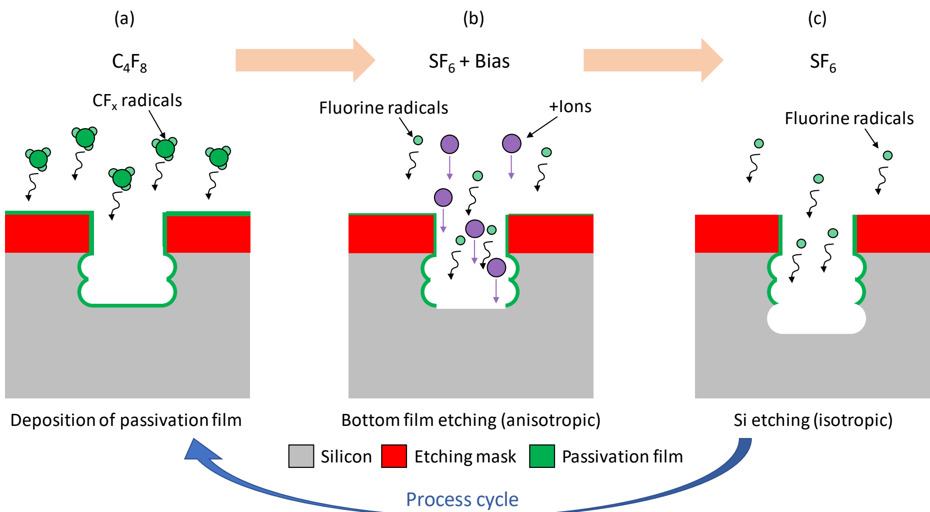

Figure 2.1: **Sequential stages of the silicon Bosch etching.** (a) The process initiates with a film deposition utilizing C_4F_8 gas. Before this step, an etching mask, typically made of materials like SiO_2, Si_3N_4, Al_2O_3, and metals or polymers as photoresist is applied. This mask is selectively etched to expose areas of the silicon where perforations are targeted. (b) The passivation film at the bottom of the silicon trenches, polymerized from the initial deposition, is selectively removed through the action of SF_6 ions, driven by an applied electric field. (c) Subsequent isotropic etching by SF_6 creates the characteristic Bosch process sidewall profiles, known as "scallops".

In a more detailed case, the chemical dynamics of the process involve breaking C_4F_8 into chain-shaped molecules that polymerize and form a passivating film, which is crucial for protecting the sidewalls during etching. The presence of SF_6 generates fluorine radicals that terminate the polymerization, ensuring effective etching of silicon without affecting the sidewalls. Separating film deposition and etching steps is essential to prevent mixing C_4F_8 and SF_6 gases, which could otherwise interrupt the etching process due to premature polymerization termination. Finally, in the Bosch process, three primary challenges—notching, loading effects, and microloading—emerge due to the

specific conditions and requirements of the etching condition [6–8].

- **Notching**: This occurs primarily when etching Silicon-on-Insulator (SOI) wafers. Notching is a phenomenon where an undercut forms at the interface between the silicon layer and the buried oxide. This happens because of localized changes in plasma chemistry or ion directionality, which can cause more aggressive etching at the interface. Adjustments in hardware setup and etch parameters are often required to minimize this effect[6–8].

- **Loading effects**: The etch rate in the Bosch process can be dependent on the total area of silicon exposed in the etching chamber. This is known as the loading effect. When larger silicon areas are exposed, the etching gas (such as SF_6) is consumed more rapidly, which can reduce the etch rate across the wafer. This effect must be managed carefully to ensure uniformity in the etching process across different wafers and within the same wafer[6–8].

- **Microloading effects**: As the aspect ratio of etched features increases, the probability of fluorine radicals being transported to the bottom of deep trenches or holes diminishes. This results in a pattern-dependent etch effect known as microloading. It adversely affects the depth uniformity of etched features because the reactants (etching gases) become depleted in areas with higher local feature density. The microloading effect is exacerbated in high aspect ratio etching, where the physical dimensions and density of the features constrain the reactivity and availability of radicals[6–8].

2.3. VAPOR HF

The membrane release steps in MEMS fabrication involve the removal of a sacrificial layer, termed "the floor," allowing a 3D structure to stand freely with anchor points remaining post-release. This thin film layer is a temporary mechanical support for constructing the MEMS device through standard semiconductor patterning and etching techniques.
Silicon or polysilicon layers are typically etched away using fluorine-based dry etch processes or XeF_2 when they act as the sacrificial layer, with metals or dielectrics forming the structural layer [9]. SiO_2 is often the material of choice for the sacrificial layer, deposited by LPCVD, PECVD or thermal growth, making hydrofluoric acid the etchant of choice for oxides [9, 10].
Post-release, any contact between the released elements and the ultra-clean, flat substrate can result in permanent adhesion, known as "stiction," which can be due to capillary forces, hydrogen bridging, electrostatic, or Van der Waals forces, especially prevalent in wet-etching processes.
To mitigate stiction, microfabricated anti-stiction dimples [11] or films and techniques like critical point drying with supercritical carbon dioxide are employed[9, 10].
Vapor HF etching, initiated with water or alcohol vapor catalysts combined with HF, effectively etches SiO_2, necessitating precise control of all processing conditions to avoid accelerated and not uniform etching. This process typically proceeds at atmospheric pressure, ensuring better integrity of the MEMS structures than any wet release steps.

The SiO_2 etching starts if water or alcohol (A) vapor catalysts are combined with HF. The catalytic role activities are carefully managed to control the etching speed. For the Vapor HF based on anhydrous HF and alcohol vapor catalysts, the process usually occurs under reduced pressure, with gas (g) molecules physically adsorbing (ads) onto the silicon oxide surface.

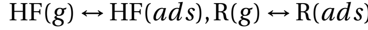

$$\mathrm{HF}(g) \leftrightarrow \mathrm{HF}(ads), \mathrm{R}(g) \leftrightarrow \mathrm{R}(ads)$$

When methanol is used, the ionization interaction between adsorbed HF and adsorbed CH_3OH results in HF_2^-:

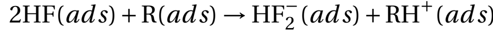

$$2\mathrm{HF}(ads) + \mathrm{R}(ads) \rightarrow \mathrm{HF}_2^-(ads) + \mathrm{RH}^+(ads)$$

In more detail, two HF molecules adsorb onto the surface (denoted as HF(ads)), along with the alcohol (A). The methanol acts as a catalyst to facilitate the ionization of HF when adsorbed on the surface. In this ionization step, one HF molecule donates a proton (H+) to the alcohol, which can stabilize the proton through its oxygen atom, forming an oxonium ion or alcohol cation $AH^+(ads)$ leavening behind a fluoride ion (F-). The fluoride ion then pairs with another HF molecule to form the bifluoride ion HF_2^-(ads). More particularly, bifluoride is a species where two fluoride ions share a single proton, resulting in a hydrogen bond between the two fluorides. This bifluoride ion is more reactive toward silicon dioxide than HF alone, which makes the etching process more efficient.
Subsequently, the ionized HF engages with the silicon oxide, with the comprehensive chemical reaction for pure silicon oxide being as follows:

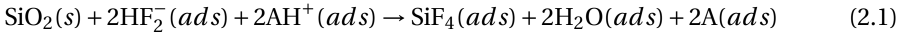

$$\mathrm{SiO}_2(s) + 2\mathrm{HF}_2^-(ads) + 2\mathrm{AH}^+(ads) \rightarrow \mathrm{SiF}_4(ads) + 2\mathrm{H}_2\mathrm{O}(ads) + 2\mathrm{A}(ads) \quad (2.1)$$

In this case, ionization refers to the transfer of a hydrogen ion (H^+) from one of the HF molecules to the methanol molecule, turning it into a methoxycation (CH_3O^+) and leaving behind a bifluoride anion (HF_2^-). This ionization is facilitated by the close proximity of the HF and CH_3OH molecules on the surface, making it energetically favorable for hydrogen transfer. As for the bifluoride ion, it is formed when two fluoride ions share a single hydrogen ion between them. This can happen when hydrogen fluoride is in high concentration, as the fluoride ions attract hydrogen ions from neighboring HF molecules.
It's important to recognize that the by-products, such as SiF_4, alcohol, and water, are desorbed from the oxide surface. This aspect is crucial for vapor-phase etching in MEMS fabrication, as it should avoid intermediate liquid steps that might lead to stiction. Conducted under reduced pressure, this method allows for straightforward control over the production and desorption of water by-products, a contrast to the more challenging control in atmospheric pressure methods.

$$\mathrm{SiF}_4(ads) \rightarrow \mathrm{SiF}_4(g), \mathrm{H}_2\mathrm{O}(ads) \rightarrow \mathrm{H}_2\mathrm{O}(g), \mathrm{A}(ads) \rightarrow \mathrm{A}(g)$$

This thesis involves Vapor HF based on ethanol and anhydrous 100% HF (Primaxx® uEtch) due to its immediate accessibility in the laboratory. Contrary to systems employing Vapor HF, which typically use only water and HF, introducing certain materials, especially polymers, introduces constraints. Polymers swell upon exposure to organic

solvents like methanol, isopropyl alcohol (IPA), or acetone. This swelling can lead to the absorption of HF, presenting potential safety risks. Therefore, in this research, polymers are not employed as etching masks to avoid any safety complications.

2.4. MATERIAL COMPATIBILITY WITH TRANSFER-FREE GRAPHENE

Three primary constraints for the thin film stack choice are CVD growth of graphene, dielectric properties, and compatibility with Vapor HF etching. The transfer-free approach has a high-temperature step (900–1000 °C) at 25 mbar [12, 13]. Regarding Vapor HF compatibility, the future process-flow should involve a sacrificial layer and a clamping layer that must resist Vapor HF.
Given the available resources in the laboratory, thermal SiO_2 and Plasma-enhanced chemical vapor deposition annealed Tetraethyl orthosilicate (TEOS) are chosen as a sacrificial layer. PECVD SiH_4-based oxides are excluded since post-treatments such as baking or O_2 plasma are required to remove the residuals generated by the etching step, as described by the tool manufacturer, SPTS. LPCVD TEOS is not investigated because growing layers thicker than 500 nm requires multiple steps, each with a maximum of 500 nm, leading to time-consuming load and unload processes. However, LPCVD TEOS is an excellent material for a sacrificial layer. Low-pressure chemical vapor deposition (LPCVD) silicon-rich SiN_x is utilized for the clamping layer and as an etching mask with its expected selectivity from 1:10 to 1:40 compared to thermal SiO_2[14, 15]. Therefore, experimental tests have been conducted to confirm the reported etching selectivity and the suitability of LPCVD SiN_x for the Mo-based transfer-free graphene synthesis.
Alternative explored etching masks include PECVD a-SiC, LPCVD a-SiC, and atomic layer deposition (ALD) aluminum oxide (AlO_x) that are generally highly selective to the Vapor HF compared to LPCVD silicon-rich SiN_x.

2.4.1. SILICON NITRIDE AS BUFFER LAYER FOR GRAPHENE SYNTHESIS

Following the transfer-free methodology [5, 12, 13, 16, 17], resistive strip test structures are fabricated to assess the quality of graphene with Raman spectroscopy and perform electrical characterization to explore its sheet resistance R_{sheet}. This evaluation is essential, as the ultimate goal is to utilize graphene as an electrode material for capacitive read-out. These investigations are crucial for identifying beneficial or disadvantageous variations compared to the most extensively studied substrate, thermal SiO_2 [5].
The substrates consist of 4" silicon wafers coated with a thin film of LPCVD silicon-rich low-stress SiN_x (details are provided in the caption of Figure 2.2). The test structures (shown in Figure 2.2a) are fabricated across 52 dies on the silicon wafer, with varying channel widths ($w_{\text{strip}} = 2, 5, 10, 15, 20, 25, 30, 50, 75, 100\,\mu\text{m}$) and a constant length ($L_{\text{strip}} = 205\,\mu\text{m}$) in each die. R_{sheet} measurements yield average values between 1 kΩ/sq and 2 kΩ/sq (Figure 2.2b) calculated by Equation 2.2, aligning with previous studies on Mo-graphene on SiO_2 substrates [5].

$$R_{\text{sheet}} = \frac{V_{\text{DC}}\, w_{\text{strip}}}{I_{\text{DC}} L_{\text{strip}}} \tag{2.2}$$

A gradient in R_{sheet} is observed from the center to the edges of the wafer (Figure 2.2c),

attributed to the temperature gradient of the chuck used in the CVD graphene process across the entire area. Higher temperatures in the center are presumed to enhance the graphitization of the nucleated graphitic layers on top of the formed Mo_2C, leading to higher crystal quality [18]. Correspondingly, Raman spectroscopy reveals varying defect levels, with higher resistance areas exhibiting increased defectivity (Figure 2.2d). We adopt a qualitative correlation between defectivity (I_D/I_G) and R_{sheet} as a benchmark for future results in cases where the R_{sheet} properties are not being explored.

Having confirmed compatibility with transfer-free methods based on the Raman and electrical measurements (Figure 2.2), Mo wet etching, several tests are conducted to evaluate the etching mask properties of the proposed film. Based on experimental tests, a selectivity from 1:25 to 1:30 is found between silicon-rich SiN_x and thermal SiO_2. It is important to mention that LPCVD SiN_x leaves residuals after etching that need to be removed with high-temperature steps ($T > 120-250°C$) depending on pressure conditions) or O_2-plasma. If these residuals are not removed, they also prevent the ellipsometer from properly measuring the thickness due to the high surface roughness.

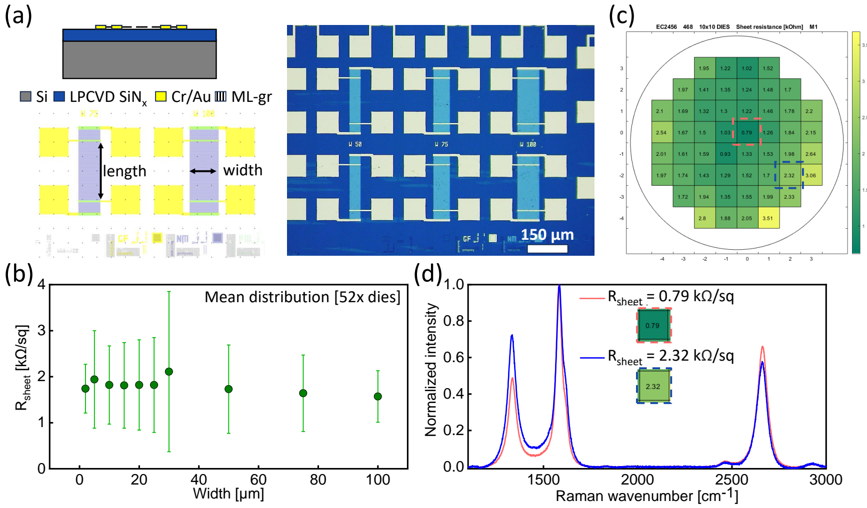

Figure 2.2: **R_{sheet} and Raman Spectroscopy characterization**(a) A schematic cross-section illustrates final fabricated structure. A p-type doped Si 4" wafer is covered with LPCVD silicon-rich SiN_x (100 nm), followed by sputter deposition of Mo (50 nm) at 50°C that is consequently patterned by dry-etching. CVD growth of graphene and lift-off of Cr/Au (10/100 nm) are performed with the final Mo wet-etching by H_2O_2. The image also presents a resistive strip structure schematic and a digital microscope image of the fabricated multi-layer graphene strips, clarifying the definitions of width (w_{strip}) and length (L_{strip}). (b) Description of the measured sheet resistance (R_{strip} measured for a strip width (w_{strip}) of 2 µm and a strip length (L_{strip}) of 205 µm, across 52 chips. (c) All R_{sheet} mean values corresponding to various w_{strip} dimensions across the entire 4" wafer. (d) Raman spectroscopy analysis, performed with a red He-Ne laser ($\lambda = 633$ nm), comparing two strips of identical width and length but differing R_{sheet} values. The first sample exhibits ω_D, ω_G, and ω_{2D} peaks at 1336, 1584.1, and 2662.3 cm^{-1} respectively, with full width at half maximum (FWHM) values of 49, 42, and 64 cm^{-1}. The more defective sample shows ω_D, ω_G, and ω_{2D} peaks at 1333.9, 1586.6, and 2659.3 cm^{-1}, with FWHM values of 52, 55, and 66 cm^{-1}, respectively.

2.4.2. SILICON CARBIDE AS BUFFER LAYERS FOR GRAPHENE SYNTHESIS

Besides confirming LPCVD silicon-rich SiN_x as a suitable substrate for the Mo-based transfer-free graphene fabrication, this study explores additional materials to expand design flexibility for future concept devices. This is particularly relevant for applications requiring hard masks in Vapor HF etching processes, where high selectivity with SiO_2 must be higher.
The chosen substrates, PECVD SiC (details in Figure 2.3 caption), with thicknesses of 48 nm and 146 nm as measured by ellipsometry, are being evaluated for their potential as a thin-film support for Mo sputtering and consequent CVD. This step is essential in developing CVD graphene growth via a transfer-free method.
After Mo sputtering (50 nm) and the growth attempt, it is observed that both wafers with a 48 nm and 146 nm a-SiC film delaminated post-CVD (Figure 2.3a).
To investigate whether delamination was only related to the high-temperature decomposition of hydrogenated bonds [19–21] within the a-SiC layer, new samples were identically fabricated and annealed at 1000°C in an N_2/Ar atmosphere for 1h. High-temperature annealing is expected to remove the hydrogenated bonds like Si-H and C-H, thereby enhancing the density of Si-C bonds. However, this hydrogen reduction is predominantly observed in the CH groups, with minimal SiH and SiH_2 concentration changes. Additionally, Si-C bonds, being significantly shorter (e.g., 1.88 Å) compared to Si-Si bonds (e.g., 2.35 Å), lead to increased distortion of bond angles within the amorphous structure as more Si-C bonds form at higher annealing temperatures. Consequently, the annealing process results in an elevated index of refraction and a reduction in film thickness [22].
After the annealing, the absence of delamination suggested that the issue was due to the interaction between Mo/SiC during CVD, not an inherent relation to the SiC film.
Furthermore, the newly annealed substrates, which featured PECVD a-SiC layers and exhibited no optical damage post-annealing, were still considered suitable for the intended application. Consequently, the layers underwent comprehensive sheet resistance testing across the entire wafer. This evaluation was conducted using a Wafer Mapping Solutions tool from CDE Creative Design Engineering, Inc., to confirm their insulating properties after annealing. As described earlier, maintaining the insulating nature of the clamping and etching mask layer is crucial for fabricating electrically conductive devices, such as microphones with capacitive read-out, wherein the membranes must be electrically isolated.
Moreover, both wafers exhibited a R_{sheet} mean value of approximately 30 Ω/sq with a standard deviation of 0.29 Ω/sq. Ellipsometry measurements also revealed the post-anneal film thicknesses to be 23 nm and 87 nm , indicating significant shrinkage due to a possible reduction in hydrogenated bonds [22].
In conclusion, high-temperature annealing not only expels hydrogen species, possibly enhancing crystallinity, but it may also introduce a larger density of conductive pathways. Thus, Mo diffusion has been found for both annealed samples after Mo sputtering and CVD (Figure 2.3b). More particularly, diffusion has also been found through the silicon substrate at its back-side (Figure 2.3b). The Mo diffusion could also be attributed to increased Mo atom mobility at elevated temperatures that find several diffusion paths, particularly in the presence of defects. These results suggest that growing graphene with Si/PECVD a-SiC/Mo is unsuitable.

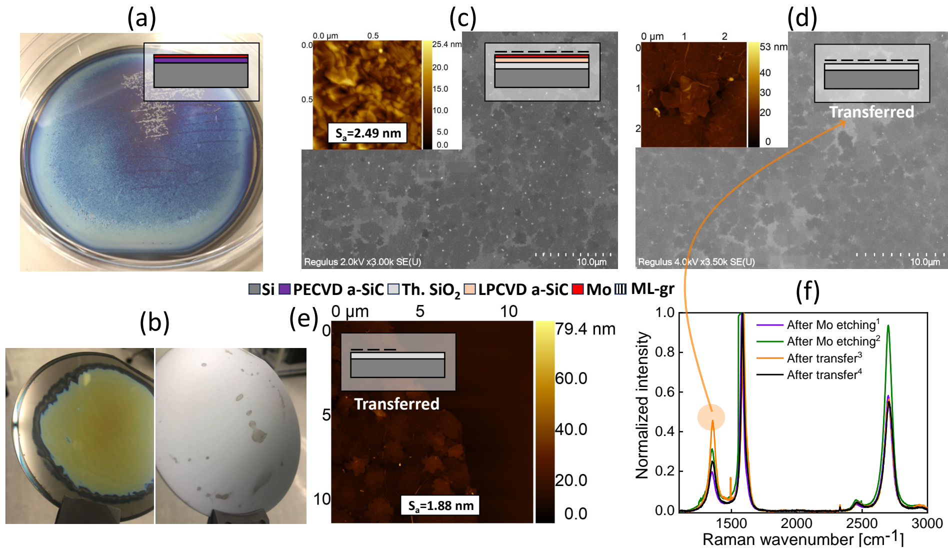

Figure 2.3: **Transfer-free multilayer graphene and LPCVD a-SiC.** (a) Post-CVD wafer appearance and schematic cross-section. The PECVD a-SiC layer measures 146 nm, with a 50 nm Mo layer atop. (b) The wafer's back-side shows residuals of a-SiC/Mo diffusion through the silicon substrate. PECVD a-SiC main deposition parameters were NH_3 (4.110 sccm), SiH_4 (0.250 sccm) at 400°C. (c) SEM image of graphene synthesized on the sample detailed in the schematic, where LPCVD a-SiC was deposited with C_2H_2 (435 sccm), DCS (65 sccm) at 600°C, resulting in a 49 nm layer. (d) Following Mo wet etching, the graphene layer is detached from the original substrate in water and transferred onto a flat thermal oxide surface for subsequent inspections, particularly assessing thickness and structural integrity. (e) Thickness evaluation of the transferred layer. Hillocks remain visible, marked by the highest peak in the image. (f) Raman spectroscopic analysis utilizing a Horiba HR800 Raman spectrometer equipped with a 514.4 nm Ar+ laser, 100× objective with an NA of 0.9 across four distinct sample points, as detailed in the insight legend.

Due to the incompatibility of PECVD a-SiC with the transfer-free process, LPCVD a-SiC is also explored as an alternative clamping and etching mask thin film for the transfer-free graphene. Despite its slower deposition rate, making the creation of thicker layers both time-intensive and costly, LPCVD a-SiC is assessed for its potential application. Under identical processing conditions, except for adding a thermal SiO_2 layer, divergent outcomes are observed compared to PECVD a-SiC.
Post-CVD, the multi-layer graphene exhibits Raman imprints close to those found on the SiN_x and thermal oxide substrates, as illustrated in Figure 2.2d and referenced in the literature [5, 12, 13, 16].
SEM and AFM comparisons presented in Figure 2.3c demonstrate that the graphene grown on Mo achieved a mean roughness S_a of 2.4 nm , which reduced to 1.8 nm upon transfer to a flat thermal oxide substrate for thickness assessment (Figure 2.3d, e) due to Mo removal and absence of any possible voids into the buffer layer [23]. A thickness of $t = 7 \pm 1$ nm has been measured after its wet transfer on thermal SiO_2 (Figure 2.3e). Raman spectral analysis revealed peaks at ω_D, ω_G, and ω_{2D} of 1351.5, 1578.0, and 2700.1 cm^{-1}, respectively, with FWHM values of 57, 33, and 67 cm^{-1}. These peak positions and the FWHM of ω_{2D} slightly increased post-transfer.

A distinct disparity observed with the LPCVD a-SiC substrate, in contrast to growth on thermal SiO_2 and SiN_x, was the presence of hillocks in the graphene layer post-growth and subsequent transfer. These hillocks, which likely represent stress distributions within the layer, persist after transfer but with lower density, indicating that the graphene retains its original morphology, thereby affecting the layer's post-transfer morphology.
In conclusion, the successful delamination and mechanical integrity of the graphene layer, alongside its comparable thickness to those observed on thermal oxide benchmarks, underscores its potential suitability for transfer-free applications. Contrary to the previous case where annealed PECVD a-SiC became conductive, the LPCVD a-SiC layer remains non-conductive, affirming its utility as a substrate for forthcoming thesis applications.

2.4.3. ALUMINIUM OXIDE AS BUFFER LAYERS FOR GRAPHENE SYNTHESIS

For the targeted application, AlO_x can also be an effective etching mask, and thin-film support for transfer-free Mo-grown multi-layer graphene.
ALD AlO_x films exhibit high etching selectivity towards SiO_2, a property that significantly improves post-annealing at temperatures above 900°C [24].
Consequently, two experimental approaches were followed: one involving Mo sputtered onto unannealed ALD AlO_x, and the other onto annealed ALD AlO_x. Detailed descriptions of the layers and additional insights are presented in Figure 2.4 caption. All other processing steps and conditions were kept consistent across experiments.
Post-CVD analysis indicates that the annealing step is crucial in affecting the crystallinity, quality, and thickness of the synthesized graphene.
AFM analysis, illustrated in Figure 2.4a and Figure 2.4c, shows that both samples maintain similar surface roughness S_a when graphene remains on Mo. However, the annealed samples exhibit larger and more defined Mo grains (Figure 2.4c) compared to the more uniformly flat topography of the non-annealed samples (Figure 2.4a). Following Mo etching with H_2O_2, rinsing with DI-Water, and drying, further changes emerge, as detailed in AFM and SEM analyses (Figure 2.4b, d, f, h). The non-annealed samples show a mean roughness S_a of 0.94 nm, in contrast to the S_a = 1.90 nm observed for the annealed samples.
These figures suggest that the synthesized graphene on annealed substrates is thinner and flatter than that on reference thermal SiO_2 substrates [17].
SEM images (Figure 2.4f, h) further highlight these differences, with the annealed samples showing characteristic wrinkles that feature consistent findings from studies on thermal SiO_2 and underlying film substrates beneath Mo [25]. This suggests that the annealed samples' morphology more closely resembles that of the reference thermal SiO_2 substrates.
Raman spectroscopy reveals significant differences in the synthesized graphene, notably, the $I_\mathrm{D}/I_\mathrm{G}$ ratio is substantially higher for non-annealed samples than for annealed ones. Furthermore, the $I_\mathrm{2D}/I_\mathrm{G}$ and $I_\mathrm{D}/I_\mathrm{G}$ ratios are respectively higher and lower in the annealed samples, indicative of a possibly lower defect density than in non-annealed samples. Distinctly, the FWHM values of ω_D, ω_G, and ω_2D peaks are approximately 45 cm^{-1}, 33 cm^{-1}, and 65 cm^{-1} for annealed samples, compared to approximately 55 cm^{-1}, 85 cm^{-1}, and 90 cm^{-1} for their non-annealed counterparts.

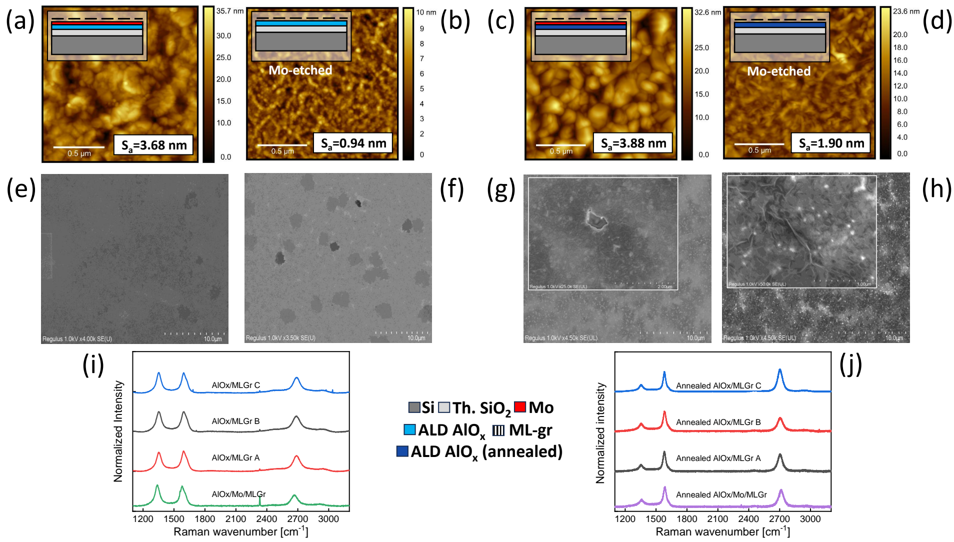

Figure 2.4: **Transfer-free multilayer graphene and ALD AlO$_x$.** The ALD AlO$_x$ is deposited at 300°C with Trimethylamine/TMA (120), H_2O (40) on top of thermal SiO_2 (2000 nm), designated as a future sacrificial layer, and subsequently is covered by sputtered Mo, according to previous methodologies. The annealing is performed at 1000°C under N_2 for 2 min using rapid thermal annealing (RTA). (a, b) AFM images showing the graphene surface before and after Mo wet-etching on the non-annealed sample. (c, d) Same inspection after Mo wet-etching on the annealed sample. (e, f) SEM images corresponding to conditions (a, b) provide detailed morphological insights into the surface of the non-annealed sample. (g, h) SEM images corresponding to conditions (c, d), offering a comparative look at the annealed sample's surface morphology. Raman spectroscopy was conducted with a Horiba HR800 spectrometer equipped with a 514.5 nm Ar+ laser to assess the structural integrity and crystallinity of the graphene layers under different conditions. (i) Analysis of the non-annealed sample, examining the graphene both on Mo and post-Mo etching. (j) Examination of the annealed sample, focusing on graphene characteristics while on Mo and after Mo removal.

This disparity underscores the higher crystalline nature of graphene synthesized on annealed AlO$_x$ substrates, highlighting the critical role of annealing in achieving desirable graphene properties.

To comprehensively assess differences in CVD-grown graphene quality, transfer onto flat SiO_2 substrates is performed to accurately measure thickness and evaluate mechanical integrity for potential membrane applications. Figure 2.5a - d present AFM and SEM images of multi-layer graphene transferred onto flat SiO_2/Si substrates for both annealed and non-annealed samples. A comparison of the AFM data reveals significant differences in thickness between the samples. Specifically, the non-annealed sample exhibits thicknesses of approximately $t < 2$ nm, in contrast to the $t < 5$ nm observed for the annealed sample. This disparity is further underscored by surface roughness measurements, with the annealed sample displaying a roughness $S_a = 1.73$ nm compared to 0.271 nm for the non-annealed sample. Interestingly, the annealed sample exhibits specific residues or clusters, possibly remnants of Mo/AlO$_x$ interactions not entirely removed by the standard H_2O_2 etching method used.

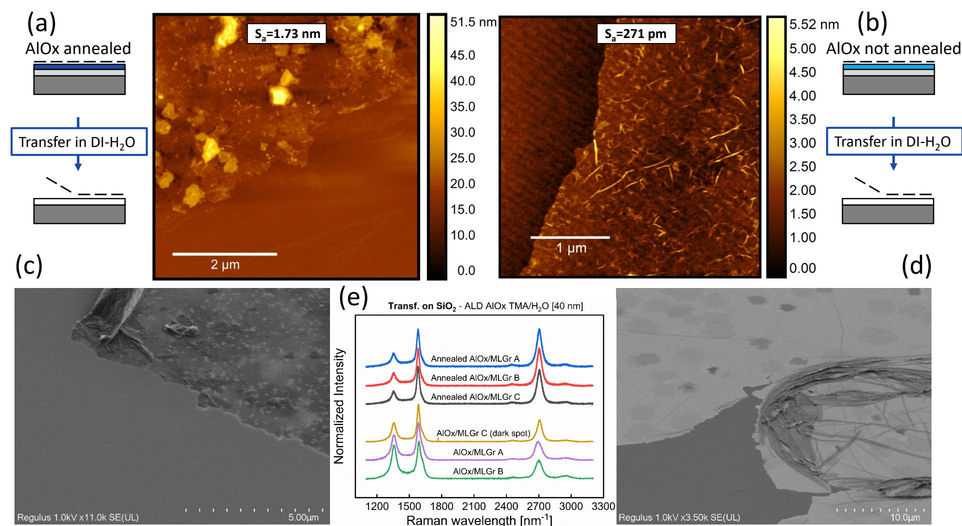

Figure 2.5: **Raman spectroscopy and thickness for multi-layer transfer-free graphene based on ALD AlO_x.** (a) Multi-layer graphene transferred and annealed. (b) Multi-layer graphene transferred without annealing, both applied to the same target thermal SiO_2 wafer. (c, d) SEM images of the samples described in (a) and (b), respectively. (e) Raman spectroscopy analysis used a 514.4 nm Ar+ laser, 100× objective with an NA of 0.9.

Contrarily, no such residuals were detected in the non-annealed sample except for some voids or cracks randomly distributed after Mo-etching. The SEM images also verify these observations in Figure 2.5c, d. Thus, Figure 2.5d illustrates a remarkably flat layer, despite some folding attributed to the manual wet-transfer process, alongside various patches within the graphene film. Raman spectroscopy analysis, shown in Figure 2.5e, indicates that the annealed sample exhibits FWHM values of 45, 32, and 58 cm^{-1} corresponding to the ω_D, ω_G, and ω_{2D} bands, respectively. For the non-annealed sample, FWHM values are 55, 50, and 87 cm^{-1} for the same wavelength interval. The broader FWHM values observed, without significant shifts in peak positions between samples, suggest a diminished crystallinity in the non-annealed sample. Notably, within darker spots of the graphene layer on the non-annealed sample, improved quality is evident, with FWHM values of 52, 31, and 58 cm^{-1} corresponding to ω_D, ω_G, and ω_{2D}.
These variations in FWHM are also accompanied by differences in the intensity ratio of I_D/I_G, where a broader FWHM correlates with a higher ratio, indicating structural differences in the graphene layers. Thus darker spots show $I_D/I_G = 0.5$ compared to $I_D/I_G = 0.8$ for the brighter spots. In subsection 2.2.3, the role of aluminum oxide (AlO_x), both annealed and non-annealed, as a buffer layer between SiO_2 and molybdenum (Mo) was explored to assess its effects on graphene synthesis. Differences in thickness, surface roughness, and hole density distribution across the layer were observed. These findings prompted further investigations into the lower hole distribution noted in the non-annealed AlO_x cases (Figure 2.5b).
Graphene growth experiments were initially performed using a standard stack configuration illustrated in Figure 2.6a. Subsequent experiments utilized the proposed stack

configurations shown in Figure 2.6b, Figure 2.5a, and Figure 2.4a. Following graphene synthesis, Mo was etched away, and the resulting structures were wet -transferred in DI-water onto pre-patterned, perforated silicon substrates for additional analysis using Transmission Electron Microscopy (TEM). The bright field inspections of the suspended areas in Figure 2.6a and Figure 2.6b demonstrated the absence of holes in the carbon layers previously synthesized on the non-annealed Al_2O_3 compared to the SiO_2 case in Figure 2.6a. Additional insights were provided by a tilted view of a SEM image of the respective sample shown in Figure 2.6a. This view included the holder used for analysis and a more detailed TEM image in Figure 2.6b, further illustrating the microstructural characteristics of the samples.

In summary, ALD AlO_x shows potential as an etching mask and clamping layer in a process flow designed to produce free-standing graphene via a transfer-free approach. The optional inclusion of an annealing step provides further control over material morphology, thickness, and defectivity, properties that could significantly influence graphene's mechanical and electrical performance as employed as a diaphragm in MEMS microphones.

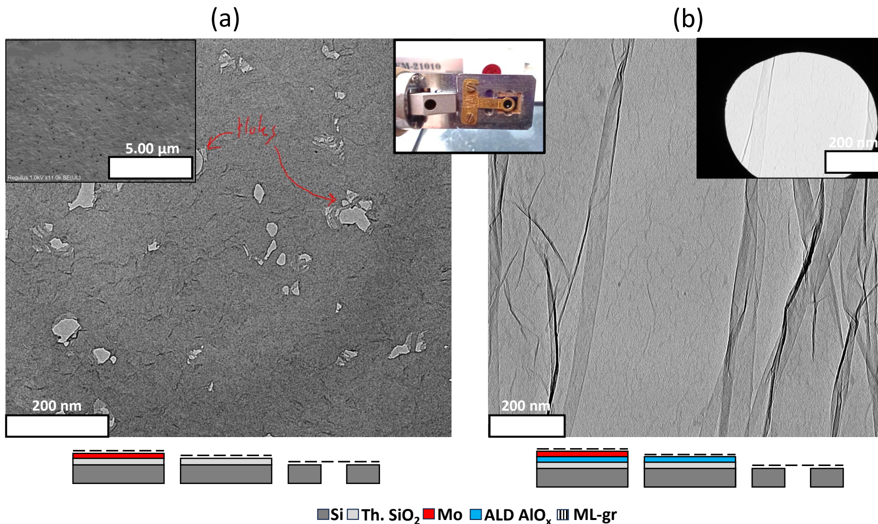

Figure 2.6: **Bright field TEM characterization of suspended graphene**The images were taken on a 120kV Jeol JEM-1400 plus TEM and TVIPS TemCam-XF416 camera.(a) TEM and SEM tilted image (insight) of suspended multi-graphene area initially synthesized on a Si/SiO_2/Mo (50 nm) stack. (b) TEM images of suspended multi-layer graphene initially grown on Si/SiO_2 (2 µm)/AlO_x (50 nm)/Mo (50 nm) thin film stack. The graphene synthesis for both samples was carried out under identical CVD processing conditions.

Film type	Gas [sccm]	T [°C]
PECVD a-SiC	CH_4 (4.110), SiH_4 (0.250)	400
LPCVD a-SiC	C_2H_2 (435), DCS (65)	600
ALD AlO_x	TMA (120), H_2O (40)	300
Annealed ALD AlO_x	TMA (120), H_2O (40)	300

Table 2.1: **Materials and process conditions.** Description of material used for Mo-based graphene synthesis compatibility with respective gas flows and deposition temperatures.

2.5. SURFACE MICROMACHINING DRUMS USING LPCVD SiN_x

An initial process flow is proposed to investigate the compatibility of transfer-free multi-layer graphene to fabricate membranes. It involves releasing graphene through surface micromachining using vapor HF, primarily aiming to create small membranes with $2R < 10\,\mu m$. Moreover, they are not aimed to be the targeted diaphragms for MEMS-microphones in this thesis, but they could be potentially used as resonators, bolometers, or pressure sensors. This concept could also lead to a directional capacitive MEMS-microphone or other devices based on various drums.
With this attempt to release the monolithically grown graphene with vapor HF, it is possible to explore its feasibility and highlight this method's potential benefits or limitations. Also, no additional etching vias are considered to etch the sacrificial layer due to the intrinsic presence of holes or defects within the graphene due to the Mo-based growth.
Figure 2.7 shows the process flow starting with an LPCVD SiN_x layer that is patterned by C_2F_6 chemistry with RIE, as described in the previous section. Then, once the silicon has been exposed, thermal oxidation is performed to target a SiO_2 layer with the same height of SiN_x (typically, this approach is called LOCOS as in Figure 2.7(1)).

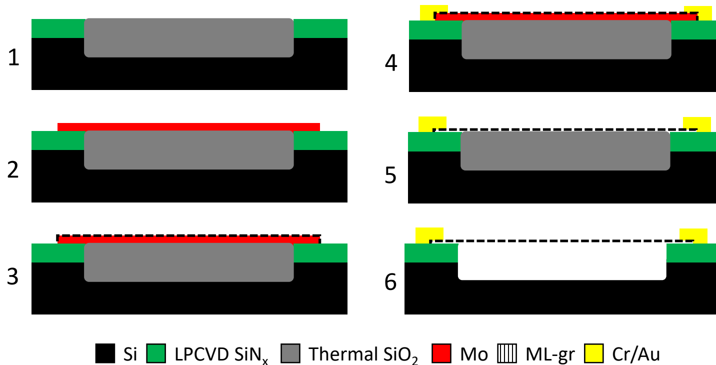

Figure 2.7: **Process-flow for surface-micromachining drums.** (1) LOCOS step to have SiO_2 thermally grown in Si with same height of SiN. (2) Mo sputtering and its patterning by dry-etching. (3) CVD of ML-gr. (4) Cr/Au electrodes by e-beam and lift-off. (5)Transfer-free step with Mo etching by H_2O_2. Vapor HF releasing the SiO_2 by the ML-Gr defects and holes.

With a flat profile within the different layers, it is expected to have a thin film of Mo entirely flat between the SiN_x and SiO_2 (Figure 2.7(1)), trying to prevent any discontinuity in the thin metal film that might affect the graphene growth and its integrity at the interface SiN_x/SiO_2. If LOCOS had not been performed, the graphene would have been grown in all the vertical side walls of the opening window of the SiN_x.
Once SiO_2 has reached the same height of SiN_x with a margining of ±10 nm, Mo has sputtered at 50°C, forming 50 nm of film, and then is patterned with Cl_2/O_2 ICP RIE (Figure 2.7(2)).
Then, graphene is grown at 935°C using CH_4 and low-pressure (Figure 2.7(3)), lift-off to have Cr/Au electrodes (Figure 2.7(4)), and finally, Mo etching with H_2O_2 and subsequent DI-water washing and drying (Figure 2.7(5)).
The graphene is released with VHF directly through the graphene holes used as an etching window at this step (Figure 2.7(6)).
The results related to each step are shown in Figure 2.8 wherein (a) graphene is on Mo, SiN_x and SiO_2 regions showing the same height, but trenches at its discontinuity are found. These pits are formed by the bird's beak effect, a result of the LOCOS process, occurring at the discontinuity between SiN_x and SiO_2 layers grown during thermal oxidation

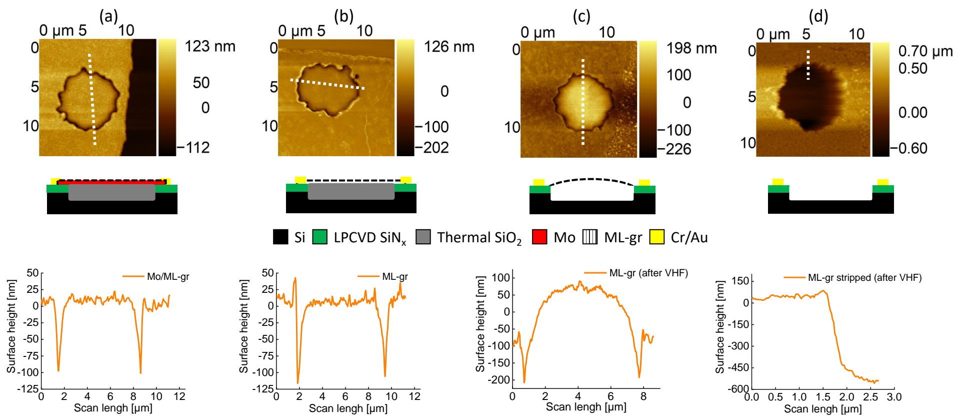

Figure 2.8: **AFM analysis of surface-micromachining drums.** (a) Scan length on ML-gr/Mo/SiN_x/SiO_2, (b) after Mo etching and (c) Vapor HF. (d) Cavity depth measurement after ML-gr stripping.

Due to the Vapor HF, the SiN_x has been residually etched, as it is possible to see in (c) outside the patterned multi-layer graphene region. Thus, in correspondence with the multi-graphene, less etching of SiN_x is expected due to the lower etching window areas. The ML-gr/SiN_x regions before and after the VHF showed an increase from $S_a = 3$ nm to $S_a = 5$ nm (3 µm×3 µm). This increase likely results from the partial etching beneath the carbon layer, introducing greater roughness due to morphological surface changes. While these alterations are minor compared to those in the directly exposed SiN_x areas, where roughness increased from $S_a = 1.57$ nm to $S_a = 21.3$ nm over the same scanned area. The drastic roughness increase in SiN_x is attributed to the formation of etching residuals (c), necessitating further processing by either baking or O_2 plasma cleaning. Given the potential for O_2 plasma to damage graphene, a baking step at 250°C was performed, reducing SiN_x roughness to 13.9 nm after just one minute. Conversely, the graphene's surface roughness in the ML-gr/SiN_x region increased from $S_a = 7.4$ nm to $S_a = 16.17$ nm post-baking. This escalation can be attributed to the thermal expansion coefficient mismatch between graphene and the underlying substrates (silicon and any residual SiN_x).

These trenches are a well-known effect of the LOCOS and are called bird's beak, and they have not been considered during the initial process concept. Despite the discontinuity, Mo is etched as in Figure 2.8b, and the same height between SiN_x and SiO_2 is still shown (Figure 2.8b).
After the membrane release, it is possible to notice surprisingly that the membrane shows a dome shape (Figure 2.8c). The dome shape could be related to a compressive stress of the membrane after release or a bent behavior due to the trenches or the Mo rough surface after the 935°C graphene growth. However, this is an open question that needs to be further investigated. Differential thermal expansion during baking induces mechanical stress within the graphene, leading to buckling and wrinkling as it adapts to these stresses. Implementing controlled temperature ramping steps during the baking process could potentially reduce the formation of folds and wrinkles in the multi-layer graphene.
Despite the dome shape, to verify that the sacrificial layer is etched, the multi-layer graphene is stripped with tape or removed by oxygen plasma, and as in Figure 2.8d, the cavity is found after vapor HF. The same cavity was not present in Figure 2.8a, b, as it is possible to see from the AFM and correspondent height profile between the different films. Figure 2.9 and Figure 2.10 also compare another batch with a similar approach, where the graphene shows the same results in the suspended region and its continuity at SiN_x/etched cavity.
These membranes have been characterized using a system [26–28] where an Ar intensity modulated 405 nm blue laser drives the graphene membrane via optical absorption and thermomechanical force. A 632 nm red He-Ne laser beam targets the drum and cavity bottom, and interference is detected at a photodiode. The mechanical motion of the graphene drum modulates the intensity. A vector network analyzer (VNA) modulates the blue diode intensity and detects the red laser light intensity on the photodiode to determine the frequency spectrum of the membrane. The results are shown in Figure 2.11.

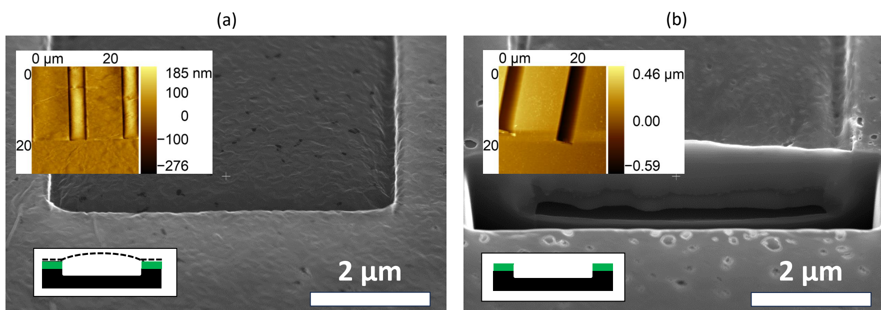

Figure 2.9: **AFM and SEM/FIB analysis of surface-micromachining drums.** (a) AFM/SEM-tilted image of ML-gr after VHF. (b) FIB-investigation on suspended graphene (protected with Pt). (b) AFM inspection of the same drum after stripping of ML-gr.

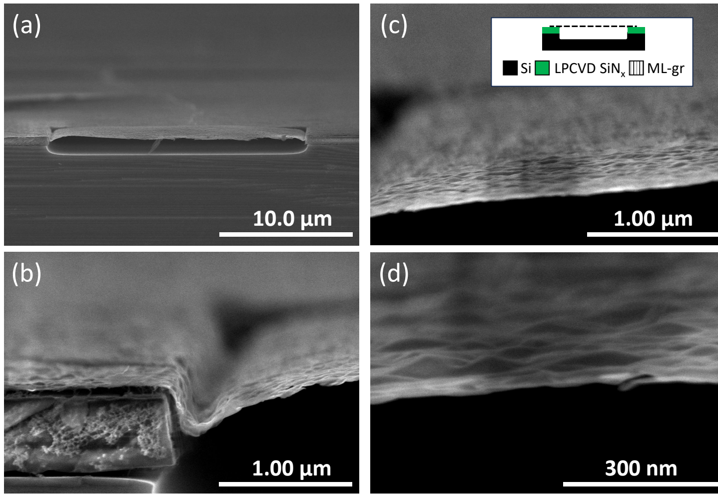

Figure 2.10: **Cross-section of ML-gr drum by SEM.** (a-d) All images depict a chip that has been manually cleaved along the drum area. Vapor HF treatment is applied after the cleaving process.

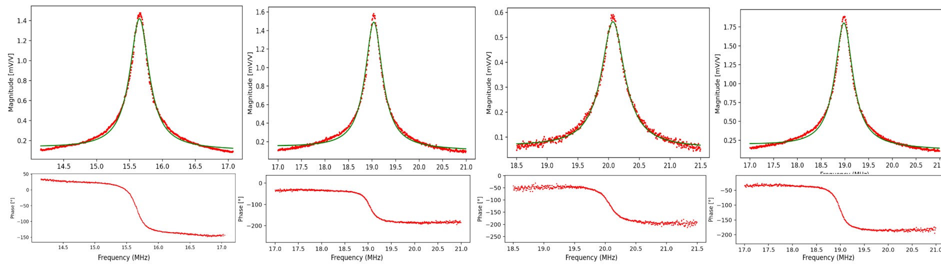

Figure 2.11: **Resonance frequency analysis of surface-micromachining drums.** The plots display the magnitude [mV/V] and phase [degrees] at the resonance frequency of the analyzed drums. The raw data have been fitted using Lorentz functions to determine the resonance frequency positions. In total, 14× drums with diameters ranging from 6 µm to 10 µm were characterized, revealing f_{01} values in the range of 12.4 MHz to 26.4 MHz.

2.6. CONCLUSIONS

This chapter has explored the integration of various materials in offering a portfolio of suitable material for next free-standing Mo-based graphene membranes purpose. Key findings include:

- Demonstrated the suitability of several thin film stacks such as SiN_x, a-SiC, and AlO_x for Mo-based graphene synthesis. Based on their characteristics and results, SiN_x and a-SiC are identified as more suitable for the next process flow development, particularly for free-standing graphene by bulk micromachining.
- A correlation between Raman spectroscopy effectivity I_D/I_G and sheet resistance R_s [Ohm/sq] is investigated to be used as a reference for subsequent analyses in

2

this thesis. It has been found that high defectivity translates into high R_s. Also, the heating gradient distribution over the wafer during the CVD plays a crucial role in the final graphene quality.

- PECVD a-SiC was found to be incompatible for Mo-based process flows, unlike LPCVD a-SiC, which shows potential for future process flows. However, further investigation is needed regarding hillocks and graphene film integrity, which can be inspected once the layer is free-suspended.
- The choice of AlO_x as a buffer layer can drastically impact the graphene quality in terms of defectivity and thickness. Without annealing, the same AlO_x film can reduce the number of holes that have been found in the synthesized carbon layer compared to other thin films such as thermal SiO_2, LPCVD SiN_x, LPCVD a-SiC, and annealed AlO_x.
- A surface micromachining technique has been developed to fabricate multi-layer graphene drums, utilizing SiN_x as both an etching mask and clamping layer. Thermal SiO_2 serves as the sacrificial layer. Several membranes have been dynamically analyzed to evaluate their resonance frequencies, confirming their proper suspension and potential for use as resonators.

These insights are essential for the upcoming work described in the following chapters, offering clear directions to refine fabrication processes and enhance device performance. The methodologies and experimental outcomes discussed herein pave the way for future research and solidify the foundational techniques essential for the scalable production of high-quality graphene-based devices.

REFERENCES

[1] G. Kaur, K. Kavitha, and I. Lahiri, *Transfer-free graphene growth on dielectric substrates: A review of the growth mechanism,* Critical Reviews in Solid State and Materials Sciences **44**, 157–209 (2018).

[2] W. Kong, H. Kum, S.-H. Bae, J. Shim, H. Kim, L. Kong, Y. Meng, K. Wang, C. Kim, and J. Kim, *Path towards graphene commercialization from lab to market,* Nature Nanotechnology **14**, 927–938 (2019).

[3] A. Castellanos-Gomez, V. Singh, H. S. J. van der Zant, and G. A. Steele, *Mechanics of freely-suspended ultrathin layered materials,* Annalen der Physik **527**, 27–44 (2014).

[4] S. Wagner, C. Weisenstein, A. Smith, M. Östling, S. Kataria, and M. Lemme, *Graphene transfer methods for the fabrication of membrane-based NEMS devices,* Microelectronic Engineering **159**, 108 (2016).

[5] J. Romijn, S. Vollebregt, H. W. van Zeijl, and P. M. Sarro, *A wafer-scale process for the monolithic integration of cvd graphene and cmos logic for smart mems/nems sensors,* in *2019 IEEE 32nd International Conference on Micro Electro Mechanical Systems (MEMS)* (IEEE, 2019).

[6] F. Laermer, S. Franssila, L. Sainiemi, and K. Kolari, *Deep reactive ion etching,* in *Handbook of Silicon Based MEMS Materials and Technologies* (Elsevier, 2020) p. 417–446.

[7] I. W. Rangelow, *Critical tasks in high aspect ratio silicon dry etching for microelectromechanical systems,* Journal of Vacuum Science amp; Technology A: Vacuum, Surfaces, and Films **21**, 1550–1562 (2003).

[8] B. Wu, A. Kumar, and S. Pamarthy, *High aspect ratio silicon etch: A review,* Journal of Applied Physics **108** (2010), 10.1063/1.3474652.

[9] *Silicon Sensors and Actuators: The Feynman Roadmap* (Springer International Publishing, 2022).

[10] P. Hammond, *Vapor-phase etch processes for silicon mems,* in *Handbook of Silicon Based MEMS Materials and Technologies* (Elsevier, 2020) p. 519–530.

[11] X.-J. Zhang, *Anti-adhesion/stiction surface design, fabrication, and applications,* in *Encyclopedia of Tribology* (Springer US, 2013) p. 83–85.

[12] S. Vollebregt, B. Alfano, F. Ricciardella, A. J. M. Giesbers, Y. Grachova, H. W. van Zeijl, T. Polichetti, and P. M. Sarro, *A transfer-free wafer-scale cvd graphene fabrication process for mems/nems sensors,* in *2016 IEEE 29th International Conference on Micro Electro Mechanical Systems (MEMS)* (IEEE, 2016).

[13] Y. Grachova, S. Vollebregt, A. L. Lacaita, and P. M. Sarro, *High quality wafer-scale cvd graphene on molybdenum thin film for sensing application,* Procedia Engineering **87**, 1501–1504 (2014).

[14] B. Du Bois, G. Vereecke, A. Witvrouw, P. De Moor, C. Van Hoof, A. De Caussemaeker, and A. Verbist, *Hf etching of si-oxides and si-nitrides for surface micromachining,* in *Sensor Technology 2001* (Springer Netherlands, 2001) p. 131–136.

[15] D. Drysdale, *Vapour phase hf and xef2 etching methods with improved selectivity for mems manufacturing,* (2015).

[16] F. Ricciardella, S. Vollebregt, T. Polichetti, M. Miscuglio, B. Alfano, M. L. Miglietta, E. Massera, G. Di Francia, and P. M. Sarro, *Effects of graphene defects on gas sensing properties towards no2 detection,* Nanoscale **9**, 6085–6093 (2017).

[17] F. Ricciardella, S. Vollebregt, B. Boshuizen, F. J. K. Danzl, I. Cesar, P. Spinelli, and P. M. Sarro, *Wafer-scale transfer-free process of multi-layered graphene grown by chemical vapor deposition,* Materials Research Express **7**, 035001 (2020).

[18] F. Ricciardella, S. Vollebregt, E. Kurganova, A. J. M. Giesbers, M. Ahmadi, and P. M. Sarro, *Growth of multi-layered graphene on molybdenum catalyst by solid phase reaction with amorphous carbon,* 2D Materials **6**, 035012 (2019).

[19] S. Ray, D. Das, and A. Barua, *Infrared vibrational spectra of hydrogenated amorphous silicon carbide thin films prepared by glow discharge,* Solar Energy Materials **15**, 45–57 (1987).

2

[20] Y. Liu, S. Yoon, J. Ahn, and W. Milne, *Effect of hydrogen dilution on the deposition of carbon-rich a-sic:h films by the electron cyclotron resonance method,* Materials Science and Engineering: B **39**, 188–194 (1996).

[21] K. Eberhardt, E. Lotter, M. Heintze, H.-D. Mohring, and G. Bauer, *Structural properties of high electronic quality a-si1-xcx:h by infrared spectroscopy,* MRS Proceedings **258** (1992), 10.1557/proc-258-673.

[22] L. Tong, M. Mehregany, and W. Tang, *Amorphous silicon carbide films by plasma-enhanced chemical vapor deposition,* in *[1993] Proceedings IEEE Micro Electro Mechanical Systems* (IEEE).

[23] Z. A. Van Veldhoven, *Integrated catalytic fabrication approaches for graphene-based electronic devices,* (2019), 10.17863/CAM.44853.

[24] M. Broas, O. Kanninen, V. Vuorinen, M. Tilli, and M. Paulasto-Kröckel, *Chemically stable atomic-layer-deposited al2o3 films for processability,* ACS Omega **2**, 3390–3398 (2017).

[25] B. Vasić, U. Ralević, K. Cvetanović Zobenica, M. M. Smiljanić, R. Gajić, M. Spasenović, and S. Vollebregt, *Low-friction, wear-resistant, and electrically homogeneous multilayer graphene grown by chemical vapor deposition on molybdenum,* Applied Surface Science **509**, 144792 (2020).

[26] R. J. Dolleman, D. Davidovikj, S. J. Cartamil-Bueno, H. S. J. van der Zant, and P. G. Steeneken, *Graphene squeeze-film pressure sensors,* Nano Letters **16**, 568–571 (2015).

[27] R. J. Dolleman, D. Chakraborty, D. R. Ladiges, H. S. J. van der Zant, J. E. Sader, and P. G. Steeneken, *Squeeze-film effect on atomically thin resonators in the high-pressure limit,* Nano Letters **21**, 7617–7624 (2021).

[28] M. Lee, D. Davidovikj, B. Sajadi, M. Šiškins, F. Alijani, H. S. J. van der Zant, and P. G. Steeneken, *Sealing graphene nanodrums,* Nano Letters **19**, 5313–5318 (2019).

3

MINIATURIZED MULTI-LAYER GRAPHENE DIAPHRAGMS

This chapter introduces a novel approach utilizing micromachining techniques to fabricate transfer-free multi-layer graphene membranes directly on 100 mm silicon wafer, eliminating the need for transfer steps. The primary objective of this study is to address a significant bottleneck in integrating graphene into MEMS devices from a fabrication viewpoint. Following the experimental findings of Chapter 2, this chapter introduces a process flow for fabricating large free-standing graphene membranes, characterizing them primarily through optical measurement techniques. The analysis explores the fabrication yield, assessing the consistency and efficiency of this process aiming also to indicate possible improvements for the upcoming work. Furthermore, this chapter involves the assessment of the suitability of these membranes for acoustic applications. Combining these efforts will provide a holistic understanding of the fabricated diaphragms, paving the way for their potential applications across diverse technological domains.

Parts of this chapter have been published in: R.Pezone et al., *Sensitive Transfer-Free Wafer-Scale Graphene Microphones*, ACS Applied Materials & Interfaces, 2022 [1] and R.Pezone et al., *High-Performance Wafer-Scale Transfer-Free Graphene Microphones*, 2023 IEEE 36th International Conference on Micro Electro Mechanical Systems (MEMS) [2].

3.1. Introduction

Reflecting on the current challenges and limitations in integrating graphene into MEMS microphones as highlighted in Chapter 1 ([3–8, 8, 8–10, 10, 11, 11], this work explores a novel wafer-scale, transfer-free methodology. Specifically, it investigates material analysis to examine process viability and evaluate material integrity. This analysis includes yield characterization, initial mechanical assessments, resonance frequency measurements, and mechanical compliances.

These measurements are essential for quantifying the mechanical properties of the proposed multi-layer graphene, allowing us to determine its suitability for subsequent device design and potential applications.

It is important to note that for graphene, the properties can vary significantly due to various factors such as synthesis methods, processing techniques, and other variables [12–17].

This chapter is essential to identify the material characteristics and their implications for the potential use of the proposed multi-layer, especially as MEMS microphone diaphragms.

3.2. Experimental section

3.2.1. Bulk micromachining process flow

The device process design incorporates multi-layer transfer-free graphene and materials compatible with vapor HF to ensure structural integrity during sacrificial layer etching. The choice of this process flow is based on the discussed results shown in Chapter 2.

A pre-patterned Mo catalyst seed-layer is used for localized graphene synthesis on silicon substrates, following the procedure outlined in prior studies[18, 19]. Multi-layer graphene is preferred over single-layer graphene as it offers superior mechanical robustness, an essential property for fabricating membranes with the adequate size required in MEMS-microphones [20–23].

Thermal SiO_2 and LPCVD silicon-rich low-stress SiN_x are chosen as the primary materials for the proposed process flow. Thermal SiO_2 is chosen as sacrificial layer while SiN_x layer serves a dual purpose, functioning as a clamping support layer and etching mask along the periphery of the patterned graphene membrane protecting specific areas of SiO_2 during both the silicon backside DRIE and Vapor HF sacrificial layer SiO_2 release etch (Figure 3.1).

Thus, a 110 nm layer of LPCVD silicon-rich low-stress material (SiH_2Cl_2 315 sccm/NH_3 85 sccm) is deposited at 850°C onto a 1 µm thermal oxide layer on a 100 mm $t = 525$ µm silicon p-type wafer. The SiN_x layer undergoes dry-etching in defined regions on the topside, and complete removal occurs on the backside.

A 5 µm PECVD TEOS (tetraethoxysilane)-based layer is then deposited, serving as the etching mask for silicon DRIE (refer to Figure 3.1, step 1).

A 50 nm Mo thin film is sputtered at a low temperature of 50°C and etched using a dry-etching process with Cl_2, O_2 chemistry. Due to the sputtering process nature, Mo uniformly covers all topography steps, preventing any discontinuities that may affect the future released CVD-grown graphene membrane (Appendix 3.5, Figure 3.6). This approach provides extensive freedom in process integration for developing more complex

devices and geometries incorporating graphene.
Subsequently, positive photoresist removal is carried out using O_2 plasma, and all remaining residuals are washed in N-Methyl-2-Pyrrolidone (NMP), followed by DI-water washing (see Figure 3.1, step 2). At this stage, graphene synthesis occurs at 935 °C using an in-house AIXTRON Black Magic reactor with a pressure of 25 mbar H_2 as a reducing agent for oxidized Mo, and a CH_4 step for growth (refer to Figure 3.1, step 3). Afterward, Cr/Au 20/200 nm are evaporated by ion-beam evaporation in a vacuum and patterned through a lift-off technique with NMP at 65°C for 1 h, followed by a final low-power sonication of 90 s (see Figure 3.1, step 4). Following NMP, the wafer undergoes washing in acetone and DEMI-water.
Mo is chemically etched with H_2O_2 for 5 min and gently washed with DEMI-water to eliminate all chemical etching residuals (refer to Figure 3.1, step 5).
Deep reactive etching on the backside, with the graphene side facing the chuck, is performed to avoid exposure to SF_6 plasma that could potentially damage the material (see Figure 3.1, step 6).
Finally, after dicing 1 cm x 1 cm chips, VHF etching is conducted at 45°C with 100% anhydrous HF, N_2, EtOH, in a commercially available Primaxx μEtch system at 125 Torr as depicted in Figure 3.1 (step 7).
Importantly, in the last isotropic etching phase, the use of polymers or tapes to protect the graphene side, which could potentially entrap HF molecules because of their porous characteristics when exposed to solvents like EtOH, is avoided. In addition, such materials typically require aggressive removal methods like O_2 plasma or other dry-etching

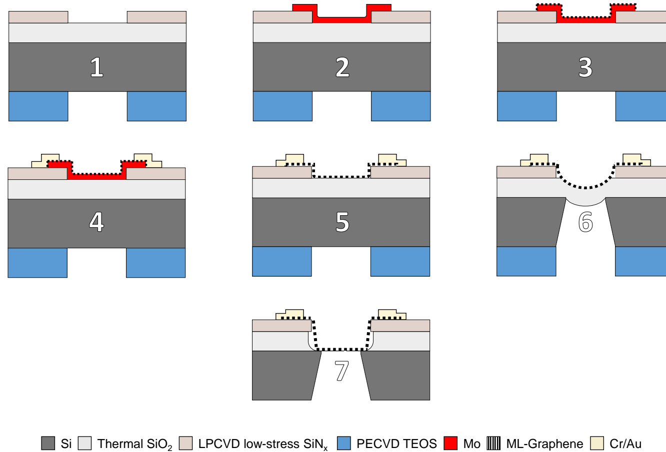

Figure 3.1: **Main fabrication steps.** (1) Patterning of the 110 nm LPCVD SiN_x layer (top-side) and 5 µm PECVD TEOS layer (back-side) by dry-etching. (2) Sputtered and drie-etch patterned 50 nm Mo layer. (3) Graphene synthesis at 935°C at low-pressure of 25 mbar. (4) Evaporated 20/200 nm Cr/Au layer after lift-off patterning. (5) Structure after sacrifical Mo wet-etch in H_2O_2. (6) Backside Deep Reactive Ion Etch (DRIE) of the silicon substrate. (7) Vapor HF etching of the SiO_2 finally resulting in suspended ML-gr membranes.

chemistry, which can potentially damage or remove the suspended graphene.
Finally, this proposed approach allows for lower-temperature thermal treatments where the cleaning temperature ($T > 110°C$) to eliminate residuals originating from LPCVD SiN_x growth and vapor HF reaction[24] results significantly lower compared to the $T > 250°C$ typically needed for removing the polymer used in transferring graphene onto pre-patterned holes [25–28]. The lower temperature in this approach is advantageous, as thermal removal of transfer polymer residuals generally results in a lower number of surviving membranes, especially for larger membranes due to the thermal expansion coefficient mismatch between the suspended graphene and the substrate.
A potential limitation affecting the quality of graphene could be the use of vapor HF, as it has been reported that it might lead to the fluorination of the carbon film, thereby transforming it into a material resembling Teflon. Such a transformation typically alters the material's intrinsic properties, turning it into an insulator and affecting its mechanical characteristics [29].

3.2.2. Mechanical compliance measurement

The input sound pressure emitted from a speaker is quantified through a reference microphone (Sonarworks XREF20) positioned underneath the sample. A Moku:Lab hardware platform by Liquid Instruments captures the signals from the reference microphone, the mechanical frequency response of the graphene membrane, as identified by a Polytec vibrometer focused at the membrane's center, and the speaker's output signal. Following appropriate adjustments for the sensitivities of the vibrometer controller and reference microphone, mechanical compliance is derived from the ratio of the signals received by the Moku:Lab. Further details are provided in the Appendix 3.5 (Figure 3.7).

3.3. Results and discussion

3.3.1. Membrane fabrication results

The topography of the SiO_2/ML-gr heterostructure, before VHF etching of the SiO_2, undergoes optical inspection using a 3D laser scanning confocal microscope across over 100 drums.
The graphene exhibits out-of-plane deformation (Figure 3.2a) due to compressive stress in the SiO_2 layer, causing a downward bend in the diaphragm. This undesired deformation arises primarily from the difference in coefficients of thermal expansion (CTE) between the SiO_2 layer ($0.5 \times 10^{-6}\,K^{-1}$) and the silicon substrate ($2.6 \times 10^{-6}\,K^{-1}$)[30–32]. As the substrate heats up or cools down, the silicon and oxide layers expand or contract at different rates, leading to mechanical stress that can be relieved with high deformation.
In more detail, the drum's first buckling state is observed for smaller diameter membranes, as depicted in the inset of Figure 3.2a. In this case, the buckled shape can be approximated differently by a single sinusoidal or half-sinusoidal wave pattern rather than higher buckling modes. Larger diameter drums ($2R = 300 - 350\,\mu m$) exhibit wavy deformations along the membrane's edge, corresponding to higher buckling modes[33]. In Figure 3.2a, the maximum values of the out-of-plane deflection h_0 at the center of the membranes are plotted for various membrane diameters. The deflection of the het-

erostructures is modeled using an analytical equation[30–32].

$$h_0 = \pm\frac{1}{8}\sqrt{-35\left(\frac{3\sigma(1-\upsilon^2)R^2}{E}+4t^2\right)} \tag{3.1}$$

The Poisson's ratio $\upsilon = 0.2$, Young's modulus $E = 74\,\text{GPa}$, thickness $t = 0.95\,\mu\text{m}$, and radii R are detailed in the legend of Figure 3.2a. The analytical calculation, based on considering only the stress σ in SiO_2[32], yields a compressive stress of $\sigma = -275\,\text{MPa}$[31], aligning well with the observed correspondence indicated by the three colored bands in Figure 3.2a. Specifically, when considering Equation 3.1, we exclude graphene parameters as effective contributors to stress and Young's modulus in a system composed of thermal oxide and graphene. This is because graphene's stress levels are expected to be very low, and its thickness being less than 10 nm, significantly diminishes its influence on the system's properties compared to the thicker SiO_2 ($t = 1000\,\text{nm}$).

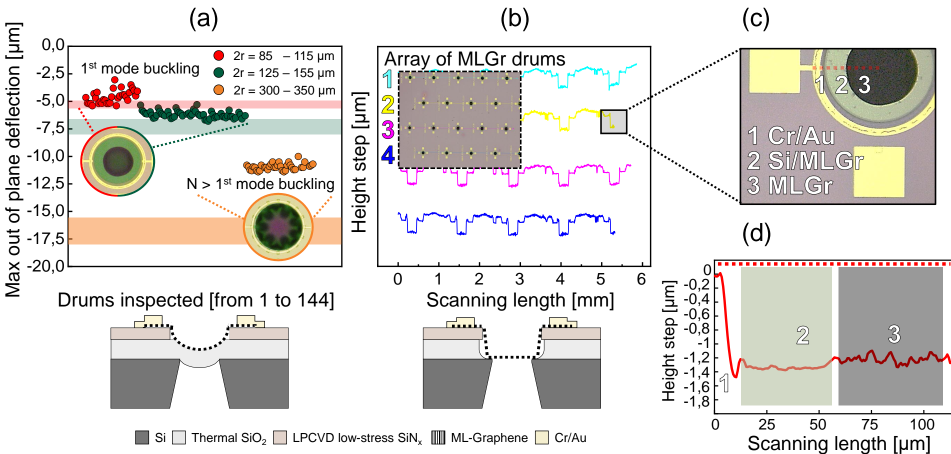

Figure 3.2: **Topographic analysis of the graphene membranes before and after SiO_2 etch using 3D laser scanning confocal microscope.**(a) Maximum out-of-plane deflection h_0 of the suspended SiO_2/ML-gr heterostructure at the center of the drum. The analytically predicted h_0 for the different diameters, based on a compressive stress in the SiO_2 of $\sigma = -275\,\text{MPa}$, is indicated by the colored bands. The membranes with $2R < 155\,\mu\text{m}$ show an experimental behaviour close to the analytical trend with a first buckling mode (inset microscope image $n = 1$). Larger membranes deviate from this trend and reveal higher order modes of buckling ($n > 1$ inset microscope image). (b) Cross-section of the wafer containing multiple membranes performed on the released ML-gr membranes after the vapor HF removal of the SiO_2 layer. The membrane on the wafer have reproducible shapes and buckling observed in (a) has disappeared with a flat suspended membrane region. (c) Microscope image showing a Cr/Au electrode for contacting the graphene (not used in this work) and the supported and suspended part of the ML-gr. (d) Step height measurement with the confocal microscope along the red dashed line in c) showing that the ML-gr is around $1.3\,\mu\text{m}$ lower than the electrode. This height difference is due to the thickness of the SiO_2, SiN_x and electrodes.

The measured deflection (h_0) on the large diameter drums ($2R = 300-350\,\mu\text{m}$) diverges from the theoretical prediction, attributed to the presence of higher buckling modes[33].

Upon SiO_2 etching, the graphene regains its original flat shape in the suspended region through adhesion to the unetched silicon substrate along its circumference (refer to Figure 3.2b, c, d and Appendix 3.5 in Figure 3.9). In this case, the flatter look of graphene post-etching can be explained by releasing the compressive stresses previously exerted by the oxide layer. Given graphene's lower stress and ability to withstand significant strain without permanent deformation, eliminating the compressive stress from the oxide permits the graphene to revert to a flat state [34][35]. Without the compressive stress from the underlying oxide, it does not buckle but instead tends to flatten because of its own expected low tensile stress. Additionally, the unetched silicon may contribute to this flattening as in Figure 3.2b, c.
The flatness is confirmed by measuring the step-height between the surface of the Cr/Au electrode and the Si surface of the suspended ML-gr (see Figure 3.2d), which is approximately 1.3 µm, equal to the sum of the thicknesses of SiO_2, SiN_x, and the electrode. As depicted in Figure 3.2b, the membranes successfully withstand the processing.
Yield quantification via optical inspection (Table 3.1) reveals a 100% yield for membranes with diameters ranging from 85 µm to 155 µm, with all 132 suspended devices surviving post vapor HF release. Large SiO_2/ML-gr heterostructures with diameters of 300 to 350 µm exhibit a 37% yield on 117 fabricated drums after DRIE. Post SiO_2 etching, the yield decreases from 37% to 18%. After one week of storage and handling, small membranes maintain a 100% yield, while the survival rate of large membranes decreases to 8%. The variation in yield among drum sizes could be attributed to high deformations causing wrinkles, distortions, and even cracks in the oxide before the final release, especially for large drums (Appendix 3.5 in Figure 3.12). These deformations may adversely affect graphene integrity, leading to randomly distributed tears and localized stress. Throughout VHF processing, handling, and storage, these deformations could serve as sources of crack propagation, potentially resulting in membrane breakage. Gas pressure on the membrane during handling and storage might also reduce yield in larger membranes. Addressing this could involve tuning the stress and thickness of the oxide layer or incorporating strain compensation measures, such as suspending the ML-gr from a SiN_x frame generating tensile stress[36].
The yield measurements refer to 10× chips, each measuring 10 mm × 10 mm. It is significant to mention that the full wafer area (100 mm) also has additional regions patterned for various other objectives. Thus, for this study, only the specific wafer area of interest for the membranes is considered.

Table 3.1: Fabrication membrane yield (surviving membranes/total membranes).

Diameter	85 – 155 µm	300 – 350 µm
ML-gr/SiO_2 @DRIE[a]	132/132	44/117
ML-gr @VHF[a]	132/132	22/117
ML-gr @7 days[a]	132/132	10/117

[a]Survived at the mentioned step without ruptures or cracks;

3.3.2. GRAPHENE CHARACTERIZATION

The crystallinity of the ML-gr is examined using a Horiba HR800 Raman spectrometer featuring a 514.5 nm Ar+ laser. A 100× objective with a numerical aperture of 0.9 is employed, resulting in a spot size of approximately 696 nm.

Two prominent Raman bands characterize graphene properties: the G band, centered at 1580 cm^{-1}, indicative of all graphitic sp^2-type structures in a stress and doping-free state; and the 2D band, centered at 2700 cm^{-1}, providing information about the layer number and stacking order.

In Figure 3.3a, illustrating a Raman spectrum of an ML-gr trampoline after VHF normalization to the G band, a third notable D band is observed with an intensity of approximately 0.68 suggesting the presence of defects. The D band is associated with various defects distorting the graphene lattice, such as edges, wrinkles, Stone-Wales defects, and vacancies. The relatively high intensity of the D band indicates the possible invasiveness of the process on the graphene, exceeding the defect intensity reported in previous works for the same material[18, 19]. The heightened defectivity is primarily attributed to the lift-off step involving N-methyl pyrrolidone (NMP) during Cr/Au electrode fabrication. The graphene on Mo is exposed for 40 min at 65°C with a final low-power ultrasonic bath of 90 s to remove cross-linked photoresist (PR). The intercalation of NMP into the stacked layers, the lift-off and the short ultrasonic bath likely might affect the material's quality, consistent with findings reported in other works[37, 38].

The elevated defectivity noted may be partially ascribed to the suboptimal performance of the reactor, especially after prolonged operation without adequate cleaning, resulting in reduced quality of the synthesized graphene due to a possible higher density of amorphous carbon (a-C), or a reduction of heat coupling to the substrate caused by carbon deposits on the quartz underneath the susceptor.

Raman characterization on these samples was not performed before the lift-off process. The DRIE process is excluded as a source of invasiveness since the graphene is shielded from the plasma etch by the backside of the wafer, facing the tool's chuck. Additionally, VHF is not considered a potential source of defects, as the I_D/I_G ratio shows no significant change after release (Figure 3.3b).

Comparing the G and 2D peak positions of the material before and after suspension reveals a noticeable red-shift or softening. After the VHF removal of SiO_2 from the suspended ML-gr (Figure 3.3d), ν_G shifts from 1582.1 cm^{-1} to 1574.1 cm^{-1}, and ν_{2D} shifts from 2696.3 cm^{-1} to 2682.8 cm^{-1}. These shifts might be attributed to phonon softening, reflecting the transition of graphene stress from compressive to a more tensile state during the removal of the buckled SiO_2 layer, as schematically illustrated in Figure 3.3a,b. These findings align with previous literature on mono-layer, few-layer graphene, and graphite[39–41]. The Raman 2D-peak ratios, as illustrated in Figure 3.3a, serve as representative indicators for multi-layer graphene[42], where $I_{2D}/I_G < 1$ ratios are measured.

For graphene thickness measurement, a semi-contact mode Atomic Force Microscope (AFM) from Cypher Asylum Research is employed, yielding a thickness value of approximately $t = 7 \pm 2$ nm. The standard deviation of 2 nm reflects the non-uniformity, as evidenced by variations in the line scans in Figure 3.3c. Given the challenges of directly measuring the step height of carbon layers on SiN_x, the reported AFM thickness measurements are obtained on graphene processed through all reported steps except VHF.

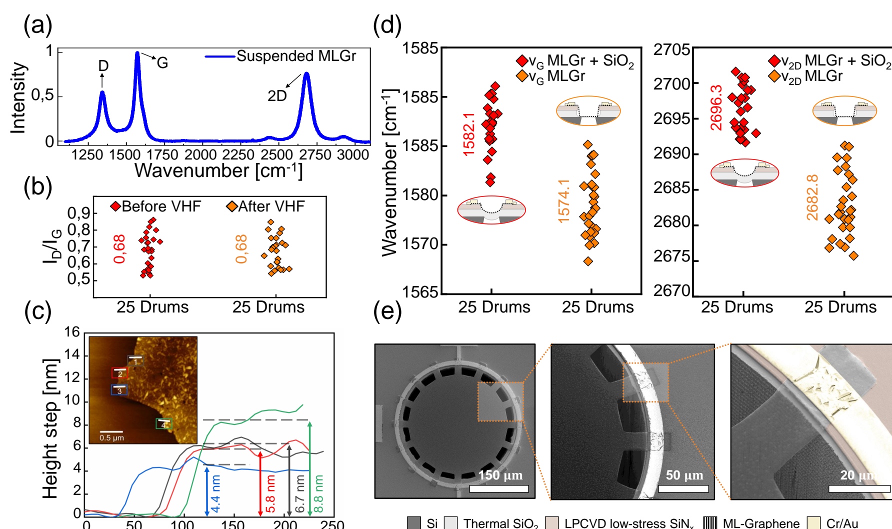

Figure 3.3: **Graphene characterization.** (a) Raman spectrum from 1100 – 3200 cm^{-1} of the trampoline ML-gr in the suspended region after the VHF release. (b) Comparison of the Raman peak ratio I_D/I_G before and after the VHF treatment in the suspended region for 25 drums. (c) Thickness measurement of the ML-gr graphene after transfer by AFM in semi-contact mode. (d) Raman peak frequencies of the G and 2D bands before and after VHF etch in the free-suspended area. (e) Scanning electron microscope pictures made by SEM Hitachi Regulus 8230 of suspended graphene trampoline with a diameter of $2R = 300\,\mu$m. Cr/Au electrodes and SiN_x substrate clamp the suspended graphene membrane.

Subsequently, the graphene is wet-transferred in DI-water onto a clean thermally oxidized silicon chip. This transfer is necessary due to partial etching of SiN_x during Mo patterning and VHF exposure, making it unsuitable as a flat reference point.
The small wrinkles observed in Figure 3.3c are generally attributed to the small grains on the Mo catalyst surface, which emerge during the CVD synthesis temperature of 935°C, imprinting their topography onto the graphene[43] or some residuals from the cross-linked PR. Figure 3.3e presents a suspended membrane patterned in a trampoline geometry with a diameter of 300 µm. At the supports of the ML-gr trampoline, it is evident that the Cr-Au/SiN_x/Si interface functions as a clamping support for the suspended graphene.

3.3.3. RESONANCE FREQUENCY AND MECHANICAL COMPLIANCE

The resonance frequency's initial mode is determined using a digital holographic microscope (LyncéeTec) equipped with a 666 nm laser and a 10× objective lens. By analyzing the interference between the reflected laser beam from the sample and the reference path, the intensity and phase information for each pixel are obtained, defining the 3D topography. These measurements are conducted in a vacuum chamber at 10^{-3} mbar to minimize air-damping effects. The samples are vibrated by shaking them with a piezoelectric element beneath the chip, actuated using a voltage-controlled stage with a 0.5 V sine-wave in the frequency range up to $f = 350$ kHz, where the fundamental resonance

frequency is expected to be accordingly the Equation 3.2 [44].

$$f_0 = \frac{2.405}{2\pi R}\sqrt{\frac{n_0}{\rho t}} \tag{3.2}$$

Here, n_0 represents the pre-tension in N/m of the graphene, ρ denotes the mass density, and t indicates the thickness of the graphene. The bending rigidity contribution is neglected in this relation due to its estimated low quantity [45].
The investigated membranes exhibit fundamental frequencies ranging from ≈ 156 – 318 kHz for diameters of $2R$ = 120 – 155 µm (see Figure 3.4a) and ≈92 kHz for trampolines with diameters of $2R$ = 300 µm. These measured values show lower resonance frequencies than previous results for mono-layer and bi-layer graphene of similar diameter [11]. Using a graphene thickness of 7 nm, a density of 2260 kg/m^3, and a diameter range between 120 – 155 µm, the experimental results align with the analytical values within a pre-tension window of n_0 = 0.03 – 0.05 N/m (see Figure 3.4a). Deviations between experimental and theoretical resonance frequencies might be attributed to variations in pre-tension due to small non-uniformities in graphene boundary conditions, variations in hole geometries, differences in clamping electrode geometries, mass density variations, or unetched SiO_2 residuals between the graphene and the silicon substrate.
When the membrane is actuated at its resonance frequency, the LyncéeTec captures its mechanical mode shape through optical phase shifts resulting from the oscillating membrane (Figure 3.4b).
Finally, the acoustic membrane displacement is characterized in the presence of sound at a frequency of 1 kHz, and the compliance or sensitivity in nm/Pa of the fabricated graphene membranes is determined optically using a single-point Laser Doppler Vibrometer (LDV) (OFV-5000 Polytec GmbH) at the center of the membrane. Further details of the experimental setup and procedure can be found in our collaboration work [46] and in the Appendix 3.5 (Listing 3.1, Listing 3.2 andFigure 3.7).
The experimental mechanical compliance at 1 kHz is compared with the analytical results based on Equation 3.3, which relates the applied pressure to the maximum deflection of the membranes [47]. Far below the resonance frequency in the linear regime (such that cubic terms in z can be neglected), the membrane displacement z is related [47] to the sound pressure level ΔP by the equation:

$$\Delta P = \frac{4n_0}{R^2} z = \frac{z}{S_{m0}} \tag{3.3}$$

Thus, a quadratic relation is expected between the mechanical compliance, or sensitivity $S_{m0} = \frac{z}{\Delta P}$ and radius R for a constant sound pressure level ΔP. The reported mechanical compliances of 76 drums shown in Figure 3.4c range from ≈ 3 - 10 nm Pa^{-1} for the smaller membranes with $2R$ = 85 – 155 µm, and ≈ 43 – 92 nm Pa^{-1} for large membranes with $2R$ = 300 µm.
Figure 3.4c also shows a MEMS microphone with a membrane diameter of 950 μm, which is measured using the same procedure, resulting in a value of S_{m0} = 3 nm Pa^{-1}. The graphene data are fit by Equation 3.3, showing that different pretensions n_0 are needed to fit the large ($2R$ = 300 µm) and small membranes. Large membranes are closer to the analytical results obtained with lower pre-tension n_0 = 0.1 N/m, whereas the smaller

membranes yield n_0 = 0.2 N/m. This could be attributed to a lower pre-tension due to the larger suspended region where membrane sagging might be more profound.
Moreover, the tension is also affected by the graphene clamping geometry, where for the same diameter of 300 µm, the trampoline shows an even higher mechanical compliance (by a factor 1.4) due to lower tension of n_0=0.07 N/m compared to the fully clamped geometry [48].
The mechanical compliance of drums with different sizes, over the entire audible range, is also reported in Appendix 3.5 (Figure 3.10).
Furthermore, when comparing the pre-tension extracted from Equation 3.2 and Equation 3.3, we note that different values of n_0 are obtained as in Figure 3.4c. These differences might be caused by uncertainty in mass and thickness affecting Equation 3.2, gas damping and permeation effects at 1 kHz affecting Equation 3.3, and differences in the deflected mode-shapes from theory. More study is needed to quantitatively account for these differences.
The discrepancy between the pre-tensions extracted from resonance frequency and mechanical compliance measurements may also be attributable to inaccuracies in the mechanical compliance setup. This error could occur if the pressure difference is not con-

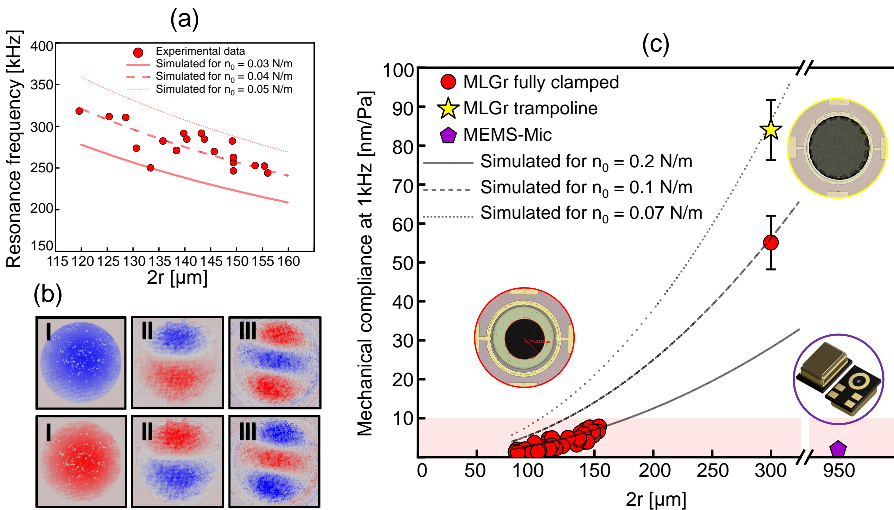

Figure 3.4: **Resonance frequency and mechanical compliance measurements.** (a) Resonance frequency as a function of diameter for ML-gr membranes with 120 – 155 µm diameters inspected by LyncéeTec holographic microscope. Comparison to Equation 3.2 suggests the tension in the membranes is n_0=0.04 N/m. (b) Three first modes of the trampoline membranes recorded by LyncéeTec microscope at resonance frequency of 92, 136, 195 kHz. Blue and red colors indicate the phase of the motion, corresponding to upward and downward moving parts of the membrane. The color saturation is a measure for the motion amplitude. (c) Comparison of the mechanical compliance of the ML-gr membranes with a commercial MEMS microphone MP23DB01HP, MP34DT04 STMicroelectronics (purple pentagon). ML-gr shows comparable and higher mechanical compliance despite its smaller dimension. Large membranes are more sensitive due to their larger diameter. The experimental measurements are also compared with the ideal analytical trend of Equation 3.3 with different pre-tension values, suggesting that the pre-tension reduces for larger membranes.

fined to a sealed volume, allowing the membrane to be influenced from the backside, leading to a more directional system. This hypothesis is partly supported by further tests conducted with a more advanced setup at Infineon Technologies AG. In these tests, similar membranes exhibited higher values of 2× higher (Appendix 3.5, Figure 3.10. Detailed comparisons of the different measurement setups and methodologies are also provided in Appendix 3.5 (Figure 3.7).
Furthermore, we demonstrate that music can be recorded using an ML-gr drum with $2R = 300\,\mu$m by monitoring the motion of the graphene membrane using the Polytec vibrometer [46]. The output signal from the Polytec in response to an arbitrary sound file is recorded with a sampling frequency of 20 kHz to detect the sound waveform, and the measured trace is then reconverted to an audio file with Python.
The performance of the proposed wafer-scale transfer-free multi-layer graphene is visually compared in Figure 3.5 with transfer-based graphene and graphene heterostructures condenser microphones reported in the literature. The comparison predominantly re-

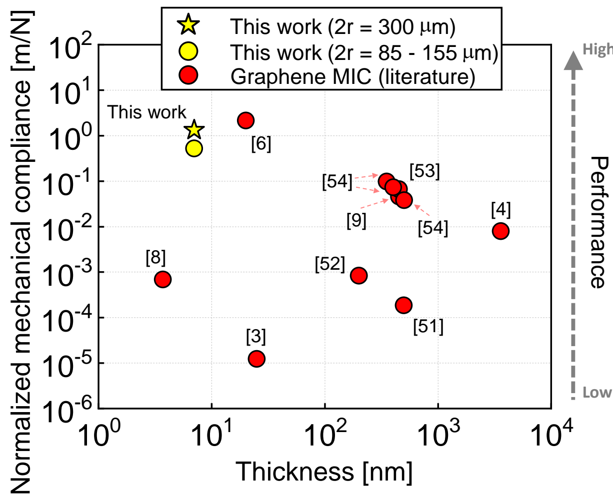

Figure 3.5: **Comparison of the normalized mechanical compliance by the graphene microphone's area.** The extrapolated mechanical compliances related to principal graphene microphone works[3, 4, 6, 8, 9, 49–52], and the proposed results are presented. The area of the suspended graphene normalizes the values to ensure an accurate correlation across different works.

veals the superior performance of the presented membranes, attributed to the absence of polymer supports, resulting in higher deflection under sound pressure. Additionally, the new fabrication method employed is more suitable to mass production. In these studies, the microphone sensitivity S, defined as open-circuit sensitivity[53], is typically measured using electrical read-out. Theoretically, it is expressed as the product of electrical sensitivity S_e and mechanical sensitivity S_{m0}, as indicated by the equation[53]:

$$S = S_e S_{\mathrm{m0}} = \frac{V_{\mathrm{bias}}}{g_0} S_{\mathrm{m0}} \tag{3.4}$$

To compare these results, the respective mechanical compliances are indirectly calculated using Equation 3.4, as well as Equation 3.2 and Equation 3.3, following the approach described in our work [54]. The input values S_e (mV Pa^{-1} or dB), pre-tension (N/m), resonance frequency (Hz), the distance membrane-bottom electrode g_0 (m), and V_{bias} (V) are obtained from reported works[3, 4, 6, 8, 9, 49–51]. For most of the presented data (obtained through electrical read-out), the mechanical compliance is indirectly derived from Equation 3.4. Consequently, Figure 3.5 may exhibit limitations in the comparison with results obtained by optical read-out (as in this work). This discrepancy may be attributed to the presence of a bias voltage V_{bias}, potentially leading to an underestimation of the extrapolated reported mechanical compliance.

3.4. CONCLUSIONS

In this chapter, we introduce a novel and efficient method for creating wafer scale graphene drums without the need for transfer processes, spanning diameters from $2R = 85-300\,\mu\text{m}$. We successfully produced large arrays of graphene drums, reaching up to approximately 155 μm in diameter, achieving a perfect yield of 100% using a CMOS-metal compatible workflow. These graphene membranes have been demonstrated to function as microphones, exhibiting mechanical compliances up to 92 nm Pa^{-1}. This level of compliance significantly surpasses that of typical commercial MEMS microphones, which usually have a compliance of around 3 nm Pa^{-1}. Remarkably, the graphene achieves this heightened sensitivity with a membrane area of just one-tenth the size of those found in MEMS devices. This underscores the immense potential of graphene in microphone technology. Additionally, the process developed for trampoline-like structures opens new avenues for designing and engineering innovative suspended graphene shapes, capable of achieving extremely high mechanical compliances at the wafer scale. This advancement paves the way for future high-volume, wafer-scale graphene microphone technologies, especially when combined with electrodes and read-out electronics.

3.5. APPENDIX

CONTINUOUS MO THIN FILM OVER ETCHED WINDOW

To ensure effective coverage over the height variations at the etched SiN_x windows, the Mo layer's deposition and thickness are critical.
It must be sufficiently thick to guarantee a continuous graphene membrane transition from the clamping to the suspended areas. Choosing a Mo ($t > 100$ nm) is not recommended, mainly due to the increased difficulties in controlling the wet-etching process of Mo. Additionally, to avoid thick deposition of Cr/Au, it's essential not to consider high topography. Such thickness can also lead to significant folding after the Mo etching and subsequent drying step.

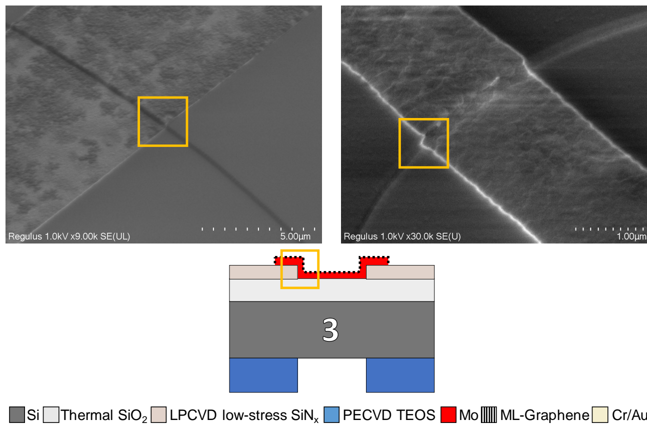

Figure 3.6: **SEM image of Mo/ML-gr at the etching mask window height step.** The variation in colors observed in the Mo/ML-gr patterns is likely attributed to differences in the thickness of the synthesized graphene. This inference is supported by the uniformity in color transitions at the step interface, which suggests a consistent conformity of the graphene layer across these thickness variations.

MEASUREMENT SETUP AND PYTHON CODES

The setup for measurements described in Figure 3.4c involves placing each silicon chip containing membranes onto a 3D-printed plastic hollow square stage, which in turn is positioned atop a reference microphone (Figure 3.7a, b). The silicon chip is precisely aligned with the opening of the stage, ensuring that the Bosch opening/membrane is aligned with the open area of the stage. This arrangement enables the microphone to detect the sound pressure applied by the micro-speaker placed close to the silicon die. Additionally, the LDV system is focused on the center of the membrane to capture velocity and displacement data. The readings of membrane displacement are normalized to 1 Pa, utilizing pressure data obtained from the reference microphone. Measurements are carried out across a range of 600 Hz to 20 000 Hz. Since the micro-speaker's response is not flat within the audible range, the membrane displacement signal from the LDV is normalized to 1 Pa after microphone calibration.
All data obtained from these measurements are subsequently processed using the Python

script depicted in Listing 3.1, Listing 3.2. Figure 3.7c illustrates the measurement setup utilized for Figure 3.4c, which Infineon Technologies developed. In this setup, the reference microphone is enclosed within a sealed chamber and positioned near the reference speaker at the bottom. The speaker is oriented perpendicular to the Bosch opening/membrane position, and the chamber is perfectly sealed to ensure accurate measurement of 1 Pa. Before measurements, proper calibration is conducted to minimize sound leaks, thereby guaranteeing accuracy. In contrast to the previous setup (depicted in Figure 3.7)a, this configuration ensures a sound pressure amplitude of 1 Pa across the frequency range of 10 Hz – 10 000 Hz. Compared to our in-house developed setup, the broader frequency response is expected to be attributed to the speaker's larger dimensions, which are not described in Infineon Technologies' confidential specifications. In fact, speakers with larger diaphragms can generate higher sound pressures at lower frequencies differently than smaller diaphragm-based microspeakers. At lower frequencies, sound waves have longer wavelengths and require significant displacement of air molecules to produce audible sound. Larger diaphragms have a greater surface area, which enables them to displace more air with each oscillation, thereby generating higher sound pressure levels. This enhanced low-frequency performance is critical for achieving a comprehensive acoustic range. In addition, unlike our initial experimental setup, the current configuration actuates the samples exclusively from one side, avoiding the directional influence of acoustic energy on the samples and allowing for a more precise interpretation of the results.

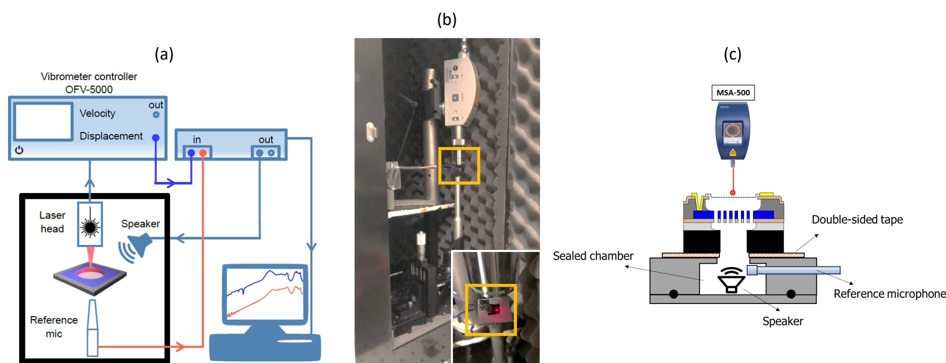

Figure 3.7: **Mechanical compliance measurement setup.** (a) A comprehensive schematic diagram of the entire measurement setup. It details all the necessary equipment and electronic components for data acquisition and processing. (b) An interior view of the anechoic chamber showcases all physical components in their assembled state. Featured is a detailed zoomed-in view of the experimental setup, highlighting the chip, micro speaker, 3D printed support, and the position of the reference microphone. (c) Schematic of the measurement setup used at Infineon Technologies AG (Munich, Germany).

The Python script Listing 3.1 is designed for remote control of the Moku:Lab. Its primary functions include setting the speaker's frequency driving range and determining the voltage amplitude required to drive the speaker's sound pressure.

```
import os
import scipy.io as sio
import matplotlib.pyplot as plt
import numpy as np
from datetime import date
from pymoku import Moku
from pymoku.instruments import FrequencyResponseAnalyzer
import General as G
# Connect to Moku
myMoku = Moku('192.168.1.167')
#Create output folder and figure settings
os.chdir(r'C:/Users/LocalAdmin/Desktop/Data/Roberto')
date = date.today().strftime("%Y_%m_%d")
G.figure('Frequency (kHz)', 'Amplitude (mV)')
#Folder and file name
foldername =  date + '\Chip'
filename = 'Chip1_tramp3_20mmsV_speakerhigher)'
fig = G.folder(foldername)
# Define frequency range
f_start = 200
f_end = 20e3
# Define output signal (piezo or speaker)
amplitudes = [0.5]
sensitivity = 20e-3
try:
    # Start spectrum analyzer instruments and set settings
    i = myMoku.deploy_or_connect(FrequencyResponseAnalyzer)
    i.set_defaults()
    i.set_frontend(channel = 1, fiftyr = False, atten = False, ac =
    True)
    i.set_frontend(channel = 2, fiftyr = False, atten = False, ac =
    True)
    for A in amplitudes:
            i.set_sweep(start_frequency=200, stop_frequency=20000,
    num_points=512,
            averaging_time=110e-3, averaging_cycles=3, settling_cycles
    =1,
            settling_time=1e-3)
            i.set_output(1, A)
            i.start_sweep(single = True)
            data =  i.get_data()
            amplitude = data.ch1.magnitude
            amplitudeDB = data.ch1.magnitude_dB
            phase = data.ch1.phase
            frequency = data.frequency
            soundP = data.ch2.magnitude
            soundPDB = data.ch2.magnitude_dB
            soundPphase = data.ch2.phase
            fig = G.figure("Frequency (kHz)", "Amplitude (mV)")
            ax1 = fig.add_subplot(1,1,1)
            ax2 = ax1.twinx()
            ax1.loglog(np.divide(frequency, 1e3), np.multiply(amplitude
    ,1e3), color = 'blue', lw = 2, label = 'Membrane')
```

```
49            ax1.loglog(np.divide(frequency, 1e3), np.multiply(soundP,1
    e3), color = 'orange', lw = 2, label = 'Mic')
50            ax2.loglog(np.divide(frequency, 1e3), np.divide(amplitude,
    soundP), color = 'red', lw = 2, label = 'Sensitivity')
51            plt.xlim(0.5, f_end/1e3)
52            plt.legend()
53            # Output files
54            name = filename + '_FreqResp_A'+ str(int(1e3*A)) + 'mV_f' +
     str(int(1e-3*f_end)) + 'kHz'
55            plt.savefig(name +'.png',dpi = 300)
56            plt.show()
57            plt.clf()
58            sio.savemat(name + '.mat', {'Frequency' : frequency, '
    Polytec': amplitude, 'AmplitudeDB': amplitudeDB, 'Phase' : phase, '
    Microphone' : soundP, 'SoundPDB' : soundPDB, 'soundPhase':
    soundPphase, 'fRange' : [f_start, f_end], 'Drive': A, '
    SensitivityDec': sensitivity})#, 'Sensitivity': Sensitivity})
59              # sio.savemat(name + '.mat', {'Frequency' : frequency, 'Polytec':
     amplitude, 'AmplitudeDB': amplitudeDB, 'Phase' : phase, 'fRange' :
     [f_start, f_end], 'Drive': A, 'SensitivityDec': sensitivity})#, '
    Sensitivity': Sensitivity})
60 finally:
61     myMoku.close()
62 print('Done')
```

Listing 3.1: Python code for data acquisition of membrane displacement - reference microphone - speaker drive.

A secondary script Listing 3.2 processes the raw data acquired by the initial script to compute the normalized membrane displacement at a sound pressure of 1 Pa. Additionally, the code performs microphone calibration based on the calibration file supplied by Sonarworks, which is tailored to the specific model of the reference microphone being used.

```
1 import os
2 import scipy.io as sio
3 import matplotlib.pyplot as plt
4 import numpy as np
5 os.chdir(r'C:\Users\rpezone\surfdrive2\PhD All Shared Material\Results\
    Microphone\Mechanical Compliance')
6 import General as G
7 import numpy
8 
9 mic = np.loadtxt(r'C:/Users/rpezone/surfdrive2/PhD All Shared Material/
    Results/Microphone/Mechanical Compliance/MicCalibration.txt',
    unpack = True)
10 sens = 14e-3
11 micResponse = sens*10**(mic[1]/20)
12 
13 path = r'C:/Users/rpezone/surfdrive2/PhD All Shared Material/Results/
    Transfered Graphene/30_01_23/2023_01_30/MLGr_PaC_Chip1'
14 os.chdir(path)
15 files = G.files(path)
16 G.figure('Frequency (kHz)', 'Amplitude (nm/Pa)')
17 #Plot Frequency response
18 for file in files:
```

```
19      print(file)
20      data = sio.loadmat(file) #'It is taking all matrix values
21
22      freq = data['Frequency'][0]
23      ampP = data['Polytec'][0] #'Polytec, it should be the displacement/
        velocity value'
24      phaseP = data['Phase'][0]
25      ampM = data['Microphone'][0] #'Microphone'
26      ampMDB = data['SoundPDB'][0]
27      phaseM = data['soundPhase'][0]
28      S = data['SensitivityDec'][0] #'SensitivittyDec'
29
30      memResp = []
31      micResp = []
32      for i in range(len(mic[0])):
33          ind = G.find_nearest(freq,mic[0][i])[1]
34          memResp = np.append(memResp,ampP[ind])
35          micResp = np.append(micResp,ampM[ind]/micResponse[i])
36
37      sens = S*memResp/(micResp*2*np.pi*mic[0])
38
39      plt.semilogx(mic[0]/1e3, sens/1e-9)
40      plt.xlim(0.02,20)
41
42  np.savetxt('Chip1_tramp3_20mmsV_diff_sk.txt', np.column_stack([mic[0],
        sens/1e-9]))
```

Listing 3.2: Python code for mechanical compliance calculation and saving.

3D AUTOMATED HEIGHT TOPOGRAPHY SCAN

The yield, as detailed in Table 3.1, is derived from an automated height topography scan performed on 10× diced chips following the vapor HF treatment. Each chip is analyzed using the Multi-file Analysis Application software by Keyence (VK-250).
This characterization is based on the post-processing images to verify the presence of the membrane in the suspended regions. Figure 3.8a,b visually compares the membrane's profile before and after the VHF treatment. In Figure 3.8a, the membrane's downward shift offers a clear view of its initial state. At the same time, Figure 3.8b reveals the membrane adopting a flatter profile after the oxide removal, illustrating its stuck to the unetched silicon substrate.
This methodical approach ensures a precise assessment of the yield, highlighting the effectiveness of the vapor HF process in membrane suspension. The efficacy of this approach is further compared with analogous results acquired using a Bruker White Light Interferometer.
A SEM image showing a broken membrane instance is shown in Figure 3.9 (tilted view). The tilted view accurately verifies the membrane ramp and collapse over the unetched silicon substrate. The collapsing phenomenon is attributed to any possible stiction issues, electrostatic attraction and Van der Waals forces. These issues would be particularly significant due to the thin residual gap of 1 μm and the large under-etching due to the micro-loading effects after Bosch etching.

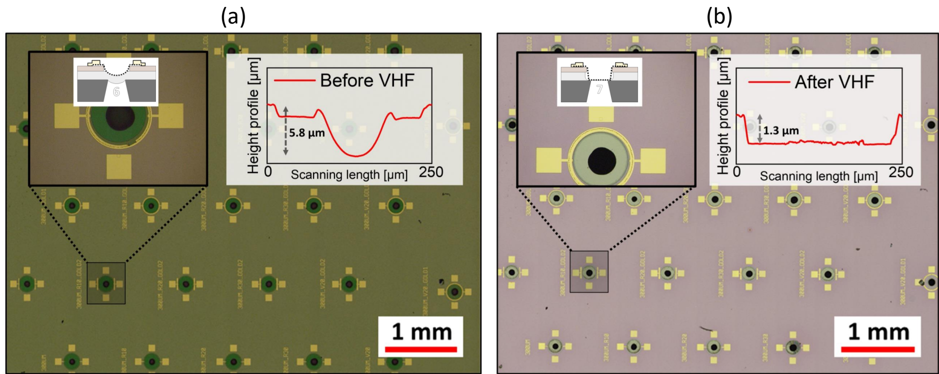

Figure 3.8: **Comparison of Keyence VK-X250 3D images of two chips before and after the Vapor HF.** (a) Presented is a reference image, taken prior to the vapor HF treatment, featuring over 20× membranes. (b) The height profiles of these membranes, post-vapor HF treatment, are quantified and displayed.

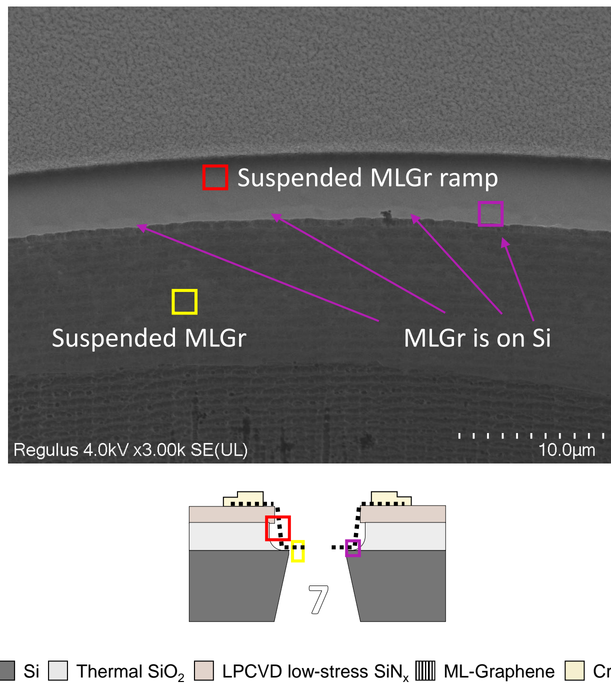

Figure 3.9: **SEM image of broken membrane.** A tiled view of a broken ML-gr membrane showing its different areas: ramp (red square), collapsed (purple square) and suspended (yellow square).

FREQUENCY RESPONSE

The results in Figure 3.4c illustrate the device's performance at a singular frequency of 1 kHz, commonly used as a benchmark. However, these devices must demonstrate a uniform response across the entire audible bandwidth to ensure their optimal application in microphones. Figure 3.10a presents the RMS displacement resulting from sound actuation, spanning frequencies from 600 Hz to 20 000 Hz and the displacement is normalized at 1 Pa using our custom-built setup, as detailed in Figure 3.7a. Subsequently, Figure 3.10b displays the frequency response of the displacement (peak to peak) for a different fabricated batch at Infineon Technologies, tested previously with our setup shown in Figure 3.7c for measurement comparisons. These tests revealed an increased displacement of ≈ 2× the value of those conducted with our in-house setup. Furthermore, Figure 3.10c provides an example of the LDV characterization, demonstrating the harmonic motion of the membrane when subjected to actuation by a single-tone frequency. Given the observed discrepancies, we propose an alternative setup (Figure 3.11). This new approach is anticipated to yield more accurate results for future research and development efforts.

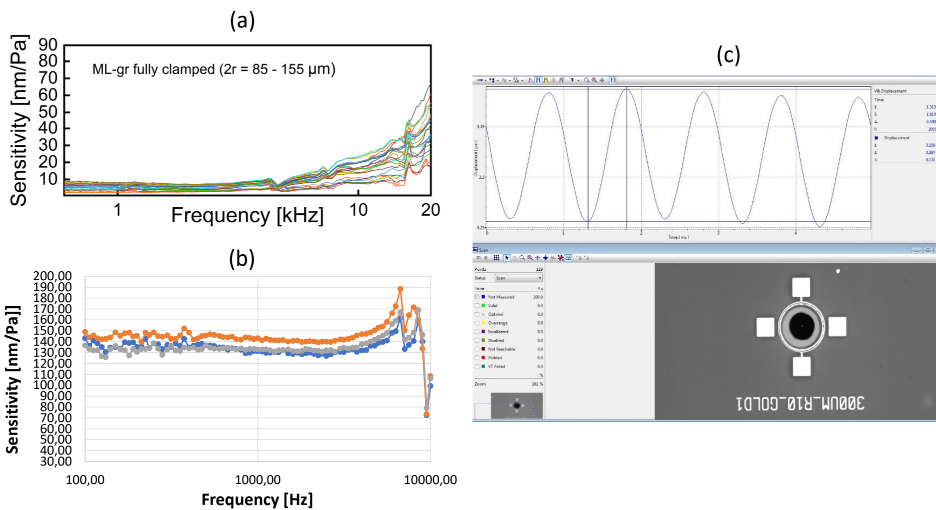

Figure 3.10: **Frequency response of ML-Gr diaphragms.**(a) Frequency response of the in-house setup from 600 Hz to 20 000 Hz (RMS displacement), as shown in Figure 3.7a,b. (b) Using our in-house setup, the frequency response from 10 Hz to 10 000 Hz of membranes from a second fabricated batch demonstrates a response of approximately 40 nm/Pa at 1 kHz. To further assess the accuracy of our setup for further development, these membranes were also tested using a commercial MEMS-microphone testing setup, depicted in Figure 3.7c. The setup from Infineon Technologies AG showed a response up to 10× higher than our setup reported. Additionally, no resonance behavior was observed in these membranes, indicating a flat response from 10 Hz to 10 000 Hz, expected to continue up to 20 kHz. (c) Characterization of one membrane showing peak-to-peak displacement at a single frequency tone.

Table 3.2: Overview of ML-gr membranes with $2R = 120 - 155\mu m$ measured at Infineon Technologies.

Wafer - Chip	Drum	Sensitivity [nm/Pa]
1 - 1	1	130.5
1 - 1	2	138.7
1 - 1	3	123.0
2 - 2	1	61.0
2 - 2	2	122.0
2 - 2	3	130.0
2 - 2	4	47.0

The reported sensitivities refer to 1 kHz tone.

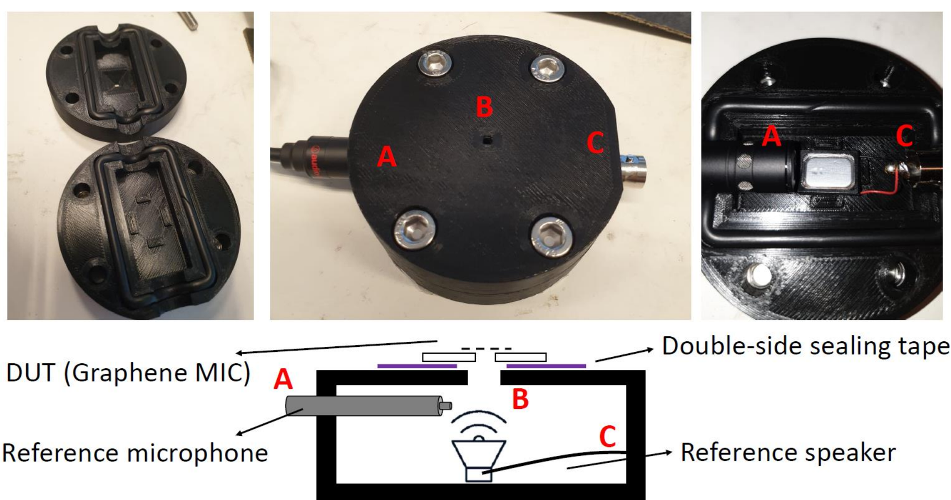

Figure 3.11: **Second in-house improved setup.**The chamber, designed for 3D printing, is tailored to the dimensions of a microspeaker and a reference microphone. The reference microphone, positioned close to the speaker, accurately measures the sound pressure emitted, minimizing leakage due to the new design. The lid, which can be tightened onto the bottom of the chamber, features a hole where the chip is placed directly above the Bosch cavity. This setup allows the sound to actuate the membrane from one side only. Positioned perpendicularly to the membrane, the laser Doppler vibrometer is used to measure the membrane's motion. For further enhancement, a larger chamber with a bigger speaker could be implemented to provide 1 Pa across the entire audible range.

BUCKLING N>1-MODES IN LARGE MEMBRANES

The deformation of the SiO_2/ML-gr layer following the DRIE of the silicon substrate, particularly at the sites of openings is shown in Figure 3.12. This deformation is characterized by significant wrinkles and cracks, which adversely affect the structural integrity of the membranes. As a consequence, the yield of the final ML-gr membranes, with diameters varying between 2R=300-500 µm, is substantially reduced. This observation underscores the challenges in maintaining membrane quality during the DRIE process, especially in the context of larger membrane dimensions.

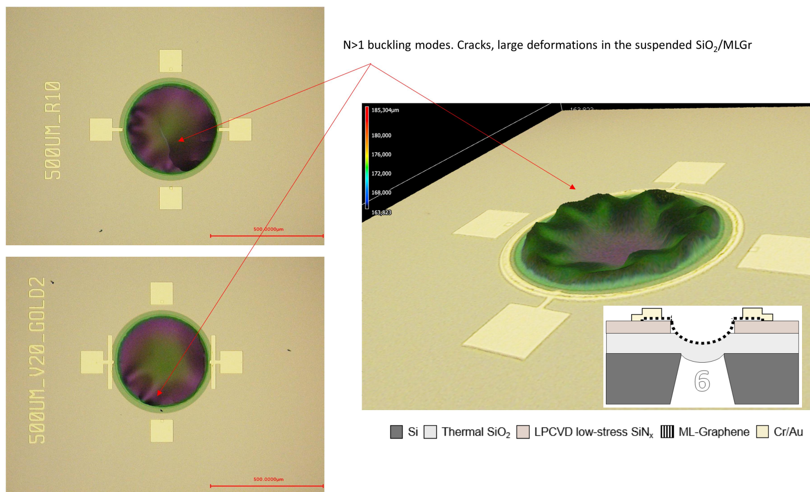

Figure 3.12: **High deformation in the large membranes up to** $2R = 0.5$ mm**.** Optical and 3D tilted view made by Keyence VK-250 of highly buckled SiO_2/ML-gr heterostructures, highlighting cracks in large membranes affecting low yield of suspended ML-gr. Similar deformations were observed in membranes 2R=0.3-0.35 mm with maximum downward displacements ranging between 1.5 µm and 15 µm

REFERENCES

[1] R. Pezone, G. Baglioni, P. M. Sarro, P. G. Steeneken, and S. Vollebregt, *Sensitive transfer-free wafer-scale graphene microphones,* ACS Applied Materials amp; Interfaces **14**, 21705–21712 (2022).

[2] R. Pezone, G. Baglioni, P. M. Sarro, P. G. Steeneken, and S. Vollebregt, *High-performance wafer-scale transfer-free graphene microphones,* in *2023 IEEE 36th International Conference on Micro Electro Mechanical Systems (MEMS)* (IEEE, 2023).

[3] D. Todorović, A. Matković, M. Milićević, D. Jovanović, R. Gajić, I. Salom, and M. Spasenović, *Multilayer graphene condenser microphone,* 2D Materials **2**, 045013 (2015).

[4] S. Woo, J.-H. Han, J. H. Lee, S. Cho, K.-W. Seong, M. Choi, and J.-H. Cho, *Real-*

ization of a high sensitivity microphone for a hearing aid using a graphene–PMMA laminated diaphragm, ACS Applied Materials & Interfaces **9**, 1237 (2017).

[5] S. Wittmann, C. Glacer, S. Wagner, S. Pindl, and M. C. Lemme, *Graphene membranes for hall sensors and microphones integrated with CMOS-compatible processes,* ACS Applied Nano Materials **2**, 5079 (2019).

[6] Q. Zhou, J. Zheng, S. Onishi, M. F. Crommie, and A. K. Zettl, *Graphene electrostatic microphone and ultrasonic radio,* Proceedings of the National Academy of Sciences **112**, 8942 (2015).

[7] G. S. Wood, A. Torin, A. K. Al-mashaal, L. S. Smith, E. Mastropaolo, M. J. Newton, and R. Cheung, *Design and characterization of a micro-fabricated graphene-based mems microphone,* IEEE Sensors Journal **19**, 7234 (2019).

[8] A. F. Carvalho, A. J. Fernandes, M. B. Hassine, P. Ferreira, E. Fortunato, and F. M. Costa, *Millimeter-sized few-layer suspended graphene membranes,* Applied Materials Today **21**, 100879 (2020).

[9] J. Xu, G. S. Wood, E. Mastropaolo, M. J. Newton, and R. Cheung, *Realization of a graphene/PMMA acoustic capacitive sensor released by silicon dioxide sacrificial layer,* ACS Applied Materials & Interfaces **13**, 38792 (2021).

[10] C.-K. Lee, Y. Hwangbo, S.-M. Kim, S.-K. Lee, S.-M. Lee, S.-S. Kim, K.-S. Kim, H.-J. Lee, B.-I. Choi, C.-K. Song, J.-H. Ahn, and J.-H. Kim, *Monatomic chemical-vapor-deposited graphene membranes bridge a half-millimeter-scale gap,* ACS Nano **8**, 2336 (2014).

[11] S. A. Akbari, V. Ghafarinia, T. Larsen, M. M. Parmar, and L. G. Villanueva, *Large suspended monolayer and bilayer graphene membranes with diameter up to 750 µm,* Scientific Reports **10** (2020), 10.1038/s41598-020-63562-y.

[12] A. Castellanos-Gomez, V. Singh, H. S. J. van der Zant, and G. A. Steele, *Mechanics of freely-suspended ultrathin layered materials,* Annalen der Physik **527**, 27 (2014).

[13] R. J. Nicholl, H. J. Conley, N. V. Lavrik, I. Vlassiouk, Y. S. Puzyrev, V. P. Sreenivas, S. T. Pantelides, and K. I. Bolotin, *The effect of intrinsic crumpling on the mechanics of free-standing graphene,* Nature Communications **6** (2015), 10.1038/ncomms9789.

[14] A. King, G. Johnson, D. Engelberg, W. Ludwig, and J. Marrow, *Observations of intergranular stress corrosion cracking in a grain-mapped polycrystal,* Science **321**, 382–385 (2008).

[15] F. Colangelo, P. Pingue, V. Mišeikis, C. Coletti, F. Beltram, and S. Roddaro, *Mapping the mechanical properties of a graphene drum at the nanoscale,* 2D Materials **6**, 025005 (2019).

[16] J. W. Suk, V. Mancevski, Y. Hao, K. M. Liechti, and R. S. Ruoff, *Fracture of polycrystalline graphene membranes by in situ nanoindentation in a scanning electron microscope,* physica status solidi (RRL) – Rapid Research Letters **9**, 564–569 (2015).

3

[17] T. Zhong, J. Li, and K. Zhang, *A molecular dynamics study of young's modulus of multilayer graphene,* Journal of Applied Physics **125** (2019), 10.1063/1.5091753.

[18] S. Vollebregt, B. Alfano, F. Ricciardella, A. J. M. Giesbers, Y. Grachova, H. W. van Zeijl, T. Polichetti, and P. M. Sarro, *A transfer-free wafer-scale CVD graphene fabrication process for MEMS/NEMS sensors,* in *2016 IEEE 29th International Conference on Micro Electro Mechanical Systems (MEMS)* (IEEE, 2016).

[19] F. Ricciardella, S. Vollebregt, T. Polichetti, M. Miscuglio, B. Alfano, M. L. Miglietta, E. Massera, G. D. Francia, and P. M. Sarro, *Effects of graphene defects on gas sensing properties towards NO2 detection,* Nanoscale **9**, 6085 (2017).

[20] S. Shubham, Y. Seo, V. Naderyan, X. Song, A. Frank, J. Johnson, M. da Silva, and M. Pedersen, *A novel mems capacitive microphone with semiconstrained diaphragm supported with center and peripheral backplate protrusions,* Micromachines **13**, 22 (2021).

[21] M. Fueldner, *Microphones,* in *Handbook of Silicon Based MEMS Materials and Technologies* (Elsevier, 2020) p. 937–948.

[22] S. A. Zawawi, A. A. Hamzah, B. Y. Majlis, and F. Mohd-Yasin, *A review of mems capacitive microphones,* Micromachines **11**, 484 (2020).

[23] M. A. Shah, I. A. Shah, D.-G. Lee, and S. Hur, *Design approaches of mems microphones for enhanced performance,* Journal of Sensors **2019**, 1–26 (2019).

[24] B. D. Bois, G. Vereecke, A. Witvrouw, P. D. Moor, C. V. Hoof, A. D. Caussemaeker, and A. Verbist, *HF etching of si-oxides and si-nitrides for surface micromachining,* in *Sensor Technology 2001* (Springer Netherlands, 2001) pp. 131–136.

[25] Y. Liu, C. Li, S. Fan, and X. Song, *Effect of pmma removal methods on optomechanical behaviors of optical fiber resonant sensor with graphene diaphragm,* Photonic Sensors **12**, 140–151 (2021).

[26] K. Jia, J. Luo, R. Hu, J. Zhan, H. Cao, Y. Su, H. Zhu, L. Xie, C. Zhao, D. Chen, and T. Ye, *Evaluation of pmma residues as a function of baking temperature and a graphene heat-free-transfer process to reduce them,* ECS Journal of Solid State Science and Technology **5**, P138–P141 (2015).

[27] B. Zhuang, S. Li, S. Li, and J. Yin, *Ways to eliminate pmma residues on graphene —— superclean graphene,* Carbon **173**, 609–636 (2021).

[28] J.-H. Park, W. Jung, D. Cho, J.-T. Seo, Y. Moon, S. H. Woo, C. Lee, C.-Y. Park, and J. R. Ahn, *Simple, green, and clean removal of a poly(methyl methacrylate) film on chemical vapor deposited graphene,* Applied Physics Letters **103** (2013), 10.1063/1.4824877.

[29] R. R. Nair, W. Ren, R. Jalil, I. Riaz, V. G. Kravets, L. Britnell, P. Blake, F. Schedin, A. S. Mayorov, S. Yuan, M. I. Katsnelson, H. Cheng, W. Strupinski, L. G. Bulusheva, A. V. Okotrub, I. V. Grigorieva, A. N. Grigorenko, K. S. Novoselov, and A. K. Geim, *Fluorographene: A two-dimensional counterpart of teflon,* Small **6**, 2877–2884 (2010).

[30] D. Ratnayake, M. D. Martin, U. R. Gowrishetty, D. A. Porter, T. A. Berfield, S. P. McNamara, and K. M. Walsh, *Engineering stress in thin films for the field of bistable MEMS,* Journal of Micromechanics and Microengineering **25**, 125025 (2015).

[31] D. Ratnayake, M. Derakhshani, T. A. Berfield, and K. M. Walsh, *Bistability study of buckled MEMS diaphragms,* Journal of Physics Communications **4**, 105008 (2020).

[32] U. R. Gowrishetty, K. M. Walsh, and T. A. Berfield, *Fabrication of polyimide bi-stable diaphragms using oxide compressive stresses for the field of 'buckle MEMS',* Journal of Micromechanics and Microengineering **20**, 075013 (2010).

[33] N. Yamamoto, D. J. Quinn, N. Wicks, J. L. Hertz, J. Cui, H. L. Tuller, and B. L. Wardle, *Nonlinear thermomechanical design of microfabricated thin plate devices in the post-buckling regime,* Journal of Micromechanics and Microengineering **20**, 035027 (2010).

[34] W. Ahmad, Z. Ullah, N. I. Sonil, and K. Khan, *Introduction, production, characterization and applications of defects in graphene,* Journal of Materials Science: Materials in Electronics **32**, 19991–20030 (2021).

[35] C. Si, Z. Sun, and F. Liu, *Strain engineering of graphene: a review,* Nanoscale **8**, 3207–3217 (2016).

[36] A. Shchepetov, M. Prunnila, F. Alzina, L. Schneider, J. Cuffe, H. Jiang, E. I. Kauppinen, C. M. S. Torres, and J. Ahopelto, *Ultra-thin free-standing single crystalline silicon membranes with strain control,* Applied Physics Letters **102**, 192108 (2013).

[37] I. V. Antonova, I. A. Kotin, R. A. Soots, V. A. Volodin, and V. Y. Prinz, *Tunable properties of few-layer graphene–n-methylpyrrolidone hybrid structures,* Nanotechnology **23**, 315601 (2012).

[38] A. Verna, S. L. Marasso, P. Rivolo, M. Parmeggiani, M. Laurenti, and M. Cocuzza, *Lift-off assisted patterning of few layers graphene,* Micromachines **10**, 426 (2019).

[39] D. Liu, B. Gludovatz, H. S. Barnard, M. Kuball, and R. O. Ritchie, *Damage tolerance of nuclear graphite at elevated temperatures,* Nature Communications **8** (2017), 10.1038/ncomms15942.

[40] G. Tsoukleri, J. Parthenios, K. Papagelis, R. Jalil, A. C. Ferrari, A. K. Geim, K. S. Novoselov, and C. Galiotis, *Subjecting a graphene monolayer to tension and compression,* Small **5**, 2397 (2009).

[41] G. Tsoukleri, J. Parthenios, C. Galiotis, and K. Papagelis, *Embedded trilayer graphene flakes under tensile and compressive loading,* 2D Materials **2**, 024009 (2015).

[42] L. Malard, M. Pimenta, G. Dresselhaus, and M. Dresselhaus, *Raman spectroscopy in graphene,* Physics Reports **473**, 51 (2009).

[43] B. Vasić, U. Ralević, K. C. Zobenica, M. M. Smiljanić, R. Gajić, M. Spasenović, and S. Vollebregt, *Low-friction, wear-resistant, and electrically homogeneous multilayer graphene grown by chemical vapor deposition on molybdenum,* Applied Surface Science **509**, 144792 (2020).

[44] P. G. Steeneken, R. J. Dolleman, D. Davidovikj, F. Alijani, and H. S. J. van der Zant, *Dynamics of 2d material membranes,* 2D Materials **8**, 042001 (2021).

[45] A. Castellanos-Gomez, V. Singh, H. S. J. van der Zant, and G. A. Steele, *Mechanics of freely-suspended ultrathin layered materials,* Annalen der Physik **527**, 27–44 (2014).

[46] G. Baglioni, R. Pezone, S. Vollebregt, K. Cvetanović Zobenica, M. Spasenović, D. Todorović, H. Liu, G. J. Verbiest, H. S. J. van der Zant, and P. G. Steeneken, *Ultra-sensitive graphene membranes for microphone applications,* Nanoscale **15**, 6343–6352 (2023).

[47] M. Šiškins, M. Lee, D. Wehenkel, R. van Rijn, T. W. de Jong, J. R. Renshof, B. C. Hopman, W. S. J. M. Peters, D. Davidovikj, H. S. J. van der Zant, and P. G. Steeneken, *Sensitive capacitive pressure sensors based on graphene membrane arrays,* Microsystems & Nanoengineering **6** (2020), 10.1038/s41378-020-00212-3.

[48] M. Fu, A. Dehe, and R. Lerch, *Analytical analysis and finite element simulation of advanced membranes for silicon microphones,* IEEE Sensors Journal **5**, 857 (2005).

[49] H. M. Mustapha, M. R. W. M.F., A. R. M. Zain, and M. A. Mohamed, *Characterization of graphene based capacitive microphone,* Sains Malaysiana (2019).

[50] G. S. Wood, A. Torin, A. K. Al-mashaal, L. S. Smith, E. Mastropaolo, M. J. Newton, and R. Cheung, *Design and characterization of a micro-fabricated graphene-based mems microphone,* IEEE Sensors Journal **19**, 7234 (2019).

[51] J. Xu, G. S. Wood, A. K. Al-mashaal, E. Mastropaolo, M. J. Newton, and R. Cheung, *Realization of closed cavity resonator formed by graphene-pmma membrane for sensing audio frequency,* IEEE Sensors Journal **20**, 4618 (2020).

[52] A. K. Al-mashaal, G. S. Wood, A. Torin, E. Mastropaolo, M. J. Newton, and R. Cheung, *Dynamic behavior of ultra large graphene-based membranes using electrothermal transduction,* Applied Physics Letters **111**, 243503 (2017).

[53] P. Scheeper, A. van der Donk, W. Olthuis, and P. Bergveld, *A review of silicon microphones,* Sensors and Actuators A: Physical **44**, 1 (1994).

[54] G. Baglioni, R. Pezone, S. Vollebregt, K. C. Zobenica, M. Spasenović, D. Todorović, H. Liu, G. J. Verbiest, H. S. J. van der Zant, and P. G. Steeneken, *Ultra-sensitive graphene membranes for microphone applications,* Nanoscale **15**, 6343 (2023).

4

MULTI-LAYER GRAPHENE-BASED MEMS CONDENSER MICROPHONES

This chapter focuses on incorporating multi-layer graphene within MEMS-microphones, following previous findings to advance them into capacitive architectures for electrical read-out. Focused on overcoming the previously described conventional fabrication techniques, we present a novel processing approach to enable wafer-scale, transfer-free manufacturing of graphene-based capacitive devices. Within the capacitive architecture, the impact of multi-layer graphene on the key performance indicators of MEMS microphone indicators are examined, such as sensitivity and pull-in voltage, which are essential for the operational efficacy of MEMS microphones. The investigation not only highlights the process technology suitability but also investigates the potential enhancements and limits in device performance attributed to the properties of the multi-layer graphene. This chapter contributes to the field by offering a comprehensive pathway toward integrating multi-layer graphene in MEMS microphones, setting the stage for future innovations in acoustic sensing technologies and other potential applications.

Parts of this chapter have been published in: R.Pezone et al., *Highly-sensitive wafer-scale transfer-free graphene MEMS condenser microphones*, Microsystems & Nanoengineering, 2024 [1] and R.Pezone et al., *Wafer-scale Transfer-free Graphene MEMS Condenser Microphones*, In 22nd International Conference on Solid-State Sensors, Actuators and Microsystems (TRANSDUCERS 2023) [2].

4.1. INTRODUCTION

DISHERNING from Chapter 3, which was confined to diaphragm fabrication, this chapter broadens the scope to realize the capacitive architecture essential for manufacturing a condenser mic. This includes a perforated back-plate (bottom electrode), a sacrificial layer (air gap), and the multi-layer graphene membrane (top electrode) as described in Figure 4.1 and Chapter 1 (Section 1.2).
This sets the stage for a future detailed evaluation of an optimized design, taking into account of all process feasibility, technology and material performance limitations.
This chapter also examines the potential of releasing transfer-free multi-layer graphene onto a residual layer by VHF following Chapter 2 (Section 2.4) and assesses the feasibility of growing it on such a new heterostructure that has not been investigated in previous works. Previous research on Mo-based transfer-free graphene has not investigated SiN_x/TEOS/doped Poly-Si/SiO_2/Si multilayer stack as a supporting growth substrate. Additionally, the potential of a capacitive architecture has not been evaluated for Mo-based transfer-free graphene, with past efforts primarily focusing on resistive read-out applications.
In alignment with the objectives from Chapter 3, the research rigorously challenges the state-of-the-art market-available MEMS microphones by investigating devices with diameters significantly smaller than the standard 2R>950µm. This effort seeks to reduce device footprints while trying to maintain or improve the device sensivitiy.
Compared to the state-of-the-art graphene-based microphones, the focus is also on smaller graphene diaphragms and perforated backplates with reduced thicknesses reducing the self-noise generated by oscillatory air movement within elongated openings of its structure, as discussed by S. Shubham et al. [3] and other works ([4]). Notably, earlier graphene microphone research employed counter electrodes with thicknesses exceeding $t > 100$µm [5–8]. It's worth mentioning that none of these prior works embraced wafer-scale fabrication, which holds potential for seamless integration with ASICs and essential large-scale manufacturing processes.

4.2. EXPERIMENTAL SECTION

4.2.1. DESIGN CONCEPT AND SIMULATIONS

Designing a MEMS condenser microphone involves several fields of study, including mechanics, fluid dynamics, electronics, and others.
To effectively and efficiently create a proper design, it is crucial to know the mechanical properties of all involved layers, especially all moving parts.
The devices presented in this chapter were not designed based on the results obtained in Chapter 3 (mechanical properties) or other published works from our group that are not included in this thesis [9]. Specifically, Chapter 3 focused on determining whether diaphragms could be realized without transfer and on estimating membrane performance. For that work, a mask set based on a complete capacitive architecture design was used, but some layers were omitted since only the diaphragm was being targeted. In this chapter, the results of the complete capacitive design are presented. A qualitative approach was adopted for the capacitive design, considering the mechanical properties of CVD graphene as reported in various fabrication methods from the literature [10]. This ap-

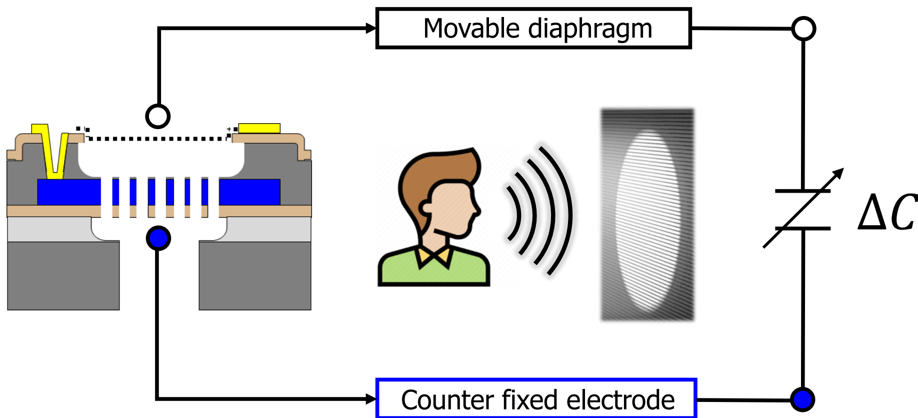

Figure 4.1: **MEMS condenser microphone functionality.** This schematic illustrates the basic architecture of a MEMS condenser microphone with a single backplate. It includes three main elements: the flexible top electrode (diaphragm or membrane), the air gap, and the fixed perforated back-plate (counter electrode). The movement of the membrane due to sound pressure changes the capacitance, enabling the sound to be electrically sensed.

4

proach was chosen because the design was finalized before the results of Chapter 3 were available. Therefore, a simplified design was preferred to allow for a qualitative evaluation, with the plan to pursue a final optimized design if fabrication proved successful, as will be discussed in Chapter 6. Additionally, without precise knowledge of the material properties, there was a significant margin of error in the design simulation, which could lead to inaccurate predictions.
The conceptual design is based on simulations performed with COMSOL Multiphysics using the "Axisymmetric Condenser Microphone (ID:12377)" model provided by COMSOL Multiphysics 5.2[11].
It is important to note that, for simplicity, a different backplate without venting holes but with a unique slit around it was considered accordingly with the mentioned existing model. This choice was made to avoid extra complexity during the design phase, as there was no clarity in process feasibility and material properties since the current design was made before the Chapter 3 outcomes. All design study details are included in our previous work [12].
It is essential to highlight that one of the most critical aspects for estimating membrane displacement under pressure (in this case, sound pressure) in COMSOL Multiphysics is the "Initial Stress and Strain" setting defined in the Boundary Physics of the Linear Elastic Material within the "Membrane" Physics module. Due to the unknown mechanical properties of the Mo-based multi-layer graphene used in our work, a pre-tension value of $n_0 = 0.45$ N/m was set[10]. This pre-tension value is higher than the values reported in Chapter 3.
Besides these preliminary studies, the choice of thickness for the backplate that will be integrated is also determined with COMSOL Multiphysics simulations.
Due to lab availability and the transfer-free method, LPCVD Poly-Si was identified as a

great candidate for the backplate. This material is CMOS compatible, can be doped to achieve lower resistivity, and can withstand the thermal budget of the CVD process used to grow graphene at 935 – 1000°C, despite possible changes in the lattice and its final stress. It is also a well-known material, allowing the use of existing models to simulate its response under pressure loads and estimate its resonance frequency for accurate process integration.

Finally, it is Vapor HF compatible, and this etching step does not attack it.

In Figure 4.2a-c, the maximum membrane displacement (center of the circle) under pressure of $p = 1\,\text{Pa}$ is shown, considering a range of radii between $R = 100\,\mu\text{m}$ and $R = 200\,\mu\text{m}$, thicknesses between $t = 0.1\,\mu\text{m}$ and $t = 1\,\mu\text{m}$, and stresses (σ) between $\sigma = 1-300\,\text{MPa}$.

The goal is to estimate whether the back-plate vibration due to sound pressure can affect the final device performance. Ideally, the back-plate should not move under sound actuation; otherwise, the capacitance change would not be solely related to the diaphragm change, and the device might suffer from an incorrect response. Additionally, air movement during sound actuation could affect diaphragm displacement.

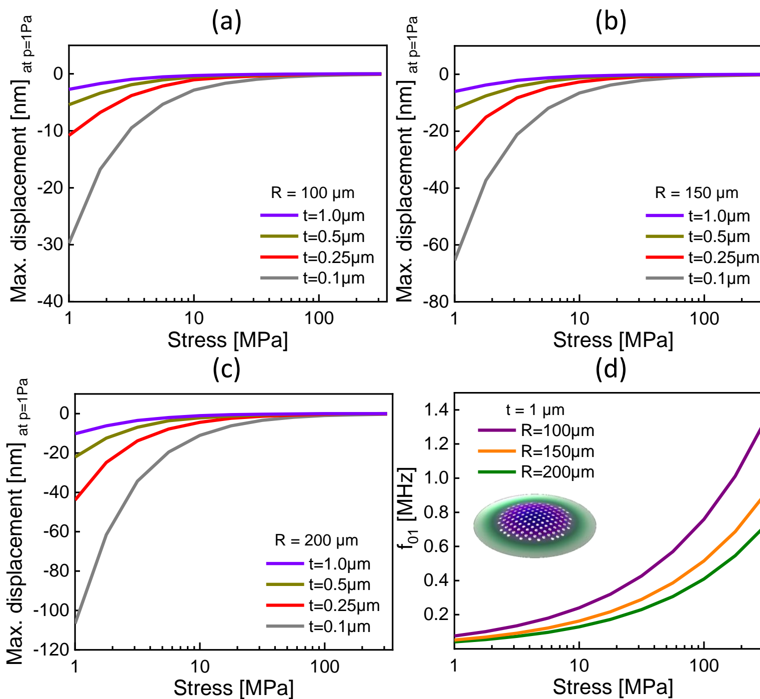

Figure 4.2: **Back-plate response under sound actuation and resonance frequencies.**(a-c) Display the maximum displacement at the center of the circle for the perforated back-plate under a static pressure of $p = 1\,\text{Pa}$. The variations include radii of $R = 100\,\mu\text{m}$, $R = 150\,\mu\text{m}$, and $R = 200\,\mu\text{m}$, thicknesses of $t = 0.1\,\mu\text{m}$, $t = 0.25\,\mu\text{m}$, $t = 0.5\,\mu\text{m}$, and $t = 1\,\mu\text{m}$, and $\sigma = 1-300\,\text{MPa}$. (d) Plot the f_{01} frequencies of the proposed devices considering $t = 1\,\mu\text{m}$ with the same variations in R and σ.

The simulations confirmed that thinner membranes with larger radii exhibit higher displacements for the same pressure, while lower stress also leads to higher displacement, as expected. It was found that selecting the thicker option of $t = 1\,\mu\text{m}$ could benefit from an almost static behavior when targeting stress greater than $\sigma > 50\,\text{MPa}$. Also, this thickness would be the easiest choice from a fabrication point of view since it is expected to be the most robust option that can withstand all the fabrication processes that were not yet optimized.
Thus, keeping the same thickness of $t = 1\,\mu\text{m}$, the resonance frequencies were estimated using eigenfrequency simulations in COMSOL Multiphysics, varying the radius. All results showed resonance frequencies above the audible bandwidth of ($f_{01} = 10\text{–}20\,000\,\text{Hz}$) (Figure 4.2d), which is needed for this application. Nevertheless, these simulations are based on a perforated backplate with a venting hole distribution of approximately 20% of the entire backplate area, as described in previous work [13].
The final mask set incorporated diverse geometries and sizes to explore various methods for enhancing the chance to fabricate the devices successfully. This strategic diversification responded not only to budget constraints limiting the number of masks available but also aimed to investigate the correlation between device performance and physical dimensions. The proposed fabrication strategy, developed based on preliminary tests and insights from Chapter 3, emphasized feasibility over maximizing yield to define the practical limits of our process flow. The main mask layers are shown in Figure 4.3.

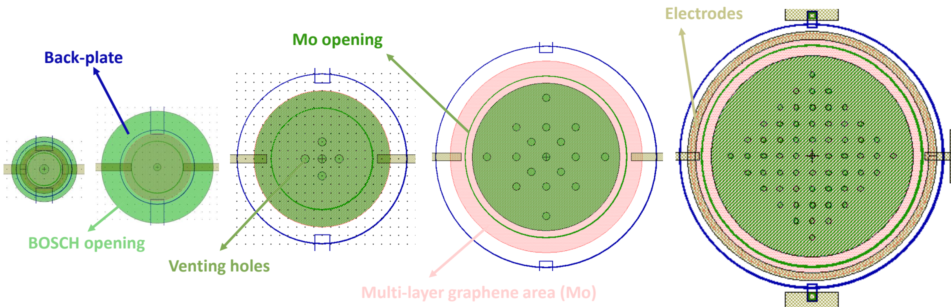

Figure 4.3: **Mask Layout of the Proposed devices.** These images represent the L-Edit design of the proposed devices, which involve six layers (six masks) as indicated by the colors and name descriptions. Various sizes ranging from $2R = 50\,\mu\text{m}$ to $2R = 500\,\mu\text{m}$ are shown. Differences in BOSCH diameters for the clamping electrodes are shown, which are adjusted to counteract the micro-loading effect, where smaller openings lead to smaller diameters at the back-plate. Different clamping geometries are proposed to study the effect of clamping on the graphene release.

4.2.2. BULK MICROMACHINING PROCESS FLOW

For incorporating a capacitive sensor design, the methodology outlined in Chapter 3 for fabricating wafer-scale graphene membranes necessitates enhancements, including a perforated counter electrode serving as the back-plate.
PECVD TEOS is employed as the sacrificial layer. It undergoes high-temperature annealing at 1000°C to enhance its density by removing hydrogen and impurities, resulting in a more etch uniformity and a more consistent and controller etching step, which is ad-

vantageous for achieving uniform VHF etching post-release. Thus, the annealing step mitigates the rapid etch rate of PECVD TEOS, which poses challenges in controlling the etching step and undercut.
Moreover, the annealing step may also alleviate layer stress and reduce the risk of cracking in subsequent higher-temperature deposition steps. Thus, annealing helps stabilize film stress, a crucial factor in constructing composite MEMS structures.
The fabrication started with a p-type 100 mm silicon wafer that is thermally oxidized at a temperature of 1000°C, resulting in the formation of a 1 µm thick SiO_2 film. This layer

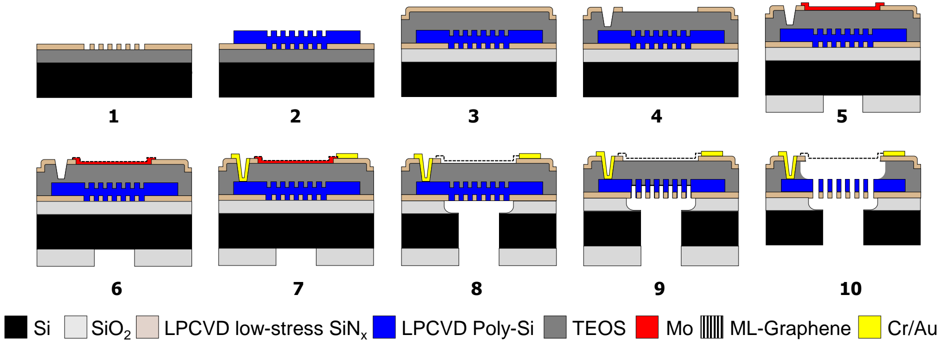

Figure 4.4: **Micromachining process flow.**The process steps to fabricate transfer-free multi-layer graphene condenser microphones are shown. (1) Definition of 1 µm SiO_2 landing layer and 100 nm LPCVD SiN_x etching mask for final back-side DRIE of the poly-Si venting-holes. (2) LPCVD poly-Si (1 µm) and patterning, (3) PECVD TEOS (5 µm) and LPCVD SiN_x (100 nm), (4) Dry-etching of SiN_x for membrane area definition and vias for bottom-electrode contacts. (5) Mo sputtering (50 nm) and patterning, (6) CVD run for graphene growth, (7) Cr/Au 20/200 nm evaporation and lift-off, (8) Bosch process and SiO_2 removal, (9) DRIE of poly-Si and (10) VHF of sacrificial layer.

serves dual purposes: it acts as an insulating barrier for the back-plate and facilitates the final bulk silicon etching by providing a landing platform.
Subsequently, a 100 nm layer of LPCVD SiN_x with SiH_2Cl_2 (295 sccm) and NH_3 (105 sccm) is deposited at 850°C. This layer is strategically patterned to align with the future venting holes in the suspended back-plate, as delineated in the initial step of Figure 4.4(1).
LPCVD is also used to deposit 1 µm poly-Si layer, utilizing SiH_4 (45 sccm) at 605°C, followed by Boron doping to achieve a concentration of 10^{15} atoms/cm^2 at an energy of 45 keV. A post-doping annealing step is performed for 1 hour at 950°C in a N_2/Ar atmosphere to activate the doping leading to a R_{sheet}=250 Ω/sq, after which the poly-Si layer is precisely etched to outline the back-plate area using ICP-RIE Cl_2/HBr chemistry, as shown in step 2 of Figure 4.4. Using positive photoresist AZ3012 or AZ3027 with thicknesses between 3.1 µm and 4 µm is effective as an etching mask. However, when using ICP-RIE Cl_2-based recipes for Poly-Si etching, residuals are observed in the photoresist area even after extended O_2-plasma treatments and HNO_3 wet-etching typically also used as organic removal (Figure 4.5a-d). It is important to note that these residuals may not be easily noticeable even with an optical microscope. Thinner photoresist films have

not been tested for this type of etching.
Similar residuals are also present for Mo etching using Cl_2/O_2 ICP-RIE (Figure 4.5e) and a-SiC etching with ICP-RIE Cl_2/HBr (Chapter 6). These residuals can be removed with a 15 s BOE (1:7) treatment and O_2 plasma. This method is successful probably due to the lifting of the residuals due to the formation of a thin oxidized superficial layer. A comparison is shown in Figure 4.5e-f. This method is repeatable and consistent for Poly-Si, Mo, and a-SiC. Other materials have not yet been tested.

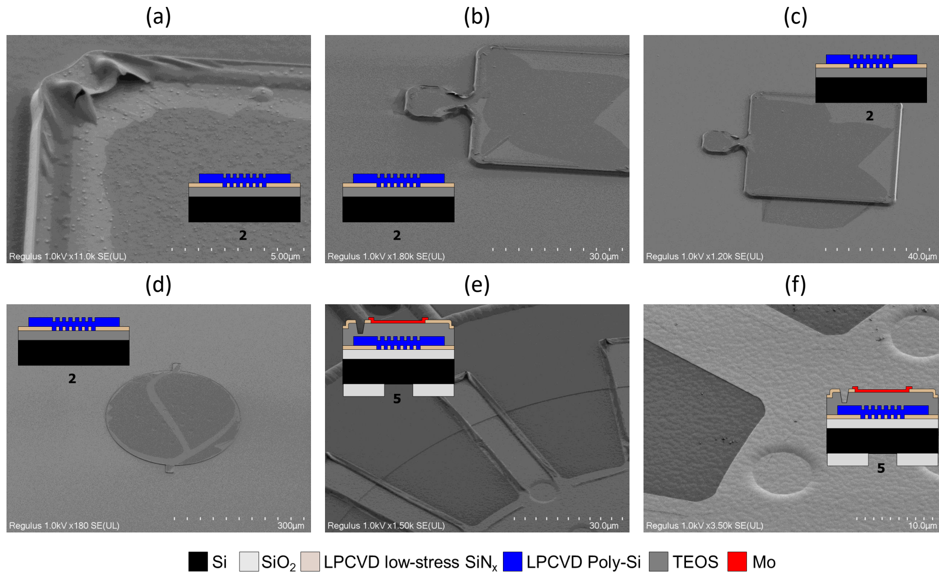

Figure 4.5: **SEM images of unwanted Residuals After ICP-RIE.**(a-d) Thin residuals are observed on top of the LPCVD Poly-Si after ICP-RIE, specifically in the areas that were protected by photoresist. These images show the etched Poly-Si islands (future counter electrodes) following O_2 plasma and HNO_3 cleaning for photoresist removal. (e) Similar residuals are found at the pattern edges of Mo after ICP-RIE etching. (f) An image of the patterned area of Mo after a BHF dip shows no residuals. For both Poly-Si and Mo etching, the same ICP-RIE equipment was used, with recipes based on Cl_2. In each SEM image, a draft schematic of the corresponding process flow step from Figure 4.4 is included to describe which part of the process the image refers to.

These residuals, if not removed, are expected to affect subsequent depositions, leading to adhesion issues, non-flat topography, and future non-ohmic contact problems.
For the creation of a sacrificial layer intended for future removal, different thicknesses of TEOS (on several wafers), applied via PECVD, are deposited and subsequently annealed at 1000°C in an Ar/N_2 atmosphere as previously explained.
A layer of LPCVD SiN_x (100 nm) is added as an etching mask and clamping area, crucial for the ultimate sacrificial etching process. This is detailed in steps 3 and 4 of Figure 4.4, where etching patterns are prepared for the graphene suspension areas and the vias for counter electrode contacts. A 50 nm Mo film is then sputtered at a low temperature of 50°C and shaped through a dry-etching process employing Cl_2/O_2 chemistry, as indicated in step 5 of Figure 4.4. Graphene synthesis is carried out at 935°C using an in-house

4-inch AIXTRON "Black Magic Pro" reactor under a pressure of 25 mbar, with H_2 reducing the oxidized Mo layer and CH_4 facilitating growth, as noted in step 6 (Figure 4.4). Further processing includes the deposition and patterning of Cr/Au (20 nm/200 nm) through electron-beam evaporation and a lift-off technique (with AZnLOF2020) using acetone, IPA, and DI-water.
The process, described in step 7 of Figure 4.4, is followed by DRIE on the wafer's backside and the removal of the SiO_2 layer (1 µm) using Buffered oxide etch (BOE) 7:1 chemistry. The final etching steps, including DRIE through the back-side to remove exposed poly-Si in alignment with venting holes and remove the Mo layer, as illustrated in steps 8 and 9 (Figure 4.4). The Mo layer is carefully removed using H_2O_2 and a gentle wash with DEMI-water as described in the previous chapters.
The process terminates in the dicing of 1 cm x 1 cm chips, each including several devices, followed by VHF etch in an anhydrous HF, N_2, and EtOH atmosphere within a Primaxx μEtch system at 125 Torr, as detailed in the final step of Figure 4.4.

4.3. RESULTS AND DISCUSSION

4.3.1. SACRIFICIAL LAYER RELEASE AND DEVICE INSPECTION

Several wafers were planned to be fabricated, with the only difference being in gap thickness, as described in the design concept in the previous section.
Only one wafer has been fully fabricated, specifically the one with a gap (g_0 = 5µm. Other wafers were not finished due to sufficient data obtained from the first wafer and the lengthy process of the entire wafer fabrication batch. Moreover, the wafers were not processed simultaneously to mitigate possible errors that could compromise the entire batch of wafers.
It is important to highlight that the sacrificial layer thickness is a trade-off: a thinner layer might enhance readout sensitivity. However, it could introduce undesirable damping effects and decrease the yield of the final membrane release. Reducing the gap distance to achieve high aspect ratios ($\frac{2R}{g_0}$) introduces complexities and reliability concerns due to various forces like hydrogen bridging, capillary, electrostatic, and Van der Waals, potentially leading to membrane collapse [14]. Larger gaps are favored for highly compliant membranes to preserve a significant dynamic range. In this way, choosing the first process involving a gap g_0 = 5µm should also result in less risk than lower gap thicknesses from fabrication feasibility but with lower device sensivity.
A schematic of the proposed device is shown in Figure 4.6, where the radii have different values across the full mask design on the 100 mm wafer (Figure 4.3).

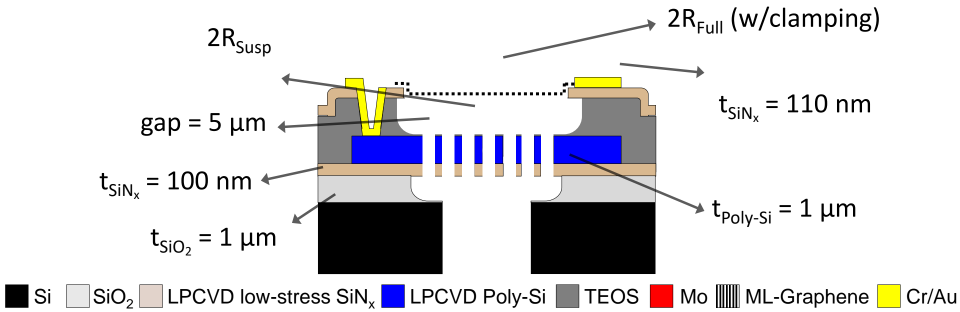

Figure 4.6: **Geometry schematic of the proposed devices.** Optical microscope images of devices (after VHF) of the three geometries are shown. These parameters pertain to the idealized scenario in which any residual etching effects on the SiN_x etching mask, distortions caused by stress, or other unexpected factors are not considered for simplicity. These parameters pertain to the idealized scenario in which any residual etching effects on the SiNx etching mask, distortions caused by stress, or other unexpected factors are not considered for simplicity.

The results analyzed in this chapter refer to the device geometries illustrated in Figure 4.7, also used as a reference for understanding the device layouts. They refer to distinct graphene membrane geometries: trampoline membranes (Figure 4.7) with $2R$ dimensions of$2R = 320\mu m$ (Geometry A) and $2R = 220\mu m$ (Geometry C), as well as a fully clamped membrane with $2R = 220\mu m$ (Geometry B). The yield related to the proposed

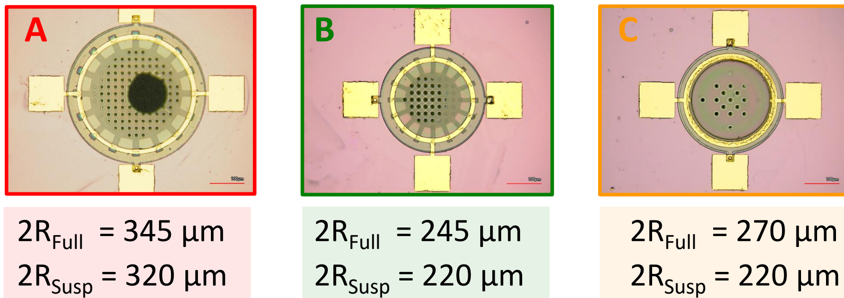

Figure 4.7: **Geometry schematic of the proposed devices.** Optical microscope images of devices (after VHF) of the three geometries are shown. These parameters pertain to the idealized scenario in which any residual etching effects on the SiN_x etching mask, distortions caused by stress, or other unexpected factors are not considered for simplicity. Several key variables are shown within the design, each contributing to the device's overall functionality. These design variables describe the clamping geometry, the free-standing area's diameter, and the air cavity's dimensions. In the context of Geometry A, it is important to note the presence of a distinctive black region, as shown in A. This black region results from a prolonged over-etching process under isotropic SF_6. During this process, multiple venting holes have merged, forming a fully etched region, visually represented as the black hole.

process flow is found to be influenced by variations in back-plate diameters $2R = 380\mu m$, $2R = 280\mu m$, $2R = 200\mu m$, and $2R = 180\mu m$. Devices with a backplate smaller than

$2R = 180\,\mu m$ were not considered, as they did not fully open due to micro-loading issues (Chapter 2, section 2.1) and a not fully optimized DRIE recipe. Optimizing the recipe for different sizes with such a large variation on the same wafer is very challenging in order to maintain uniform results.
Yield variability was notably pronounced across the processed wafer and directly linked to the dimensions of device geometries.
Initially, a yield of approximately 80% of all proposed device designs ($2R = 180-280\,\mu m$) were found after completing the Bosch process (Figure 4.4, step 8). Following the Bosch process, without dicing the wafer, a new DRIE step was executed following the removal of the SiO_2 landing layer via BHF (1:7), aimed at opening venting holes (Figure 4.4, step 9). This step revealed substantial variance in the sizes of openings between the largest ($2R = 380\,\mu m$) and smallest ($2R = 180\,\mu m$) back-plates, influencing the optimization of subsequent processing steps.

To facilitate targeted analysis, the wafer was divided into four quarters. One particular quarter, which contained six $10\times\ 2R = 10\,mm$ silicon chips with devices based on back-plates of $2R = 380\,\mu m$ and $2R = 280\,\mu m$, showed significant low yield due to the merging of venting holes during the DRIE step (Figure 4.4, step 9), occasionally resulting in the complete removal of the Poly-Si backplate (Figure 4.7, geom. A). Moreover, some devices showed large crack in the final suspended heterostructures, which was not directly expected to be related to the merging of the venting holes but potentially attributed to compressive stresses due to the several high-temperature steps not optimized in this process.
One main source of stress could be related to the TEOS annealing process. It has been found that for silicon substrates with a $5\,\mu m$ layer of PECVD TEOS, the stress dramatically changes from -65MPa to -208MPa after annealing considering a dummy silicon wafer without other films. Even if annealing is not performed, the film must be exposed to $T \approx 1000^{\circ}C$ during the CVD graphene growth process. Instead of maintaining a continuous layer of TEOS across the wafer, it is advisable to investigate the outcome of designing the process where TEOS is only confined to the sacrificial regions. Another cause of the high compressive stress of the entire heterostructure of Ml-Gr/TEOS/Poly-Si could be addressed as the compressive stress of the Poly-Si after the high-temperature steps.
Differently, devices with back-plate diameters of $200\,\mu m$, and $180\,\mu m$ maintained an 80% integrity rate without evident cracking, although several chips were compromised by less than optimal etching steps (Figure 4.4, step 9).
Moreover, this etching step showed large variations in etching rates across different locations within the wafer quarter. To have better control, each $10\times\ 10\,mm$ chip was processed individually due to the suboptimal etching method used to open the venting holes.
Ultimately, approximately six chips yielded a satisfactory number of devices suitable for VHF. The yield of these chips was assessed based on the devices that remained intact, without cracks in the back-plate or in the heterostructure, following the opening of venting holes.
Notably, for devices featuring trampoline structures (Geometry A and C), a yield of approximately 70% was achieved for 24 fully suspended devices, and 18% for 87 devices.
Finally, after completing the devices, a visual inspection is conducted (Figure 4.8b-d) to

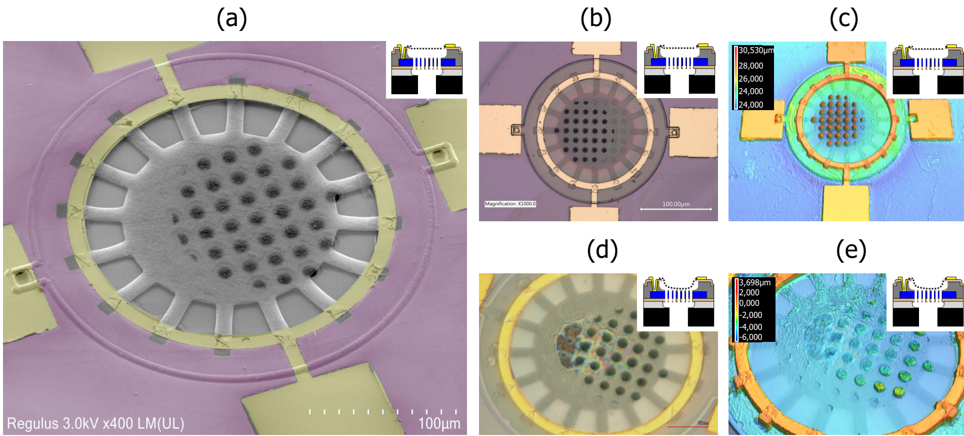

Figure 4.8: **Device visualization by SEM and 3D laser scanning confocal microscope.** (a) SEM false color image of one final device (geom. C) in tilted view and low-magnification mode. Partial Cr/Au cracks are present on top of the multi-layer graphene tethers due to thermal stress experienced during the Cr/Au evaporation. A slower evaporation rate is found to improve the reported state. Undesired mask shift during the back-alignment step in hard contact resulted in misalignment and the unintended closure of venting holes. (b) Optical microscope image of the same device as in (a). (c) Laser topography image of the same device as in (a). (d, e) Optical microscope, and topography images of a collapsed device. As inset in (c), (e), a height scale is added showing a downward deformation of the Si back-plate due to thermal stress of ≈ 1.5% (center) of the suspended region.

4

assess the fabrication process. It has also been found that the geometry of the clamping electrode plays a significant role in the final release of the graphene, with fully clamped configurations showing higher success in membrane release compared to partially clamped configurations (Figure 4.16).

We identified suspended microphone membranes using the topography mode in a Keyence VK-X250 confocal microscope. In Figure 4.8d, the measured height in the venting holes corresponds to the case of a collapsed device, while Figure 4.8c shows a suspended one. The membrane thickness ($t < 10$ nm) is measured with an atomic force microscope (AFM) from Cypher Asylum Research in air topography mode, determining the multi-layer graphene thickness (t) as described in Appendinx 4.5 (Figure 4.17) and previous work [15]. The image refers to the multi-layer graphene before the VHF step. Some polymer residuals on the membrane are also found due to the lift-off step, but these should be potentially avoided with an encapsulation layer such as ALD AlO_x [16], which is compatible with the proposed process flow. Some details have been proposed in Appendix 4.5 where electrodes on multi-layer graphene are integrated using AlO_x as a protective layer (Figure 4.18, Figure 4.19, Figure 4.20). This approach could also be beneficial since ALD AlO_x is highly selective with VHF.

Crystallinity characterization of the multi-layer graphene is conducted using a Horiba HR800 Raman spectrometer equipped with a 514.4 nm Ar+ laser, 100× objective with a NA of 0.9 (Figure 4.9). After finalizing the complete process, a Raman spectrum of a suspended microphone membrane is presented. The peak position values are based

on three inspected membranes, with different locations averaged three times within the same acquisition. All data are fitted with Lorentzian functions to determine the crystallinity of the material. The ω_D, ω_G, ω_{2D} values are centered at 1348.1 cm^{-1}, 1572.2 cm^{-1}, and 2682.5 cm^{-1} with standard deviations of 4.1 cm^{-1}, 3.5 cm^{-1}, and 5.3 cm^{-1}. The full-width half-maximum FWHM at the points D, G, and 2D are calculated from the Lorentzian fits as 58.3, 47.3, and 76.9 cm^{-1}. Additionally, the I_D/I_G and I_{2D}/I_G are found to be 0.2 ± 0.03 and 0.89 ± 0.25. These measurements are typical for multi-layer Mo-grown graphene, characterized as turbostratic graphene based on the peak and shape of FWHM 2D, where the stacked layers are more twisted with respect to each other [17]. Furthermore, no evidence of damage due to final DRIE and VHF etching is found, consistent with previous work [15].

In conclusion, the Raman data indicate the low invasiveness of the presented process flow, with defectivity similar to other works based on the same material [18–20].

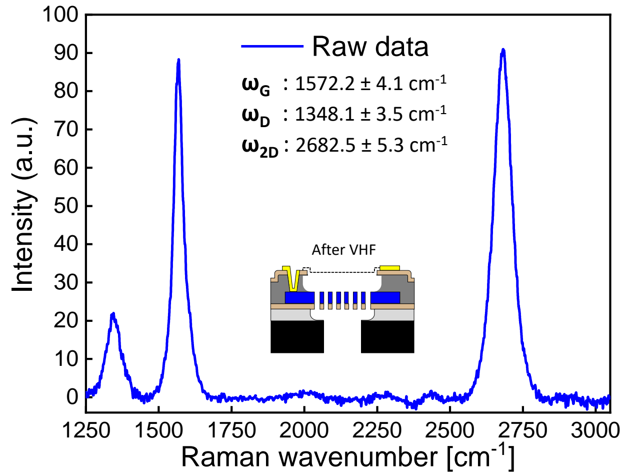

Figure 4.9: **Raman Spectroscopy.** An example of material crystallinity at the end of the process after final release is shown in a wavenumber range of 1250 - 3000 cm^{-1}. As an insight, all mean values and standard deviations are summarized. All acquisitions have been performed on the suspended multi-layer graphene in correspondence with the venting holes. Taking point in the free-standing area in correspondence with the back-plate leads to incorrect measurements due to suspended polysilicon influence on the backscattered signal.

4.3.2. EIGENFREQUENCY ANALYSIS

Regarding the potential of these devices as microphones, the fundamental resonance frequency f_{01} holds significant importance. A resonance frequency f_{01} falling within the audible frequency range can adversely affect the flatness of the microphone response and sound recording. All geometries are thoroughly examined to evaluate these resonance frequencies, and the corresponding measurements are shown in Figure 4.10. Digital holographic Lyncée Tec DHM R2200 microscopy is employed to visualize and quantify the first mode shape (f_{01}) in stroboscopic mode. The membranes exhibit resonance

frequencies above the audible range ($f_{01} > 20$ kHz) at 1×10^{-3}mbar through piezo-shaker actuation. Utilizing amplitude and phase acquisition by the holographic microscope LynceeTec and Koala Software, the mode shapes are generated post-processing with the MEMS Analysis Tool (Vibration Maps), confirming the examination of fundamental modes. The choice of venting holes for visualization is crucial to mitigate amplitude errors arising from the less transparent polysilicon area. This approach is particularly necessary as the height profile in correspondence to the polysilicon is inaccurately captured.
The use of low pressure (1×10^{-3}mbar) minimizes energy losses and damping. Additionally, the study incorporates a Polytec MSA-400 operating in scanning mode through piezo-shaker actuation to assess membrane velocities at resonance frequencies, where membrane motions are observed.

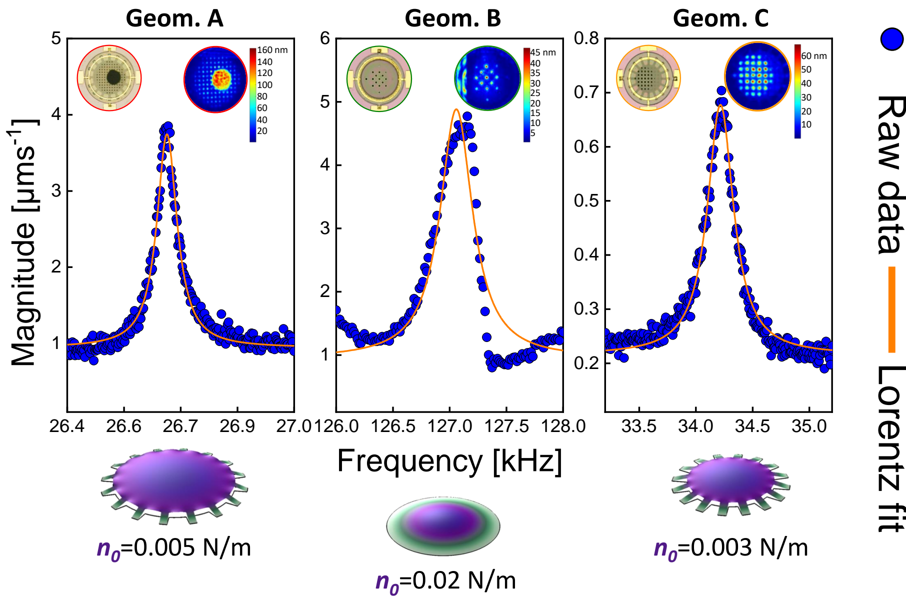

Figure 4.10: **Membrane eigenfrequency.** First resonance frequency modes of the three different membranes are compared and fitted with Lorentz functions. The insets show stroboscopic topography data of the +z membrane displacement through the venting holes. Below, is a COMSOL simulation of the mode-shapes of each of the geometries for different pre-tensions to match the experimental resonance frequencies. Appendix 4.5 (Figure 4.21), an example is provided of the membrane center dynamics (detected by Lyncée Tec DHM R220) under piezo actuation at its resonance frequency with an increasing V_{AC} voltage applied to the piezo. The harmonic displacement of the membrane center over time is depicted and fitted.

In the context of an undamped circular drum vibrating in its linear regime, the physical parameters associated with the solution of a harmonic oscillator can be derived from Equation 4.1 [21].
For the fundamental mode, the modal stiffness k_{01} is given by 4.8967 n_0, where n_0 represents the pre-tension. The modal mass m_{01} is determined as 0.2695 m, with m denoting the total mass calculated as $\rho t \pi R^2$. Here, ρ stands for the mass density of the graphene,

and t is the membrane thickness.

$$f_{01} = \frac{1}{2\pi}\sqrt{\frac{k_{01}}{m_{01}}} = \frac{2.405}{2\pi R}\sqrt{\frac{n_0}{\rho t}} \quad (4.1)$$

Taking into account $t = 7\,\text{nm}$, $\rho = 2267\,\text{kg/m}^3$, and $R = 110, 160\,\mu\text{m}$, and excluding potential influences from polymer residuals or wrinkles, the extracted pre-tension values from Equation 4.1 for the three geometries are 0.002 N/m (geom. A), 0.02 N/m (geom. B), and 0.0015 N/m (geom. C). Moreover, based on the relationship between pre-stress σ and pre-tension n_0 given by $\sigma = n_0 t$, the calculated residual stresses are 0.28 MPa (geom. A), 2.8 MPa (geom. B), and 0.21 MPa (geom. C).
The three geometries are also simulated using Finite Element Analysis (FEA) to align with the experimental eigenmodes. The FEA results align well with the experimentally determined n_0 values described in Figure 4.10. Notably, in the fully clamped geometry (geom. B), where the analytical $n_0 = 0.02\text{N/m}$, the FEA results match this value precisely. In contrast, geom. A and C exhibit different values of $n_0 = 0.005\text{N/m}$ ($\sigma = 0.71\,\text{MPa}$) and 0.003 N/m ($\sigma = 0.42\,\text{MPa}$), respectively, deviating from the analytical results. These differences with Equation 4.1 (valid for fully clamped) are attributed to differences between a circular drum and a trampoline.

4.3.3. BASE CAPACITANCE AND PULL-IN

Establishing the operational voltage window is crucial for validating the suitability of the proposed devices for the microphone application. The operational range of a condenser microphone is defined for $V_{\text{bias}} < V_{\text{pull-in}}$, as higher voltages lead to the membrane snapping onto the back-plate electrode.
Before measuring the capacitance change due to the V_{bias} effect, more than 70 devices were characterized to measure the base capacitance C_0 before VHF, verifying fabrication success following the simulated devices based on the analytical model as in Appendix 4.5, (Table 4.2, Table 4.3, Table 4.4). The differences in results are related to the various membrane geometries and electrode clamping for the exact membrane sizes.
In Figure 4.11a, the capacitive-voltage $C_0 - V_{\text{bias}}$ curves illustrate the voltage window of the fabricated devices, compared with FEA simulations of the pull-in. These electrical measurements are conducted using a Cascade Summit probe station connected to an Agilent 4294A Precision Impedance Analyzer. As V_{bias} increases, the base capacitance C_0 (Equation 4.3) exhibits a non-linear increase, attributed to the quadratic scaling of electrostatic forces with voltage, reducing the gap between the membrane and the back-plate. The three geometries (geom. A, B, C) demonstrate pull-in at a voltage $V_{\text{pull-in}}$ within the range of 2.0 to 9.5 V based on ten inspected devices.

$$C_0 = \frac{\epsilon_0 \epsilon_{\text{medium}} A}{g_0} \quad (4.2)$$

The experimental C_0 and $V_{\text{pull-in}}$ results are compared to FEA results of the same suspended area, considering the extracted pre-tension n_0 shown in Figure 4.11. Parasitic capacitances (C_p), corresponding to the common area between the electrodes and the back-plate, are analytically calculated using the parallel plate approximation and added

to the FEA results. The experimental capacitances C_0 closely align with the FEA results, with an error bar of $< 15\%$, which may be attributed to device imperfections such as film deformations (stress-induced) of the counter electrode or TEOS not being completely removed. The minimum capacitance does not precisely occur at $V_{\text{bias}} = 0V$. From a parabolic fit of the experimental C_0 - V_{bias} in Figure 4.11a, the three geometries exhibit built-in voltages $V_{\text{bi}} = -316, -289,$and $-219\,\text{mV}$. This discrepancy might arise from a poor connection between the metal and the graphene or Si or could be associated with residual trapped charges in the TEOS.
The fully clamped geometry exhibits the highest $V_{\text{pull-in}}$ at approximately 8.5 V, corresponding to a static displacement of approximately 1.65 µm, which is about 1/3 of the gap, as indicated by FEA analysis in Appendix 4.5 (Figure 4.22). This outcome aligns with expectations, considering that this device also demonstrated a higher resonance frequency and stiffness, as illustrated in Figure 4.10. As depicted in Figure 4.11b, beyond $V_{\text{pull-in}}$, the capacitance C_0 continues to increase. This phenomenon may be attributed to the expanding contact area with increasing voltage (Figure 4.11d). Subsequently, as

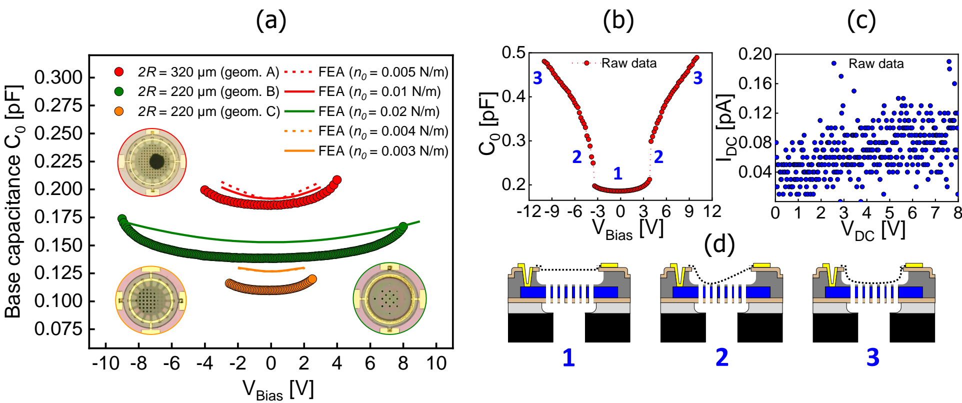

Figure 4.11: **Base capacitance and pull-in.** (a) $C_0 - V_{\text{bias}}$ curves of the three geometries are compared with FEA results. The devices are driven with $V_{\text{AC}} = 100\,\text{mV}$ and $f_1 = 100\,\text{kHz}$. (b) $C_0 - V_{\text{bias}}$ linear sweep from -9.5 V to 9.5 V describes the asymmetric membrane displacement of geom. (b, d) The blue numbers describe the membrane dynamics under V_{bias} increase of the inspected Geom. A device (also in Movie 2, Supp. mat. for geom. C). (c) Both electrodes are driven with a V_{bias} linear sweep from 0 V to 8 V. Despite the partial membrane collapse at $V_{\text{bias}} = 3.8\,\text{V}$, no short circuits are found due to a residual TEOS thin layer (geom. A). (d) Membrane deflection under non-uniform electrostatic forces.

V_{bias} surpasses $V_{\text{pull-in}}$, C_0 exhibits a distinct trend deviating from the parabola-shaped deflection typically assumed for circular plates.
The precise membrane collapse is outlined in three steps in Figure 4.11d, with a more detailed visual representation in a movie in our published work [1]. Notably, all examined membranes are observed to revert to their original state after the complete collapse for $V_{\text{bias}} = V_{\text{pull-out}}$ within the range of $15-30\%$ of $V_{\text{pull-in}}$.
This behavior indicates the typical hysteresis inherent to electrostatic force non-linearity, and the entire hysteresis cycle can be found in Figure 4.12.

In Figure 4.11c, the $V-I$ curve demonstrates minimal electrical leakage current between the top and bottom electrodes ($I_{leakage} < 0.20\,pA$). The limited current leakage is likely attributed to the presence of a thin residual layer of unetched TEOS on top of the backplate.

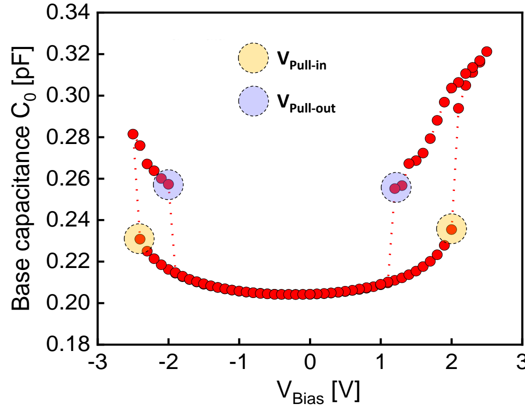

Figure 4.12: **Hysteresis behavior of C-V relation.** A DUT of geom. A is driven by the impedance analyzer with $V_{AC} = 100\,mV$ at $f_1 = 100\,kHz$ and a V_{bias} sweep between $-2.5\,V$ - $2.5\,V$. A comprehensive assessment of the reliability of all devices has not been conducted. It has been observed that after multiple cycling tests (> 10 cycles) investigating the pull-in voltages, there are minor variations in the capacitance-voltage (CV) measurements of the devices. These variations may stem from partial membrane delamination or a shift in position from their original locations.

4.3.4. DEVICE RESPONSE UNDER SOUND ACTUATION

In this investigation, the three geometries (Geom. A, B, and C) undergo sound pressure excitation at a constant $p = 1\,Pa$, following meticulous calibration within the frequency range of $10 - 10\,000\,Hz$. A LDV captures the corresponding membrane motions, as detailed in Chapter 3 (Appendinx 3.5, Figure 3.7c and Figure 3.10c). Notably, all responses exhibit a low-pass trend without indicating Low-Frequency Roll-Off (LFRO). The mechanical compliances for Geom. A, B, and C are determined to be 1.07, 0.081, and 0.56 µm, respectively, under 1 kHz and 1 Pa actuation (Figure 4.13). These values closely align with our previous research on the same free-standing graphene as in Chapter 3 and other work not described in this thesis[9], showcasing remarkably high mechanical compliances.

Importantly, comparable high compliances for small diameters ($2R < 320\,\mu m$) have not been reported in existing literature. Displacement variations are further observed about distinct membrane diameters and pre-tension values extracted from eigenfrequency studies and FEA analysis as in Figure 4.10. The experimental results are compared with the analytical response by employing the damped harmonic oscillator represented by Equation 4.3. The fit, incorporating the pre-tension (n_0) extracted from FEA eigenfrequency,

exhibits an error range of 6-25 %, considering the respective geometry radius (R).

$$C_m(\omega) = \frac{R^2}{4n_0\sqrt{(1-\frac{\omega^2}{\omega_0^2})^2 + \frac{\omega^2}{\omega_0^2 Q^2}}} \tag{4.3}$$

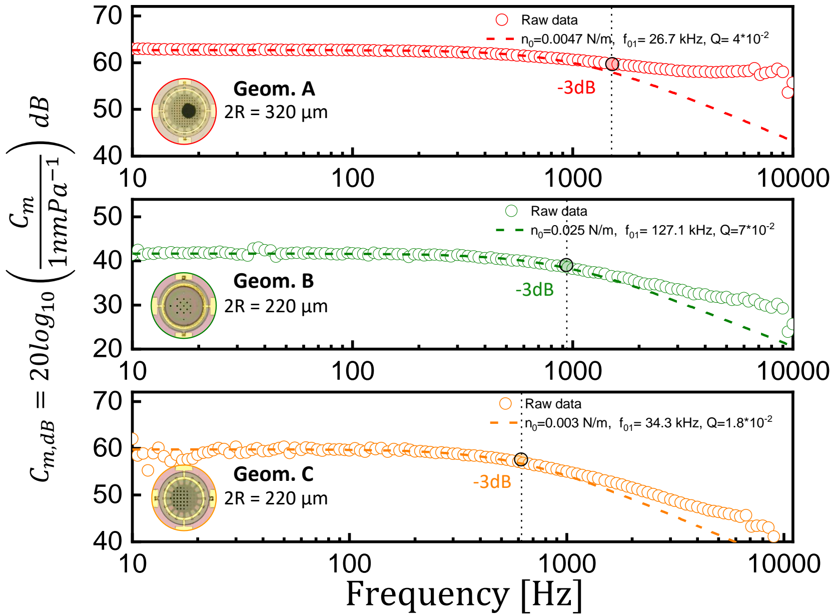

Figure 4.13: **Mechanical sensitivity at** 1 Pa **in** 10 – 10 000 Hz**.** In the legends are described the main parameters that have been used to fit the data with (Eq.4.3). The slope response for $f > 10$ Hz is mainly affected by n_0 and the quality factor (Q). A better fitting for all proposed geometries in the slope for $f > 800$ Hz is found for low Q (overdamped systems) and original natural modes f_{01} values. The cut-off frequencies are 1500 Hz (Geom. A), 940 Hz (Geom. B), and 620 Hz (Geom. C).

The observed low-pass behavior is predominantly attributed to the back-plate design, which introduced acoustic resistance. This is primarily due to air volume within the perforations and the consequent impact of the air mass (inertia) on its movement through the holes, leading to damping effects caused by membrane displacement. An additional analysis was conducted using lumped element circuit to evaluate the device responses further. A comprehensive damping analysis for the suggested devices is elaborated in (Figure 4.14) where a lumped-element model circuit replicate the device responses across various damping scenarios.
The resonance frequencies (f_{01}) for all devices are found to exceed 20 kHz under low pressure conditions, as shown in Figure 4.10. However, under sound actuation, these devices exhibit cutoff frequencies within the audible range (Figure 4.13).
In Figure 4.14a, we present a direct comparison between experimental results and simulated mechanical compliances at a sound pressure level of 94dBSPL. By incorporating an optimized back-plate ($R_{BP} \approx 1 - 8 \cdot 10^8 [\frac{Pa \cdot s}{m^3}]$), all proposed devices display a flat

response up to f_{01} = 16kHz (Geometry A), 63kHz (Geometry B), and 25.1kHz (Geometry C), as indicated by the dashed lines in Figure 4.14a. These simulated resonance

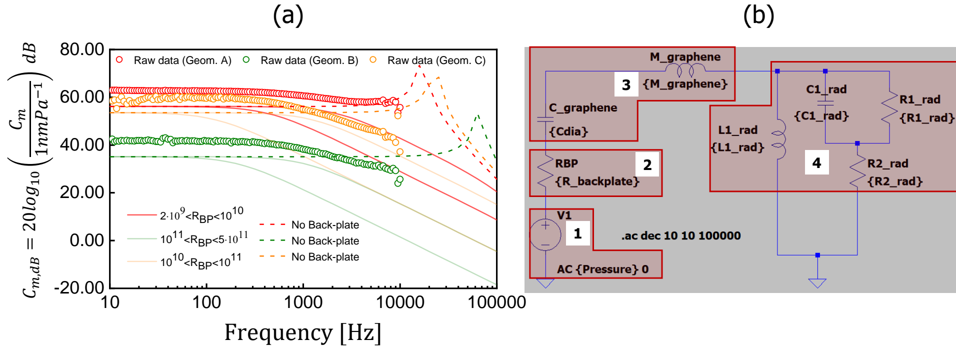

Figure 4.14: **Damping estimation of Geom. A, B, C based on lumped-element model.** (a) A comparison of experimental and simulated mechanical compliance is shown. Empty circles denote the experimental results, while the modeled results, considering very low damping with $R_{\mathrm{BP}} \approx 1\cdot10^{-8}[\frac{Pa\cdot s}{m^3}]$ are represented by dashed lines. Notably, the damping magnitudes reported in the Figure 4.13 an inset are used to replicate the low-pass behavior observed in the experimental results. These inset R_{BP} intervals refer to the plotted semi-transparent line areas. The interval of values closely aligns with the analytical R_{BP}, derived using the prescribed equation and parameters from the geometries outlined in Figure 4.6. (b) The figure includes a schematic of the lumped-element model employed to generate the modeled responses, utilizing a network similar to LTSpice.

frequencies remain lower than those obtained under low-pressure conditions, as discussed in the main manuscript Figure 4.10, due to the influence of air-loading on the membrane as discussed in Chapter 5 [22]. The experimental results' low-pass behavior is then compared with the simulated responses under high damping conditions with a non-optimized back-plate (continuous lines). This comparison offers valuable insights into the damping magnitude of the proposed geometries. Considering the analytical acoustic resistance values provided in Table 4.1 as $R_{\mathrm{BP}} = 6.4\cdot10^9[\frac{Pa\cdot s}{m^3}]$ (Geometry A), $R_{\mathrm{BP}} = 3.4\cdot10^{10}[\frac{Pa\cdot s}{m^3}]$ (Geometry B), and $R_{\mathrm{BP}} = 1.35\cdot10^{10}[\frac{Pa\cdot s}{m^3}]$ (Geometry C), the model predicts cutoff frequencies of 700 Hz (Geometry A), 3 kHz (Geometry B), and 950 Hz (Geometry C). However, these predicted frequencies differ from the experimental values shown in Figure 4.14, which are 1500 Hz (Geometry A), 940 Hz (Geometry B), and 620 Hz (Geometry C).

In the case of Geometry A, the experimental results suggest a higher resonance frequency, possibly due to the larger back-plate opening resulting from over-etching, which is not considered in the current analytical calculations for simplicity (Figure 4.7). On the other hand, the analytical calculations for Geometries B and C are likely overestimations due to the assumption of equivalent hexagonal cell distributions for the venting openings, a different scenario from the proposed back-plates where the perforations are not distributed across the entire plate area. Thus, the increased damping observed in the experimental results indicates an expected decrease in the resonance frequency. Moreover, the analytical calculations do not account for unopened venting holes, further contributing to the increased resonance frequency in the analytical results.

The results presented in Figure 4.14a were obtained through simulation using a lumped

Table 4.1: Parameter calculations for lumped modeling of Geom. A, B, C.
($\psi = A_{\text{perf}}/A_{\text{cell}}$, $A_{\text{eff}} = \frac{1}{3}\pi R^2_{\text{graphene}}$)

Element	Geom. A	Geom. B	Geom. C
$d_S = \frac{3\eta A^2_{\text{cell}}(4\psi-\psi^2-3-4\ln(\sqrt{\psi}))}{2\pi g_0^3}$ $[\frac{N\cdot s}{m}]$	$1.16\cdot10^{-8}$	$8.82\cdot10^{-8}$	$1.16\cdot10^{-8}$
$d_E = \frac{3\eta A_{\text{cell}} A_{\text{plate}}}{2R^3_{\text{perf}}}$ $[\frac{N\cdot s}{m}]$	$2.88\cdot10^{-8}$	$1.23\cdot10^{-7}$	$2.88\cdot10^{-8}$
$d_I = \frac{3\eta 0.84 A^2_{\text{plate}}}{2R_{\text{perf}} g_0^2}$ $[\frac{N\cdot s}{m}]$	$1.95\cdot10^{-8}$	$9.38\cdot10^{-8}$	$1.95\cdot10^{-8}$
$d_C = \frac{8\eta t_{\text{BP}} A_{\text{cell}} A_{\text{plate}}}{\pi R^4_{\text{perf}}}$ $[\frac{N\cdot s}{m}]$	$9.8\cdot10^{-9}$	$4.20\cdot10^{-8}$	$9.8\cdot10^{-9}$
$C_{\text{graphene}} = \frac{R^4_{\text{graphene}}\pi}{12n_0}$ $[\frac{m^3}{Pa}]$	$3.65\cdot10^{-14}$	$1.53\cdot10^{-15}$	$1.27\cdot10^{-14}$
$M_{\text{graphene}} = \frac{9\rho_{\text{graphene}} t_{\text{graphene}}}{5R^2_{\text{graphene}}\pi}$ $[\frac{kg}{m^4}]$	355.3468	751.4270	751.4270
$L1_{\text{rad}} = \frac{0.27\rho_{\text{air}}}{R_{\text{graphene}}}$ $[\frac{kg}{m^4}]$	$2.0328\cdot10^3$	$2.95\cdot10^3$	$2.95\cdot10^3$
$C1_{\text{rad}} = \frac{5.94R^3_{\text{graphene}}}{\rho_{\text{air}} c^2}$ $[\frac{m^3}{Pa}]$	$1.715\cdot10^{-16}$	$5.58\cdot10^{-17}$	$5.58\cdot10^{-17}$
$R1_{\text{rad}} = \frac{0.1404\rho_{\text{air}} c}{R^2_{\text{graphene}}}$ $[\frac{Pa\cdot s}{m^3}]$	$2.26\cdot10^9$	$4.79\cdot10^9$	$4.79\cdot10^9$
$R2_{\text{rad}} = \frac{0.318\rho_{\text{air}} c}{R^2_{\text{graphene}}}$ $[\frac{Pa\cdot s}{m^3}]$	$5.12\cdot10^9$	$1.08\cdot10^{10}$	$1.08\cdot10^{10}$
$R_{\text{BP}} = \frac{d_S+d_E+d_I+d_C}{A_{\text{eff}} A_{\text{cell}}}$ $[\frac{Pa\cdot s}{m^3}]$	$6.4\cdot10^9$	$3.45\cdot10^{10}$	$1.35\cdot10^{10}$

model in LTSpice. Following the approach described by Beranek et al. [23] and other works concerning silicon-based MEMS microphones [24, 25], each component of the microphone has been represented as a lumped element.
In this simplified model (Figure 4.14b), the first block represents the voltage source, symbolizing the pressure wave magnitude ($p = 94$dBSPL). The second block, represented by a resistor, characterizes damping effects as F/v, encompassing all energy dissipation associated with the membrane's movements, primarily influenced by viscous losses within the membrane-back-plate system.
The model identifies four distinct regions associated with a single hexagonal cell (A_{cell}): a squeeze film damping region between the membrane and the back-plate (d_S), a segment accounting for end effects of viscous air flow within the channel (d_E), an intermediate region connecting the squeeze film (d_I), and a channel region formed by the perforation hole (d_C) [25].
These four regions, used to simulate the proposed devices, contribute to the analytical damping factor $d = d_S + d_E + d_I + d_C$. The damping factor pertains to the single hexagonal cell A_{cell}, including the single perforation area A_{perf}. The third block characterizes the diaphragm, where the capacitance C_{graphene} and the inductor M_{graphene} correspond to the spring constant and mass of the proposed diaphragm. The fourth block accounts for the air-loading effect [23], attributed to the higher gas density in the atmospheric environment where the microphone operates. In this context, $L1_{\text{rad}}$ represents the air mass loading on the membrane, while the components $R1_{\text{rad}}$, $R2_{\text{rad}}$, and $C1_{\text{rad}}$ enable consideration of frequency-dependent acoustic effects [23]. To enhance the system response

with a flatter broader bandwidth, it is advisable to consider increasing the gap between the membrane and back-plate or maximizing the size of the perforations while reducing their pitch, with a consequent sensitivity reduction according to Equation 4.2. Another potential cause for the relatively high motion of the membrane at low frequencies could be wind noise actuation[26].

The damping effect caused by the back-plate on the frequency response of MEMS condenser microphones has already been explored in silicon-based diaphragms, showing similar trends [27, 28].

Despite the low-pass behavior shown in Figure 4.13, the measured devices still demonstrate substantial compliance as they approach 10 kHz, with corresponding amplitudes of 794, 31, and 19 nmPa^{-1} for geometries A, B, and C, respectively. These values exceed the mechanical compliances typically reported in the literature for silicon-based diaphragms, which usually feature membrane diameters 3-4 times greater than the results shown in this study [9].

Further improvements to the flatness of the response of the microphones will require more engineering efforts or might be mitigated using signal processing techniques to correct for the frequency response.

The measurements are limited to 10 kHz due to the presence of a sealed chamber utilized for monitoring pressure changes via a reference microphone as detailed in Chapter 3 (Appendinx 3.5, Figure 3.7c and Figure 3.10c). This limitation arises from the Helmholtz resonance observed around this frequency, stemming from the volume discrepancy between the speaker area (inside the chamber) and a larger opening where the sample is securely fixed, ensuring minimal pressure leakage and thus assuring precisely a difference in pressure of 1 Pa.

4.3.5. ELECTRICAL RESPONSE UNDER SOUND ACTUATION

Finally, we characterize the electrical readout of a device under test (DUT) of Geom. A with $V_{\text{pull-in}} = 3.8\,\mathrm{V}$. The device is actuated by sound pressure with respective pressure amplitudes of $p = 0.05 - 0.35\,\mathrm{Pa}$. To detect the electrical response from the DUT, the counter electrode is biased with $V_{\text{bias}} = 2.8\,\mathrm{V}$ with a BK Precision 9130 DC Power Supply, and the capacitive current that flows via the ML-Gr membrane is monitored for the membrane motion as shown in Figure 4.15a. In this scenario, synchronization and data acquisition involve utilizing a LabVIEW script to control a Stanford SR830 Lock-In Amplifier (LIA). The AC current from the DUT is acquired using this setup. Additionally, the reference microphone signal is received through a MOKU:Lab operating in IN/OUT mode, enabling the calculation of sound pressure. Furthermore, the MOKU:Lab also provides an AC voltage signal to drive the speaker and serves as the signal reference for lock-in detection. The measurements in Figure 4.15 involve a high mid-range frequency $f_1 = 3\,\mathrm{kHz}$ determined by the emitted sound frequency of a reference micro-speaker used in this specific setup. Considering the constraints of the setup, a small speaker is used, which cannot generate high sound pressures at lower frequencies.

Under sound pressure, the induced motion generates a current due to the time-dependent charge variation ($\frac{\Delta Q}{\Delta t} = \frac{\Delta(CV)}{\Delta t}$) of the proposed capacitor. Thus, by increasing the sound pressure, the distance between the electrodes reduces, forcing higher motion current

i_{mot} as in Eq.4.4.

$$i_{mot}(t) = V_{\text{bias}} \frac{\mathrm{d}}{\mathrm{d}t} \int_0^R \frac{2\pi r dr}{g_0 - x_{\text{sound}}(1 - \frac{r^2}{R^2})^2} \approx \frac{V_{\text{bias}} \pi \epsilon_0 R^2}{3g_0^2} \frac{\mathrm{d}}{\mathrm{d}t} x(t) \tag{4.4}$$

The equation deals with the determined capacitance in the context of a fully clamped circular membrane, assuming that the deflection (x_{sound}) remains smaller than the gap between both electrodes. Thus, the sound pressure magnitude is proportional to the membrane displacement amplitude x_{sound}. In this way, the amplitude of the graphene displacement under sound actuation x_{sound} can be extracted from the following equation Equation 4.5.

$$|x_{\text{sound}}| = \frac{3g_0^2}{V_{\text{bias}} \epsilon_0 A\omega} |i_{\text{mot}}(t)| \tag{4.5}$$

In Figure 4.15b, the relationship between the current output of the LIA and sound pressure is depicted, and it exhibits a trend that is compared to a linear fit. Specifically, the current from the LIA represents the amplitude of the induced current at the driving sound frequency.

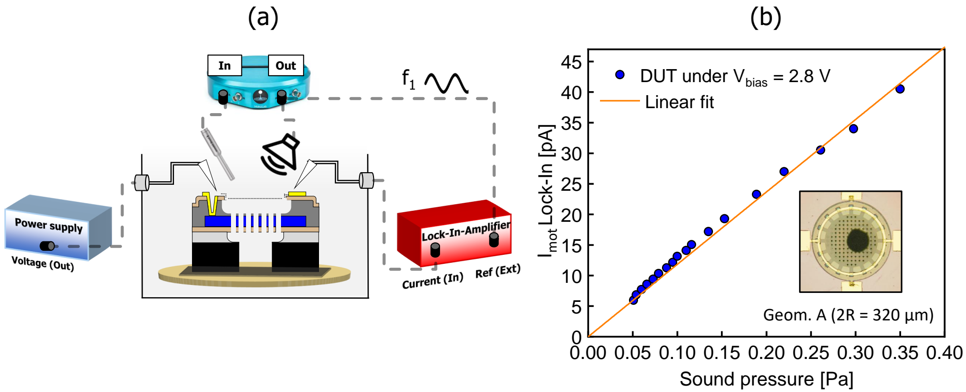

Figure 4.15: **Electrical response under sound actuation.** (a) The measurement setup employed for characterizing the device under test involves several components. The sample is secured to the chuck using double-sided tape covering the entire back side of the chip. Practical constraints drive this decision, as vacuum fixation is unfeasible within the experimental setup. Double-sided carbon tape serves the dual purpose of ensuring chip stability and that the sound pressure waves are only incident on the top side of the microphone. We note that this results in a relatively small back volume that increases the effective stiffness of the microphone compared to the configuration in Figure 5. A power supply is utilized to bias the device, which connects to the counter electrode. Simultaneously, a V_{AC} driving signal from Moku:Lab (output) drives the speaker and serves as the external reference signal for the lock-in amplifier SR830. The membrane electrode is connected to the input of the lock-in amplifier in current mode. The LabVIEW script records the current output obtained from the lock-in amplifier. Additionally, the sound pressure is captured using a reference microphone connected to the Moku:Lab (input) positioned near the device under test. (b) A trampoline with geom. A is driven by sound at $f_1 = 3\,\text{kHz}$ at different pressure sound waves amplitudes $p = 0.05 - 0.35\,\text{Pa}$. The $I - p$ experimental curve is fitted with a linear fit.

By utilizing Equation 4.5, considering the highest device response under $p = 0.35\,\mathrm{Pa}$ of $i_{\mathrm{mot}} = 40\,\mathrm{pA}$, an estimated membrane displacement of $x_{\mathrm{sound}} \approx 141\,\mathrm{nm}$ is calculated. Upon normalization of the measured value at 0.35 to 1 Pa, a displacement of $x_{\mathrm{sound}} \approx 403\,\mathrm{nm}$ is obtained. Remarkably, this value differs by approximately 2.6× from the experimental results depicted in Figure 4.13. The observed amplitude difference is expected to be influenced by the V_{bias} effect on the membrane dynamics. The V_{bias} may cause a hardening effect, potentially leading to the elimination of foldings or wrinkles, thereby stretching the membrane and increasing its stiffness. Also, the observed stiffening of the diaphragm might result from the electrostatic force causing a nonlinear static displacement in the diaphragm [3]. These factors could contribute to a significant effect on the final device response. Unlike the mechanical compliance measurements, at this time, the cavity can also exhibit a form of spring-like behavior, wherein when the membrane is deflected, the enclosed air volume undergoes compression and expansion. This phenomenon generates a counteractive force, effectively reducing the membrane's compliance. In the end, a current attenuation can also be attributed to the current leakage through the wiring connections. However, to gain a deeper understanding and establish a more comprehensive understanding of the influence of the V_{bias} on mechanical compliance, further experiments are required, thereby paving the way for future research in 2D materials integration for MEMS condenser microphones.

4.4. CONCLUSION

This research introduces a novel approach for integrating multi-layer graphene into condenser MEMS microphones without transferring or polymer support. The method addresses previous limitations of fabricating graphene microphones on a wafer scale without polymer supports. Various designs using this approach, enabling the tuning of device sensitivity, are proposed. The resulting devices exhibit $V_{\text{pull-in}} = 2 - 9.5\mathrm{V}$, making them compatible for future ASIC integration. Despite the limited acoustic bandwidth, primarily attributed to the counter electrode design, the devices demonstrate an estimated sensitivity of up to $S_{1\mathrm{kHz}} = 24.3 - 321\mathrm{mV\,Pa^{-1}}$. This sensitivity is more than two times that of reported state-of-the-art MEMS microphones, despite having a diameter three times smaller. While the proposed devices exhibit very high sensitivity, further exploration and enhancement of various relevant performance metrics of microphones need consideration in future work. This will be critical before graphene microphones surpass commercial devices in all aspects. Finally, this study unveils a promising and viable way to integrate multi-layer graphene into condenser MEMS microphones, opening up new possibilities for future microphone technology.

4.5. APPENDIX

VHF AND CLAMPING GEOMETRY

During the isotropic VHF etching process, the top layer etching mask SiN_x undergoes partial etching. Notably, graphene becomes more prone to delamination in regions corresponding to the graphene edges where Cr/Au layers are absent (as shown in Figure 4.16). In an SEM image illustrating a broken device, the over-etched polysilicon back-plate is observed, as previously discussed in Figure 4.7 (geom. A). The membrane cuts can be attributed to two primary factors: firstly, the large folding that occurs after delaminations, and secondly, the presence of possible residuals resulting from handler and chuck due to the final DRIE step, wherein the front-side is exposed to the mechanical arm and chuck. A potential solution to mitigate these challenges involves introducing an additional capping material, such as ALD thin films or polymers, as photoresists to be further investigated.

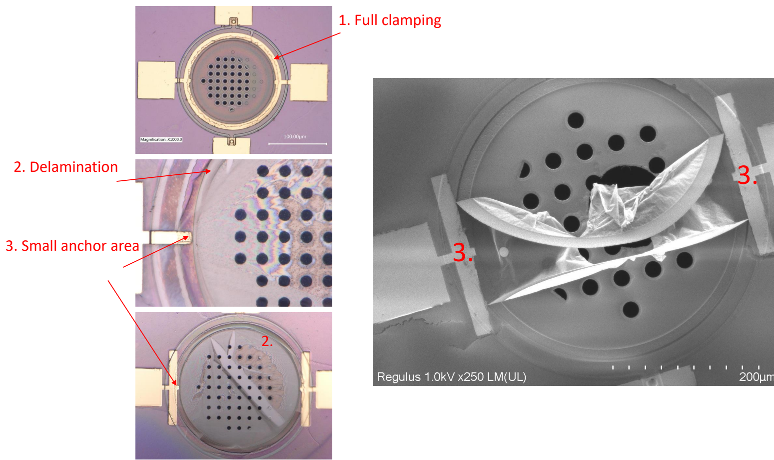

Figure 4.16: **Comparison of over-etched and broken devices.** An image comparison of a suspended device (geom. B), partially suspended, and broken devices. It is evident the effect of a full electrode clamping that helps to avoid larger delaminations.

THICKNESS MEASUREMENT

AFM thickness measurements are conducted on graphene that has undergone all the specified processing steps, excluding the VHF treatment. When subjected to mechanical agitation and the high surface tension of deionized water, the graphene detaches from its substrate and is lifted onto a flat thermal SiO_2 surface (as illustrated in Figure 4.17).

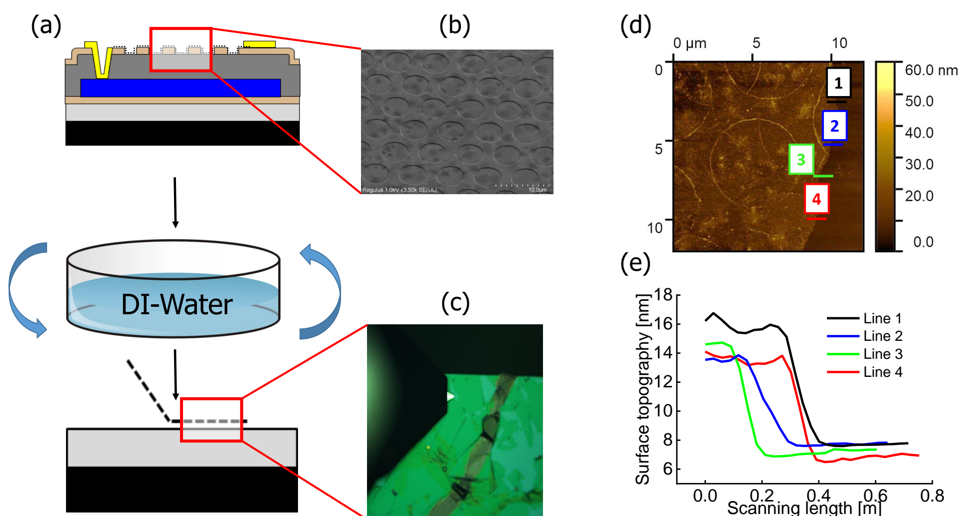

Figure 4.17: **Graphene thickness.** (a) Wet-transfer method is used to transfer a part of 5 mm x 5 mm patterned area of the graphene, designed and fabricated in the same mask-set for other application. (b) SEM image of the patterned region in a tilted view where graphene is conformally covering the entire topography. (c) Optical image through the AFM camera of the inspected area. Large foldings are present due to the rough transfer step. The flattest areas are used as references. (d-e) AFM thickness measurements in the drawn four regions. The circular foldings are related to the imprinted deformation that arises due to the pre-patterned cavities where the graphene was conformally grown.

ALD AlO_x ENCAPSULATION

The encapsulation test began with a previously processed wafer, where LOCOS was performed, as described in Chapter 2 (section 2.5). The SiN_x layer has a thickness of 300 nm, and the thermal oxide was grown to match the height of the SiN_x layer. After sputtering 50 nm of Mo and growing graphene according to the methods described in Chapters 2, 3, and this chapter, ALD AlO_x was deposited on the entire wafer following the recipe used in Chapter 2, resulting in a thickness of 55 nm, as measured by ellipsometry (Figure 4.18(1)).

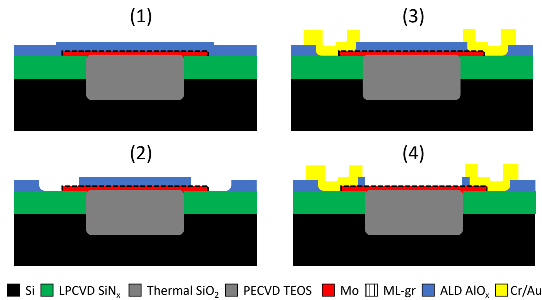

Figure 4.18: **ALD AlOx ML-gr encapsulation.** (1) LOCOS, Mo sputtering and patterning, CVD ML-gr growth and final ALD AlOx deposition. (2) Wet-Eching of AlOx for future Cr/Au evaporation. (3) Cr/Au evaporation. (4) Opening of the ML-gr area by wet-etching.

The great coverage of ALD AlO_x on top of the Mo/ML-gr can be observed by comparing Figure 4.19a and Figure 4.19b. In Figure 4.19a, the pattern corresponds to the Mo/ML-graphene area, showing different colors due to varying thicknesses across the same area. Figure 4.19b shows a zoomed-in region where the top part includes Mo/ML-Graphene/AlO_x and the bottom part includes SiN_x/AlO_x. The lack of variation in black gradient colors between Figure 4.19a and Figure 4.19b can be attributed to the 1 kV voltage used during imaging. This setting primarily detects the top AlO_x layer on the ML-gr in Figure 4.19b, rather than the exposed ML-gr seen in Figure 4.19a. Subsequently, a lift-off mask was used, and after lithography, the AlO_x was etched with BHF for approximately 1 min (Figure 4.18(2)). Figure 4.19c demonstrates that after the AlO_x removal, the difference in colors on the ML-graphene becomes visible again. Following Cr/Au evaporation and lift-off (Figure 4.18(3)), another lithography step was performed, followed by BHF etching to remove the AlO_x in the future suspended area (Figure 4.18(4) and Figure 4.19d). Figure 4.19d shows the color difference across the future suspended area, confirming the absence of AlO_x. Mo etching was then performed using H_2O_2 followed by DI-water washing (Figure 4.18(4)). Compared to the standard transfer-free method without encapsulation, some issues were encountered. These issues are related to the formation of blisters in certain patterns. These blisters are likely due to stress release during the Mo etching under the AlO_x. Unlike the standard Mo etching without encapsulation, where the graphene has more freedom to release stress, the encapsulated layer might pin the graphene, leading to blister formation. It is important to note that blisters primarily form in regions where the Mo edges are fully covered, as shown in Figure 4.19e

and Figure 4.19f. In Figure 4.19e, the Mo strip has three edges without ALD AlO_x, while in Figure 4.19f, all the edges are encapsulated.

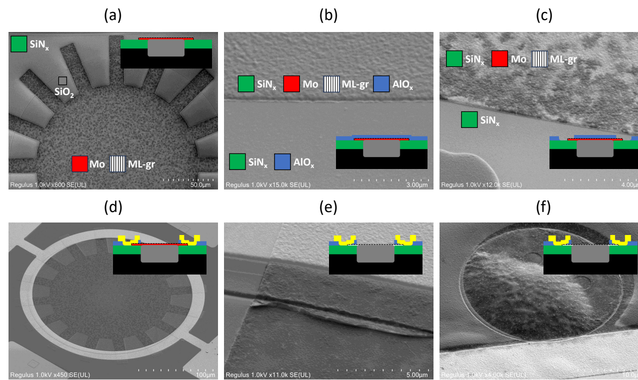

Figure 4.19: **ML-gr encapsulation with ALD AlO_x.**(a-f) ML-gr transfer-free method integrated with ALD AlO_x encapsulation. All SEM images are compared with the corresponding schematics (miniatures) that illustrate the proposed process flow shown in Figure 4.18.

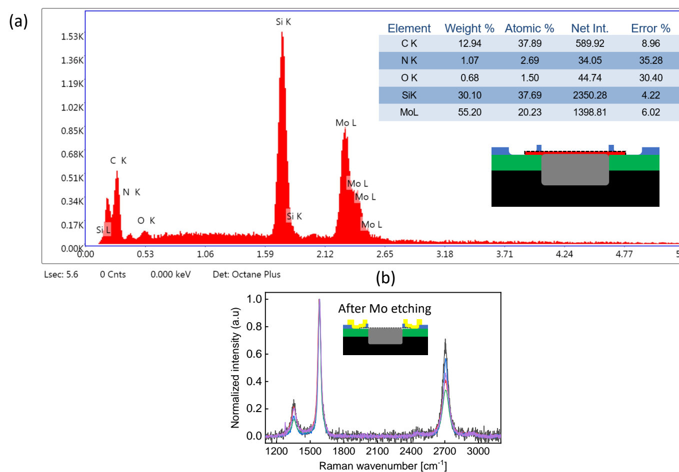

Element	Weight %	Atomic %	Net Int.	Error %
C K	12.94	37.89	589.92	8.96
N K	1.07	2.69	34.05	35.28
O K	0.68	1.50	44.74	30.40
SiK	30.10	37.69	2350.28	4.22
MoL	55.20	20.23	1398.81	6.02

Figure 4.20: **Energy-dispersive X-ray spectroscopy and Raman spectroscopy characterization.**(a) EDX analysis in the exposed ML-gr/Mo region after BHF treatment to check for any remaining AlO_x residues. (b) Raman spectroscopy was conducted after AlO_x and Mo etching on the ML-gr. The variation between the traces corresponds to different spots across the inspected area, indicating differences in material thickness. The Raman signature closely matches what is reported in this thesis, confirming that the encapsulation process does not compromise the quality of the film.

DYNAMIC MOTION AT THE RESONANCE FREQUENCY (1ST MODE)

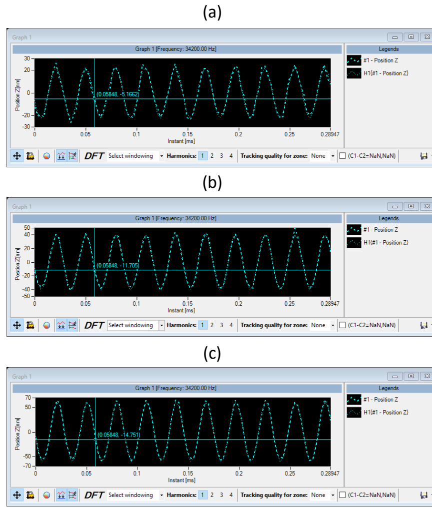

Figure 4.21: **Membrane oscillation at its resonance frequency.** (a-c) The oscillation of the membrane's center over time under piezoelectric actuation at the membrane's resonance frequency is shown. The increasing amplitude of membrane displacement corresponds to different applied voltages, $V_{\text{AC}} = 1, 2$, and $3\,\text{V}$. These measurements are obtained using DHM system as discussed in the previous chapters.

PULL-IN VOLTAGE ESTIMATION

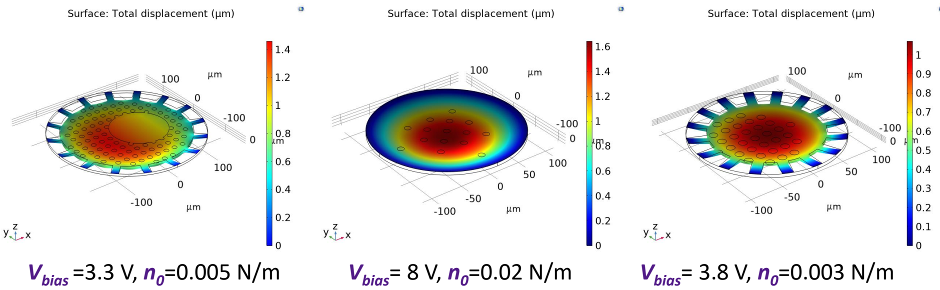

Figure 4.22: **FEA simulations (COMSOL Multiphysics).** The three geometries are modeled with different V_{bias} to extract the membrane displacement.

4

BASE CAPACITANCE (C_0) BEFORE VHF

Position	Measure Value [pF]	Analytical Modeled Value [pF]
1_1	0.02449	0.02597
1_2	0.02398	0.02597
1_3	0.02371	0.02597
1_4	0.02476	0.02597
1_5	0.0238	0.02597
3_1	0.01832	0.01641
3_3	0.01924	0.01641
3_4	0.01826	0.01641
3_5	0.01879	0.01641
4_1	0.01784	0.0156
6_1	0.01296	0.01123
6_2	0.01321	0.01123
6_3	0.01232	0.01123

Table 4.2: Comparison of measured and simulated capacitances after DRIE for Chip with membranes $2R = 50-60\,\mu\text{m}$

Position	Measure Value [pF]	Analytical Modeled Value [pF]
1_1	0.11734	0.10582
1_2	0.11751	0.10582
1_3	0.11811	0.10582
1_4	0.11835	0.10582
1_5	0.15996	0.15840
1_6	0.15994	0.15840
1_7	0.16022	0.15840
2_1	0.16003	0.15907
2_2	0.1603	0.15907
2_3	0.16039	0.15907
2_4	0.16139	0.15907
2_5	0.16141	0.15907
2_6	0.16108	0.15907
2_7	0.16128	0.15907
2_8	0.16151	0.15907
3_1	0.16742	0.16644
3_2	0.16744	0.16644
3_3	0.16777	0.16644
3_4	0.16732	0.16644
3_5	0.16706	0.16644
3_6	0.16741	0.16644
3_7	0.16766	0.16644
4_1	0.14112	0.14834
4_2	0.14133	0.14834
4_3	0.1431	0.14834
4_4	0.14152	0.14834
4_5	0.14407	0.14834
4_6	0.14395	0.14834
5_2	0.05217	0.05148
5_4	0.04779	0.04911
6_2	0.04778	0.04911
6_3	0.04783	0.04911
7_1	0.04788	0.04911
7_2	0.04532	0.04911
8_1	0.03893	0.03200
8_2	0.03865	0.03200
8_3	0.03858	0.03200
8_4	0.03843	0.03200

Table 4.3: Comparison of measured and simulated capacitances after DRIE for Chip with membranes $2R = 400 - 500\mu\text{m}$

4

Position	Measure Value [pF]	Analytical Modeled Value [pF]
3_1	0.3613	0.35400
3_2	0.36116	0.35400
3_3	0.36135	0.35400
3_4	0.3611	0.35400
3_5	0.36152	0.35400
3_6	0.38619	0.40165
4_1	0.3896	0.4041
4_2	0.39106	0.4041
4_3	0.39112	0.4041
4_4	0.39089	0.4041
4_5	0.39046	0.4041
5_1	0.38333	0.38743
5_2	0.39267	0.40392
5_3	0.39232	0.40392
5_4	0.39232	0.40392
5_5	0.39217	0.40392
6_1	0.38597	0.39579
6_2	0.36051	0.37904
6_3	0.36105	0.38156
6_4	0.36105	0.38156
6_5	0.36201	0.38156
7_1	0.29698	0.27515
7_2	0.29437	0.27515
7_3	0.29516	0.27515
7_4	0.29514	0.27515
7_5	0.29531	0.27515
7_6	0.29477	0.27515

Table 4.4: Comparison of measured and simulated capacitances after DRIE for Chip with membranes $2R = 300\mu m$

REFERENCES

[1] R. Pezone, S. Anzinger, G. Baglioni, H. S. Wasisto, P. M. Sarro, P. G. Steeneken, and S. Vollebregt, *Highly-sensitive wafer-scale transfer-free graphene mems condenser microphones,* Microsystems amp; Nanoengineering **10** (2024), 10.1038/s41378-024-00656-x.

[2] R. Pezone, G. Baglioni, P. M. Sarro, P. G. Steeneken, and S. Vollebregt, *High-performance wafer-scale transfer-free graphene microphones,* in *2023 IEEE 36th International Conference on Micro Electro Mechanical Systems (MEMS)* (IEEE, 2023).

[3] S. Shubham, Y. Seo, V. Naderyan, X. Song, A. Frank, J. Johnson, M. da Silva, and M. Pedersen, *A novel MEMS capacitive microphone with semiconstrained di-*

aphragm supported with center and peripheral backplate protrusions, Micromachines **13**, 22 (2021).

[4] N. Mohamad, P. Iovenitti, and T. Vinay, *Modelling and optimisation of a spring-supported diaphragm capacitive mems microphone,* Engineering **02**, 762–770 (2010).

[5] D. Todorović, A. Matković, M. Milićević, D. Jovanović, R. Gajić, I. Salom, and M. Spasenović, *Multilayer graphene condenser microphone,* 2D Materials **2**, 045013 (2015).

[6] S. Woo, J.-H. Han, J. H. Lee, S. Cho, K.-W. Seong, M. Choi, and J.-H. Cho, *Realization of a high sensitivity microphone for a hearing aid using a graphene–PMMA laminated diaphragm,* ACS Applied Materials & Interfaces **9**, 1237 (2017).

[7] A. F. Carvalho, A. J. Fernandes, M. B. Hassine, P. Ferreira, E. Fortunato, and F. M. Costa, *Millimeter-sized few-layer suspended graphene membranes,* Applied Materials Today **21**, 100879 (2020).

[8] J. Xu, G. S. Wood, E. Mastropaolo, M. J. Newton, and R. Cheung, *Realization of a graphene/PMMA acoustic capacitive sensor released by silicon dioxide sacrificial layer,* ACS Applied Materials & Interfaces **13**, 38792 (2021).

[9] G. Baglioni, R. Pezone, S. Vollebregt, K. C. Zobenica, M. Spasenović, D. Todorović, H. Liu, G. J. Verbiest, H. S. J. van der Zant, and P. G. Steeneken, *Ultra-sensitive graphene membranes for microphone applications,* Nanoscale **15**, 6343 (2023).

[10] M. Šiškins, M. Lee, D. Wehenkel, R. van Rijn, T. W. de Jong, J. R. Renshof, B. C. Hopman, W. S. J. M. Peters, D. Davidovikj, H. S. J. van der Zant, and P. G. Steeneken, *Sensitive capacitive pressure sensors based on graphene membrane arrays,* Microsystems & Nanoengineering **6** (2020), 10.1038/s41378-020-00212-3.

[11] COMSOL, *Axisymmetric condenser microphone,* `https://www.comsol.com/model/axisymmetric-condenser-microphone-12377` (2024), accessed: 2024-08-15.

[12] L. di Paola, *Wafer-Scale Fabrication of Graphene-Based Condenser Microphones,* Master's thesis, Delft University of Technology (2022), accessed: 2024-08-15.

[13] S. A. Zawawi, A. A. Hamzah, B. Y. Majlis, and F. Mohd-Yasin, *A review of mems capacitive microphones,* Micromachines **11**, 484 (2020).

[14] B. Vigna, P. Ferrari, F. F. Villa, E. Lasalandra, and S. Zerbini, eds., *Silicon Sensors and Actuators* (Springer International Publishing, 2022).

[15] R. Pezone, G. Baglioni, P. M. Sarro, P. G. Steeneken, and S. Vollebregt, *Sensitive transfer-free wafer-scale graphene microphones,* ACS Applied Materials & Interfaces **14**, 21705 (2022).

[16] R. H. J. Vervuurt, B. Karasulu, M. A. Verheijen, W. E. M. M. Kessels, and A. A. Bol, *Uniform atomic layer deposition of al2o3 on graphene by reversible hydrogen plasma functionalization,* Chemistry of Materials **29**, 2090 (2017).

[17] D. R. Lenski and M. S. Fuhrer, *Raman and optical characterization of multilayer turbostratic graphene grown via chemical vapor deposition,* Journal of Applied Physics **110**, 013720 (2011).

[18] N. B. Babaroud, M. Palmar, A. I. Velea, C. Coletti, S. Weingärtner, F. Vos, W. A. Serdijn, S. Vollebregt, and V. Giagka, *Multilayer CVD graphene electrodes using a transfer-free process for the next generation of optically transparent and MRI-compatible neural interfaces,* Microsystems & Nanoengineering **8** (2022), 10.1038/s41378-022-00430-x.

4

[19] F. Ricciardella, S. Vollebregt, T. Polichetti, M. Miscuglio, B. Alfano, M. L. Miglietta, E. Massera, G. D. Francia, and P. M. Sarro, *Effects of graphene defects on gas sensing properties towards NO2 detection,* Nanoscale **9**, 6085 (2017).

[20] S. Vollebregt, B. Alfano, F. Ricciardella, A. J. M. Giesbers, Y. Grachova, H. W. van Zeijl, T. Polichetti, and P. M. Sarro, *A transfer-free wafer-scale cvd graphene fabrication process for mems/nems sensors,* in *2016 IEEE 29th International Conference on Micro Electro Mechanical Systems (MEMS)* (2016) pp. 17–20.

[21] P. G. Steeneken, R. J. Dolleman, D. Davidovikj, F. Alijani, and H. S. J. van der Zant, *Dynamics of 2d material membranes,* 2D Materials **8**, 042001 (2021).

[22] R. Pezone, *Air-loading effect on sub-mm polymer-free graphene membranes for microphone applications,* (In prep. 2023).

[23] L. Beranek and T. Mellow, *Acoustic components,* in *Acoustics: Sound Fields, Transducers and Vibration* (Elsevier, 2019) pp. 143–229.

[24] T. Veijola, *Analytic damping model for an mem perforation cell,* Microfluidics and Nanofluidics **2**, 249 (2006).

[25] S. Anzinger, H. S. Wasisto, A. Basavanna, M. Fueldner, and A. Dehé, *Non-linear behavioral modeling of capacitive MEMS microphones,* in *2023 IEEE 36th International Conference on Micro Electro Mechanical Systems (MEMS)* (IEEE, 2023).

[26] F. D. Shields, *Low-frequency wind noise correlation in microphone arrays,* The Journal of the Acoustical Society of America **117**, 3489 (2005).

[27] A. Dehe and M. Fueldner, *Micromechanical sensors and methods of manufacturing same,* (2006), uS 2006/0141656 A1.

[28] J. Esteves, L. Rufer, D. Ekeom, and S. Basrour, *Lumped-parameters equivalent circuit for condenser microphones modeling,* The Journal of the Acoustical Society of America **142**, 2121 (2017).

5

AIR-LOADING ON THE PERFORMANCE LIMITS OF GRAPHENE MICROPHONES

Membranes with very high aspect ratios, such as those in this study where the thickness $t < 10\,\mathrm{nm}$*, are nearly 3-4 orders of magnitude thinner than their surface length. This extreme thinness introduces additional effects that must be considered. One such effect is air-loading, which can significantly influence the membrane's dynamics and its intended functionality. Specifically, air-loading can act as an additional mass on the already low intrinsic mass of multi-layer graphene, thereby shifting the resonance frequency lower as the pressure increases from vacuum to atmospheric conditions, where the membrane is intended to operate. This chapter explores the magnitude of the atmospheric pressure's impact on the membrane's resonance frequency and provides an estimate of the ultimate performance of such membranes for audio application. These estimates aim to define the performance limits of these membranes when used as microphone diaphragms with a flat response across the audible bandwidth.*

Parts of this chapter have been published in: R.Pezone et al., *Effect of air-loading on the performance limits of graphene microphones*, Applied Physics Letters, 2024 [1].

5.1. INTRODUCTION

IN parallel with the previous chapters, where a fabrication method for multi-layer graphene diaphragms and MEMS-condenser microphones based on graphene is proposed along with an investigation into their performance, this chapter explores the influence of the bare effect of the air on membrane resonance frequency.
For silicon-based state-of-the-art diaphragms or general thicker resonators ($t < 500\,\text{nm}$) [2], the natural mode position is not significantly affected by different pressures [3].
Considering the atmosphere as a fluid in which particles interact, these particles can engage with any movable components, such as those found in MEMS devices, potentially influencing their response. Thus, the increased collision frequency between air molecules at elevated pressures due to their higher density and the membrane surface leads to more significant energy loss from the system and an "added virtual mass increment" denoted as "AVMI" in the field of fluid-structure interaction [4, 5]. Both phenomena could introduce more energy dissipation, primarily in heat due to viscous forces, and increase the system's inertia, affecting the frequency position of its natural mode and sharpness. Thus, both effects could significantly degrade the device's performance to the point where it may no longer be suitable for its intended application.
The broadening of the resonance peak might limit the operational frequency bandwidth and introduce additional noise, further compromising the device's SNR.
Generally, the enhanced damping effect broadens the resonator's frequency response, reducing its quality factor [6–8]. The broadening of Q implies that the resonator becomes less selective, with energy dissipation occurring over a wider frequency range. In practical terms, resonators operating under high-pressure conditions may exhibit reduced sensitivity and resolution, potentially impacting their performance in applications that require precise frequency control. Understanding and mitigating these effects is crucial for designing and optimizing such devices, especially for nm-thick diaphragms where such effects are predominant.
Recent advancements over five years highlight that involving large multi-layer graphene membranes shows its suitability for audio devices like microphones and speakers, exhibiting impressive capabilities and some limitations that need further investigations [9–16].
For example, improving the microphone's sensitivity, either by decreasing diaphragm tension or enlarging its diameter, reduces the resonance frequency and bandwidth of the microphones. In addition to the described effects of using an nm-thick low-tension membrane, this scenario poses a unique challenge, where achieving superior performance is not directly intricately dependent on only both characteristics.
This study begins by describing the fabrication methods of the devices, discussing the quality of the materials used, and detailing the experimental methods utilized to conduct the measurements. Following this, the frequency response of the devices under varying pressure conditions in both air and helium environments is evaluated. Subsequent sections align these findings with AVMI theory and utilize models to discern their effects on the ultimate performance capabilities of graphene microphones.

5

5.2. EXPERIMENTAL SETUP

The membranes utilized in this study refer to the same material synthesised accordingly with previous chapters, with a thickness of $t \approx 8$ nm and released by a transfer method. The graphene is grown initially on a Si/SiO_2(1000 nm)/Mo(50 nm) substrate, employing an LPCVD technique [17–21]. The membranes are realized by transferring the multi-layer graphene onto a pre-fabricated silicon substrate of 10 mm×10 mm with BOSCH perforations. The multi-layer graphene film is initially detached in water from its original substrate following the Mo etching process using H_2O_2 in a transfer-free approach, according to the previous chapters and previously published works [17–21]. Subsequently, the nm-film is placed on the target substrate while immersed in water. A comprehensive description of this process is illustrated in Figure 5.1.

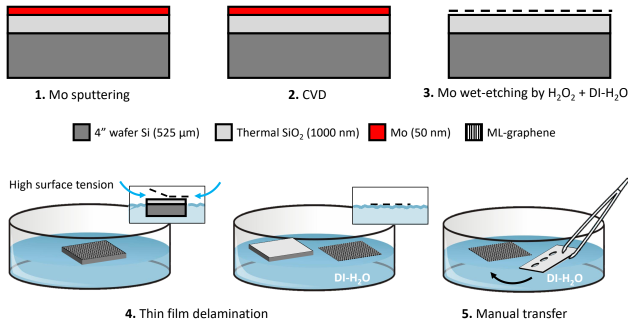

Figure 5.1: **Fabrication Process of ML-gr Transferred Membranes.**This image illustrates the step-by-step process of fabricating ML-graphene transferred membranes. Initially, ML-gre is synthesized on a sputtered Mo layer (steps 1-2). Following the wet-etching of Mo using H_2O_2, the unpatterned ML-gr collapses onto the underlying SiO_2 layer due to capillary and Van der Waals forces (step 3). Subsequently, the wafer undergoes atmospheric drying at room temperature. The wafer is then diced into 10 mm×10 mm chips, which are left to float on the surface of deionized water (DI-H_2O) (step 4). As water begins to penetrate the edges of the die, the entire film gently detaches from the substrate and floats on the DI-H_2O surface (step 4). At this stage, the film is carefully transferred onto a perforated silicon chip (step 5), previously etched using Bosch bulk-micromachining techniques. The final chip is left to dry in the atmosphere overnight, completing the fabrication process.

This fabrication method is chosen for this study for two primary reasons. First, the goal is to produce membranes completely free from any potential fabrication residuals, which were a concern in previous chapters due to the possibility of polymer residues on the membranes. In this way, any minimal added masses on the ML-gr are excluded. Second, this study targets larger membrane sizes, which are preferred to observe better the air-loading effect, particularly in high surface-area geometries. As discussed in earlier chapters, achieving larger sizes $R > 250\,\mu$m has also been associated with zero yields due to the large SiO_2 buckling after DRIE.

Unlike the state-of-the-art approaches [22–27], it is important to emphasize that this transfer method does not involve any polymer support, as found in literature , ensuring a cleaner membrane surface.

The transfer method involved in the fabrication process results in each membrane exhibiting different pre-tension values, even though they have uniform thickness (t_m) and radius (R). These significant pre-tension (n_0) variations were not observed with the fab-

rication methods used in the previous chapters. They are likely a result of the manual transfer and drying steps, which substantially impact the membrane's final shape. As the water trapped in the silicon perforations evaporates during drying, it pulls on the membrane. This process usually does not cause breakage for membranes with smaller thicknesses but often leads to considerable wrinkling.

It is important to highlight that the membrane's flatness is significantly affected by the edges of the BOSCH perforations, where the membrane will be clamped. Even micrometer-scale imperfections in these boundary edges have been found to induce local stress, leading to folding in the multi-layer graphene membranes. For this transfer method, avoiding imperfections in the etched area is preferable to ensure optimal membrane topography.

In Figure 5.2, an optical microscope image depicts a multi-layer membrane with a 250 µm radius. Adjacent to this, side-view and top-view Scanning Electron Microscope (SEM) images reveal small holes with diameters below 100 nm within the membrane. These holes likely originate either during the graphene CVD process or after Mo etching and transfer, where weaker grains may be dislodged. While these holes may alleviate static pressure build-up across the membrane, their size cannot significantly impact the membrane's high-frequency acoustic response. The characterization setup, depicted in Figure 5.3, involved measuring the fundamental mode's eigenfrequency using a LDV system.

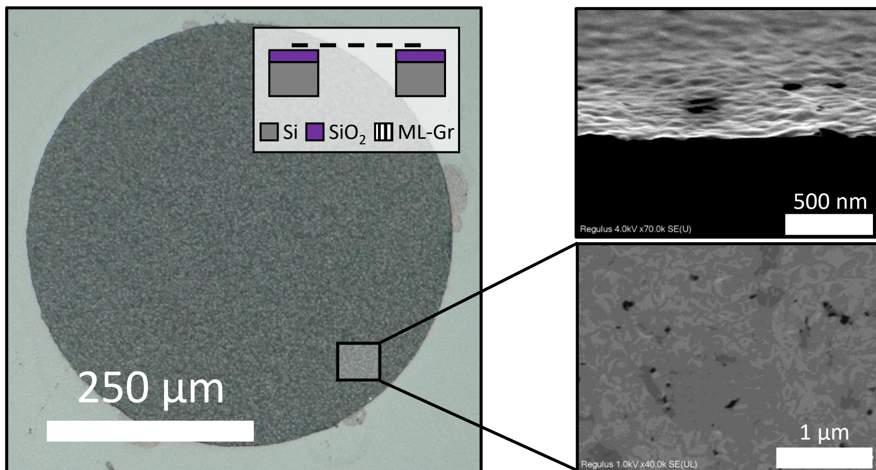

Figure 5.2: **Graphene membrane characterization.** Optical microscope image of a free-standing graphene membrane with a radius of $R = 250\mu$m. The inset includes a top view of the membrane and a side view of a fractured one showing the existence of nm holes.

This setup comprised a Polytec OFV-534 laser head and an MSA-5000 decoder. The LDV focused on the membrane center, targeting the area of maximal displacement. Excitation of the membrane motion is achieved using a piezo-shaker, controlled by an AC voltage within the relevant frequency band.

The experiments are conducted within a pressure-controlled vacuum chamber, with

pressures ranging from 30 to 1000 mbar. A Moku:Lab system was employed both for generating the AC voltage and analyzing the LDV signal. Additionally, a computer equipped with Python scripts was used for managing experimental parameters and data acquisition, interfacing seamlessly with the Moku:Lab system.

In this study, the Thermoviscous Acoustics interface within COMSOL's Acoustics Mod-

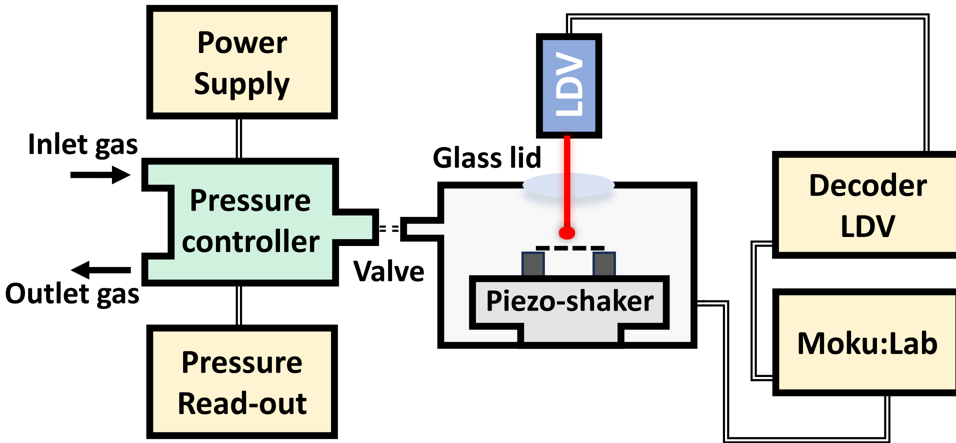

Figure 5.3: **Schematic setup for mechanical compliance measurements.**The schematic illustrates the experimental configuration wherein the ML-Gr is actuated through a piezo-shaker controlled by an AC-voltage (frequency sweep) generated by a Moku:Lab system. The membrane frequency response is analyzed by a Laser Doppler Vibrometer that is connected to the Moku:Lab. A pressure controller is used to perform and monitor the upward pressure sweeps.

ule is employed to model the experimental observations of frequency shifts in thin graphene membranes. This interface is typically utilized for modeling small acoustic transducers, such as condenser and MEMS microphones, and miniature loudspeakers, where incorporating thermal and viscous losses is crucial. The thermoviscous effects, which are particularly pronounced at resonances, cause a broadening and downward shift in frequency. To accurately capture these phenomena, the model included thermal conduction effects and viscous losses by solving the momentum (via the Navier-Stokes equations), mass (through the continuity equation), and energy conservation equations.
The acoustic environment surrounding the membrane is modeled as a sphere of air (Figure 5.4), which interacts with the membrane, adding mass and damping effects, thus modifying its resonance frequency. This air volume must permit unobstructed acoustic wave propagation. However, modeling this becomes challenging at the boundary of the air sphere, as waves should ideally continue without reflection to avoid standing waves and geometrical resonances within the modeled volume.
To address this, the pressure is set to zero at the outer boundary. It is a simple approach to simulate an open boundary condition. This method assumes that the acoustic wave is radiated into an infinite domain without any reflection. However, this boundary con-

dition may not be entirely accurate, as it assumes that the pressure at the boundary is always zero, which may not be the case in reality. It's a straightforward method but may introduce some level of error, especially if the domain size is not large enough to prevent the influence of the boundary on wave propagation.

A more precise method involves modeling a volume that extends for at least 3-5 wavelengths, followed by implementing a "perfectly matched layer" (PML) at the boundary [28–30]. This approach ensures minimal reflection and accurate wave propagation. Referring to this approach, for simplicity, the outer sphere radius is initially estimated to be higher than twice the diameter of the membrane to account for air-loading effects. However, for optimal accuracy, the sphere should be significantly larger, spanning several millimeters or even centimeters. This would better represent the extensive wave propagation and its effects on the membrane's resonance.

In the course of this simulation, a comprehensive set of simulations is also conducted to assess the impact of wall boundary conditions on the final resonance frequency shift. The mechanical conditions tested are 'Slip' and 'No slip,' representing two extremes of boundary interaction, allowing for tangential fluid motion and prohibiting it, respectively. The thermal conditions 'Adiabatic' and 'Isothermal' are also employed to determine the influence of thermal energy exchange at the boundary. These conditions are paired to form four distinct simulation environments. The simulation results across all four scenarios displayed negligible differences, suggesting that the resonance frequency of the graphene membranes remained insensitive to these boundary condition variations within our study's parameter space. This invariance can be attributed to the dominant role of the membrane's mechanical properties and the air-loading effect over the viscous and thermal boundary interactions in determining the resonance characteristics.

Given the thinness of the graphene membranes and the small scale of the system, it is plausible that the boundary layer effects—both viscous and thermal—are minimal compared to the inertia of the air mass loading, which is primarily responsible for the observed frequency shifts. Furthermore, the high thermal conductivity of graphene coupled with the small size of the system suggests that temperature gradients, and hence the distinction between adiabatic and isothermal conditions, have a limited effect on the acoustic response.

5.3. Results and Discussion

Figure 5.5a displays three sets of data on the relationship between the fundamental resonance frequency f_{01} and pressure for multi-layer graphene membranes with a radius of $R = 250\,\mu\text{m}$ and a thickness of $t_m = 8\,\text{nm}$. The measurements B and C focus on the same membrane under conditions of air and He gas, respectively, while the measurement A investigates a membrane with lower pre-tension in air. Figure 5.5b presents the frequency response data for case B across the entire spectrum of frequency and pressure.

At low pressure, the fundamental resonance frequency of a membrane adheres to the formula:

$$f_{01} = \frac{2.405}{2\pi R}\sqrt{\frac{n_0}{\rho_m t_m}} \tag{5.1}$$

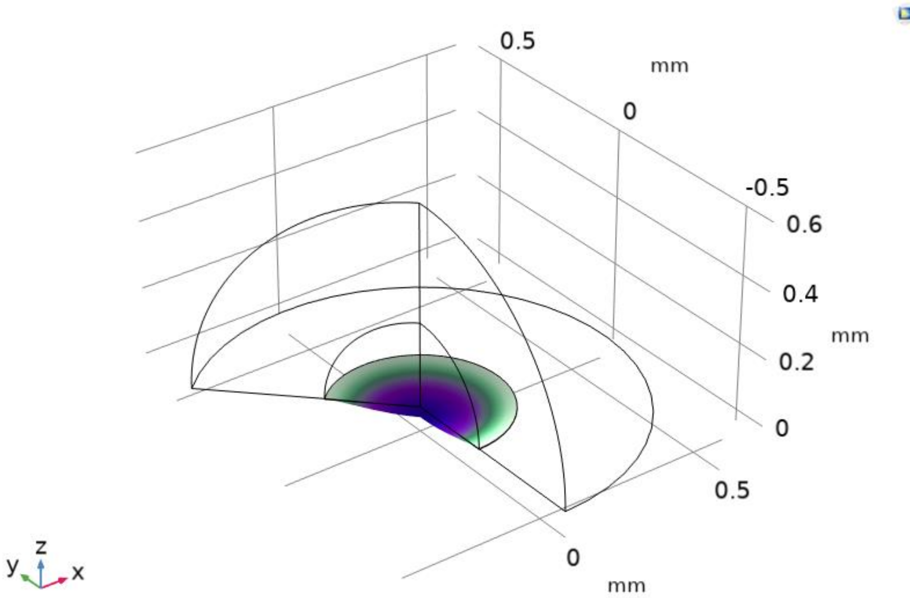

Figure 5.4: **Resonant Displacement of a Graphene Membrane within an Air Boundary Sphere.** Three-dimensional representation of the first mode shape of the graphene membrane with $R = 0.25\,\text{mm}$, as implemented in COMSOL Multiphysics. The outer sphere, representing the air volume boundary, has a $R_{\text{sphere}} = R + 0.35\,\text{mm}$, encapsulating the membrane. The surrounding air volume, set by the sphere, has been modeled to investigate the air loading effect on the membrane's resonance behavior.

For all three scenarios, an increase in pressure correlates with a decrease in resonance frequency, a phenomenon not previously observed experimentally in gases and not considered by Equation 5.1. This effect is, however, already investigated in fluid-structure interaction studies [4, 5, 31], where contact with a liquid significantly lowers the resonance frequency of plates and membranes.
The phenomenon of air-loading contributes to an "additional virtual mass index" (AVMI) factor β, defined as:

$$\beta = \Gamma \frac{\rho_f}{\rho_m} \frac{R}{t_m}, \tag{5.2}$$

Here, ρ_f represents the fluid or gas density, ρ_m the membrane density, and $\Gamma = 0.65$ is the nondimensional AVMI (NAVMI) factor for the fundamental resonance mode of a clamped circular plate [4, 5].
In air, this results in the membrane's effective mass density increasing by a factor of $1+\beta$, yielding a pressure-dependent resonance frequency $f_{01}(P)$:

$$f_{01}(P) = \frac{2.405}{2\pi R} \sqrt{\frac{n_0}{\rho_m t_m + \rho_f(P) R}}, \tag{5.3}$$

where $\rho_f(P)$, the pressure-dependent gas density, equals $\frac{P}{C_p T}$, and C_p denotes the gas's specific heat capacity, with values of $C_{\text{p,helium}} = 2076.9\,\text{J}/(\text{kg}\cdot\text{K})$ and $C_{\text{p,air}} = 287.5\,\text{J}/(\text{kg}\cdot\text{K})$. To validate the hypothesis that air-loading reduces the resonance frequency, Figure 5.5 correlates equation Equation 5.3 with Comsol finite element method (FEM) results, demonstrating strong agreement in both air and helium gas environments. This confirms that the observed effects stem from a significant effective mass increase due to air-loading, leading to a reduction of more than a factor 2.
Notably, the factor β from Eq.Equation 5.2 remains minimal for air and graphene due to the small value of $\Gamma\rho_f/\rho_m = 4.6\times10^{-5}$, making air-loading effects generally imperceptible. However, the substantial aspect ratio $R/t_m = 31,250$ of the membrane, facilitated by graphene's low thickness, allows for these effects to be observed.
Additionally, in capacitive condenser microphones, the squeeze-film effect [32] can increase resonance frequency, partially compensating for air-loading effects.
It's also crucial to note that condenser microphones are typically coupled with a readout circuit such as an ASIC, which provides a constant bias voltage (V_{bias}) to the electrodes. This V_{bias} introduces electrostatic forces, causing 'electrostatic softening' that significantly reduces the resonance frequency, thereby influencing the system's dynamic response.

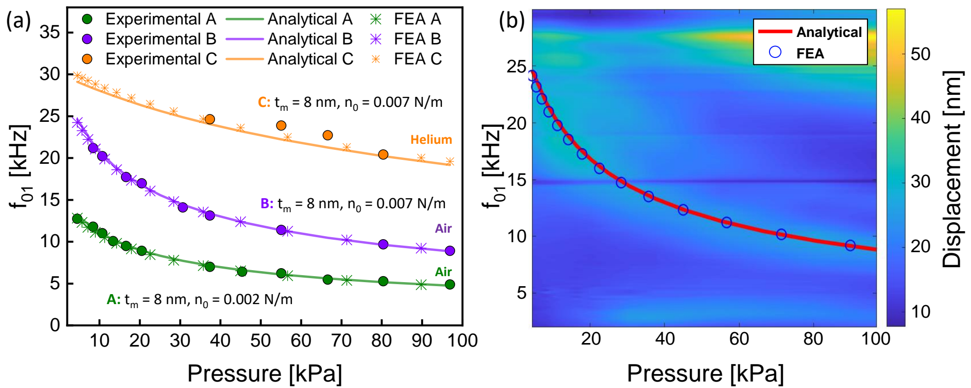

Figure 5.5: **Frequency reduction of f_{01} as a function of increasing pressure due to the air-loading effect.** Three measurements are performed on ML-Gr membranes with $R = 250\,\mu\text{m}$ and $t_m = 8\,\text{nm}$. Membranes A and B are measured in air, and membrane C is a measurement of the same membrane as in B in helium gas. Note that the lowest pressure plotted is 3 kPa. Lines and stars represent analytical and finite element simulation results based on the "Multiphysics" physics that couples the "Thermoviscous Acoustics, Frequency Domain" and "Membrane" modules. (b) Waterfall plot presenting results from membrane B in air.

5.4. PERFORMANCE LIMITS AND IMPLICATIONS

Having established the significance of air-loading in the performance of graphene microphones, the study now employs models to estimate its impact on the ultimate performance of these membranes. With the assumption of a fabrication method that allows for the free adjustment of pre-tension, it is set to a value $n_{20\text{kHz}}$, ensuring that the mem-

brane's resonance frequency at 1000 mbar is $f_{01}(1000\text{mbar}) = 20\,\text{kHz}$. This adjustment is crucial for achieving a bandwidth that covers the entire audible range. The resulting pre-tension $n_{20\text{kHz}}$ for graphene membranes of various radii R and thicknesses t_m is calculated and illustrated in Figure 5.6a using Equation 5.1 and Equation 5.3.
The impact of air-loading, more pronounced in membranes with larger radii and thinner thicknesses, is evident from the disparity between curves with (continuous lines) and without air-loading (dashed lines). Based on these pre-tension values, Figure 5.6b explores the mechanical compliance and sensitivity of the membrane. The linear compliance S_m of a circular membrane, defined as its average deflection per unit pressure difference, is represented by $S_m = R^2/(8n_0)$, a measure of the microphone's mechanical sensitivity[16, 33]. The sensitivity of graphene membranes under air-loading is depicted in Figure 5.6b using:

$$S_{\text{m,20kHz}} = \frac{R^2}{8n_{\text{20kHz}}} = \frac{2.405^2}{32\pi^2 \cdot (20\text{kHz})^2 \left(\rho_m t_m + \frac{P_{\text{air}} R}{C_p T}\right)} \tag{5.4}$$

An intriguing finding from Figure 5.6b is the independence of sensitivity $S_{\text{m,20kHz}}$ from membrane radius in scenarios with higher thickness or absence of air-loading, due to $n_0 \propto R^2$ maintaining a constant resonance frequency as per Equation 5.1. However, sensitivity increases with reduced membrane thickness up to a limit imposed by air-loading, where $S_{\text{m,20kHz}} = \left(\frac{2.405}{2\pi 20\text{kHz}}\right)^2 \frac{C_p T}{8P_{air} R}$. Since the AVMI factor $\beta \propto \frac{R}{t_m}$, this threshold is reached at higher thicknesses for larger radius membranes, indicating the highest achievable sensitivity S_m for smaller radius membranes in Figure 5.6b.
Nevertheless, smaller membranes, despite their potential for record sensitivity, face a drawback: they become mechanically nonlinear at lower sound pressures, leading to reduced sensitivity and harmonic distortion at high sound pressure levels. The mechanical nonlinearity is expressed as:

$$\Delta P = \frac{4n_0}{R^2} z + \frac{8Et_m}{3R^4(1-\nu)} z^3 = \Delta P_{\text{lin}} + \Delta P_{\text{nl}}, \tag{5.5}$$

where E and ν represent the Young's modulus and Poisson's ratio of the membrane material, respectively. To prevent significant nonlinearities at a maximum operating sound pressure ΔP_{max}, the center deflection z should remain below a limiting value z_{lim}, ensuring the nonlinear pressure term remains a fraction $\alpha = \Delta P_{\text{nl}}/\Delta P_{\text{lin}}$ smaller than the linear term.
For small α (here $\alpha = 0.1$), the amplitude and sensitivity limits are:

$$z_{\text{lim}} = \sqrt{\alpha \frac{3R^4(1-\nu)}{16Et_m S_{\text{m}}}} \tag{5.6}$$

$$\Delta P_{\text{max}} \approx \frac{z_{\text{lim}}}{2S_{\text{m}}} \tag{5.7}$$

$$S^3_{\text{m,max}} \approx \frac{3\alpha R^4(1-\nu)}{(8\Delta P_{\text{max}})^2 Et_m} \tag{5.8}$$

Figure 5.6c, plotted using Equation 5.8 with $\Delta P_{\text{max}} = 1\,\text{Pa}$, and graphene properties of $E = 1\,\text{TPa}$, $\nu = 0.16$, reveals that while small membranes achieve maximum sensitivity

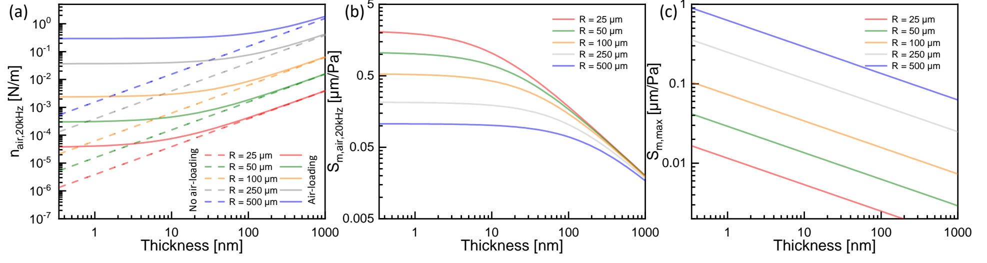

Figure 5.6: **Pre-tension and mechanical sensitivity within the audible frequency range, based on the proposed analytical model.** (a) Required pre-tension values to ensure a flat frequency response up to f_{01} = 20 kHz, evaluated across different membrane radii and thicknesses, with and without accounting for air-loading effects. (b) The peak mechanical sensitivity under atmospheric pressure, derived using Equation 5.4, and consistent with the results shown in (a). (c) To minimize nonlinearities in the pressure–deflection behavior, the deflection amplitude at maximum operating pressure is limited. This restriction also imposes a cap on the maximum mechanical sensitivity $S_{m,max}$ shown here for various graphene membrane designs with $\alpha = 0.1$ and $\Delta P_{\max} = 1$ Pa.

in Figure 5.6b, larger membranes exhibit higher sensitivity in Figure 5.6c. Thus, an optimal membrane radius can be determined, balancing bandwidth, sensitivity, and nonlinear distortion performance. Thinner membranes generally offer benefits, although they may impact robustness and manufacturability.
Finally, assessing the robustness of the membranes, considering a maximum yield strain[34] $\epsilon_{\mathrm{y}} = \frac{2}{3} z_y^2 / R^2$ of $\epsilon_y = 0.012$ for graphene[35], the maximum deflection (disregarding pre-tension) is $z_y = R\sqrt{1.5\epsilon_{\mathrm{y}}}$, leading to a maximum yield pressure $\Delta P_y = 8Et_m z_y^3 / [3R^4(1-\nu)]$:

$$\Delta P_y = \frac{\sqrt{24} E t_m \epsilon_y^{3/2}}{R(1-\nu)} \tag{5.9}$$

Therefore, for a graphene membrane to withstand a pressure difference of $\Delta P_y = 10^5$ pascal, the aspect ratio must be less than $R/t_m < 76 \times 10^3$. The membranes under study, with $R/t_m = 31.5 \times 10^3$, meet this criterion.
In addition to yield pressure considerations, pressure robustness tests on 4× membranes, each with a radius (R) of 350 µm, revealed robustness values of 1×10^5 Pa, 0.86×10^5 Pa, 0.4×10^5 Pa, and 0.64×10^5 Pa, lower than the estimated $\Delta P_y = 1.75 \times 10^5$ Pa from Equation 5.9. This discrepancy might be attributed to variations in maximum yield strain and Young's modulus of the multi-layer graphene, influenced by the synthesis method and clamping geometries [36]. Additionally, the presence of holes, as depicted in Figure 5.2, could further reduce the maximum yield pressure of the proposed membranes compared to Equation 5.9's prediction.

5.5. CONCLUSION

In conclusion, this study provides an experimental analysis of the impact of air-loading on the sensitivity of multi-layer graphene membranes, supported by both analytical and FEM models that capture the pressure-dependent resonance frequency through the AVMI factor. These findings highlight that air-loading can substantially reduce the resonance

frequency by more than half compared to its low-pressure value. By employing an experimentally validated model, we estimate the maximum mechanical sensitivity achievable for multi-layer graphene microphones, considering the constraints of bandwidth and the effects of air-loading. Additionally, we discuss the limitations imposed by the membrane's nonlinear mechanics, concluding that reducing the membrane thickness generally enhances microphone sensitivity. However, the air-loading effect limits further gains beyond a certain thinness. Regarding the microphone membranes' radius, the relationship is more complex, necessitating an optimization process that balances linearity, bandwidth, and other critical parameters, such as capacitance, electrical sensitivity, and pull-in voltage requirements. This research, therefore, offers a comprehensive set of equations that can guide the multi-objective optimization of microphone membranes, enabling their operation near the theoretical performance limits.

REFERENCES

[1] R. Pezone, G. Baglioni, C. van Ruiten, S. Anzinger, H. S. Wasisto, P. M. Sarro, P. G. Steeneken, and S. Vollebregt, *Effect of air-loading on the performance limits of graphene microphones,* Applied Physics Letters **124** (2024), 10.1063/5.0191939.

[2] M. Fueldner, *Microphones,* in *Handbook of Silicon Based MEMS Materials and Technologies* (Elsevier, 2020) p. 937–948.

[3] K. B. Gavan, J. van der Heijden, E. W. J. M. van der Drift, and H. S. J. van der Zant, *Effect of pressure on the q factor and the resonance frequency of sin microcantilevers,* in *2009 4th IEEE International Conference on Nano/Micro Engineered and Molecular Systems* (IEEE, 2009).

[4] M. Kwak and K. Kim, *Axisymmetric vibration of circular plates in contact with fluid,* Journal of Sound and Vibration **146**, 381 (1991).

[5] M. Amabili, G. Frosali, and M. Kwak, *Free vibrations of annular plates coupled with fluids,* Journal of Sound and Vibration **191**, 825 (1996).

[6] C. Chapus, F. Augereau, J. Podlecki, G. Lévêque, A. Foucaran, and J. Attal, *Carrier lifetime influence on clamped silicon wafer resonance by pta effect,* The European Physical Journal Applied Physics **50**, 30301 (2010).

[7] J. Gaspar, V. Chu, and J. Conde, *High-q thin-film silicon resonators processed at temperatures below 110°c on glass and plastic substrates,* in *17th IEEE International Conference on Micro Electro Mechanical Systems. Maastricht MEMS 2004 Technical Digest*, MEMSYS-04 (IEEE).

[8] Q. Li, J. Goosen, F. van Keulen, and J. van Beek, *Gas ambient dependence of quality factor in mems resonators,* in *2009 IEEE Sensors* (IEEE, 2009).

[9] A. F. Carvalho, A. J. Fernandes, M. B. Hassine, P. Ferreira, E. Fortunato, and F. M. Costa, *Millimeter-sized few-layer suspended graphene membranes,* Applied Materials Today **21**, 100879 (2020).

[10] D. Todorović, A. Matković, M. Milićević, D. Jovanović, R. Gajić, I. Salom, and M. Spasenović, *Multilayer graphene condenser microphone,* 2D Materials **2**, 045013 (2015).

[11] S. Wittmann, C. Glacer, S. Wagner, S. Pindl, and M. C. Lemme, *Graphene membranes for hall sensors and microphones integrated with CMOS-compatible processes,* ACS Applied Nano Materials **2**, 5079 (2019).

[12] B. Xu, P. Zhang, J. Zhu, Z. Liu, A. Eichler, X.-Q. Zheng, J. Lee, A. Dash, S. More, S. Wu, Y. Wang, H. Jia, A. Naik, A. Bachtold, R. Yang, P. X.-L. Feng, and Z. Wang, *Nanomechanical resonators: Toward atomic scale,* ACS Nano **16**, 15545–15585 (2022).

[13] R. Pezone, G. Baglioni, P. M. Sarro, P. G. Steeneken, and S. Vollebregt, *Sensitive transfer-free wafer-scale graphene microphones,* ACS Applied Materials & Interfaces **14**, 21705 (2022).

[14] R. Pezone, G. Baglioni, P. M. Sarro, P. G. Steeneken, and S. Vollebregt, *High-performance wafer-scale transfer-free graphene microphones,* in *2023 IEEE 36th International Conference on Micro Electro Mechanical Systems (MEMS)* (IEEE, 2023).

5

[15] R. Pezone, S. Anzinger, G. Baglioni, H. S. Wasisto, P. M. Sarro, P. G. Steeneken, and S. Vollebregt, *Highly-sensitive wafer-scale transfer-free graphene mems condenser microphones,* Microsystems amp; Nanoengineering **10** (2024), 10.1038/s41378-024-00656-x.

[16] G. Baglioni, R. Pezone, S. Vollebregt, K. C. Zobenica, M. Spasenović, D. Todorović, H. Liu, G. J. Verbiest, H. S. J. van der Zant, and P. G. Steeneken, *Ultra-sensitive graphene membranes for microphone applications,* Nanoscale **15**, 6343 (2023).

[17] S. Vollebregt, B. Alfano, F. Ricciardella, A. Giesbers, Y. Grachova, H. Van Zeijl, T. Polichetti, and P. M. Sarro, *A transfer-free wafer-scale cvd graphene fabrication process for mems/nems sensors,* in *2016 IEEE 29th International Conference on Micro Electro Mechanical Systems (MEMS)* (IEEE, 2016) pp. 17–20.

[18] F. Ricciardella, S. Vollebregt, B. Boshuizen, F. J. K. Danzl, I. Cesar, P. Spinelli, and P. M. Sarro, *Wafer-scale transfer-free process of multi-layered graphene grown by chemical vapor deposition,* Materials Research Express **7**, 035001 (2020).

[19] F. Ricciardella, S. Vollebregt, E. Kurganova, A. J. M. Giesbers, M. Ahmadi, and P. M. Sarro, *Growth of multi-layered graphene on molybdenum catalyst by solid phase reaction with amorphous carbon,* 2D Materials **6**, 035012 (2019).

[20] J. Romijn, S. Vollebregt, H. W. van Zeijl, and P. M. Sarro, *A wafer-scale process for the monolithic integration of cvd graphene and cmos logic for smart mems/nems sensors,* in *2019 IEEE 32nd International Conference on Micro Electro Mechanical Systems (MEMS)* (IEEE, 2019).

[21] F. Ricciardella, S. Vollebregt, T. Polichetti, M. Miscuglio, B. Alfano, M. L. Miglietta, E. Massera, G. Di Francia, and P. M. Sarro, *Effects of graphene defects on gas sensing properties towards no2 detection,* Nanoscale **9**, 6085–6093 (2017).

[22] S. Wagner, C. Weisenstein, A. Smith, M. Östling, S. Kataria, and M. Lemme, *Graphene transfer methods for the fabrication of membrane-based NEMS devices,* Microelectronic Engineering **159**, 108 (2016).

[23] S. Ullah, X. Yang, H. Q. Ta, M. Hasan, A. Bachmatiuk, K. Tokarska, B. Trzebicka, L. Fu, and M. H. Rummeli, *Graphene transfer methods: A review,* Nano Research **14**, 3756–3772 (2021).

[24] X. Langston and K. E. Whitener, *Graphene transfer: A physical perspective,* Nanomaterials **11**, 2837 (2021).

[25] Y.-M. Chen, S.-M. He, C.-H. Huang, C.-C. Huang, W.-P. Shih, C.-L. Chu, J. Kong, J. Li, and C.-Y. Su, *Ultra-large suspended graphene as a highly elastic membrane for capacitive pressure sensors,* Nanoscale **8**, 3555–3564 (2016).

[26] I. Cheliotis and I. Zergioti, *A review on transfer methods of two-dimensional materials,* 2D Materials **11**, 022004 (2024).

[27] M. Chen, R. C. Haddon, R. Yan, and E. Bekyarova, *Advances in transferring chemical vapour deposition graphene: a review,* Materials Horizons **4**, 1054–1063 (2017).

[28] K. Duru, J. E. Kozdon, and G. Kreiss, *Boundary conditions and stability of a perfectly matched layer for the elastic wave equation in first order form,* Journal of Computational Physics **303**, 372–395 (2015).

[29] Q. Qi and T. L. Geers, *Evaluation of the perfectly matched layer for computational acoustics,* Journal of Computational Physics **139**, 166–183 (1998).

[30] E. Turkel and A. Yefet, *Absorbing pml boundary layers for wave-like equations,* Applied Numerical Mathematics **27**, 533–557 (1998).

[31] Proceedings of the Royal Society of London. Series A, Containing Papers of a Mathematical and Physical Character **98**, 205–216 (1920).

[32] R. J. Dolleman, D. Davidovikj, S. J. Cartamil-Bueno, H. S. van der Zant, and P. G. Steeneken, *Graphene squeeze-film pressure sensors,* Nano letters **16**, 568 (2016).

[33] P. Scheeper, A. van der Donk, W. Olthuis, and P. Bergveld, *A review of silicon microphones,* Sensors and Actuators A: Physical **44**, 1 (1994).

[34] R. J. Dolleman, D. Davidovikj, S. J. Cartamil-Bueno, H. S. van der Zant, and P. G. Steeneken, *Graphene squeeze-film pressure sensors,* Nano letters **16**, 568 (2016).

[35] M. Goldsche, J. Sonntag, T. Khodkov, G. J. Verbiest, S. Reichardt, C. Neumann, T. Ouaj, N. von den Driesch, D. Buca, and C. Stampfer, *Tailoring mechanically tunable strain fields in graphene,* Nano letters **18**, 1707 (2018).

[36] A. Castellanos-Gomez, V. Singh, H. S. J. van der Zant, and G. A. Steele, *Mechanics of freely-suspended ultrathin layered materials,* Annalen der Physik **527**, 27–44 (2014).

6

GRAPHENE MICROPHONE ARRAYS

In the previous chapters, a repeatable and scalable approach for developing MEMS microphones using multi-layer graphene as sensitive diaphragms was explored. The adoption of graphene introduces several design challenges that must be addressed, particularly in comparison to the thicker, silicon-based diaphragms traditionally used. These challenges arise from graphene's ultra-low tension and thickness, which demand careful consideration in the design process. This chapter proposes a new design aimed at achieving a device with flatter sensitivity across the audible bandwidth and larger base capacitance. The proposed approach focuses on optimizing the backplate and reducing the diaphragm area. These modifications are expected to enhance device yield and mitigate pull-in effects while still targeting considerable sensitivities. An array of graphene drums is introduced to maintain high performance despite the lower individual sensitivity. This array design is intended to increase the base capacitance, which is critical for compatibility with future ASIC readout circuits. Due to their parasitic capacitances, these circuits require a higher input capacitance to achieve a high signal-to-noise ratio (SNR).

6.1. INTRODUCTION

IN this chapter, a new optimized sensor design, including a new concept, is introduced to target a flat response in the audible bandwidth, a base capacitance suitable for the current state-of-the-art ASIC read-out present in the commercially available System-In-Pakage MEMS microphones and a more reliable fabrication yield.
The design of a custom ASIC, while essential for fully evaluating MEMS performance within a System-In-Package platform, is beyond the scope of this thesis. However, evaluating the sensor's performance within a commercially available, fully optimized system is expected to provide the most accurate and reliable performance data. In this way, it would also be possible to investigate the graphene performance as a real demonstrator compared to the state-of-the-art.
Achieving the packaged demonstrator, or at least the ASIC read-out, leads to investigating several essential microphone properties that have not been studied in the previous chapters and literature. To achieve this, an extensive design has been proposed based on the properties of the Mo-based ML-gr found in the previous chapters.

6.2. SENSOR CONCEPT, DESIGN, AND PROCESS-FLOW

The new design builds on the concept of a device discussed in Chapter 4 and introduces a novel concept featuring even smaller drums in a parallel configuration. The main innovation in this work is the use of multiple graphene microphone membranes in parallel, rather than relying on a single large graphene membrane. This concept (Figure 6.1, Figure 6.2) offers several advantages. First, graphene membranes with smaller radii are stronger and more robust, allowing them to withstand higher pressures before breaking. Second, the fabrication process for these smaller membranes is expected to achieve higher yields, thanks to various process improvements introduced in this work.
Although the size of the microphone membranes is reduced in this new approach, the suspended backplate radius remains unchanged. This is because the backplate is formed by backside etching, which is challenging to scale down. To accommodate smaller microphone membranes, these membranes are connected to the suspended backplate using a clamping layer. In addition, the smaller membrane area is expected to enhance the frequency bandwidth, making it also suitable for ultrasound applications.
Figure 6.1a illustrates the parallel configuration integrated into a packaged example, comparing the existing concept from Chapter 4 (Figure 6.1b) with the new design (Figure 6.1c). The new capacitive condenser microphone concept remains consistent with Chapter 4, except for the array configuration (Figure 6.2a), an optimized more perforated (lower damping) back-plate made of monocrystalline silicon and a new a-SiC clamping support (Figure 6.2b). Therefore, this chapter elaborates only on these new design concepts in detail.
SOI wafers are employed to enhance the stress stability of the device layer after release, taking advantage of the superior properties of monocrystalline silicon. Unlike polysilicon, the stress in monocrystalline silicon is less affected by thermal stresses arising from differences in thermal expansion within the layer stack at high temperatures. The device layer (silicon layer), with a resistivity of 0.0025 Ωcm, it serves as an excellent back-plate counter electrode of the condenser microphone featuring a back-plate silicon layer

thickness of $t = 1.5\mu m$. The sacrificial buried oxide layer has a thickness of $t = 1\mu m$, similar to Chapter 4. While thinner back-plate could provide an even better-damping response because they reduce the flow resistance of air through the back-plate holes[1–6], the chosen specifications were based on the ready availability of wafers, avoiding months of waiting, which was not possible within the time frame
In addition to the steps outlined in Chapter 4, a Chemical Mechanical Polishing (CMP) step is introduced to flatten the TEOS sacrificial layer after PECVD deposition on top of the patterned back-plate. Unlike in Chapter 4, the back-plate is first patterned and fully etched in correspondence with the future venting holes and their outline, which simplifies the final release by eliminating the need to open venting holes from the back-side, thus avoiding an uncontrollable etching step found in Chapter 4 (one of the main yield-reducing steps). Etching the venting holes before the TEOS deposition should simplify and reduce the time of the final release process, requiring only a single step to release the sacrificial layer.

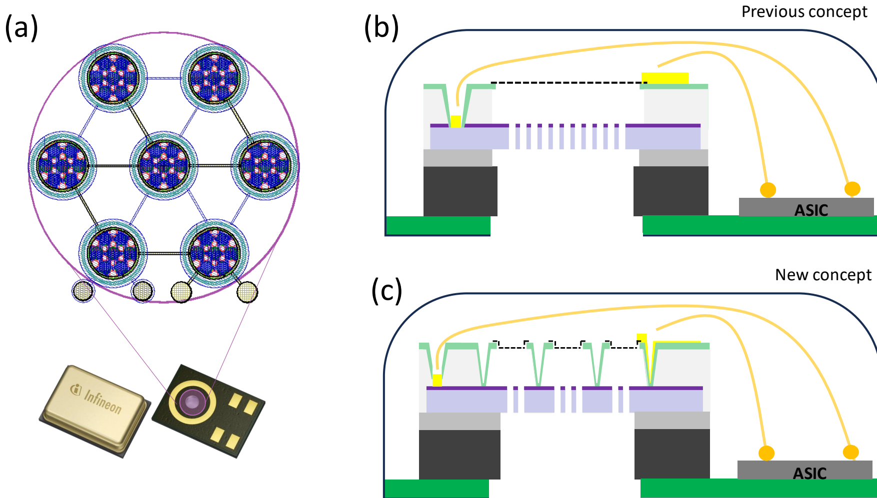

Figure 6.1: **Previous and new concepts for ML-Gr MEMS Condenser microphones.** (a) A draft of the new design architecture featuring a 7× cell array corresponding to 7× holes in the silicon substrate made by a BOSCH back-side etching process. Each of these holes results in a suspended silicon back-plate. Each cell contains 7× suspended ML-gr, clamped onto a partially suspended clamping layer. The purple circle highlights a potential soundport opening that might include all BOSCH openings. (b) The final schematic, showing the bonding of ASIC and MEMS via die-bonding within a single package. The design is similar to that in Chapter 4, with a single suspended graphene membrane above a perforated silicon backplate. This design mirrors the previous concept (see Chapter 4), with the primary distinction being that instead of featuring a singl emembrane, 7× cells are connected in parallel. Each single ML-gr membrane is related to the designs of Chapter 4. (c) A variation of the schematic in (b), where each cell now consists of 7× suspended membranes, such that the full microphone comprises of 49× ML-gr membranes. This new approach, based on an innovative concept, is discussed further in the following sections of the thesis.

Further improvements to the sacrificial layer include adding a SiC outer ring to prevent under-etching issues of the TEOS layer beneath the clamping layer, allowig HF sacrificial

layer etching to be performed for a long enough time to ensure a complete release without any HF time limitations (Figure 6.2c).
The clamping area has also been designed to minimize its suspended area, preventing any vibration during sound actuation. Amorphous silicon carbide (a-SiC) is now used as the clamping layer and etching mask due to its higher resistance to VHF etching, low-conductivity, and stability at high temperatures [7, 8]. Before integrating a-SiC into this process flow, it was tested with a previous mask set used in Chapter 4, confirming its suitability through base capacitance measurements that are not included in this thesis.
It is important to note that the design discussed here has not been optimized specifically for maximum area reduction, thus minimal sensor size. Specifically, the two main designs comprising 7-parallel cells are presented (Figure 6.1a), based on the Chapter 4 design with an optimized back-plate (Figure 6.1b) and a new different concept (Figure 6.1c and Figure 6.2). These designs feature a pitch of 400 μm and 550 μm from the center of each cell, organized using a hexagonal packing approach. While an optimized design could reduce the pitch by nearly 50% or more, leading to a significant area reduction and increase of the processing complexity. Such complexity requires further process optimization that has not been feasible within the scope of this thesis.
Additionally, these more compact designs were not included in the mask-set to maintain uniformity in the mask design, avoiding potential process issues (e.g. large variations in sacrificial layer etch times or additional yield risks) arising from differing design optimizations.

6

It is important to highlight that the increased unused area may reduce the SNR due to higher parasitic capacitance, which can negatively impact the system's electrical output [9–11]. However, this effect can be quantified after measurements, allowing for an accurate assessment of the SNR related to the device.

6.2.1. ANALYTICAL AND LUMPED CIRCUIT SIMULATION

For this design, an existing analytical non-linear model for the capacitive transduction in MEMS transducers with perforated counter-electrodes is utilized, particularly applicable to capacitive MEMS microphones [4, 12, 13].
The considered membrane-back-plate system can be divided into hexagonal unit cells of area A_{cell} containing a single circular perforation hole of area A_{perf} and radius R_{perf}. Approximating the unit cell by a circular symmetric equivalent of cell radius R_{cell}, the back-plate's perforation density Ψ can be defined as $\Psi = \frac{A_{\text{perf}}}{A_{\text{cell}}}$ [4, 12, 13].
The capacitance of the unit cell can be divided into two sub-capacitances accounting for a plate region $C_{\text{m,p}}$ where the membrane directly opposes the back-plate with a thickness t_{c}, and a fringing field region $C_{\text{m,f}}$, where the membrane opposes the perforation hole. Considering the radius of the unit cell to be smaller than the total membrane radius, the bending of the membrane within a single unit cell can be neglected, resulting in a constant gap between the membrane and back-plate in the unit cell. A simple parallel plate capacitor separated by a gap g_0 can describe the capacitance of the plate region $C_{\text{cell,p}}$.
Equation 6.1 and Equation 6.2 refer to an approximation by Taylor series expansion where for strongly increased non-linearity, higher order serial terms are required for a precise approximation of the capacitance's spatial derivative. More importantly, these

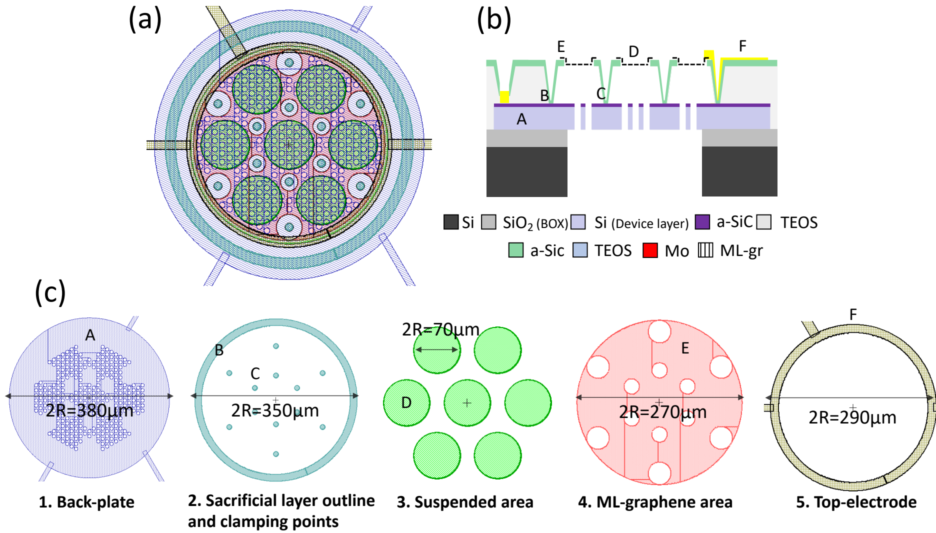

Figure 6.2: **Mask design and layer explanation of the new concept device.** (a) A single cell from the 7× parallel array, as introduced in Figure 6.1a and Figure 6.1c, is shown. In the zoomed image, the 7× parallel ML-gr membranes can be observed within the greenish circles, arranged in a hexagonal pattern. (b) A cross-sectional view of the new concept device, each letter corresponding to a linked mask layer described in (c). (c) Five of the seven mask layers for a single cell are illustrated. From left to right: the bottom electrode and venting holes are defined first, followed by the sacrificial layer and clamping points where the clamping layer connects to the back-plate. Next, the suspended area for the future ML-gr is shown, followed by the entire ML-gr area and the top electrodes. Notably, the mask associated with the bottom electrode contact and the BOSCH opening is omitted for simplicity. The BOSCH opening is approximately the same size as mask layer 4.

6

equations refer to the Taylor approximation of the analytical case of a variable capacitance considering a deflected circular membrane from the theory of plates, where the displacement profile $z(r)$ of a circular plate clamped at its perimeter and loaded by a uniform stationary pressure can be seen as $z(r) = z_{\text{pk}}\left(1-\frac{r^2}{R^2}\right)^2$ where z_{pk} is the largest membrane displacement at its center [4, 12, 13].
More particularly, the variable capacitance can be calculated via a surface integration over an infinitesimal area element of a capacitive unit cell.

$$C_{\text{m,p}} = \sum_{n=0}^{\infty} \frac{\epsilon_0 \pi R^2 (1-\Psi) z_{\text{pk}}^n}{(2n+1) g_0^{n+1}}, \tag{6.1}$$

$$C_{\text{m,f}} = \sum_{n=0}^{\infty} \frac{\epsilon_0 \pi R^2 \Psi z_{\text{pk}}^n}{(2n+1)(g_0+t_c)^{n+1}}, \tag{6.2}$$

Once the base capacitance, defined as $C_0 = C_{\text{m,p}} + C_{\text{m,f}}$, is calculated for each device (new concept in Figure 6.1c and in Figure 6.2) and previous design in Figure 6.1b (Chapter 4) in an array architecture of 7× devices in parallel, the sensitivity S is calculated according to Equation 6.3.

Figure 6.3 - Figure 6.5 report all the simulation and analytical results based on the proposed analytical model. Importantly, knowing the range of pre-tension extracted from the previous chapters, we calculated all responses based on a reasonable correspondent peak displacement (z_{pk}).

$$S_{\mathrm{dB}} = 20\log_{10}\left(\frac{V_{\mathrm{bias}}}{C_{\mathrm{tot}} \cdot (1\,\mathrm{V/Pa})} \cdot \frac{\Delta C}{\Delta P}\right) \tag{6.3}$$

Once the sensitivities are analytically simulated and aligned with the ASIC requirements ($C_0 > 700\,\mathrm{fF}$), the device frequency response is analyzed under realistic conditions (packaged device) following lumped-element analysis [4, 12, 13].

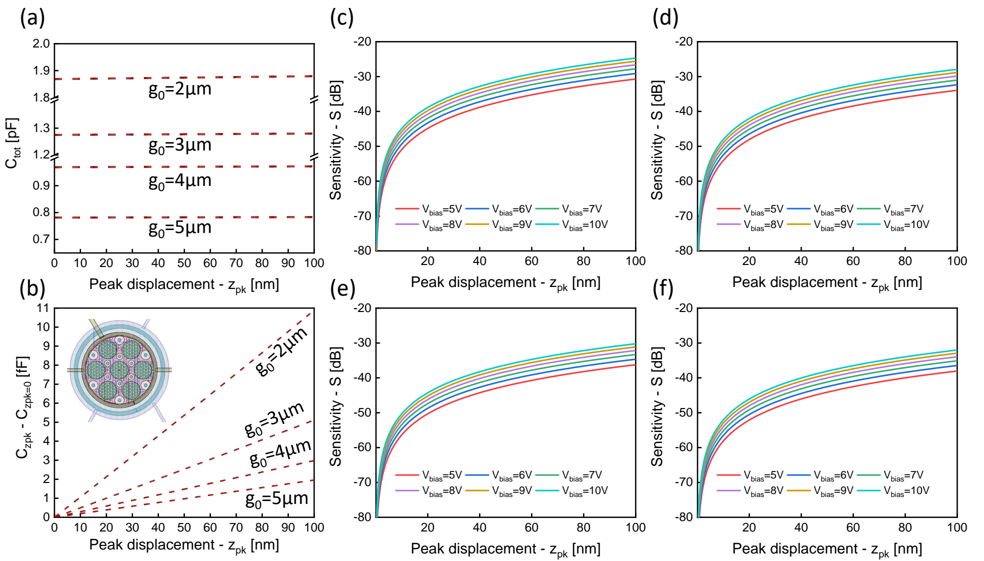

Figure 6.3: **Analytical simulation for the new design concept based on R=35 µm ML-gr drums and g_0=2,3,4 and 5 µm.** a) The total capacitance (C_0) after release is presented, considering different gap (g_0) sizes and the corresponding changes in z_{pk}. (b) The difference in capacitance is shown for various gap sizes, accounting for the z_{pk} variation. (c-f) The expected sensitivities, calculated using Equation 6.3, are presented for each gap size, starting from the smallest ($g_0 = 2\,\mu\mathrm{m}$) to the largest ($g_0 = 5\,\mu\mathrm{m}$). Each plot illustrates the relationship between sensitivity and the applied bias voltage V_{bias}. All measurements were initially calculated based on a single drum and then extended to account for the parallel arrangement of 49× drums, as each of the 7× cells contains 7× drums, as previously described.

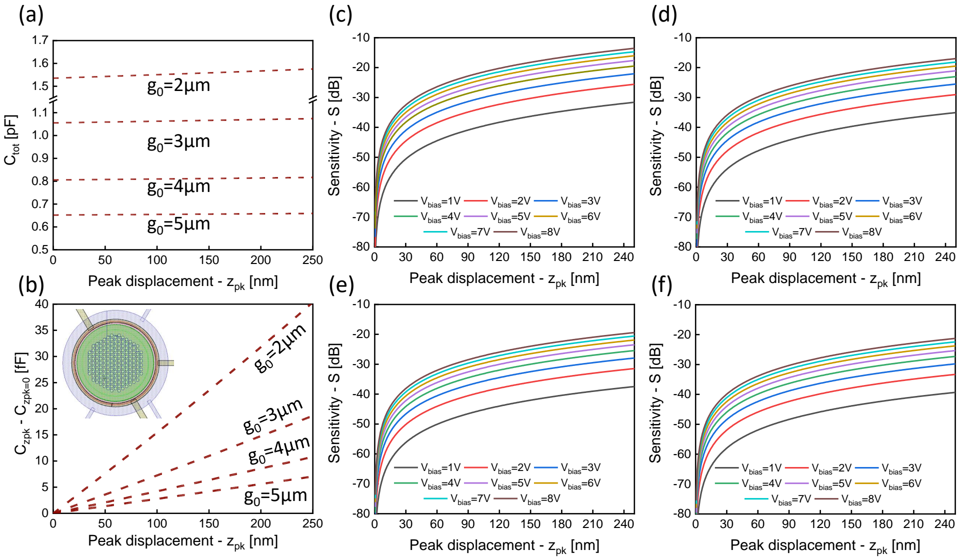

Figure 6.4: **Analytical simulation for the new design concept based on full-clamped R=110 µm ML-gr drums and g_0=2,3,4 and 5 µm.** a) The total capacitance (C_0) after release is presented, considering different gap sizes and the corresponding changes in z_{pk}. (b) The difference in capacitance is shown for various gap sizes, accounting for the z_{pk} variation. (c-f) The expected sensitivities, calculated using Equation 6.3, are presented for each gap size, starting from the smallest ($g_0 = 2\mu m$) to the largest ($g_0 = 5\mu m$). Each plot illustrates the relationship between sensitivity and the applied bias voltage V_{bias}. All measurements were calculated based on a single drum and then extended to account for the parallel arrangement of 7× drums.

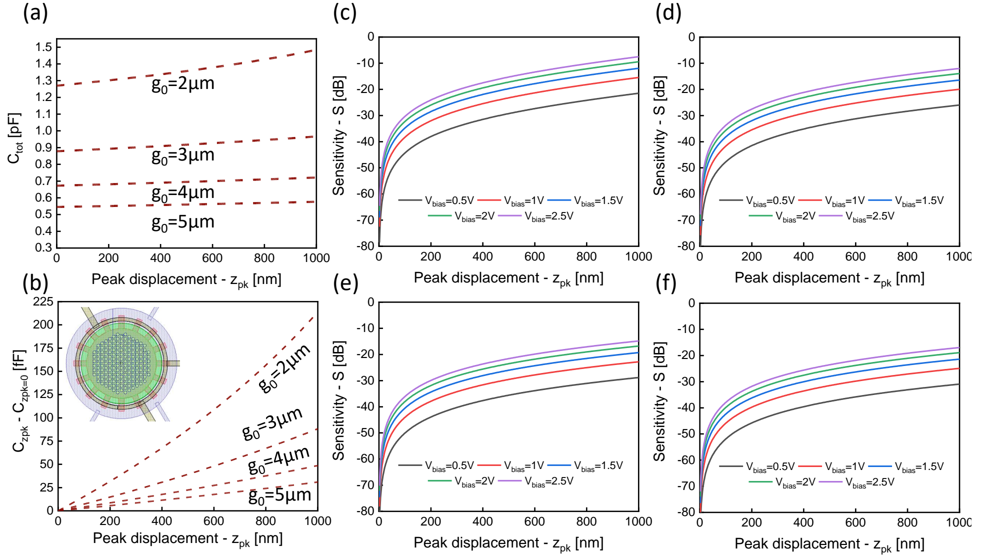

Figure 6.5: **Analytical simulation for the new design concept based on trampoline 2R=220 µm ML-gr drums and gap=2,3,4 and 5 µm.** (a-f) These plots follow same description of Figure 6.4.

Chapter 4 employs a simple lumped circuit to qualitatively estimate the low-pass frequency behavior observed in the fabricated devices. However, this initial simulation overlooks several critical factors that require further evaluation, including the sound port effect, the closed volume case, and the electrostatic force influence on the membrane due to the V_{bias}. Finally, the values of each discrete component shown in Figure 6.7, where an existing lumped circuit model is proposed, building upon previously published works [4, 12, 13].

This model incorporates three energy domains: acoustic, mechanical, and electrical. Specifically, Block 1 represents the air volume outside the package where the sound arrives, which is connected to Block 2, which describes the Helmholtz resonance caused by the difference in sound port radius and the device's DRIE opening. Block 3 accounts for the effect of the package's closed volume through the R_{vent} that describes the acoustic resistance due to the membrane holes. To transition from the acoustic to the mechanical domain, a Verilog block is implemented following published methodologies [4, 12, 13]. The membrane is represented by Block 4, where the membrane back-plate is described in the mechanical domain and connected through the bias circuit (Block 5). Here, the Verilog block incorporates the nonlinear behavior of the soft spring effect due to electrostatic forces, which also describes capacitive transduction accordingly with Equation 6.4 - Equation 6.6 and previous works [4, 12, 13].

$$F_{el} = \frac{1}{2}V^2\left(\frac{dC_{\text{m,p}}}{dz} + \frac{dC_{\text{m,f}}}{dz}\right), \tag{6.4}$$

$$\frac{dC_{\mathrm{m,p}}}{dz} = \sum_{n=0}^{\infty} \frac{\epsilon_0 \pi R^2 (1-\Psi)(n+1) z_{\mathrm{pk}}^n}{(2n+3)\, g_0^{n+2}}, \tag{6.5}$$

$$\frac{dC_{\mathrm{m,f}}}{dz} = \sum_{n=0}^{\infty} \frac{\epsilon_0 \pi R^2 \Psi (n+1) z_{\mathrm{pk}}^n}{(2n+3)(g_0 + t_c)^{n+2}}, \tag{6.6}$$

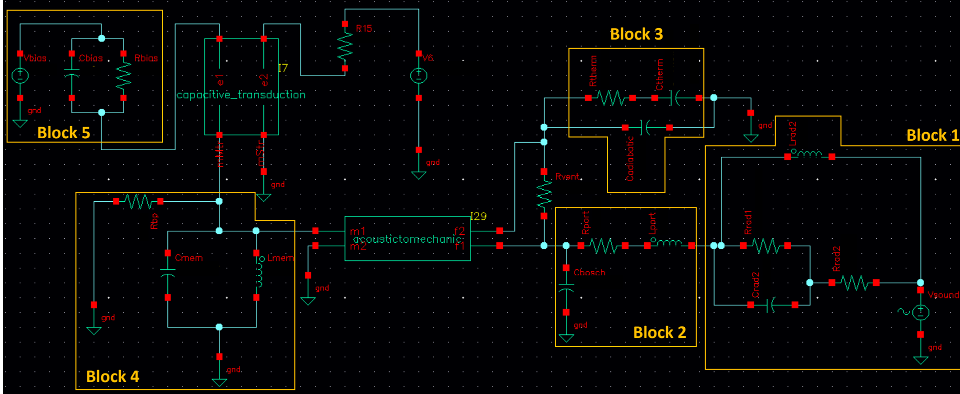

Figure 6.6: **Lumped element circuit of the proposed ML-gr MEMS Microphone in packaged configuration.** As described in this chapter, the lumped element circuit offers a quick method for predicting membrane dynamics in response to sound pressure across a frequency bandwidth. The model incorporates atmospheric effects, the Bosch soundport opening, diaphragm ventings, package volumes, membrane mechanics, damping from the membrane-back-plate configuration, and electrostatic forces resulting from the applied bias voltage (V_{bias}).

Following the simulations performed using the lumped circuit in Figure 6.6, two additional simulations were carried out with $R = 35\,\mu\mathrm{m}$ and $n_0 = 0.02 - 0.002\,\mathrm{N/m}$. In the simulation for R= 35 µm and $n_0 = 0.02\,\mathrm{N/m}$ (Figure 6.7a), the compliance shows the most significant changes in the frequency range of $f = 10\,\mathrm{Hz}$ to $f = 0.5\,\mathrm{MHz}$, with sharp peaks observed at $f = 71.31\,\mathrm{kHz}$. A downshift in resonance frequency is found in Figure 6.7b for $V_{\mathrm{bias}} = 5\,\mathrm{V}$ and $V_{\mathrm{bias}} = 10\,\mathrm{V}$ compared to $V_{\mathrm{bias}} = 1\,\mathrm{V}$. This is attributed to membrane softening, as electrostatic forces reduce membrane stiffness, increasing the membrane displacement under the same sound pressure. This softening effect is particularly noticeable when the membrane is fully flat, with no wrinkles present; otherwise, the electrostatic force may instead unfold the wrinkles, causing a form of "virtual stiffening" in the membrane similar to other previous works [14].
As expected, due to the lower pre-tension in Figure 6.7b, it is evident that V_{bias} strongly influences the resonance frequency shift. Therefore, the choice of V_{bias} must be made carefully, particularly in comparison to state-of-the-art MEMS-based silicon microphones, which have higher stiffness and are therefore relatively less susceptible to electrical softening.

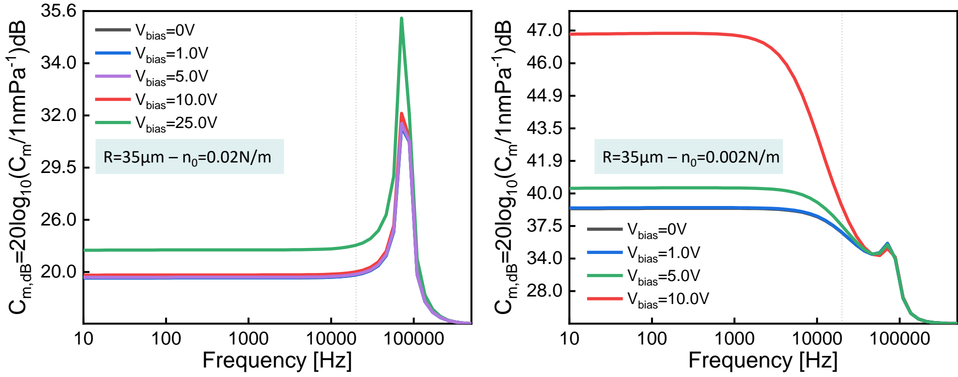

Figure 6.7: **Simulated mechanical compliances of ML-graphene in a packaged device across a frequency band.** (a), (b) illustrate the frequency response of the ML-graphene drum with a diameter of R = 35µm, accounting for a pre-tension range between n_0 = 0.02 N/m and n_0 = 0.002 N/m. The responses show a flat behavior within the audible bandwidth, except for (b), where V_{bias} = 10V and f_{01} = 8.15kHz.

6

6.2.2. PROCESS-FLOW

The SOI wafers with the previously described specifications are processed using LPCVD to deposit a 120nm-thick layer of a-SiC at 760°C based on DCS (Dichlorosilane) (46 sccm) and C_2H_2/H_2 (454 sccm) gases. This layer serves as a dielectric in case of membrane collapse, preventing short circuits. The device layer and a-SiC are etched using PR photoresist as an etching mask and RIE-ICP with Cl_2/HBr initially etching the a-SiC, followed by a BOSCH step to remove the monocrystalline silicon (device layer) entirely. PR is then removed using an O_2 plasma, followed by quick immersion in BHF and subsequent DI-water washing to eliminate residual PR or etch byproducts, as discussed in Chapter 4.

At this stage, PECVD TEOS is deposited to fill the perforations (R = 4µm), aiming to reach a thickness of approximately 2.5× the perforation gap for an optimal CMP step. Once the target thickness is achieved, the wafers are externally processed by CMP to eliminate any height variations ((Figure 6.8(1))) that could affect future Mo sputtering, thus the ML-graphene topography.

After polishing, the wafers are characterized, and the wafer is annealed at 1000°C in an N_2 atmosphere, as described in Chapter 4.

A lithography step is performed to define the area to be etched for the back-electrode contact. A BHF wet-etch is performed, leaving a few hundred nm of TEOS on the a-SiC (Figure 6.8(2)). Alternatively, dry etching could be used to etch the TEOS layer. After PR removal with an acetone bath at 40°C and subsequently HNO_3 and DI-water clean, the wafers are again patterned with positive PR at the future clamping points on the backplate and sacrificial layer definition are microfabricated by wet-etching based on BHF (1:7) (Figure 6.8(3)). Wet etching was attempted in these areas but proved challenging, as the etching rates were inconsistent across the clamping holes. Some small openings exhibited significantly different etching rates. An alternative approach was proposed to

address this, utilizing a wet-dry etch step to remove PR residues that might remain after developing in these smaller openings. In this step, slightly sloped sidewalls are desirable, as they will later be covered by a-SiC, which will serve as both the future clamping layer and an etching mask. It is essential to highlight that evaluating if PR was fully developed

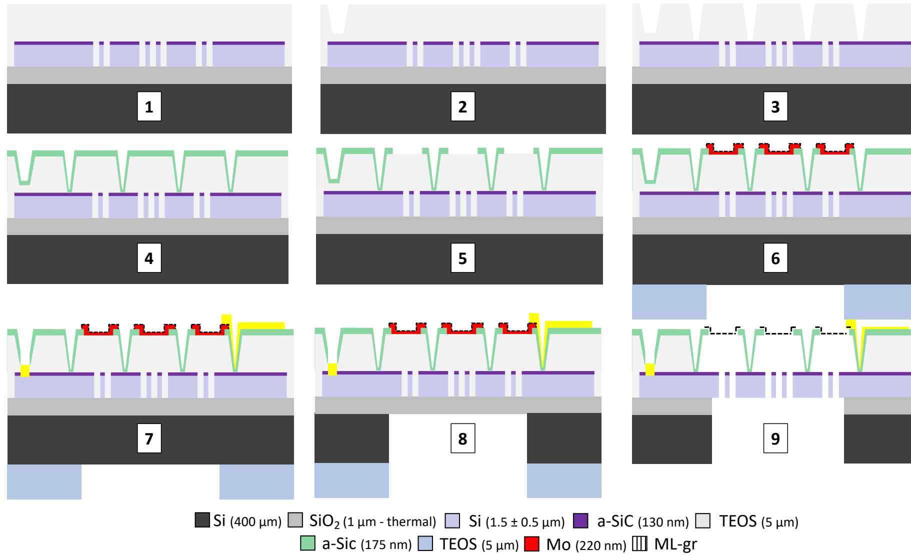

Figure 6.8: **ML-gr array MEMS condenser microphones process-flow.** (1)LPCVD a-SiC is deposited on the SOI device layer. Using the same patterning step, LPCVD a-SiC and the device layers are dry-etched to define venting holes and back-plate areas. TEOS is deposited by PECVD and flattened by CMP, followed by annealing at 1000°C in an N_2 environment. (2)Partial openings in TEOS are made by wet-etching with BHF to expose future pad areas for contacting the bottom electrode (back-plate). (3)The sacrificial layer and clamping areas are defined by wet-etching or a combination of wet- and dry-etching of the TEOS. (4)LPCVD a-SiC is deposited and fully etched in areas where the ML-gr will be suspended. (6)PECVD TEOS is deposited on the back-side and patterned by dry-etching for use as a future mask in the BOSCH process. As described in previous chapters, Mo is sputtered on the front side, and ML-gr is grown by LPCVD. (7)Lift-off is performed to form Cr/Au electrodes that contact both the bottom electrode and ML-gr. This follows dry-etching of the residual TEOS/a-SiC layers from step (6). The top side is encapsulated with positive PR, and the BOSCH process exposes the BOX layer. (9)After dicing Vapor HF removes the BOX and TEOS, releasing the ML-gr.

in the small clamping hole was challenging since a thick positive PR of 12 µm was used. Once the openings were fully etched and a-SiC on top of the device layer was exposed, PR was removed using an O_2 plasma, followed by a quick BHF and DI-water wash and a thorough HNO_3/Di-water clean (Figure 6.8(3)).
At this stage, a 180 nm-thick a-SiC layer is deposited via LPCVD with the same deposition conditions as the previous layer(Figure 6.8(4)), which is then patterned on the top using developed PR and dry etching by RIE-ICP (Figure 6.8(5)). Post-etch, O_2 plasma and BHF are required to remove any residuals, as O_2 plasma alone was found insufficient for complete residue removal. Subsequently, all layers on the back-side, except the original thermal SiO_2 from the SOI wafers, are etched. PECVD TEOS is deposited on the back-side and then etched using RIE (C_2F_6/CHF_3) at the locations corresponding to

the future BOSCH openings, with PECVD TEOS serving as a future etching mask (Figure 6.8(6)). During this process, TEOS is etched using a patterned positive PR.
Next, a 220 nm-thick molybdenum (Mo) layer is sputtered into the etched openings in the a-SiC at 350°C to prolong the ion mean free paths and ensure a more uniform coating along the sharp a-SiC sidewalls (Figure 6.8(6)).
The Mo is then etched using RIE-ICP with SF_6 or Cl_2/O_2 (Figure 6.8(6)). This step resulted in significant over-etching of the a-SiC for the Cl_2/O_2 etching chemistry, reducing its thickness to $t = 70$ nm from the original $t = 170$ nm. This discrepancy is likely due to the different etching rates of the SOI substrate compared to the silicon wafers used in testing. The substrate's varying temperature may have also influenced the etching rates.
The graphene growth is performed by CVD at 935°C with CH_4/H_2 at low pressure, following the steps detailed in previous chapters using the AIXTRON Black Magic system (Figure 6.8(6)).
After growth, the back-side openings are fully etched to expose the device layer, using another lithography step and RIE-ICP to etch the a-SiC and TEOS (Figure 6.8(6)).
Cr/Au is patterned via lift-off using negative PR (AZ nLOF2070) (Figure 6.8(7)). Finally, the top side is encapsulated with positive PR (AZ10XT $t = 12\,\mu$m), and the BOSCH process is performed. During this step, the PR showed several cracks due to high-pressure differences. In particular, thick photoresist layers can crack under large pressure changes due to internal stress, outgassing of residual solvents, and thermal expansion differences. The same issue was found under SEM inspection, where a high vacuum was needed. Thus, another PR is preferred within this scope where AZ3027 ($t = 5\,\mu$m) has been found to work properly for this purpose. Afterward, the PR is stripped using Ni555 and a DI-water rinse for a thorough inspection before automatic dicing ((Figure 6.8(8))).
Dicing is performed with a chip size of 1.5 mm × 1.5 mm, with the top side protected by a new spin-coated positive PR. The back-side is fully covered with "Non UV Blue PVC Film" to stabilize the wafer during dicing, with the diamond blade cutting operating directly onto the PR-protected top side.
Finally, the chips are gently removed from the plastic foil using tweezers dipped in DI water and then moved into Ni555 to strip the PR from the top side. After a DI-water wash, the chips are immersed in H_2O_2 to fully etch the Mo, followed by another DI-water rinse. Finally, Vapor HF is performed, as described in previous chapters.

6.3. RESULTS AND DISCUSSION

6.3.1. MICROFABRICATION OUTCOME

The microfabrication process yielded excellent results in terms of device realization, as initially planned. Despite the increased complexity of the process flows proposed in the previous chapters, the fabrication process achieved a high yield. As explained earlier, based on the previous outcomes, the design's dimensions were carefully optimized to balance high performance with higher yield in the microfabrication process. Thus, the challenges identified in Chapters 3 and 4 were successfully overcome in this chapter. Specifically, after the BOSCH process, no cracks or heterostructure damages were detected, resulting in a 100% yield across the entire wafer. The choice to proceed with a suspended area of $2R = 380\,\mu$m (back-plate) proved successful, demonstrating high con-

tinuity and repeatability across various iterations, even when using different wafers and modified process flows compared to Chapter 4.
This also marks the first successful application of a transfer-free graphene growth method on SOI wafers, indicating the potential to extend this approach to such substrates. The SOI wafers also successfully addressed the issue of back-plate deformation, resulting in a perfectly flat back-plate, which is essential for reliable device performance, especially during capacitance (C) changes caused by diaphragm deflection.
Figure 6.9a and Figure 6.9b illustrate the dicing step and the collected chips from the same wafer. Unfortunately, several chips were lost during dicing due to the absence of

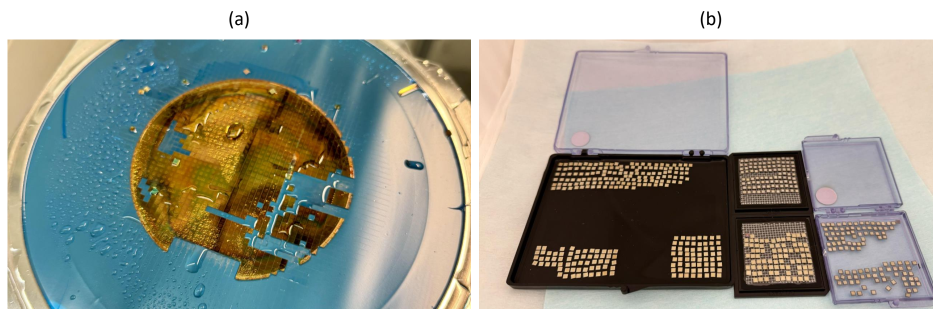

Figure 6.9: **Wafer dicing and storage.** (a) Overview of the wafer after dicing, showing several missing chips, a consequence of the water jet during the dicing process. The absence of blue film tape on the top side of the wafer contributed to the instability, as it would have provided additional support. This decision was made to avoid contact between the PVC blue film and the photoresist (PR), as previous studies have shown that such contact leads to the formation of an organic layer that is difficult to remove without causing mechanical damage to the suspended heterostructures. The yellowish color is due to a thick PR layer that protects the structures during the dicing process with a diamond tip blade. (b) Collected chips after dicing and photoresist stripping, showing the condition of the chips post-processing.

the PVC blue film on the top side, the high-pressure water jet, and a less-than-optimal dicing process. However, many chips that flew away were successfully collected, with over 30 showing no signs of damage after manual collection. Even after PR encapsulation removal and Mo etching (both wet processing steps), no damage was observed in the suspended heterostructure (device layer/a-SiC/TEOS/ML-gr), confirming the structure's robustness.
Following the optimization of the VHF recipe, all devices based on the design shown in Figure 6.1c and Figure 6.2 achieved a 90% yield across more than 30 released chips. However, unlike previous chapters, the membranes were not perfectly flat, displaying deformations with of a most a few μm (Figure 6.10). This deformation can negatively impact the read-out accuracy and repeatability, as such variations were unexpected. In previous devices, the membranes appeared primarily flat. Further investigation is required to understand the differences in the new process flow that may have contributed to this issue.
Due to time constraints, the thickness of the ML-gr was not measured via AFM, although it is expected to be similar to the values from previous chapters and other published works utilizing the same Mo-CVD ML-graphene growth method [15–20].

For subsequent measurements, only devices with relative flatter membranes were considered.

Figure 6.11 provides an overview of the final fabricated devices. The image shows that the device is successfully fabricated without major issues. However, some deformations or layer detachment are present, particularly in the clamping regions at the edges (Figure 6.11a).

In this process flow, the ML-gr was exposed several times to various types and thicknesses of PR, including AZ ECl 3027, AZ 10XT, and AZ NLOF 2070, during steps such as dry and wet etching, plasma treatment, and lift-offs. Despite the transfer-free method used and the employment of chemicals intended to remove processed PR, residues of PR could still remain on the graphene.

In Figure 6.12 TEM with bright-field imaging was employed to characterize the suspended graphene to inspect the amount of residuals left. These images correspond to a fully fabricated and diced chip inspecting the suspended graphene over the venting holes in the back-plate.

Additionally, the clamping a-SiC layer proved to be an effective etching mask, performing better than the previously used LPCVD SiN_x. However, in some samples exposed to VHF for extended periods, portions of the layer seemed partially detached (Figure 6.11). This detachment is likely due to damage in the a-SiC layer during the Mo etching process, potentially creating pinholes or etching vias that were exposed during the VHF treatment.

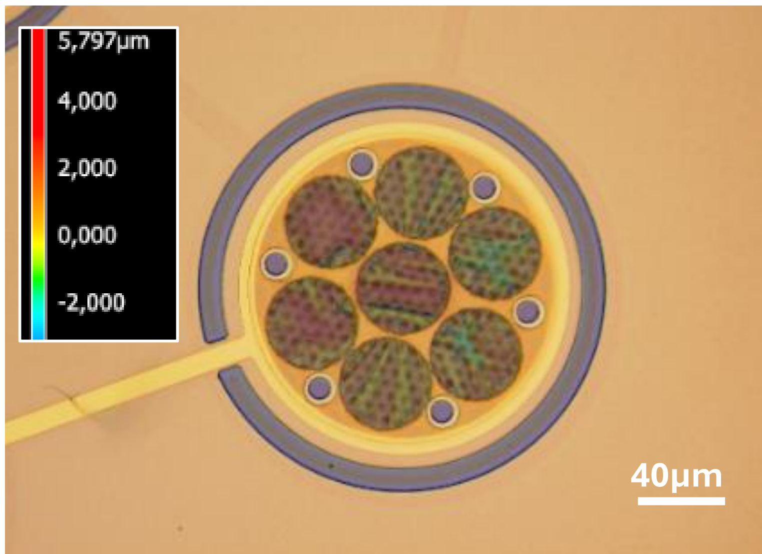

Figure 6.10: **Topography of single cell after VHF.** The image was captured using a Keyence microscope and subsequently processed with MultiFileAnalyzer software to apply false coloring, mapping topography differences across the surface. As observed, color variations within the same structure are only evident in correspondence with the multi-layer graphene drums with a radius of $R = 40$m. These variations, referenced against the flat clamping a-SiC surface, indicate height differences of $h \approx \pm 3$µm, representing the worst-case scenario identified. A more detailed inspection is required to establish statistical data across all samples and further evaluate the consistency of these observations.

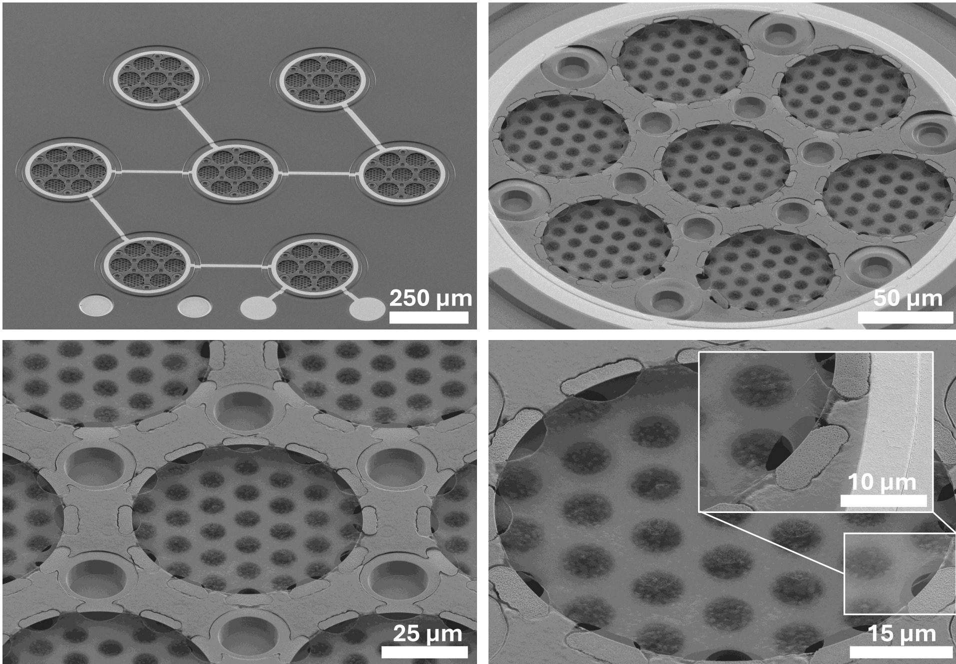

Figure 6.11: **SEM inspection of fabricated ML-Gr MEMS array condenser microphones.** Tilted SEM images of geometry shown in Figure 6.1c, Figure 6.2, in the spring clamping variant not described previosuly. It differs from the fully-clamped device shown in Figure 6.2 only in its clamping mechanism, which in this case is more spring-like, as evident in the SEM image. The images confirm that all membranes are correctly suspended, validating the feasibility of the fabrication process. No significant residuals are visible on the membranes, and their overall flatness is not highly buckled. However, further detailed inspections are necessary to assess and characterize the membrane flatness. Additionally, all venting holes, clamping points, and a-SiC clamping structures appear in proper condition, with no visible defects or issues. One device contains 49× drums, all of which are correctly suspended. A zoomed-in image is present to highlight the spring clamping of the thin ML-gr membrane, where no cuts or visible signs of damage are observed. Similarly to the previous designs, the ML-gr transfer-free method demonstrates significant flexibility in growing graphene conformally over regions with substantial height variations, such as the a-SiC/TEOS interface.

This is essential to maximize contrast and resolution, ensuring that any residuals or contaminants can be clearly distinguished without interference from an underlying substrate, which would otherwise reduce electron transparency and introduce background noise. In Figure 6.12a several venting hole regions confirm the ML-gr suspension, and a recurring area of residuals can be observed. For most of the holes examined across 3 devices from the same chip, the residuals were primarily confined within a smaller circular region inside the full diameter of the venting holes, suggesting that these residues are more effectively removed from the edges (Figure 6.12b) or during the processes they have not been deposited there. In some regions, the residuals appear mechanically displaced, folding back onto themselves in localized areas (Figure 6.12c and Figure 6.12d). Where these residuals are not present, the ML-gr surface appears completely clean.
Generally, the Ni555 solution used to dissolve the PR from the ML-gr seemed insuffi-

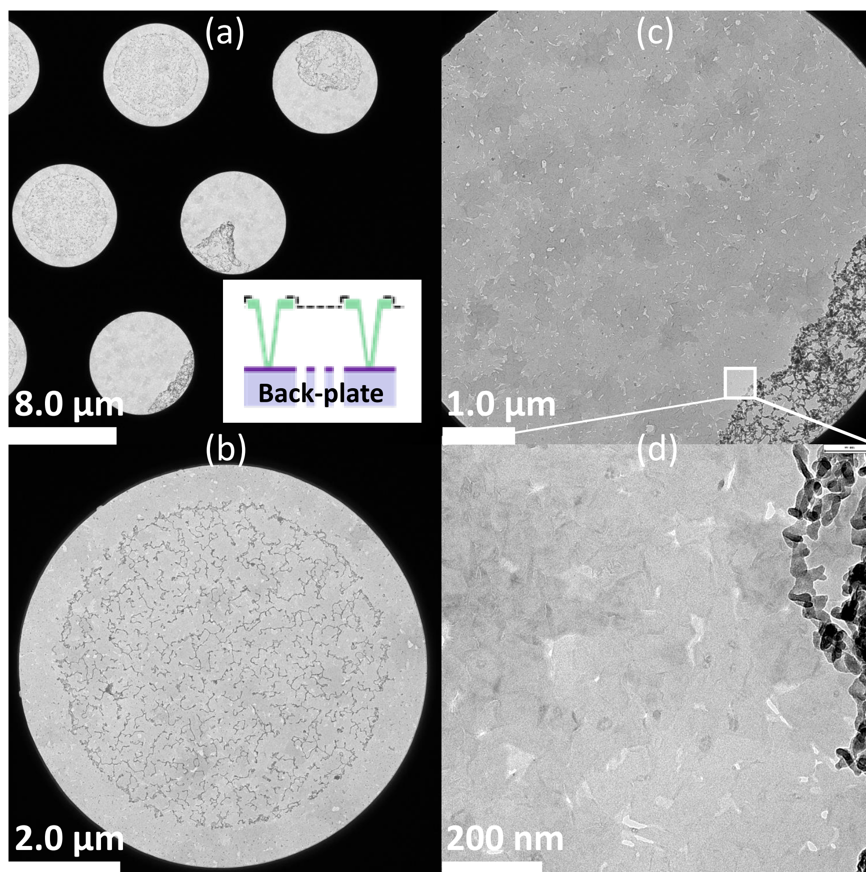

Figure 6.12: **TEM inspection of membrane residuals after fabrication.**The images are captured using a 120 kV Jeol JEM-1400 Plus TEM, paired with a TVIPS TemCam-XF416 camera. (a) The inspected brighter area is suspended over a region with no back-plate, corresponding to the venting holes, as shown in the inset cross-sectional view. The pattern of residuals follows a similar distribution to that in (b), where residuals are concentrated in the central area with a radius smaller than the entire venting holes region. Beyond this inner area, the membrane appears free of residuals within the detection limits of the microscope. (b) A typical residual pattern is one in which residuals are confined to the center, with the outer membrane remaining clear of residuals. (c) In this image, the previous residual pattern is absent. Instead, residuals are folded to one side, resulting in increased density in that region, suggesting that residuals have gathered and folded down. (d) A clearer distinction between the densely folded residuals and the clean membrane area is visible. The brightest spots indicate membrane holes, while the darker areas correspond to regions with different thicknesses of the multi-layer graphene (ML-gr) as discussed in previous chapters.

cient to entirely eliminate them, as many areas show undissolved residues that appear to have been mechanically removed instead. This suggests that more rigorous agitation and rinsing methods might improve PR removal. Further investigation is required to confirm this action and confirm if these residues are indeed PR. Additionally, from these images, particularly Figure 6.12c and Figure 6.12d, it is again clear that the thickness of the ML-gr varies across its surface due to different contrasts. From Figure 6.12c, it is evident that the transfer-free method results in a lower density of holes with smaller diameters than the transfer method, as shown in Figure 2.6.

Raman spectroscopy using a red laser was employed to verify the quality of the ML-graphene (ML-gr) after all fabrication steps. The red laser is generally more sensitive to detecting defects in graphene, often producing a higher I_D compared to the green laser, which was mostly used in previous chapters. Inspections were performed on 4× drums from four random chips to capture potential variations across the wafers with a higher chance of accuracy. Each plot in Figure 6.13 represents an average of three consecutive measurements taken at the same points, corresponding to the suspended ML-gr over the venting holes, as illustrated by the miniature images included with each plot (Figure 6.13). It was observed that performing Raman spectroscopy on ML-gr after Mo etching, when placed on a thick TEOS layer ($t = 4\,\mu m$) or suspended over the cavity on top of the back-plate (after TEOS etching), does not yield correct measurements.

The incorrect Raman spectra observed when graphene is on a thick TEOS layer or over a thick closed cavity are likely due to optical interference effects caused by the multi-layer structure of the substrate. The thick TEOS layer might induce multiple reflections of the incident laser and the scattered Raman signal, resulting in constructive and destructive interference that distorts the graphene's signal.

Furthermore, the substrate's thickness could also affect the laser focus, leading to a Raman signal dominated by the substrate rather than the graphene itself. Accurate spectra are found to be correct when the TEOS layer is thinner or when the graphene is suspended over an open cavity, as these conditions minimize interference effects and allow proper laser focus on the graphene.

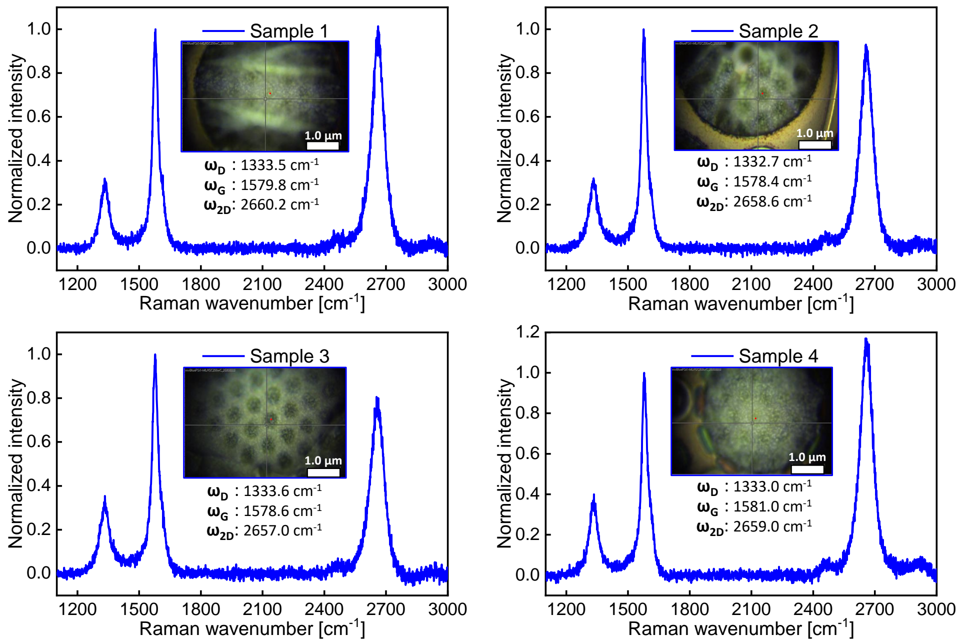

Figure 6.13: **Raman Spectroscopy of suspended ML-gr in the MEMS condenser microphones.** Raman spectroscopy plots of suspended ML-gr obtained using a Renishaw inVia Reflex spectrometer equipped with a He-Ne laser (λ = 633 nm) and a 100× objective. In each plot, the inset images show the red laser beam illuminating the inspected area, corresponding to the suspended membrane region over the venting holes, where no back-plate is present. Across the inspected areas, no significant changes or variations in Raman signal were observed, even when the focus was adjusted. The inset images also reveal slight membrane irregularities in areas where the membrane is not perfectly flat, which does not significantly affect the spectroscopy results.

Therefore, measurements were taken by focusing on areas corresponding to the venting holes. From the four plots in Figure 6.13, the I_{2D}/I_G ratios range from 0.86 to 1.25, while the I_D/I_G ratios range from 0.3 to 0.37. The FWHM of the 2D peak is between 65.22 cm^{-1} and 68.0 cm^{-1}. These values are consistent with findings from the previous chapter, reaffirming the graphene's turbostratic nature [16–20].

6.3.2. ELECTRICAL CHARACTERIZATION

The devices were characterized using an Precision Semiconductor Parameter Analyzer (Agilent 4156C) and Impedance Analyzer (Agilent 4294A) to assess their electrical functionality. Initial assessments were performed prior to the lift-off step, as shown in Figure 6.8 (Step 6 including opened vias to the back-plate) performing a $R_{\text{two-points}}$ measurements. At this stage, two electrodes on the back-plate were contacted using a probe station (Case 2), and these measurements revealed a an $V_{DC} - I_{DC}$ ohmic behavior that reached the threshold current of I_{DC} = 30 mA starting from V_{DC} = 2.5 V. After the lift-off step, Vapor HF and dicing, the same $V_{DC} - I_{DC}$ measurements were repeated. Even at very low voltages, high current limits of $I_{DC} = \pm 30$ mA were observed (Case 1). This can be explained by the fact that once the probes electrically contact it, silicon shows higher

contact resistance R_c due to a native oxide layer on its surface, further reducing the effective conductivity. To further investigate the insulation layer's functionality in preventing future short circuits in the event of membrane collapse onto the back-plate, additional two-point resistance measurements were performed as in Case 3 (Figure 6.14a). These measurements were taken between the Cr/Au pad on the back-plate and the surface of the back-plate itself, specifically contacting the a-SiC silicon device layer at the broken ML-gr drum location marked by the black circle in Figure 6.14a. In this case, unlike Case 1 or Case 2, at $V_{DC} = 2\,V$, the current was $I_{DC} = 25\,\mu A$, which is about $\approx 10000\times$ lower. This result confirmed the effectiveness of the insulation layer in maintaining electrical separation. Moreover, for this type of capacitor, the current magnitude should typically be in the pF range for very low leakages. This also helps minimize parasitic capacitance, resulting in a device with an improved final SNR. Further investigation should be conducted to quantify and evaluate the dielectric properties of the proposed a-SiC material. Once the electrical path of the back-plate have been verified in Figure 6.14a (case 1, 2), the capacitance measurements were performed accordingly with Chapter 4. They were performed on four different devices, as shown in the in Figure 6.14b in the four edge-different colors images, named as Design A, Design B, Design C and Design D. These four designs are related to the array configuration explained in Figure 6.1c, Figure 6.2, and Figure 6.3. More particularly Design A, C have a different ML-gr clamping as mentioned before. As it is possible to see from the miniature image in Figure 6.11, the clamping has several springs. Also Design B has only 6× a-SiC supports anchored to the back-plate and they have larger ML-gr drums with $R = 40\,\mu m$ different from $R = 35\,\mu m$ of Design A, Design C. Design C, finally has no additional a-SiC support connected to the back-plate and in this case the a-SiC is only anchored to the TEOS in correspondence of the Cr/Au ring electrode.

A simple schematic description of the discussed devices is provided in Table 6.1. The single-cell device (Design A, single-cell, 7× ML-gr) exhibited a base capacitance C_0 approximately five times lower than that of the array (Design A, array of seven-cells, 49× ML-gr) due to its reduced number of elements (Figure 6.14a). Notably, the $V_{pull\text{-}in}$ was not observed within the voltage range of $-20\,V < V_{bias} < 20\,V$ for the single-cell device that has 7× ML-gr (Figure 6.14a). In contrast, the array configuration showed a pull-in behaviour at approximately $V_{bias} > 10\,V$ (Figure 6.14a).

This difference can be attributed to the array's inclusion of 49× ML-gr drums, which increases the chance of having membrane collapses compared to the use of one single cell (7× ML-gr). This observation highlights a key challenge: while array configurations yield higher fabrication throughput, achieving uniform characteristics across all membranes

6

Table 6.1: Description of the measured devices.

Type	No. of ML-gr drums	Type of clamping	ML-gr radius
Design A (single-cell)	7	spring	35 µm
Design A (array)	49	spring	35 µm
Design B (single-cell)	7	full-clamped	40 µm
Design C (array)	49	spring	35 µm

remains difficult. Furthermore, it is important to highlight that, due to time constraints, extensive statistical analyses have not been conducted to more accurately assess this trend.

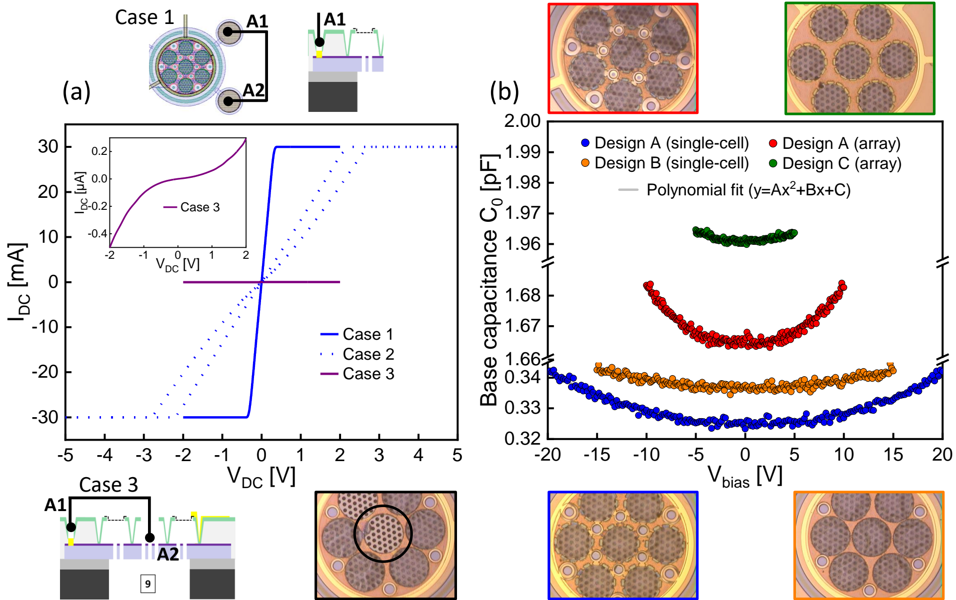

Figure 6.14: **Preliminary electrical characterization of completed devices.** (a) $I_{DC} - V_{DC}$ two-point resistance measurements are presented for three cases involving a device before and after lift-off with vapor HF treatment (finished).
In Case 1, the resistance is measured on a fully fabricated device (after lift-off and Vapor HF) between two contact points (Cr/Au) on the back-plate that connect the entire array. The current threshold for this measurement was set to ±30 mA, and the curve shows a correct Ohmic behavior. Case 2 describes the same measurement as in Case 1, but performed before the lift-off process, where the probes directly interact with the exposed silicon of the device layer without the Cr/Au metalization. Case 3 involves a two-point resistance measurement between the back-plate contact (A1 with Cr/Au) and A2, which is placed directly on the a-SiC layer, used as an insulating layer on top of the device layer. In this case, the multilayer graphene (ML-gr) has been manually broken in the measurement area. The plot for Case 3 reveals a resistance more than two orders of magnitude higher compared to the other cases, highlighting the insulating behavior of the a-SiC layer. However, a small current of $I_{DC} \approx 0.5\,\mu A$ is still detected, indicating that the a-SiC layer does not act as a perfect insulator. For fully insulated layers, currents in the order of ≈ pA were typically measured in Chapter 4. (b) The $C_0 - V_{bias}$ measurements were obtained from 4× chips, each representing three different design cases. These measurements were taken after the Vapor HF process to ensure the membranes were fully released. For Design A, which incorporates the trampoline clamping concept (as illustrated in Figure 6.1c, Figure 6.2b, c and Figure 6.4 (with only the difference of trampoline clamping), the results show that a single test cell with a membrane diameter of $R = 35\,\mu m$ exhibited a $C_0 = 0.324\,pF$. In contrast, the array structure for the same design demonstrated a significantly higher $C_0 = 1.665\,pF$, which can be attributed to the increased capacitance resulting from the array's geometry. Design B (single-cell structure), showed a C_0 value of $C_0 = 0.337\,pF$. Meanwhile, Design C, characterized by an array structure, exhibited $C_0 = 1.961\,pF$. As discussed in Chapter 4, the nonlinear increase in C_0 at higher V_{bias} values can be explained by the decreasing distance between the membrane and the back-plate as the bias voltage increases.

6.3.3. ANALYSIS OF RESONANCE FREQUENCIES

Three drums with $R = 40\,\mu\text{m}$, belonging to Design B (Figure 6.14b,Table 6.2) are actuated electrostatically to study the frequency response over the range $f = 200\,\text{Hz} - 300\,\text{kHz}$. The resonance frequencies are expected to align with the lumped circuit results shown in Figure 6.7a, b taking into account that no PCB with soundport is involved in these measurements. These are performed in an atmospheric environment using a measurement system that includes a Moku:Pro, an LDV, and a probe station.
The principle of electrostatic actuation is outlined in the following Equation 6.7 and Equation 6.8.

$$\vec{F} = -\frac{V^2}{2}\frac{\partial C}{\partial x}\vec{\upsilon}_x \tag{6.7}$$

$$\vec{F} = -\frac{1}{2}\frac{\partial C}{\partial x}\cdot\left(V_{\text{DC}}^2 + \frac{1}{2}V_{\text{AC}}^2 + \frac{1}{2}V_{\text{AC}}^2\cos 2\omega t + 2V_{\text{DC}}\upsilon_{\text{ac}}\cos\omega t\right)\hat{\upsilon}_x \tag{6.8}$$

A DC bias voltage is essential for generating the force that excites the resonator at the frequency of the AC drive voltage. The electrostatic force is observed to have components at zero frequency, at ω, and at 2ω, when the AC excitation voltage operates at a frequency ω . To achieve excitation specifically at ω, the amplitude of the DC voltage must generally be greater than that of the AC voltage where $V = V_{\text{AC}} + V_{\text{DC}}(V_{\text{DC}} >> V_{\text{AC}})$. Furthermore, as shown in Equation 6.8, the DC voltage plays a critical role in significantly amplifying the excitation strength. For these experiments, a $V_{\text{AC}} = 450\,\text{mV}$ was applied. Based on Equation 6.8, it is evident that the actuation occurs at the driving frequency ω. Lower V_{AC} values were tested; however, the resulting signal was too noisy.

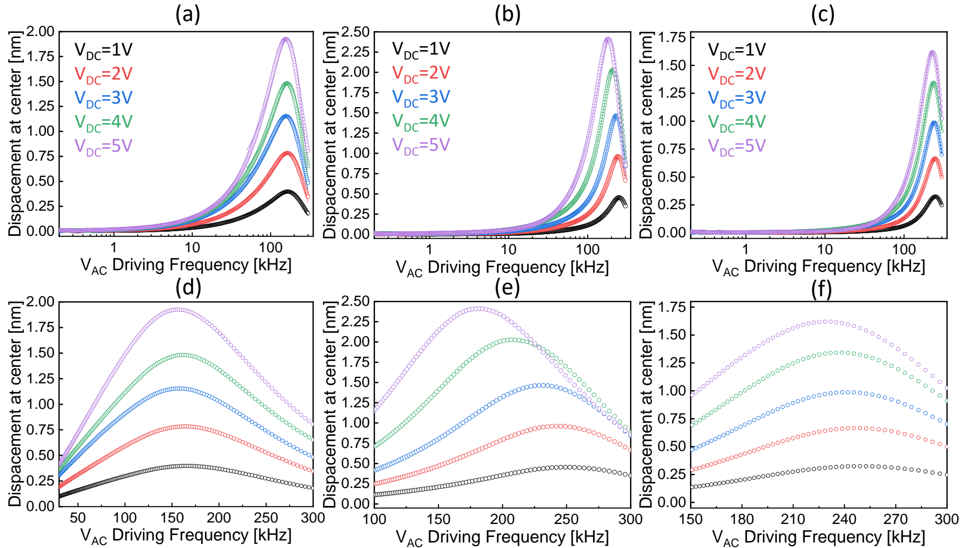

Figure 6.15: **Resonance frequency under electrostatic actuation at atmospheric pressure.** The resonance frequency measurements were performed on three different membranes, corresponding to Design B. These measurements were conducted using an LDV combined with $V_{\text{AC}} + V_{\text{bias}}$ electrical actuation across the device electrodes (top and bottom). All tests were carried out under atmospheric conditions.

The first drum exhibits a decrease in resonance frequency from f_{01} = 172 kHz to f_{01} = 166 kHz, the second drum from f_{01} = 249.9 kHz to f_{01} = 186.2 kHz, and the last drum from f_{01} = 249.2 kHz to f_{01} = 228.8 kHz when comparing V_{DC} = 1 V to V_{DC} = 5 V. The second drum showed the highest resonance frequency shift, with a softening of approximately 25.49%, compared to less than 10% for both Drum 1 and Drum 3. The discrepancy between the three sample is likely caused by variations in the distance between the graphene membrane and the back-plate, and in pre-tensions.
It is important to highlight that the measurements reported by the LDV in Figure 6.15 and Table 6.2 are not observed when the laser is focused on the a-SiC clamping, confirming that the obtained frequencies are related to the graphene drums.

Table 6.2: Overview of the measured devices.

Drum 1	V_{DC}	f_{01}	Drum 2	V_{DC}	f_{01}	Drum 3	V_{DC}	f_{01}
Design B	1V	172.0	Design B	1V	249.9	Design B	1V	249.2
Design B	2V	170.4	Design B	2V	241.8	Design B	2V	247.2
Design B	3V	164.2	Design B	3V	229.0	Design B	3V	241.5
Design B	4V	168.5	Design B	4V	208.6	Design B	4V	236.7
Design B	5V	166.0	Design B	5V	186.2	Design B	5V	228.8

When these results are compared with the lumped element simulations of Figure 6.7 a discrepancy in resonance frequency is evident taking also in account the difference in membrane radius of both samples (Figure 6.7 $R = 35\,\mu\text{m}$, Figure 6.15 $R = 40\,\mu\text{m}$). Keeping same pre-tension, considering the variation of 14.29% between both radius, the resonance frequency should decrease to f_{01} = 147.43 kHz. This value is still higher that the resonance frequencies reported in Figure 6.7.
This discrepancy is expected to be related to the fact that, in the lumped simulations (Figure 6.7), the resonance frequencies shown correspond to the resonance frequency resulting from the interaction between the sound port and the Bosch cavity (Block 2 of Figure 6.6). To verify this, following the involved parameters as port hole of radius $R = 75\,\mu\text{m}$ and a thickness of $t = 250\,\mu\text{m}$, along with a Bosch opening with a radius $R = 190\,\mu\text{m}$ and height $t = 400\,\mu\text{m}$, the helmholtz resonance is estimated considering $f_{01} = \frac{1}{2\pi\sqrt{LC}}$. This resonance frequency aligns with the simulated ones of Figure 6.7, confirming the reported difference.
Referring to Figure 6.7b, with $n_0 = 0.002\,\text{N/m}$, the damped resonance frequencies of the membrane ($f_{01} < 71.31$ kHz) can be observed along with the resonance peak of Block 2.
It is important to note that such a small port-hole size can significantly affect the SNR of the device by introducing high noise. While this effect has not been analyzed in this thesis, alternative sound port sizes could potentially be used, although they were not investigated in this work.
Excluding Block 2, the lumped element circuit simulations were repeated using the same methodology as before. This time, considering Design 2 (Table 6.1), a radius $R = 40\,\mu\text{m}$ was used. The resonance frequencies summarized in Table 6.2 align with the experimental simulation results according with Figure 6.3 method for V_{bias} = 1 V, using pre-tension values of $n_0 = 0.016\,\text{N/m}$, and $n_0 = 0.024\,\text{N/m}$. In particular, these pretension values dif-

fer by 20% from the estimated original value of $n_0 = 0.02$N/m, which was derived from the experimental results in Chapter 4.

Two non-spring-clamping Design A drums ($R = 35$µm) were actuated using piezo-shaking at low pressure to evaluate the pre-tension n_0 minimizing any damping effect. The pre-tension calculated from the resonance frequencies measured at low-pressure in Figure 6.16a, b are $n_0 = 0.0147$N/m and $n_0 = 0.0161$N/m. These values result to be close within the range of pre-tension extracted by the electrostatic actuation and lumped element simulations where back-plate and air-loading effects were taken into account.

However, we still observe very low pre-tension and varying resonance frequencies, even though both membranes belong to the same chip.

Furthermore, unlike the the results in Figure 6.15, which were based on single-point LDV, the measurements in Figure 6.16 were performed using an MSA-400. This system allowed for laser-mapped scanning, enabling visualization of the entire mode shape of the single membrane. Within this sample of Design A used for Figure 6.16a, b, a higher peak was found at $f_{01} = 732.1$ kHz. In correspondence of this peak, the entire structure showed a typical first mode shape displacement. This resonance is expected to be associated with the silicon back-plate, which, being anchored to the clamping layer of a-SiC, causes the entire structure to move.

Finally, eight drums were acoustically actuated, as described in Chapters 3 and 4, to quantify their mechanical compliance. None of the membranes exhibited resonance behavior within the $f = 10$ Hz – 10000 Hz frequency range, with mechanical compliance values ranging from 4.5 nm to 16.2 nm, respectively, under 1 kHz and 1 Pa. These results demonstrate improvements over those reported in Chapter 4, particularly by addressing the limited frequency bandwidth of earlier samples. This was achieved through the adoption of smaller membrane sizes and an improved backplate design. However, the membranes continue to exhibit pre-tension values comparable to those shown in Figure 6.7a (9 nmPa^{-1}), despite some variations observed between chips and samples, as previously reported.

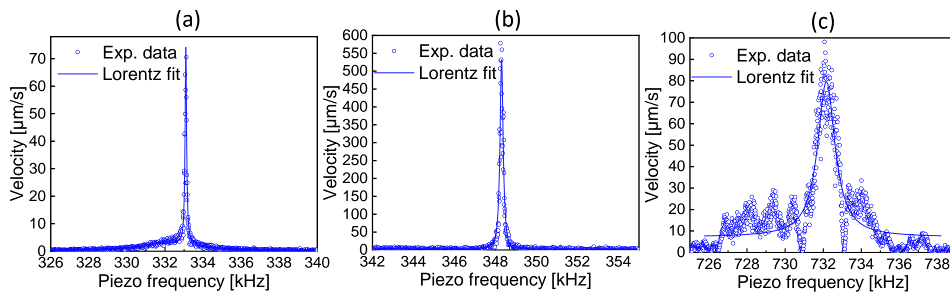

Figure 6.16: **Resonance frequency under piezo-shaker actuation at low-pressure.** (a) and (b) display the measured resonance frequencies of two drums within the same cell, each with a radius of $R = 35$µm. In contrast, (c) shows the resonance frequency of the entire structure. These measurements were performed at low frequencies using piezo-shaker actuation. For the first two peaks, (a) and (b), the membrane vibrations were visually detected using the MSA-400 system, capturing the first mode shape of only the drum areas. (c) The first mode corresponds to the entire cell geometry.

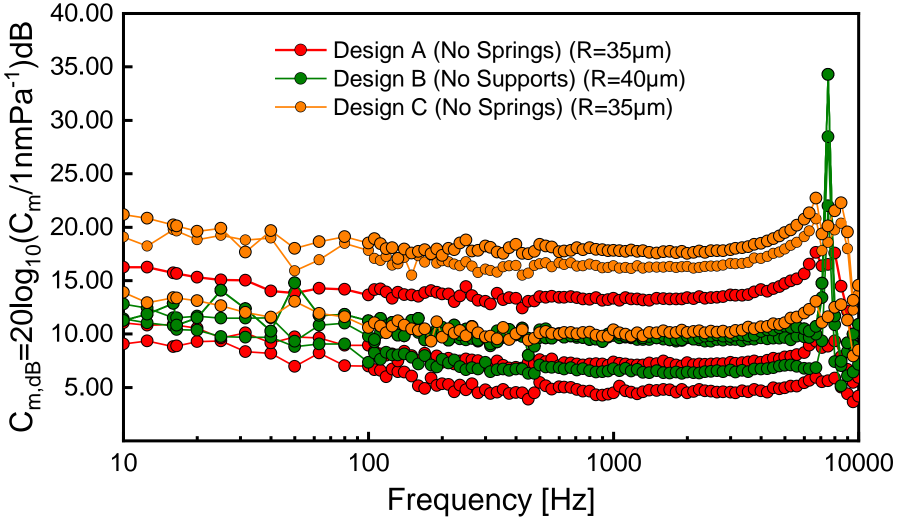

Figure 6.17: **Mechanical sensitivity at** 1 Pa **in** 10 – 10000 Hz**.** The results illustrate the mechanical compliance of eight drums with $R = 35\,\mu\text{m}$ and $R = 40\,\mu\text{m}$, from three different chips, measured using the methodologies detailed in Chapters 3 and 4. Unlike the low-pass behavior described in Chapter 4, the proposed optimized design with an improved backplate and smaller membrane size—achieves a targeted flat response within the desired frequency bandwidth. As explained in the earlier chapters, the resonance frequencies observed in the three samples are associated with the acoustic resonance of the measurement chamber used for this type of analysis. Variations in compliance among the samples may stem from slight differences in the pre-tension of the membranes. Each measurement represents the average of four repeated measurements per chip, ensuring precise system calibration and eliminating potential pressure leakage.

6.4. CONCLUSION

This final experimental chapter has demonstrated the feasibility of achieving flat mechanical compliance across the frequency range of $f = 10\,\text{Hz} - 10000\,\text{Hz}$, with significantly high mechanical compliance values (16.2 nmPa^{-1}) for small drums with a radius of $R = 35\,\mu\text{m}$. These membranes have also been successfully integrated into a capacitive architecture, making them suitable for full system-in-package integration. Notably, despite variations in pre-tension from drum to drum, the experimental results closely align with simulations based on lumped element circuit modeling. This alignment provides an initial validation for modeling membranes composed of Mo-based multi-layer graphene fabricated using a transfer-free process.

The newly developed concept and process flow have achieved a high fabrication yield, demonstrating a robust and reliable manufacturing approach. However, achieving uniform pre-tension and flat topogrpahy across drums remains a significant challenge for this type of material within this process flow. Additionally, as expected, the reduced drum size has resulted in higher pull-in voltages, with $V_{\text{bias}} > 20\,\text{V}$. These findings underscore both the potential and the challenges associated with this material system and design approach.

REFERENCES

[1] S. A. Zawawi, A. A. Hamzah, B. Y. Majlis, and F. Mohd-Yasin, *A review of mems capacitive microphones,* Micromachines **11**, 484 (2020).

[2] L. Beranek and T. Mellow, *Acoustic components,* in *Acoustics: Sound Fields, Transducers and Vibration* (Elsevier, 2019) pp. 143–229.

[3] T. Veijola, *Analytic damping model for an mem perforation cell,* Microfluidics and Nanofluidics **2**, 249 (2006).

[4] S. Anzinger, H. S. Wasisto, A. Basavanna, M. Fueldner, and A. Dehé, *Non-linear behavioral modeling of capacitive MEMS microphones,* in *2023 IEEE 36th International Conference on Micro Electro Mechanical Systems (MEMS)* (IEEE, 2023).

[5] A. Dehe and M. Fueldner, *Micromechanical sensors and methods of manufacturing same,* (2006), uS 2006/0141656 A1.

[6] J. Esteves, L. Rufer, D. Ekeom, and S. Basrour, *Lumped-parameters equivalent circuit for condenser microphones modeling,* The Journal of the Acoustical Society of America **142**, 2121 (2017).

[7] P. Hammond, *Vapor-phase etch processes for silicon mems,* in *Handbook of Silicon Based MEMS Materials and Technologies* (Elsevier, 2020) p. 519–530.

[8] J. Mo, S. Shankar, R. Pezone, G. Zhang, and S. Vollebregt, *A high aspect ratio surface micromachined accelerometer based on a sic-cnt composite material,* Microsystems amp; Nanoengineering **10** (2024), 10.1038/s41378-024-00672-x.

[9] P. Malcovati, M. Grassi, and A. Baschirotto, *Interface circuits for mems microphones,* in *Nyquist AD Converters, Sensor Interfaces, and Robustness* (Springer New York, 2012) p. 149–174.

[10] J. Abraham, H. Sanjeev, and K. Nisarga, *Design and analysis of high sensitivity mems microphone,* in *Advances in Micro and Nano Manufacturing and Surface Engineering* (Springer Nature Singapore, 2022) p. 107–118.

[11] G. Nicollini and D. Devecchi, *Mems capacitive microphones: Acoustical, electrical, and hidden thermal-related issues,* IEEE Sensors Journal **18**, 5386–5394 (2018).

[12] S. Anzinger, C. Bretthauer, H. S. Wasisto, and A. Dehé, *Dual-backplate cmuts with wide bandwidth and low driving voltage for airborne applications,* IEEE Transactions on Ultrasonics, Ferroelectrics, and Frequency Control **70**, 1286–1294 (2023).

[13] S. Anzinger, A. Fusco, D. Tumpold, C. Bretthauer, and A. Dehe, *Modeling of dual-backplate based airborne cmuts with enhanced bandwidth,* in *2020 IEEE International Ultrasonics Symposium (IUS)* (IEEE, 2020) p. 1–4.

[14] M. P. F. Wopereis, N. Bouman, S. Dutta, P. G. Steeneken, F. Alijani, and G. J. Verbiest, *Tuning dissipation dilution in 2d material resonators by mems-induced tension,* Journal of Applied Physics **136** (2024), 10.1063/5.0203122.

[15] F. Ricciardella, S. Vollebregt, T. Polichetti, M. Miscuglio, B. Alfano, M. L. Miglietta, E. Massera, G. D. Francia, and P. M. Sarro, *Effects of graphene defects on gas sensing properties towards NO2 detection,* Nanoscale **9**, 6085 (2017).

[16] S. Vollebregt, B. Alfano, F. Ricciardella, A. Giesbers, Y. Grachova, H. Van Zeijl, T. Polichetti, and P. M. Sarro, *A transfer-free wafer-scale cvd graphene fabrication process for mems/nems sensors,* in *2016 IEEE 29th International Conference on Micro Electro Mechanical Systems (MEMS)* (IEEE, 2016) pp. 17–20.

[17] S. Vollebregt, B. Alfano, F. Ricciardella, A. J. M. Giesbers, Y. Grachova, H. W. van Zeijl, T. Polichetti, and P. M. Sarro, *A transfer-free wafer-scale CVD graphene fabrication process for MEMS/NEMS sensors,* in *2016 IEEE 29th International Conference on Micro Electro Mechanical Systems (MEMS)* (IEEE, 2016).

[18] S. Vollebregt, R. J. Dolleman, H. S. J. van der Zant, P. G. Steeneken, and P. M. Sarro, *Suspended graphene beams with tunable gap for squeeze-film pressure sensing,* in *2017 19th International Conference on Solid-State Sensors, Actuators and Microsystems (TRANSDUCERS)* (IEEE, 2017).

[19] S. Vollebregt, B. Alfano, F. Ricciardella, A. J. M. Giesbers, Y. Grachova, H. W. van Zeijl, T. Polichetti, and P. M. Sarro, *A transfer-free wafer-scale cvd graphene fabrication process for mems/nems sensors,* in *2016 IEEE 29th International Conference on Micro Electro Mechanical Systems (MEMS)* (IEEE, 2016).

[20] N. B. Babaroud, M. Palmar, A. I. Velea, C. Coletti, S. Weingärtner, F. Vos, W. A. Serdijn, S. Vollebregt, and V. Giagka, *Multilayer CVD graphene electrodes using a transfer-free process for the next generation of optically transparent and MRI-compatible neural interfaces,* Microsystems & Nanoengineering **8** (2022), 10.1038/s41378-022-00430-x.

7

CONCLUSIONS AND RECOMMENDATIONS

7.1. CONCLUSIONS

THIS thesis significantly advances multi-layer graphene integration in MEMS microphones, focusing on scalable, wafer-level fabrication methods. Various process flows were developed, emphasizing a transfer-free approach to multi-layer graphene synthesis.

The work begins by exploring materials compatible with transfer-free methods to achieve graphene quality that matches or exceeds previously established benchmarks for Mo-based graphene. From a technological perspective, the research addresses the challenge of bridging industrial scalability with reliable device fabrication by proposing tailored process flows for different suspended graphene architectures. These developments align with existing manufacturing processes and enable the design of novel device configurations, expanding the potential applications of graphene beyond microphone applications.

The benefits and limitations of multi-layer graphene integration in MEMS microphones are analyzed through experimental studies and validated using analytical and finite element modeling, creating a robust framework for optimizing graphene's role in this application.

Below is a summary of the key points presented in the various chapters.

- **Chapter 2**: SiN_x, AlO_x, and a-SiC were investigated as clamping support and etch mask layers for compatible transfer-free graphene integration. SiN_x was found to be compatible with transfer-free methods, demonstrating multi-layer graphene quality comparable to the SiO_2-based Mo benchmark without significant differences. Raman spectroscopy on multiple devices and wafer-scale electrical characterization of sheet resistance (R_{sheet}) were employed as comparative metrics. Etch selectivity from 1:25 of SiN with respect to SiO_2 was experimentally observed when etching in VHF from 1:25 to 1:30 was experimentally observed for not patterned samples between silicon-rich SiN_x and thermal SiO_2 to Vapor HF, confirming its suitability for future process flows.
  PECVD a-SiC proved incompatible with Mo transfer-free methods, exhibiting delamination in non-annealed a-SiC and diffusion in annealed a-SiC after CVD growth, rendering the Si/PECVD a-SiC/Mo stack unsuitable. In contrast, LPCVD a-SiC was found to be compatible with the Mo-based transfer-free method (incorporating a thermal SiO_2 layer), producing Raman peaks of multi-layer graphene comparable to those observed with SiN_x and SiO_2 substrates.
  For AlO_x, two approaches were investigated using unannealed and annealed ALD AlO_x on SiO_2 layers. The ML-gr thicknesses were $t < 2$ nm (not-annealed) and $t < 5$ nm (annealed), making them thinner than those grown on SiO_2 , SiN_x , or a-SiC stacks ($t > 5$ nm). These findings indicate that using AlO_x as a substrate in a SiO_2/AlO_x/Mo stack results in thinner graphene compared to other substrates. However, the graphene quality on unannealed AlO_x was significantly inferior to that achieved with SiO_2, SiN_x , or a-SiC substrates.

- **Chapter 3**: a process for fabricating large free-standing graphene membranes on silicon wafers was developed, the structural and the acoustic properties of the membrane were assesed. Thermal SiO_2 was used as a sacrificial layer, with SiN_x

7

providing clamping support and etching protection. Small membranes ($2R = 85 - 155\,\mu m$) maintained a 100 % yield, while larger ones ($2R = 300 - 350\,\mu m$) saw their yield decrease from 37 % (after bulk silicon BOSCH etching) to 18 % after Vapor HF (sacrificial release).
Raman spectroscopy showed shifts in ω_G from 1582.1 cm^{-1} to 1574.1 cm^{-1} and in ω_{2D} from 2696.3 cm^{-1} to 2682.8 cm^{-1} (before and after VHF SiO_2 removal, indicating a possible strain relaxation. Mechanical analysis revealed fundamental frequencies between 156 kHz and 318 kHz for smaller membranes, 92 kHz for larger ones, with compliance ranging from 3-10 $nm\,Pa^{-1}$ for smaller membranes and 43-92 $nm\,Pa^{-1}$ for larger ones. These compliance magnitudes are higher than available literature data of commercial MEMS microphones, which usually have a compliance of a few $nm\,Pa^{-1}$. Also, the ML-gr diaphragm areas are just one-tenth diamter of those in MEMS devices.

- **Chapter 4**: it explores the integration of multi-layer graphene membranes into MEMS microphones, focusing on their performance in capacitive architectures for electrical read-out. The impact of multi-layer graphene on key performance metrics such as sensitivity and pull-in voltage was investigated.
  Yield was found to be influenced by variations in backplate diameters, and devices smaller than $2R = 180\,\mu m$ were excluded due to micro-loading issues and incomplete DRIE processing. An initial yield of 80 % was observed for devices with backplate diameters between $2R = 180\,\mu m$ and $2R = 280\,\mu m$, though challenges in etching steps affected some chips. Trampoline and full-clamped devices achieved yields of 70 % and 18 % for 24 and 87 devices, respectively. Resonance frequencies were above the audible range ($f_{01} > 20\,kHz$) under low-pressure conditions (1×10^{-3} mbar).
  Mechanical displacements for the inspected design geometries A, B, and C were 1.07 μm, 0.081 μm, and 0.56 μm, respectively under 1 kHz with 1 Pa actuation. Because of the high mechanical compliances the frequency flat responses were limited to $f < 1.5\,kHz$ (Geom. A), $f < 0.94\,kHz$ (Geom. B) and $f < 0.62\,kHz$ (Geom. C) highlighting the need for an improved sensor design. Pull-in voltages ranged from $V_{pull\text{-}in} = 2 - 9.5\,V$, making the devices suitable for sensitivity tuning by V_{bias} molulation with ASIC integration. Despite limited acoustic bandwidth due to the high mechanical compliance and not optimized counter electrode design, the estimated calculated sensitivities were of up to $S_{1kHz} = 24.3 - 321\,mV\,Pa^{-1}$.

- **Chapter 5**: It has been found that increasing the pressure significantly reduces the resonance frequency of graphene membranes resonance frequency. This phenomenon has not previously observed experimentally in different gases (Air-He) but well-studied in fluid-structure interactions. This effect, termed "air-loading," increases the membrane's effective mass density by a factor of $1 + \beta$, and it also results in a pressure-dependent resonance frequency effect, which is especially strong in ultra-thin membranes liek graphene. To validate the hypothesis that air-loading reduces resonance frequency, both analytical models and Comsol results were used, showing strong agreement in air and helium environments. This confirmed that the observed reduction in resonance frequency (by more than a factor

2 compared to the vacuum value) is due to the significant increase in effective mass from air-loading at atmospheric pressure.
The study models the impact of air-loading on graphene microphone performance, estimating its effect on sensitivity and frequency bandwidth. The findings reveal that while reducing membrane thickness improves sensitivity, air-loading limits further gains beyond a certain point. Additionally, the relationship between membrane radius and performance is not straightforward, requiring optimization of parameters like linearity, bandwidth, capacitance, electrical sensitivity, and pull-in voltage. It offers critical equations to guide the optimization of microphone graphene membranes, balancing performance with practical constraints to approach theoretical limits.

- **Chapter 6:** This final experimental chapter demonstrated the feasibility of achieving flat mechanical compliance across the frequency range of $f = 10\,\text{Hz}-10\,000\,\text{Hz}$, with high mechanical compliance values (16.2 nmPa^{-1}) for small drums of radius $R = 35\,\mu\text{m}$. These membranes were successfully integrated into a capacitive architecture, making them suitable for full system-in-package integration. Despite drum-to-drum variations in pre-tension, experimental results closely matched simulations based on lumped element circuit modeling, validating the use of Mo-based multi-layer graphene membranes fabricated through a transfer-free process. The newly developed concept and process flow achieved a high fabrication yield, demonstrating a robust and reliable manufacturing approach. However, ensuring uniform pre-tension and flat topography across drums remains a key challenge for this material and process. Additionally, as anticipated, the reduced drum size led to higher pull-in voltages, with $V_{\text{bias}} > 20\,\text{V}$. These findings highlight both the promise and the challenges of this material system and design approach.

7.2. ANSWERS TO THE RESEARCH QUESTIONS

This thesis addresses four key research questions regarding developing graphene-based MEMS condenser microphones.

First, the feasibility of developing a microfabrication method potentially compatible with standard MEMS production lines has been investigated. Chapter 2 through Chapter 6 (excluding Chapter 5) present a process flow for integrating graphene membranes suspended over open and closed cavities. The successful wafer-level fabrication of these devices demonstrates the viability of this approach, confirming that graphene-based MEMS microphones can indeed be fabricated using existing MEMS production techniques.

The second question, concerning the suitability and performance of graphene as a diaphragm material, studied in Chapters 3, 4, and 6, showed that graphene offers higher sensitivity than traditional silicon-based diaphragms, even in miniaturized devices. However, challenges such as damping and air-loading effects, which are more significant in graphene due to its low mass, stress, and thickness, must be addressed to avoid bandwidth limitations. An optimized device design is proposed to balance these factors and target the performance benefits that graphene can offer, particularly in terms of mechanical compliance, dynamic range, and expected high SNR.

Regarding the third question, the maximum achievable mechanical compliance over a flat audible bandwidth of graphene-based microphones has been investigated through both analytical models and partial experimental studies. A particular focus is on the effects of air loading on graphene membranes. Although graphene membranes demonstrate high sensitivity and mechanical performance, achieving optimal performance requires integration with ASIC systems to handle the electrical output and further enhance SNR.

Finally, in response to the fourth question, a new device design has been proposed that aligns with state-of-the-art ASIC read-out systems and packaging technologies. Based on the thesis findings, this design aims to create a packaged demonstrator that can be benchmarked against current market products. The results suggest that graphene-based MEMS microphones can be fabricated and were partially characterized, offering promising potential for full integration and future product development.

7.3. RECOMMENDATIONS FOR FUTURE WORK

This work builds on existing studies that have explored the use of graphene in acoustic applications as MEMS-microphone, but the approach taken here has aimed to move beyond rudimentary demonstrations by providing a method capable of producing more reproducible and scalable results. Several key areas for future research have been identified, which, if explored, could significantly enhance the understanding and performance of graphene-based devices.

1. **Investigation of material defects and engineering consistency:** One of the remaining challenges in fabricating graphene membranes is ensuring consistency across batches, particularly in managing defects such as wrinkles, foldings, and stress concentrations. These imperfections can adversely affect the device's performance, particularly in applications requiring high precision and repeatability.

Further research should focus on minimizing these material defects, especially by optimizing the heterostructure and substrate to manage stress and improve overall uniformity.
The role of the Mo catalyst and the substrate in influencing the mechanical properties of the graphene post-release also warrants further exploration. As the monolithic growth of graphene occurs directly on the substrate in the method developed here, the substrate's characteristics will likely impact the membrane's final mechanical behavior. Future work could use advanced techniques such as Raman spectroscopy and AFM to map stress and identify the root causes of defect formation.
A better understanding of the edge anchoring and its influence on stress distribution across the membrane would also contribute to improved device performance.

2. **Role of residuals and porosity in ML-gr:** While the transfer-free method avoids the complications associated with polymer mediums, using PR during the process introduces the possibility of residuals being left on the graphene membrane. These residuals, even in small amounts, might affect the device's performance, especially for applications with suspended graphene. Future research should focus on optimizing the cleaning process to ensure minimal residual contamination and exploring how different PRs, solvents, and etching steps could influence the formation of residuals.
In addition, porosity and the random distribution of holes in the graphene membrane present challenges for future integration into devices. The present work observed that specific substrate configurations, particularly Si/SiO_2/AlO_x (not annealed)/Mo, resulted in fewer holes. Future research should investigate why this combination reduces hole formation and whether this understanding can be leveraged to prevent defects in other configurations. Developing hole-free graphene membranes will be essential for many sensing applications where the integrity of the diaphragm is critical.

3. **Influence of substrate and graphene thickness variations on performance:** The findings from this research have shown that specific substrate configurations significantly reduce defects in the graphene membrane.
For example, the Si/SiO_2/AlO_x/Mo configuration was particularly effective in minimizing the occurrence of holes. Furthermore, variations in substrate thickness were observed to have a significant effect on the material's properties. Future research should investigate how these variations influence the acoustic performance of the graphene diaphragm, particularly in terms of compliance, mechanical stiffness, and overall performance as a microphone diaphragm.
By systematically varying substrate thickness and material composition, it may be possible to uncover relationships between these factors and the graphene diaphragm's sensitivity and acoustic response. This could lead to optimized designs for MEMS microphones and other sensing applications.

4. **SNR, Bandwidth, Distortion:** In addition to material and fabrication considerations, further research is needed to assess the performance of graphene-based microphones in terms of distortion and SNR. The membrane used in this thesis

demonstrated notable improvements in SNR using optical measurement methods compared to traditional silicon-based MEMS microphones. However, to fully evaluate the potential of graphene membranes in commercial applications, it will be necessary to integrate the diaphragm with state-of-the-art ASICs and conduct comprehensive electro-acoustic measurements on a packaged device.
These future studies should aim to quantify improvements in SNR, dynamic range, and overall audio performance, taking into account real-world conditions and usage scenarios. Only by testing fully packaged devices will it be possible to draw definitive conclusions regarding the advantages of graphene membranes over conventional silicon-based alternatives in terms of microphone performance.

5. **Quantitative Study on Acoustic Performance and Device Packaging:** Finally, the research presented here highlights the importance of considering the relationship between diaphragm properties and device packaging. The acoustic performance of graphene-based microphones is influenced not only by the membrane itself but also by how the device is packaged. Future work should include a detailed quantitative study of the effect of packaging on device performance, including the choice of encapsulation materials, venting structures, and the influence of environmental factors such as temperature and humidity.
Further research into optimal packaging designs could help to minimize interference and maximize the acoustic performance of graphene membranes. Understanding how packaging influences the diaphragm's response to external stimuli will be crucial for developing commercial-grade graphene-based microphones.

This thesis has laid the foundation for using graphene in MEMS microphones and other potential sensor applications. Future research should focus on improving the reproducibility and scalability of the wafer-scale fabrication process, as well as understanding the impact of material defects and substrate interactions. Investigating the performance of graphene-based microphones in real-world applications, particularly in terms of SNR and dynamic range, will be essential to demonstrate their superiority over conventional technologies. Finally, extending the use of graphene to a broader range of sensors could unlock new possibilities in MEMS technology and beyond.

Acknowledgements

The PhD journey is often deeply personal, like a solitary path filled with goals, doubts, and small victories that only you may notice. Everyone experiences it differently, but what is common is that it can sometimes feel lonely. Thinking about this path without anyone around would have made everything much harder and sometimes demotivating, especially with all the milestones and difficulties along the way. It has been an intense journey where I have learned a lot.
I had the opportunity to work on something truly fascinating to me, starting from a simple sketch to real-fabricated devices, and even had the opportunity to measure them using state-of-the-art setups in an industry-leading laboratory. I feel lucky to have experienced this and I will never forget many steps in this journey.

This PhD would not have been possible without the support and encouragement of the many people who have shaped my growth and work over these years.

It feels like yesterday when I moved abroad and met **Sten**, who explained the project for my MSc thesis and previous internship. At that time I had no experience in microfabrication or nanofabrication and I didn't even know much about new nanomaterials like carbon nanotubes or graphene. From the first moment on, you gave me energy and motivation and there was never any pressure. I always appreciated how you presented the research and how you motivated new students.
The way you described the project back then really caught my attention and I could see your passion, your dedication, and your trust in my independence. That made a big difference in how I approached research afterward.
I believe that this is one of the most important aspects of any kind of work.
After finishing my MSc and starting a new job, I kept thinking that I wanted to do more research. The time I had spent in the cleanrooms and labs was too short. I knew I wanted more. I still remember when we stayed in touch and this PhD position was funded. I was genuinely excited and happy to have the chance to return to Delft and start working on this project. You helped whenever I needed it, gave me feedback on both scientific ideas and general things, and kept me motivated. I am grateful for the support you gave me, even when I had doubts about myself or what I was doing.
You made this work feel like a journey of discovery, something enjoyable to explore with freedom and trust. I never felt judged. Even when things got technical and difficult, you were always there, supportive, and smiling. Every researcher should feel free to explore with passion and curiosity.

Peter, as I have told you many times, I truly appreciate all the help you gave me. I still remember our first video call, when you mentioned that a PhD is not only about doing experiments, but also about writing. Over time, I came to fully understand how important that insight was.

Your technical guidance, especially in MEMS, helped me gain a deeper understanding of many aspects of the field. I also appreciated the care and precision you put into improving my work, particularly my writing. Despite your many students and responsibilities, you always responded to my emails, corrected my mistakes, and did so efficiently and on time. You consistently guided me with the clear intention of helping me grow. I always felt that your guidance helped me improve the quality of my work.

Lina, thank you for always supporting me and believing in what I was doing. You were always encouraging me and reminding me that I was doing well. I still remember when you saw me in the cleanroom during my final months and encouraged me to focus solely on writing so I could graduate on time. I know I didn't fully follow your advice, even though I probably could have, but I really wanted to see some of the devices completed. I knew I wouldn't get another chance to finish them.
Your leadership inspired me, not only scientifically, but also on a personal level.

I feel proud to have had the opportunity to collaborate with two leading experts in the MEMS field, **Hutomo Suryo** and **Sebastian** from Infineon Technologies, who are driving innovation and technological progress today. From the very beginning, you helped me gain an industry perspective on my work. It was truly inspiring to think not only with academic curiosity but also with a more concrete, application-oriented mindset. It was an honour to bring my samples to Munich, and I am very grateful for your collaborative spirit and for taking the time to measure many of my devices, both the successful ones and those that did not perform as expected. I sincerely appreciate your support and the opportunity to work with you. You are doing incredible and innovative work.

Well, **EKL**.
I cannot count how many hours I spent in these labs. It is incredible how the desire to see results drives you to spend entire days, fully covered in a lab suit, standing for hours. For most of us, I believe it comes down to one thing: passion. Passion for this field. Otherwise, I truly do not know how it would be possible.

Paolo and **Bruno**, you were two pillars during my PhD. Especially at the beginning, you helped me a lot by discussing microfabrication results and sharing insights about the field. You gave me good moments not only through your technical support, but also through your attitude. Luckily, you helped me find the fun side of pursuing this kind of journey. Without you, my PhD would have felt a lot heavier. From the "borraccia" to the "amaretto," and much more, thank you both for everything. Especially in the last year, I was constantly coming to your offices, messaging you in the late afternoon, or finding any possible way to ask for help in fixing tools and finishing my work. I really appreciate all your support.

Hande and **Francesco**, I remember that during the final period, I was always coming to your office and urging you to join me in the cleanroom. You gave me great energy to go to the lab during my last months. You helped me a lot in the cleanroom, and I truly appreciate it. But what I appreciated even more were all the times you made me laugh, both inside and outside the lab.

Dear **Mario**, I remember many late afternoons in the cleanroom when you helped

me fixing the machines so I could continue my work. I will never forget when we opened the Drytek together to look for my fallen wafer, which by some miracle was still alive. I appreciate all your support, the time you dedicated to me, and the stories you shared about how the cleanroom and work environment were in the past.

I also want to extend a big thank you to all the other team members, including **Johannes, Daniel, Robert, Koos, Juan, Tom, Silvana, Pieter, Dennis, Sara, Dylan, Jord, Joost**, and **Anastasia**. I know it is really tough to manage such labs. Sometimes people do not realize how challenging it can be to stay patient while working with inexperienced researchers, especially those who believe that completing a process simply means following the steps written down by a supervisor. Or the new researchers who constantly ask for help without first trying to solve problems on their own.

Thank you all for your patience and for making the lab a better place to work.

To my officemates, starting with **Chen**, we shared the office alone for a while, and I enjoyed listening to you talk about China, politics, and research. You were always very hardworking and focused.
Yaqian, I remember when you used to come to the office during your MSc. You were always very kind, and I am truly glad I got to know you as a friend, not just as someone I shared an office with.
Alireza and **Romina**, I had a great time with both of you, even outside the lab. I was happy to see how much you liked my cocktails. **Alireza**, oh my fre! I really enjoyed our conversations about football and old legends like Ronaldo. Those late afternoon chats with you, **Amir**, **Pratik**, and another great addition, **Mudassir Hussein**, always brought good vibes. You were always patient with my jokes and I really enjoyed spending time with you.
Thank you to **Joost** and **Shriya**. I always had a good time with you and I cannot forget **Shriya**'s way to laugh. You are very friendly.
Thank you also to **Milica** for all the nice memories shared between inside and outside the lab, and Japan.
Jiarui, thank you for the help with discussions about MEMS and measurements and also for being patient with some of my joke-questions.
Thank you, **Leandro** and **Nasim**. You both gave me very good suggestions on transfer-free graphene and processing. I really appreciate your help getting me started in the best way possible.
Aleksandar, thank you for your helpful suggestions on my process flow and for your kind feedback on my work.
Filip, thank you for all the times you helped me. I know that managing the lab is not easy, especially when users do not always behave properly or follow the rules.
Nikki and **Marian**, I truly appreciated how readily and quickly you were always there to help with anything I needed.
I also want to extend my thanks to all ECTM members and others I met and had discussions with throughout this journey. I hope I am not forgetting anyone. Thank you to **Leonardo, Paul, Joost, Elena, Pratik, Leo, Ghandika, Xinrui, Tawab, Maria, Nerea, Merlin, Tiance, Ahmed, Yaren, Javad, Ole, Shatavisha, Sjoerd, Bram, Nikhil, Tim, Adwait, Jinglin, Friso, Leiming, Zhengwei, Alireza, Mengying, Muhammed, Feyza, Weip-**

7

ing, Luutzen, Xiao, Keyvan, Jia-Jun, Yukun, Zichuan, and Zhenhua.

From the Mechanical Engineering department, I would like to thank many other researchers as well. **Gabriele**, we worked a lot together to set up the graphene microphone project, and I really enjoyed working with you. Thank you for helping me with the measurements and for giving me useful insights into mechanics and Python.
Maurits, I always saw a strong passion in you for research. I enjoyed spending time with you during the conferences.
Cas, you are a very cool guy, and you contributed a lot to a nice piece of work. **Curry**, I enjoyed our coffee breaks while I was working in the optics lab and also playing table tennis with you.
Andrea, I remember how we used to stop and talk about our research topics, both yours and mine, in the optics lab. I really liked your resonators.
Zichao, thank you for the Polytec support and for helping me with the laser writer and the most recent measurements on my last chips.
Ashwinraj, I still remember your expression whenever I walked into the lab to use the LinceeTec while you were busy with it.
Finally, I want to thank everyone who supported me and listened to my result comments during the Nanomechanics meetings, including **Gerard, Herre**, and the entire PME group.

To all the technicians I met from EKL, NEMO, PME, and beyond, thank you so much for all your support.
I also want to thank the cleanroom cleaning staff. Most of you will probably never read this, but I want to say thank you anyway. I often spoke with some of you, and through those conversations, I got to see and learn about another side of this environment.

During these years, I also shared a house with amazing people, especially **Udit** and **Tim**. I know I may have annoyed you at times, but I was truly happy to share that time with you. I learned a lot from both of you and grew along the way. You come from different backgrounds, each intense and full of meaning, and I deeply appreciated it, especially when you shared the personal sides of your stories.

To all my friends from my hometown, thank you for always being so funny and for bringing me so much joy.
A special thank you to **Pasquale**. Last years we shared a lot, and you know exactly what I mean when I say, "Solita postazione".
Francesca, thank you too. We met many times and began our Dutch journey together, thank you for all the fun moments we shared.
Maria Chiara, thank you for the many times I called you on my way home. We talked about anything and everything. You helped me unwind whenever I felt bored or tired, and that meant a lot to me.

To all my family, especially my dad, my mother, and my brother. This journey is entirely dedicated to you. You are, and always will be, my constant motivation. I owe everything to you, and I always will.

And finally, to **Racha**. You simply changed my life. I admire you. I respect you deeply.

I believe I am the only person who truly understands how you feel each day and what you carry inside. I see both your faces. Nothing stops you. You have faced and still face some of the hardest challenges a person can go through. Yet you always find the strength to smile more than anyone I know, never letting others see the struggle behind it. You have something rare. Despite everything, you radiate the best kind of energy. In getting to know you, I learned what love really is and what it can do. I will always be by your side, standing with you and supporting you, no matter what.
Ana Bhebbik.

List of Publications

Journal Papers

6. **R. Pezone**, G. Baglioni, P. M. Sarro, P. G. Steeneken, S. Vollebregt, *Sensitive Transfer-Free Wafer-Scale Graphene Microphones*, ACS Applied Materials & Interfaces **14, 18**, pp. 21705–21712 (2022).

5. **R. Pezone**, S. Anzinger, G. Baglioni, H. S. Wasisto, P. M. Sarro, P. G. Steeneken, S. Vollebregt, *Highly-sensitive wafer-scale transfer-free graphene MEMS condenser microphones*, Microsystems & Nanoengineering **10, 27**, pp. 1–9 (2024).

4. **R. Pezone**, G. Baglioni, C. van Ruiten, S. Anzinger, H. S. Wasisto, P. M. Sarro, P. G. Steeneken, S. Vollebregt, *Effect of air-loading on the performance limits of graphene microphones*, Applied Physics Letters **124, 12**, pp. 123503 (2024).

3. G. Baglioni, **R. Pezone**, S. Vollebregt, K. C. Zobenica, M. Spasenović, D. Todorovic, H. Liu, G. Verbiest, H. S. J. van der Zant, P. G. Steeneken, *Ultra-sensitive graphene membranes for microphone applications*, Nanoscale **15**, pp. 6343-6352 (2023).

2. J. Mo, S. Shankar, **R. Pezone**, G. Zhang, S. Vollebregt, *A high aspect ratio surface micromachined accelerometer based on a SiC-CNT composite material*, Microsystems & Nanoengineering **10, 42**, pp. 3–12 (2024).

1. P. G. Steeneken, M. Soikkeli, S. Arpiainen, A. Rantala, R. Jaaniso, **R. Pezone**, S. Vollebregt, S. Lukas, S. Kataria, M. A. Houmes, R. ´Alvarez-Diduk, K. Lee, H. S. Wasisto, S. Anzinger, M. Fueldner, G. J. Verbiest, F. Alijani, D. H. Shin, E. Malic, R. van Rijn, T. K. Nevanen, A. Centeno, A. Zurutuza, H. S.J. van der Zant, A. Merko¸ G. S. Duesberg, M. C. Lemme, *Towards wafer-scale 2D material sensors*, 2D Materials (Accepted Manuscript)(2023).

Conference Attendance and Proceedings

5. **R. Pezone**, G. Baglioni, P. M. Sarro, P. G. Steeneken, S. Vollebregt, *Wafer-Scale Transfer-Free Sensitive Graphene Microphones*, Graphene Week 2022, (Poster).

4. **R. Pezone**, G. Baglioni, P. M. Sarro, P. G. Steeneken, S. Vollebregt, *High-performance wafer-scale transfer-free graphene microphones*, 2023 IEEE 36th International Conference on Micro Electro Mechanical Systems (MEMS2023), (Oral).

3. **R. Pezone**, G. Baglioni, L. di Paola, P. M. Sarro, P. G. Steeneken, S. Vollebregt, *Wafer-scale Transfer-free Graphene MEMS Condenser Microphones*, 22nd International Conference on Solid-State Sensors, Actuators and Microsystems (TRANSDUCERS 2023), (Oral).

2. **R. Pezone**, G. Baglioni, P. M. Sarro, P. G. Steeneken, S. Vollebregt, *High aspect-ratio multi-layer graphene MEMS condenser microphones*, Graphene Week 2023, (Oral).

1. G. Baglioni, **R. Pezone**, S. Vollebregt, K. C. Zobenica, M. Spasenović, D. Todorovic, H. Liu, G. Verbiest, H. S. J. van der Zant, P. G. Steeneken, *Characterization of ultra-sensitive graphene*

membranes for microphone applications, Graphene Week 2022.

RECOGNITIONS

- 3× journal papers published were selected as ’Editor’s Choice’ in Nature Microsystems & Nanoengineering and Applied Physics Letters (April 2024).
- Authored the ’Most Read Journal Paper’ in Applied Materials & Interfaces (June 2022).
- Recognized as a ’Key Innovator’ by the European Commission’s Innovation Radar for significant contributions to the GrapheneCore3 project’s ’Graphene microphones on silicon,’ a ’Business Ready’ innovation with strong market potential (Link).